Universidad de Alcalá

Programa de Doctorado en Electrónica:

Sistemas Electrónicos Avanzados, Sistemas Inteligentes

Development of solar cells based on AlInN/Si heterojunctions growth by RF-sputtering

Tesis presentada por:

Rodrigo Blasco Chicano

2020

Universidad de Alcalá

DEPARTAMENTO DE ELECTRÓNICA
Edificio Politécnico
Campus Universitario s/n
28850 Alcalá de Henares (Madrid)
Teléfono: 918856540
Fax: 918856591
Dpto.electronica@uah.es

Dra. Sirona Valdueza Felip, Personal Investigador Ramón y Cajal de la Universidad de la Universidad de Alcalá

Dr. Fernando B. Naranjo Vega, Profesor Titular de la Universidad de la Universidad de Alcalá

INFORMAN:

Que la tesis doctoral titulada "Development of solar cells based on AlInN/Si heterojunctions growth by RF-Sputtering" presentado por D. Rodrigo Blasco Chicano, y realizada bajo la dirección de los doctores Dña. Sirona Valdueza Felip y D. Fernando B. Naranjo Vega dentro del campo de la Tecnología Electrónica, reúne los méritos de calidad y originalidad para optar al Grado de Doctor.

Alcalá de Henares, a 6 de Marzo de 2020

Fdo. Dña. Sirona Valdueza Felip

Fdo. D. Fernando B. Naranjo Vega

Universidad de Alcalá

DEPARTAMENTO DE ELECTRÓNICA
Edificio Politécnico
Campus Universitario s/n
28850 Alcalá de Henares (Madrid)
Teléfono: 918856540
Fax: 918856591
Dpto.electronica@uah.es

Dr. Miguel González Herráez, Coordinador del programa de Doctorado en Electrónica

INFORMA:

Que la tesis doctoral titulada "Development of solar cells based on AlInN/Si heterojunctions growth by RF-Sputtering" presentado por D. Rodrigo Blasco Chicano, y realizada bajo la dirección de los doctores Dña. Sirona Valdueza Felip y D. Fernando B. Naranjo Vega dentro del campo de la Tecnología Electrónica, reúne los méritos de calidad y originalidad para optar al Grado de Doctor.

Alcalá de Henares, a 6 de Marzo de 2020

Fdo. D. Miguel González Herraez

Universidad de Alcalá

UNIVERSIDAD DE ALCALÁ, PATRIMONIO DE LA HUMANIDAD

INFORME DEL DIRECTOR/A DE TESIS SOBRE "ANÁLISIS DE COINCIDENCIAS" DE LA TESIS DOCTORAL A TRAVES DEL PROGRAMA TURNITIN

Directores: Dr/a. Sirona Valdueza Felip, NIF 48340762Y y Fernando B. Naranjo Vega, NIF 02628403D. Universidad de Alcalá (ambos directores).

Autor de la tesis: D Rodrigo Blasco Chicano

Título de la tesis: Development of solar cells based on AlInN/Si heterojunctions growth by RF-sputtering.

Como director/es de la tesis citada, se informa que se ha procedido al análisis de coincidencias de la tesis doctoral a través del **programa informático Turnitin** establecido por la UAH, arrojando un porcentaje de coincidencias del 28 %.

Por tanto, se emite este informe a la Comisión Académica del programa para su aprobación de la defensa de la tesis.

Justificación de las coincidencias encontradas (obligatorio en caso de que el porcentaje supere el 24%):

Es de señalar que, del valor total de coincidencia encontrado, un 28 %, sólo el 14 % corresponde con coincidencias de magnitud igual o superior a un 1 %. El restante 14 % (numeración superior al 10 en el informe de originalidad generado por la aplicación) corresponden a frases de uso común en terminología científica y pies de figura y tablas, lo que aparece tanto en los índices de figuras y tablas como en ellas mismas.

En cuanto a las fuentes con mayor nivel de coincidencia, la primera fuente, con un 3 % de coincidencia, se corresponde con una publicación (physica status solidi (b) 1900575, 2020) en la que el autor de la tesis es primer autor, y que se realizó en colaboración con la Universidad Complutense de Madrid. La segunda fuente con mayor porcentaje de coincidencia (un 3%) se corresponde con un repositorio de tesis del sistema de educación en Francia, y que ha sido consultado por el autor, que tuvo acceso a las tesis desarrolladas en la temática en una estancia que realizó durante la tesis doctoral en CEA-Grenoble. En este caso, la mayor parte de las coincidencias se corresponden con conceptos teóricos y pies de figura y tablas en los capítulos 2 y 3.

La siguiente fuente con un nivel de coincidencia por encima del 1 %, es el repositorio de tesis doctorales de la UAH, y se relacionan con tesis desarrolladas en el propio grupo de investigación, en este caso, el grado de coincidencia es de un 2%. Las fuentes de coincidencia con un grado de similitud de un 1 % (fuentes del 4 al 9) están relacionadas con trabajos del estudiante y frases de uso común relacionadas con el tema de investigación.

Por todo lo anterior, los directores de tesis consideran que el porcentaje de coincidencias que arroja el informe no afecta a la novedad y originalidad de los resultados presentados.

En Alcalá de Henares, a 06 de marzo de 2020
El Director/s de la tesis

Fdo.: Sirona Valdueza Felip   Fernando Naranjo Vega

Informada la Comisión Académica:

Fecha: 6 de Marzo de 2020

Fdo.: Coordinador de la Comisión Académica del Programa

Universidad de Alcalá

Programa de Doctorado en Electrónica:

Sistemas Electrónicos Avanzados, Sistemas Inteligentes

DEVELOPMENT OF SOLAR CELLS BASED ON ALINN/SI HETEROJUNCTIONS GROWTH BY RF-SPUTTERING

Tesis presentada por:

RODRIGO BLASCO CHICANO

Directores:

DRA. SIRONA VALDUEZA FELIP

DR. FERNANDO B. NARANJO VEGA

2020

Agradecimientos

Hace ya algo más de 4 años comenzó un viaje que jamás pensé que emprendería, un viaje que comenzó de casualidad, como todas las grandes cosas. Aún recuerdo los primeros días como si fuera ayer, las millones de explicaciones que me dio Arántzazu de todos los sistemas de medida y del sputtering anotándolo todo pensando que jamás podría recordarlo. Por todo ello querría agradecerla todo lo que me ha enseñado y todas las preguntas, absurdas la mayoría, que tuvo que soportar durante los primeros meses y por la ayuda que me dio siempre para entender todo lo que hay detrás del mundo de los nitruros y del sputtering.

Obviamente querría agradecer a mis directores de tesis, la Dra. Sirona Valdueza Felip y el Dr. Fernando Bernabé Naranjo Vega. Muchísimas gracias por darme esta oportunidad de trabajar con vosotros, por enseñarme tantísimo y no solo de nitruros o de sputtering, por las risas, por ayudarme y enseñarme siempre que lo he necesitado, porque la verdad es que todo me ha servido para aprender. Espero que todo os vaya bien y que mi sucesor, Michael Sun, tenga mucha suerte con el desarrollo de su tesis.

Además de ello, también querría agradecer a los diferentes profesores del departamento de electrónica su ayuda durante estos cuatro años, especialmente al Dr. Miguel González Herráez, a la Dra. Sonia Martin López y a la Dra Ana Isabel de Andrés por su ayuda con diversas dudas que me surgieron a lo largo de la tesis y al Dr. Óscar Esteban Martínez por sus incomparables lecciones de la medida de la calidad del aceite y por ayudarme a mantener el feudo colchonero aun estando en minoría.

También, querría dar las gracias a la Dra. Eva Monroy por darme la oportunidad de trabajar en un sitio tan increíble como el CEA de Grenoble así como por la gran ayuda que me aporto durante mi estancia, una estancia que fue increíble gracias a la Mountain Mafia. Madalina, Marion, Romy, Akanksha, Saptarshi, Nathaniel, Felix…mil gracias por todos los momentos increíbles que me hicisteis pasar allí. Pero sin duda, de mi estancia, más allá de los resultados y un montón de medidas, me lleve a dos personas que valen muchísimo la pena y que, con solo conocerles, ya esta tesis ha merecido la pena, muchas gracias por todo a la Dra. Alba Lozano y al Dr. Akhil Ajay y, espero que sepáis que aquí tenéis un amigo para lo que necesitéis siempre.

Por otro lado, querría agradecer a todos los GRIFOs y GEISERs por los momentos más amenos de este trabajo, las comidas y charlas que, aunque fueran menos de las que me hubiera gustado, siempre fueron entretenidas.

No querría olvidarme de los diversos grupos de investigación y las diversas instituciones que han colaborado en la realización de esta tesis pero, especialmente querría dar las gracias al grupo de electrónica del Departamento de Estructura de la Materia, Física Térmica y Electrónica de la Universidad Complutense de Madrid, especialmente al Dr. Daniel Montero que, aparte de seguirme a todos lados en esta tesis, me ha ayudado en la mayoría de la caracterización de los dispositivos y en otras miles de cosas que no puedo poner aquí porque no acabaría.

También querría agradecer a Chechu, a Guille a Loli y a Jesús y al resto de los hipoglúcidos el estar ahí siempre y el poder contar con ellos para lo bueno y para lo mano como si fuesen mi familia.

Finalmente quiero agradecer a toda mi familia el soportarme durante estos 4 años, a mis tíos por acogerme con 18 años y no echarme a patadas conociendo como soy, a mis padres por los sacrificios que han hecho para que yo pudiera venir a estudiar a Madrid y por estar ahí siempre y a mi hermano, mi cuñada y mis sobrinos, por darme todo lo que he necesitado siempre aunque no lo haya pedido.

Espero que si no he mencionado a alguien me disculpe. Muchísimas gracias a todos y cada uno de vosotros.

Abstract

Nowadays III-Nitrides semiconductors are being proposed for electronic and opto-electronic devices due to their unique material characteristics, such as their wide direct bandgap, high thermal stability and high radiation hardness. Particularly, Aluminum Indium Nitride (AlInN) alloys offer great potential for photovoltaic devices thanks to their wide direct bandgap energy that covers the solar spectrum from 0.7 eV (InN) to 6.2 eV (AlN), and their superior resistance to high temperatures and high-energy particles.

Besides, III-nitrides compounds has been grown using different deposition techniques, such as Molecular Beam Epitaxy (MBE), Metalorganic vapour phase epitaxy-(MOVPE) or Radio Frequency (RF) Sputtering. This thesis is focused on this latest technique, which allows obtaining cheaper and larger devices than other deposition techniques and also deposition in a wide range of temperatures (from room temperature to values below 650°C in our case) and substrates.

Along this thesis, the influence of several parameters, such as AlInN bandgap energy, AlInN thickness and carrier concentration, silicon surface recombination, interface defects and Si wafer quality, on the photovoltaic properties of AlInN on silicon heterojunctions has been carried out using the Pc1d software, with the aim to explore their potential for solar cell devices through the analysis and optimization of the aforementioned parameters.

Besides, the effect of several growth parameters, such as the deposition temperature or the power supply applied to the In and the Al targets, on the structural, morphological, electrical and optical properties of $Al_xIn_{1-x}N$ compounds deposited on Si (111), Si (100) and sapphire substrates has been studied, showing similar properties of the $Al_xIn_{1-x}N$ layers growth on both silicon substrates regardless the orientation.

After that, the photoelectrical properties of solar cell devices based on $Al_xIn_{1-x}N$/Si heterojunctions has been studied as a function of the growth temperature and the Al power supply. Their J-V curve of the devices reveals the high influence of the growth temperature on the conversion efficiency of the devices.

Resumen

Hoy en día, los semiconductores III-Nitruros se están proponiendo para su aplicación en dispositivos electrónicos y optoelectrónicos debido a sus características únicas, como son su energía de gap, su alta estabilidad térmica y alta resistencia a la radiación. En ese sentido, las aleaciones de nitruro de aluminio e indio (AlInN) ofrecen un gran potencial para su uso como dispositivos fotovoltaicos dado que su energía de gap puede cubrir un amplio rango del espectro solar, yendo desde 0.7 eV (InN) hasta 6.2 eV (AlN), y además de las ya mencionadas resistencia a altas temperaturas y a la radiación.

Además, a lo largo de las últimas décadas, los compuestos del grupo III-V se han desarrollado utilizando diferentes técnicas de crecimiento, como el crecimiento epitaxial por haces moleculares (MBE), la epitaxia en fase de vapor con precursores metalorgánicos (MOVPE) o la pulverización catódica. Esta tesis se centra en esta última técnica, que permite obtener dispositivos más baratos y con mayor área que otras técnicas de depósito y también permite el crecimiento en un amplio rango de temperaturas (en nuestro caso desde temperatura ambiente hasta valores por debajo de 650 ° C) y sustratos.

A lo largo de esta tesis, se ha estudiado la influencia de varios parámetros de la heterounión basada en el AlInN y el silicio, como son la energía de gap del AlInN, su espesor y concentración de portadores, la recombinación en la superficie del silicio, densidad de defectos en la intercara y la calidad de oblea de Si, en sus propiedades fotoeléctricas mediante el uso del software Pc1d, con el objetivo de explorar su potencial como células solares a través del análisis y la optimización de dichos parámetros

Además de ello, se ha estudiado el efecto de varios parámetros de depósito, como la temperatura de crecimiento o la potencia aplicada a los blancos de indio y aluminio, sobre las propiedades estructurales, morfológicas, eléctricas y ópticas de los compuestos $Al_xIn_{1-x}N$ crecidos sobre sustratos de Si (111), Si (100) y zafiro; mostrando propiedades similares en ambos sustratos de silicio, independientemente de la orientación.

Tras ello, se han estudiado las propiedades fotoeléctricas de los dispositivos basados en heterouniones $Al_xIn_{1-x}N$ / Si en función de la temperatura de crecimiento y la potencia

aplicada al blanco de Al. La curva I-V de los dispositivos revela la alta influencia de la temperatura de crecimiento en la eficiencia de conversión de los dispositivos.

Index

Chapter 1 Introduction **1**

1.1 Motivation 1

1.2 Properties of III-nitrides 2

1.3 Growth of InN, AlN and AlInN 3

1.4 Application of III-nitride materials 4

1.5 Objectives 6

1.6 Organization of the manuscript 6

Chapter 2 Properties of III-nitrides **9**

2.1 Crystalline structure 9

2.2 Elastic properties 12

2.2.1 Structural defects 14

2.1.1.1 Point defects 14

2.1.1.2 Line defects (dislocations) 14

2.1.1.3 Planar defects (grain boundaries) 16

2.3 Optical properties 17

2.4 Spontaneous and piezoelectric polarization 20

Chapter 3 Solar cells **23**

3.1 Introduction to solar cells 23

3.2 Basics of semiconductors 24

3.2.1 Energy bands 25

3.2.2 Solar spectrum, air mass and absorption by semiconductors 26

3.2.3 Theory of semiconductors: properties and processes 28

3.2.3.1 Carrier concentration and transport 29

3.2.3.2 Generation and recombination 32

3.2.4 *P-N* junction 33

3.2.5 Analysis of current-voltage curves of solar cells 38

3.3 Types of solar cells 41

3.3.1 1st generation: crystalline silicon solar cells 42

3.3.2 2nd generation: thin film solar cells 44
3.3.3 3rd generation: organic and novel technologies 45
3.3.4 State of art of III-nitride-based solar cells 49

Chapter 4 Sputtering deposition technique **51**

4.1 Principles of sputtering 51
4.1.1 Plasma etching 53
4.1.2 Types of cathodes 53
4.1.3 Type of gas 55
4.2 Magnetron RF sputtering system used in this thesis 56
4.3 Substrates for III-nitrides deposition 58
4.3.1 Sapphire 59
4.3.2 Silicon (100) and (111) 60

Chapter 5 Characterization techniques **63**

5.1 Structural and morphological characterization 63
5.1.1 High-resolution X-ray diffraction 63
5.1.2 Atomic force microscopy 66
5.1.3 Field emission scanning electron microscopy 67
5.2 Optical characterization 67
5.2.1 Transmittance 67
5.2.2 Reflectance 69
5.2.3 Photoluminiscence 69
5.3 Electrical characterization: Hall Effect 71
5.4 Device fabrication 73
5.4.1 Transmission line method 74
5.4.2 Back *p*-type contact 77
5.4.3 Top *n*-type contact 80
5.5 Device characterization 82
5.5.1 Current-voltage measurements 83
5.5.2 Responsiviy measurements 84

Chapter 6 Design of AlInN on *p*-silicon heterojunction solar cells **87**
6.1 Pc1d software 87
6.2 Checking the Pc1d software for III-nitrides: InGaN-based junctions 88
6.3 AlInN on Si heterojunctions 90
6.3.1 AlInN simulation parameters 90
6.3.2 Optimization of AlInN on Si parameters 92
6.3.2.1 Effect of AlInN bandgap energy 93
6.3.2.2 Effect of AlInN thickness 95
6.3.2.3 Effect of AlInN *n*-type doping 96
6.3.2.4 Effect of interface defects 97
6.3.2.5 Effect of surface recombination rate 98
6.3.2.6 Effect of silicon wafer quality 100
6.3.2.7 Effect of anti-reflective layer 100
6.4 Comparison with a *p-n* silicon solar cell 102
6.5 Conclusions 102

Chapter 7 InN layers deposited by RF sputtering **105**
7.1 Effect of the growth temperature 106
7.1.1 Structural characterization 106
7.1.2 Morphological characterization 110
7.1.3 Electrical characterization 112
7.1.4 Optical characterization 113
7.2 Effect of the In RF power 115
7.2.1 Structural characterization 115
7.2.2 Morphological characterization 118
7.2.3 Electrical characterization 121
7.2.4 Optical characterization 122
7.3 Conclusions 124

Chapter 8 Growth of low-to-mid Al content $Al_xIn_{1-x}N$ on silicon by RF sputtering **127**
8.1 Influence of the Al RF power 127
8.1.1 Structural characterization 128

8.1.2 Morphological characterization 132
8.1.3 Electrical characterization 135
8.1.4 Optical characterization 136
8.2 Conclusions 140

Chapter 9 AlInN on Si heterojunctions: effect of deposition temperature **143**
9.1. Material deposition and characterization 144
9.1.1 Structural characterization 144
9.1.2 Morphological characterization 146
9.1.3 Electrical characterization 147
9.1.4 Optical characterization 148
9.2 Effect of deposition temperature on AlInN on Si devices 149
9.2.1 Dark current-voltage curves 149
9.2.2 Current -voltage curves under illumination 151
9.3 Conclusions 152

Chapter 10 AlInN on Si structures deposited at 550°C for solar cell devices **155**
10.1 Influence of the Al RF power on the material properties of AlInN layers 156
10.1.1 Structural characterization 157
10.1.2 Morphological characterization 159
10.1.3 Electrical characterization 160
10.1.4 Optical characterization 161
10.2 Effect of the Al RF power on the photoelectrical properties of AlInN on Si devices 167
10.2.1 Dark current-voltage curves 168
10.2.2 Current-voltage curves under one sun AM 1.5G illumination 169
10.2.3 Spectral response of the devices 172
10.3 Conclusions 173

Chapter 11 Conclusions and perspectives **175**
11.1 Simulations of AlInN on Si solar cells 175
11.2 Study of InN layers deposited by RF sputtering 176

11.3 Study of AlInN layers deposited by RF sputtering at 300°C 177
11.4 AlInN on Si heterojunctions: effect of the growth temperature 178
11.5 AlInN on Si structures grown at 550°C: effect of the Al mole fraction 179
11.6 Perspectives 180

References **183**

List of publications **205**

List of figures

Figure 1.1. Evolution and prediction of energy demand since 1800 until 2125 [Zou16]. 1

Figure 1.2. Bandgap energy range of the group III-nitride alloys as a function of the *a*-axis lattice constant compared with the solar spectrum [Val11]. 3

Figure 2.1. Crystalline structures and stacking periodicity of III-nitrides (a) zinc-blend and (b) wurtzite phases [Fre17]. 10

Figure 2.2 (a) Wurtzite unit cell with lattice parameters *a* and *c* together with the internal parameter *u*. (b and c) The differences in position of second nearest neighbors between wurtzite and zinc-blend structures [Sch14]. 10

Figure 2.3. (a) *c*-plane (0001), *m*-plane $(1\bar{1}00)$ and *a*-plane $(11\bar{2}0)$ of an hexagonal unit cell [Jef10]. 12

Figure 2.4. Schematic representation of the most common point defects in crystals. 14

Figure 2.5. Determination of the Burgers vector for: (a), (c) an edge dislocation and (b), (d) a screw dislocation [Kit96]. 16

Figure 2.6. Schematic representation of the micro crystals of an epilayer when (a) tilt and (b) twist are presented [Gok13]. 17

Figure 2.7. Relationship between the bandgap energy of $Al_xIn_{1-x}N$ and the Al content (from Wavelength dispersive X-ray (WDX)). The shadow area shows the difference from a bowing parameter expression using the band-gap of pure InN [Nuñ17]. 19

Figure 2.8. Bandgap filling due to the Burstein–Moss effect [Gib13].CB and VB stand for conduction and valence band respectively. 20

Figure 3.1. Scheme of the photovoltaic effect. 24

Figure 3.2. Scheme of band structure of a) metals, b) semiconductors and c) insulators. 25

Figure 3.3. Spectral power density of the Sun as a function of the wavelength: just outside of the atmosphere (AM0 radiation) and on the Earth surface (AM1.5 radiation), the lines are reference spectra of a blackbody at T ¼ 5800K, normalized to a total power density of AM0 (~1366 W m^{-2}) and of AM1.5G (~1000 W m^{-2}) [Nay12]. 27

Figure 3.4. Absorption of incoming photons with creation of electrons in the conduction band [Muk15]. 28

Figure 3.5. Drift velocity of nitrides semiconductors [Shu13]. 31

Figure 3.6. Scheme of the carrier movement (drift and diffusion) in a *p-n* junction in equilibrium. 32

Figure 3.7. Scheme of carrier recombination process in a semiconductor: a) band to band, b) Shockley-Read-Hall and c) Auger recombination. Et stands for trap energy that occurs in the Shockley-Read-Hall process. 33

Figure 3.8. Scheme of a *p-n* junction: the energy band-diagram of a *p-n* semiconductor (a) before and (b) after the formation of the junction in thermal equilibrium. (c) The depletion region W of the *p-n* junction [Yac03]. 35

Figure 3.9. Evolution of the depletion region and the energy band diagram as a function of the applied voltage a) under equilibrium condition without external bias (V = 0), b) under forward external bias ($V = +V_{in}$), and c) under reverse external bias ($V = -V_{in}$). [Muk15]. 36

Figure 3.10. J-V curves of a *p-n* junction under dark and illumination conditions [Wür05]. 37

Figure 3.11. Typical Current density-Voltage curves and device parameters obtained under a) dark conditions and b) under one sun illumination. 38

Figure 3.12. Electric scheme of a photovoltaic cell [Boy10]. 40

Figure 3.13. Example of Dark J-V fit using the step by step process. 41

Figure 3.14. 1st generation solar cells based on (left) monocrystalline Si and (right) polycrystalline Si [Sag10]. 43

Figure 3.15. 1st generation solar cells based on AlGaAs/GaAs heterojunction [http://pvlab.ioffe.ru/about/solar_cells.html]. 44

Figure 3.16. Schemes of solar cells based on a) amorphous silicon solar cells (a-Si) [Hua12] b) CdTe [Fer00] and c) CIGS [Ram17] technologies. 45

Figure 3.17. Schemes of solar cells based on a) dye sensitized [Naz11], b) polymers [Hop07], c) HIT solar cell [Kim12] , d) quantum dots [Emi11], e) perovskite materials [Shi18] and f) tandem solar cell [Bet14]. 48

Figure 3.18. Evolution of the bets research-cell efficiencies year by year [https://www.nrel.gov/pv/cell-efficiency.html]. 49

Figure 3.19. Scheme of GaN/InGaN quatum wells solar cells developed by Dahal *et al.* [Dah10]. 50

Figure 4.1. Scheme of a high-vacuum sputtering chamber and the sputtering process with all species involved. 52

Figure 4.2. Scheme of planar a) diode b) balanced magnetron and c) unbalanced magnetron configurations. 55

Figure 4.3. Hysteresis process in reactive sputtering [Lil12]. 56

Figure 4.4. Magnetron reactive RF sputtering system used during this thesis at the University of Alcalá. 57

Figure 4.5. Scheme of the epitaxial relationship between the III-nitrides compounds and sapphire in the (0001) plane [Mon15]. 59

Figure 4.6. a) Photo of a sapphire substrate and b) the AFM image of the substrate used along this thesis. 60

Figure 4.7. Relationship between hexagonal (111) and cubic (100) planes of silicon. The red-dashed triangle shows the relationship between Si cubic and hexagonal phases [Val11]. 60

Figure 4.8. a) Photo of *p*-silicon (111) substrate and b) the AFM image of the substrate used along this thesis. 62

Figure 4.9. a) Photo of *p*-silicon (100) substrate and b) the AFM image of the substrate used along this thesis. 62

Figure 5.1. Bragg´s diffraction law [Bask10]. 64

Figure 5.2. Scheme of a typical AFM setup in tapping mode [Zha09]. 66

Figure 5.3. Scheme of the transmittance setup of GRIFO laboratories of the University of Alcalá. 69
Figure 5.4. Schematic illustration of different types of radiative recombination. 70
Figure 5.5. Scheme of the PL system of GRIFO laboratory of the University of Alcala. 71
Figure 5.6. Scheme of Hall Effect measurements. 72
Figure 5.7. Hall Effect setup (left) and sample holder (right) of the Complutense University of Madrid. 73
Figure 5.8. Photograph of the hard masks used for TLM measurements for the back (left) and top (right) contacts for *p*-type Si and *n*-type AlInN, respectively. 75
Figure 5.9. Scheme of a transmission length method (TLM). 75
Figure 5.10. Evaluation of the contact and sheet resistances from TLM measurements [Ha13]. 76
Figure 5.11. Photograph of an Al-based TLM contact deposited on silicon by RF sputtering. 77
Figure 5.12. Current-voltage characteristics from TLM measurements. Each line corresponds to the measurement between two pads of the TLM with a different distance. Results of Al contacts deposited on *p*-type silicon (111) (a) without annealing and (b) after annealing the contacts for 3 min at 450ºC under nitrogen atmosphere (optimized receipt). 78
Figure 5.13. Evolution of the back-contact resistivity (120 nm of Al on *p*-type Si) as a function of a) the annealing temperature (for 3 min under nitrogen), b) the annealing time (at 450ºC under nitrogen) and c) the annealing atmosphere (at 450ºC for 3 min). 79
Figure 5.14. Image of the back contact (Al) deposited on silicon substrate. 80
Figure 5.15. Photograph of an Al-based TLM contact deposited on AlInN layers by RF sputtering. 81
Figure 5.16. Image of a) a hard mask fabricated for the top contact to *n*-type AlInN and b) a real top contact of an AlInN on Si solar cell device deposited using the hard mask. 82

Figure 5.17. Photograph of the 4-point probe station located in the Complutense University of Madrid used for dark current-voltage measurements. 83

Figure 5.18. Scheme of the responsivity setup located at University of Alcalá. 84

Figure 6.1. a) Absorption coefficient and transmittance (inset) spectra of the AlInN on sapphire samples as a function of the AlInN bandgap energy. (b) Carrier concentration vs the bandgap energy for the same samples. The Al mole fraction of each AlInN layer is also marked. 92

Figure 6.2. J-V (a) and EQE (b) curves of the AlInN on Si heterojunctions as a function of the AlInN bandgap energy. The evolution of the V_{oc} and J_{sc}, FF and efficiency vs the AlInN bandgap energy is plotted in (c) and (d), respectively. 94

Figure 6.3. J-V (a) and EQE (b) curves of the AlInN on Si heterojunctions as a function of the AlInN thickness. The evolution of the V_{oc} and J_{sc}, FF and efficiency vs the AlInN thickness is plotted in (c) and (d), respectively. 96

Figure 6.4. J-V (a) curves of the AlInN on Si heterojunctions as a function of the AlInN background doping. 97

Figure 6.5. J-V (a) and EQE (b) curves of the AlInN on Si heterojunctions as a function of the interface defects. The evolution of the V_{oc} and J_{sc}, FF and efficiency vs the interface defects is plotted in (c) and (d), respectively. 98

Figure 6.6. J-V (a) and EQE (b) curves of the AlInN on Si heterojunctions as a function of the surface recombination. The evolution of the V_{oc} and J_{sc}, FF and efficiency vs the surface recombination is plotted in (c) and (d), respectively. 99

Figure 6.7. a) EQE spectra of the optimized AlInN on Si heterojunctions with and without ARL. Surface reflectance of the device with ARL. Inset: parameters of the optimized AlInN on Si structure. b) Comparison of the EQE between the optimized AlInN on Si heterojunction and the Silicon homojunction, both with high quality Si and ARL. The AM1.5G an AM1.0 sun radiation spectra are also plotted. 101

Figure 7.1. 2θ/ω scans of the InN layers deposited on a) Si (100), b) Si (111) and c) sapphire as a function of the growth temperature. 108

Figure 7.2. 5×5 μm^2 AFM images of InN layers deposited in Si (111) (first column), Si (100) (second column) and sapphire (third column), as a function of the growth temperature. 111

Figure 7.3. SEM images of layers grown at 300°C on a) Si (100), b) Si (111) and c) sapphire substrates. 112

Figure 7.4. Squared absorption coefficient vs energy and transmittance vs wavelength (inset) of the InN on sapphire samples as a function of the growth temperature. 114

Figure 7.5. 2θ/ω scans of InN layers deposited on a) Si (100), b) Si (111) and c) sapphire as a function of the In power supply at 300ºC. 116

Figure 7.6. Evolution of the *c* lattice parameter as a function of the In power supply. 117

Figure 7.7. FESEM images of InN samples with a) P_{In} = 20 W, b) P_{In} = 30 W and c) P_{In} = 40 Won Si (100) (top left), Si (111) (top right) and sapphire (down) substrates at 300ºC. 119

Figure 7.8. AFM images of InN samples with P_{In}= 20 W (R1) , P_{In}= 30 W (R2) and P_{In} = 40 W (R3) grown on Si (100) (a, d and g), on Si (111) (b, e and h) and on sapphire (c, f and i) at 300ºC. 120

Figure 7.9. Transmittance as a function of the In power supply of the InN layers grown on sapphire. 122

Figure 7.10. Evolution of the optical bandgap energy as a function of the carrier concentration. The line describes the optical bandgap energy values calculated taking into account the Burnstein-Moss effect and including the conduction band nonparabolicity [Wal04a]. 123

Figure. 8.1. 2θ/ω scans of the $Al_xIn_{1-x}N$ layers on a) Si (100), b) Si (111) and c) sapphire as a function of P_{Al} estimated from HRXRD measurements. 129

Figure 8.2. Evolution of the Al mole fraction as a function of the Al power supply during the growth of the samples deposited on Si (111), Si (100) and sapphire, assuming fully relaxed layers. The error bars were calculated taking into account the results obtained by Nuñez *et al.* [Nuñ17]. 130

Figure 8.3. Evolution of the *c* lattice parameter as a function of the aluminum power supply. 132

Figure 8.4. FESEM images of samples a) S1, b) S3 and c) S5 on Si (100) (top left), Si (111) (top right) and sapphire (down). 133

Figure 8.5. a) Variation of the rms surface roughness of $Al_xIn_{1-x}N$ layers as a function of the aluminum power supply; AFM images of InN, $Al_xIn_{1-x}N$, P_{Al} = 150W and $Al_xIn_{1-x}N$, P_{Al} = 225W grown on Si (100) (a, b and c), on Si (111) (d, e and f) and on sapphire (g, h and i). 134

Figure 8.6. Evolution of the carrier concentration and resistivity as a function of the Al mole fraction (squares) and comparison with obtained by Nuñez *et al.* [Nuñ17] (triangles). Open circles show the expected value for samples with an Al mole fraction above 0.38. 136

Figure 8.7. a) Squared absorption coefficient vs energy and transmittance of the $Al_xIn_{1-x}N$ layers grown on sapphire vs wavelength (inset) and b). The bandgap energy of $Al_xIn_{1-x}N$ as a function of the Al composition and the comparison with the bowing parameters obtained with this study (black line), other study using the sputtering technique by Nuñez *et al.* (red line) [Nuñ17] and a bowing parameter using the bandgap of a pure InN growth by MBE (green line) [Ter06]. 137

Figure 8.8. Normalized low-temperature (10 K) PL emission of the $Al_xIn_{1-x}N$ on a) Si (100) b) Si (111) and c) sapphire substrates. For $x > 0.36$ no PL emission was observed. 139

Figure 8.9. a) Photoluminescence spectra of InN layer grown on sapphire as a function of the temperature and b) its evolution of the PL emission energy vs the temperature. 139

Figure 8.10. Evolution of the integrated PL intensity as a function of the temperature of samples (S1, S2 and S3) grown on sapphire. 140

Figure 9.1. 2θ/ω scans of the $Al_xIn_{1-x}N$ layers on a) Si (100) and b) Si (111). 145

Figure 9.2. 5×5 μm^2 AFM images of of $Al_xIn_{1-x}N$ layers deposited on Si (111) and Si (100) at RT (a,d), 300°C (b,e) and 550°C (c,f). 146

Figure 9.3. Evolution of the rms surface roughness of the AlInN on Si (111) and Si (100) layers as a function of the growth temperature. 147

Figure 9.4. Transmittance of the $Al_xIn_{1-x}N$ layers grown on sapphire vs the deposition temperature. 148

Figure 9.5. Dark current density vs voltage curves of AlInN devices deposited on a) Si (100) and b) Si (111) as a function of the deposition temperature. 150

Figure 9.6. Current density-voltage curves of devices as a function of deposition temperature under halogen lamp illumination (P_{in} ~ 0.02 sun).a) Si (100) b) Si (111). 151

Figure. 10.1. 2θ/ω scans of the AlInN on a) Si (100) and b) Si (111) structures vs P_{Al}. c) Al mole fraction *x* of the $Al_xIn_{1-x}N$ layers estimated from the average of both XRD measurements for AlInN on Si (100) and Si (111) as a function of P_{Al}. The Al mole fraction estimation owns an error bar of ~1-4% depending on the Al mole fraction, as obtained previously by this group [Nuñ17]. 157

Figure 10.2. Evolution of the rocking curve of the $Al_xIn_{1-x}N$ layers deposited on a) Si (100) and b) Si (111) estimated from XRD measurements. 158

Figure 10.3. AFM (5×5 μm^2) pictographs of AlInN layers on Si (111) a), b) and c) and on Si (100) d), e) and f) as a function of the Al mole fraction. 160

Figure 10.4. a) Evolution of the carrier concentration (solid line), the layer resistivity (dotted blue line) and b) the carrier mobility as a function of the Al mole fraction. 161

Figure 10.5. Optical transmission spectra of $Al_xIn_{1-x}N$ (~90 nm) on sapphire films vs the Al mole fraction *x.* 162

Figure 10.6. Reflectance measurements of AlInN layers deposited on a) Si (100) and b) Si (111). 163

Figure 10.7. Normalized low-temperature PL emission of the $Al_xIn_{1-x}N$ on Si (100) samples vs the Al mole fraction. For $x > 0.35$ no PL emission was observed. 164

Figure 10.8. a) Evolution of PL emission spectra as a function of the temperature for InN on Si (100) sample (D_01) and b) Evolution of the PL emission energy vs the temperature of the same sample. 165

Figure 10.9. a) Evolution of PL emission spectra as a function of the temperature for InN on Si (100) sample D_03 and b) evolution of the PL emission energy vs the temperature of the same sample. 166

Figure 10.10. Evolution of the normalized integrated PL intensity as a function of the temperature for the InN (D_01) and the $Al_{0.28}In_{0.72}N$ on Si (100) samples (D_03). 167

Figure 10.11. Evolution of the top contact resistivity as a function of the Al power supply (P_{Al}). 168

Figure 10.12. Dark J-V measurements of a) AlInN/Si (100) and b) AlInN/Si (111) devices. 169

Figure 10.13. Current density-voltage curves of devices deposited on a) Si (100) and b) Si (111) as a function of Al power supply under ones sun AM 1.5G illumination. 170

Figure 10.14. Influence of the Al mole fraction x on the responsivity of the $Al_xIn_{1-x}N$ on (a) Si (100) and (b) Si (111) devices vs the wavelength. 173

List of tables

Table 2.1. Lattice parameters and thermal expansion coefficients of AlN, GaN and InN at room temperature. The values are taken from [Rum01] [Vur03] and [Mat99]. 11

Table 2.2. Elastic tensor component [Vur03] and piezoelectric coefficients [Vur01] for AlN, GaN and InN. 13

Table 2.3. Experimental values of $E_g(0)$, E_g at room temperature and Varshni parameters γ and β for the different III-nitride binary compounds. Data obtained from [Vur03]. 18

Table 2.4. Spontaneous polarization for wurtzite structure of AlN, GaN and InN with metal polarity. Data obtained from [Vur03]. 21

Table 4.1. Summary of lattice parameters and thermal expansion coefficients of III-nitrides [Vur03] and silicon (on both orientations) and sapphire substrates [Neu96]. Lattice and thermal mismatch between III-nitrides and the substrates are at 300 K and $\Delta\alpha_{epi}$ and Δa_{epi} are the difference between the lattices parameter and the thermal expansion coefficient of the layer and the substrate, respectively. 61

Table 5.1. Summary of the top contact resistance as a function of the Al mole fraction. 81

Table 6.1. Summary of the material parameters of GaN and InN included in the Pc1d software to develop the simulations of InGaN homo and heterojunctions [Fab14]. 88

Table 6.2. Comparison of the simulation results obtained for different InGaN-based junctions with Pc1d software and the ones obtained by Fabien *et al.* [Fab14]. 90

Table 6.3. Summary of the material parameters of AlN and InN included in the Pc1d software to develop the simulations of the AlInN/Si heterojunctions. Notes: *Obtained from Fabien et al. [Fab14]. **Obtained from experimental measurements. 91

Table 6.4. Comparison of the simulation results obtained for different InGaN-based junctions with Pc1d software and the ones obtained by Fabien *et al.* [Fab14]. 102

Table 7.1. Summary of the growth temperature of the InN samples deposited at P_{In} = 40 W. 106

Table 7.2. Evolution of the FWHM of the rocking curve of the InN layers grown on Si (100), Si (111) and sapphire extracted from HRXRD measurements. 109

Table 7.3. Evolution of the strain along the *c*-axis of the InN layers grown on Si (100), Si (111) and sapphire extracted from HRXRD measurements. 109

Table 7.4. Evolution of the grain size of the InN layers grown on Si (100), Si (111) and sapphire estimated from HRXRD measurements. 109

Table 7.5. Summary of the rms surface roughness values of the InN layers deposited on Si (100), Si (111) and sapphire as a function of the growth temperature. The values with an (*) can be affected by the morphology of the layers. 112

Table 7.6. Summary of the electrical characteristics of the InN samples grown on sapphire: InN resistivity, carrier concentration and carrier mobility, obtained by Hall Effect measurements. 113

Table 7.7. Summary of the optical properties obtained at room temperature: apparent bandgap energy (E_g) and absorption band edge broadening (ΔE) of the InN on sapphire samples. 115

Table 7.8. Summary of the deposition conditions of the InN samples. 115

Table 7.9. Evolution of the strain along the *c*-axis of the InN layers grown on Si (100), Si (111) and sapphire extracted from HRXRD measurements. 117

Table 7.10. Evolution of the FWHM of the rocking curve of the InN layers grown on Si (100), Si (111) and sapphire extracted from HRXRD measurements. 118

Table 7.11. Evolution of the grain size of the InN layers grown on Si (100), Si (111) and sapphire estimated from HRXRD measurements. 118

Table 7.12. Summary of thickness and growth rate of layers grown on Si (111), Si (100) and sapphire. 119

Table 7.13. Summary of the rms surface roughness values of InN layers as a function of P_{In} for the three substrates. 121

Table 7.14. Summary of the electrical characterization of the InN samples grown on sapphire: layer resistivity, carrier concentration and carriers mobility, obtained by Hall Effect measurements. 121

Table 7.15. Summary of the optical properties obtained at room temperature: absorption edge (E_g) and absorption band edge broadening (ΔE) of the samples growth on sapphire. 123

Table 8.1. Value of RF power applied to the Al target (P_{Al}) for each sample of the studied set. 128

Table 8.2. Summary of the structural analysis of $Al_xIn_{1-x}N$ on Si (100): layer thickness estimated from FESEM; *c*-axis parameter and Al mole fraction *x* extracted from HRXRD. 131

Table 8.3. Summary of the structural analysis of $Al_xIn_{1-x}N$ on Si (111): layer thickness estimated from FESEM; *c*-axis parameter and Al mole fraction *x* extracted from HRXRD. 131

Table 8.4. Summary of the structural analysis of $Al_xIn_{1-x}N$ on sapphire layer thickness estimated from FESEM; *c*-axis parameter and Al mole fraction *x* extracted from HRXRD. 132

Table 8.5. Evolution of the root mean square as a function of the Al power supply. 135

Table 8.6. Summary of the electrical characterization of the $Al_xIn_{1-x}N$ samples grown on sapphire obtained by Hall Effect measurements. 135

Table 8.7. Summary of optical properties obtained by transmittance measurements. 138

Table 9.1. Summary of the deposition conditions of the AlInN samples vs the substrate temperature. 144

Table 9.2. Summary of the structural analysis of $Al_xIn_{1-x}N$ on Si (100) layers. 145

Table 9.3. Summary of the structural analysis of $Al_xIn_{1-x}N$ on Si (111) layers. 145

Table 9.4. Summary of the electrical properties of $Al_xIn_{1-x}N$ on sapphire samples. 147

Table 9.5. Summary of the optical properties of $Al_xIn_{1-x}N$ on sapphire layers obtained from this work (~ 90 nm) and for thicker layers (~ 550 nm) vs the growth temperature. 148

Table 9.6. Summary of electrical properties of devices based on AlInN deposited on Si (100). * The area was calculated taking into account the shadow of the top contact (~ $0.13cm^2$). 150

Table 9.7. Summary of electrical properties of devices based on AlInN deposited on Si (111). * The area was calculated taking into account the shadow of the top contact (~ $0.13cm^2$). 151

Table 10.1. Value of RF power applied to the Al target (P_{Al}) for each sample of the studied set. 156

Table 10.2. Summary of the structural and morphological properties of the AlInN on Si (100) samples. 159

Table 10.3. Summary of the structural and morphological properties of the AlInN on Si (111) samples. 159

Table 10.4. Summary of the optical properties of $Al_xIn_{1-x}N$ on sapphire layers obtained from this chapter and from thicker layers grown at 300°C (chapter 8). 162

Table 10.5. Summary of the electrical and photovoltaic characteristics of the AlInN on Si (100) devices. 171

Table 10.6. Summary of the electrical and photovoltaic characteristics of the AlInN on Si (111) devices. 172

Chapter 1
Introduction

This chapter relates the state of art of the growth of III-nitride semiconductor compounds, mainly InN, AlN and AlInN, and their application to solar cell devices. Besides, the motivation, the main goals and the outline of this thesis are described along this chapter.

1.1 Motivation

The energy problem is currently one of the biggest problems of our time. The constant demographic increase and the arrival and development of electronic devices such as computers or mobile phones have meant to an increasingly global energy demand in the last decades and a continuous rise is foreseen for the coming years, as depicted in figure 1.1. In this sense, and thanks to the awareness of the climate change, renewable energies such wind and solar energy have become more and more important with the aim of producing cheaper and cleaner energy for global consumption.

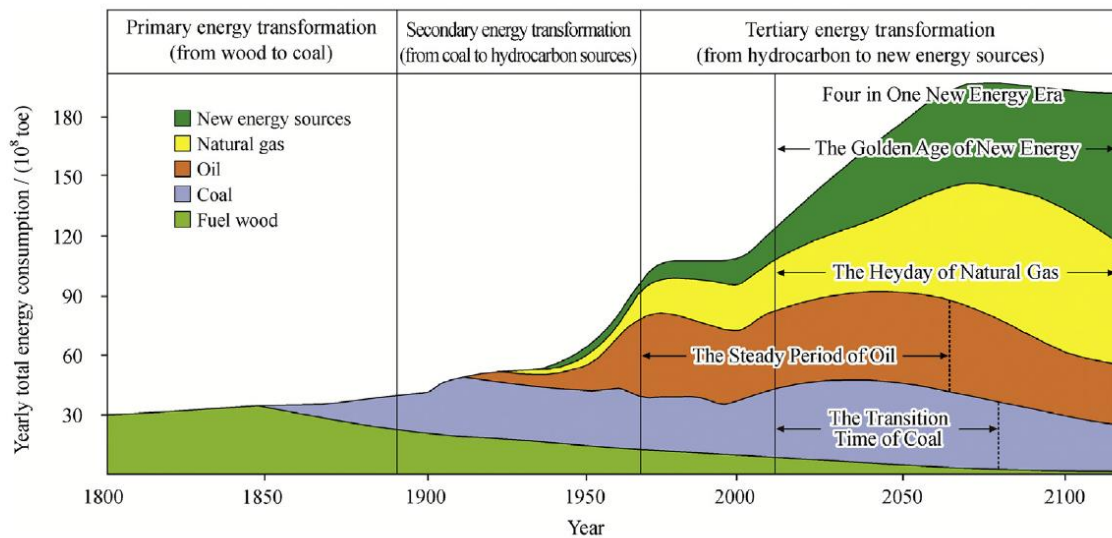

Figure 1.1. Evolution and prediction of energy demand since 1800 until 2125 [Zou16].

The potential of solar energy is much higher than the one of fossil fuels energy and of any other renewable energy inasmuch as the solar energy that arrives to the Earth during one hour is more than the world energy consumption in a year.

Beside this, two main technologies compose the solar energy production:

- Solar thermal energy, which is based on taking advantage of the incident thermal energy to heat a fluid and produce energy.
- Photovoltaic energy, which converts the solar energy directly into electricity using semiconductor materials.

Along this thesis, we will focus only on photovoltaic energy. Currently, ~90% of the solar panels are based on silicon technology, which hold commercial conversion efficiencies ≈18% and a prize per watt below 0.4€/W [Rig20].

Nowadays, the main goal of the photovoltaic industry is to reduce the cost of the solar cells as well as improving their efficiency simultaneously.

In this sense, the integration of the novel III-nitride semiconductor materials with the mature and relatively cheap silicon technology may allow the production of highly efficient and low-cost solar cells. Several studies, such as the carried out by Martí *et.al.* reveal that the theoretical efficiency for tandem solar cells with multiple bandgap materials is 31% for one junction and can be increased to 53% for a tandem solar cell based on 4 junctions under 1 sun of standard illumination [Mar96]. Besides, as detailed by Lal *et al.* [Lal17], a tandem solar cell based on the silicon technology reveals a conversion efficiency of 47% for a tandem solar cell based on 4 junctions under one sun of standard illumination (AM 1.5G).

1.2 Properties of III-nitrides

III-nitride semiconductors (InN, GaN and AlN) have become very popular in the last two decades in optoelectronic applications due to their particular mechanical and chemical properties, such as the high radiation hardness, high thermal resistivity and high mechanical hardness [Amb98, Neu96]. Besides, one of the main reasons is the suitability to tune the bandgap from the ultraviolet (6.2 eV for AlN) to the near infrared (≈0.64 eV for InN) [Vur03] spectral range by changing the composition of the AlInN and InGaN alloys, as shown in figure 1.2.

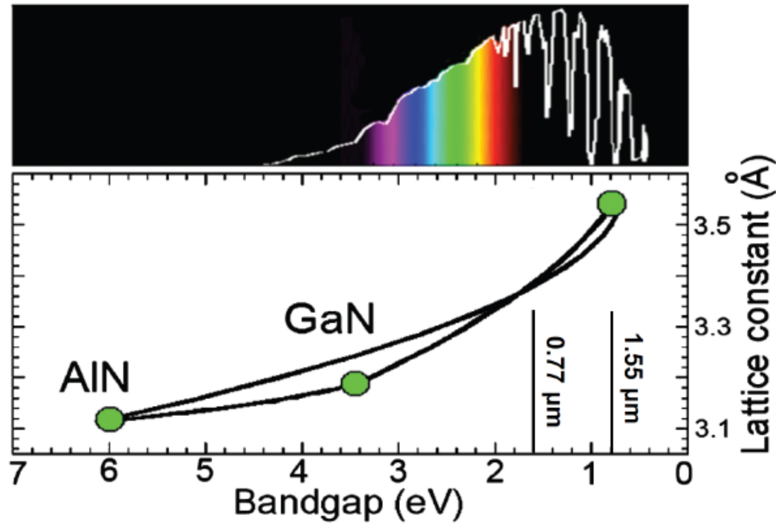

Figure 1.2. Bandgap energy range of the group III-nitride alloys as a function of the *a*-axis lattice constant compared with the solar spectrum [Val11].

Concretely, InN shows a low effective mass, a high electron mobility [Bhu03], and a bandgap energy that varies from 0.64 eV [But05] to 2 eV [Tan86, Sta00] depending on the carrier concentration of the layer. Besides, GaN layers and its alloys have also a high carrier mobility and a high drift velocity [Val11, Bhu12] with a bandgap energy around 3.4 eV in the visible spectral range [Fer17]. Furthermore, AlN layers present specific properties such as a large bandgap energy in the ultraviolet spectral range (6.2 eV) and a strong piezoelectricity [Kua12]. As a consequence of these properties, III-nitrides compounds have become very interesting materials for electronic applications.

Furthermore, the ternary alloys (AlInN and InGaN) are also very interesting for electronics, optoelectronics and photonics, due to their tunable bandgap from 0.64 eV to 3.4 eV for InGaN and from 0.64 eV to 6.2 eV for AlInN as a function of the alloy mole fraction, offering a wide variety of possibilities to develop different devices within the UV to the IR spectral range, depending on the desired application.

However, in this thesis we will focus on the study of InN, AlN and AlInN alloys for the development of solar cells, so from now on next sections will focus on these materials.

1.3 Growth of InN, AlN and AlInN

There are many reports about the growth of InN, AlN and AlInN materials using different ultra-high vacuum deposition techniques such as molecular beam epitaxy (MBE) [Che14, Che14, Lob16, Kar97, Nao07, Sai02, Spe04, Wu14, Yam09] and metalorganic vapor

phase epitaxy (MOVPE) [Ale06, Abh04, Cao02, Kel03, Ras16, Yam94] achieving single-crystalline films with high crystalline quality. However, these techniques require high maintenance cost due to the deposition under ultra-high vacuum and at high temperatures.

In that sense, the sputtering is a high vacuum deposition technique that allows the growth of III-nitrides with lower cost due to the possibility of deposition at low temperature and even at room temperature. Moreover, there are many materials available as targets and homogeneous deposition can be done on large area substrates. These advantages make the sputtering deposition technique exportable to the industry. However, the crystalline quality of the layer is lower than the one obtained by other techniques as MOVPE and MBE mainly due to the higher vacuum used in these techniques.

Along last decades, the sputtering technique has been used to growth InN [Ami11, Har16, Val12, Yam09], AlN [Gil17, Guo06, Kum17, Liu17] and AlInN layers [Afz14, Afz16, Don09, He10, Guo08, Nuñ16, Nuñ17, Yeh08] under different growth conditions and mainly on Si, sapphire and glass substrates for different targeted applications. In that sense, most of these reports use a plasma based on a mixture of N_2 and Ar gases. However, in this thesis we use a pure nitrogen plasma as reactive gas in order to achieve better crystalline properties in the layers, as demonstrated in previous results carried out by Guo *et al.* [Guo99] and also by our group [Nuñ16, Val10].

1.4 Application of III nitride materials

Nowadays III-nitrides are used in light-emitting diodes (LEDs), detectors, laser emitters with application in data storage or traffic light and the recent fast chargers for mobile phones based on GaN, among others. Besides, their aforementioned chemical, mechanical and optical properties makes them suitable candidates for power electronics.

The properties of InN layers lead to propose this material as a candidate for several opto-electronic applications in the IR spectral region, such as solar cells, optical coatings and contact layers [Bhu03, Yam94, Mal03, Wu09].

On the other hand, the bandgap energy of AlN films are suitable for devices in the ultraviolet region such LEDs [Jeo15, Sch11, Wu15] or laser diodes [Kne07]. Besides, AlN layers are usually used as buffer layer to reduce the lattice mismatch between the nitride layer and the substrate [Çör11, Pra09, Yu19].

The ternary alloy AlInN has application in the visible spectral region, as light-emitting devices [Muz15, Wei15], Bragg reflectors [Ber13, Ber15, Kro10], electron mobility transistors [Esp15, Sai15] and also as solar cells [Liu12, Liu 13], as will be detailed below.

III-nitride based solar cells

As explained above, the wide bandgap energy of the ternary compounds based on III-nitrides and their mechanical and chemical properties have made them very interesting for the new generation of solar cells.

Actually, the bandgap energy of AlInN and InGaN alloys can be modified as a function of the indium composition in order to obtain multijunction solar cells that can cover completely the solar spectrum, as theory indicates. Theoretical simulation predict a record conversion efficiency, which varies from 56% for 3 junctions to 70% for 8 junctions, changing the bandgap energy of each layer of the junction as presented by Omkar K. Jani [Jan08].

However, the poor miscibility of InN and the mismatch of the III-V compounds during its deposition onto substrates with different lattice and thermal expansion coefficient [Par05, Col13] lead to some problems during the growth of the epitaxial layers, such as phase separation, which causes high defect density (up to 10^{8} cm^{-2}) [Laz13, Pri17], leading to a lower optical and electrical quality. Besides, the problem to achieve III-nitrides with an efficient *p*-type doping [Pam17] leads to increase the cost production, being this a remaining issue to solve to have a competitive technology.

For this reason, III-nitrides are also investigated to complete an already known solar cell technology, such silicon or gallium arsenide, and improve their mechanical, thermal, optical and electrical properties. In that sense, InGaN based solar cells are currently under development reaching efficiency values of 5.95% for an $In_xGa_{1-x}N$/GaN-based multiple quantum wells (MQW) using a SiCN/Si (111) substrate and an indium tin oxide (ITO) film as an antireflective layer [Lio11].

On the other hand, the development of AlInN layers for solar cell applications has been less studied than InGaN, leading to a very few reports of solar cells based on this technology. There are some developed by the group of Liu *et al.*, which reaches a conversion efficiency record of 1.1% [Liu12], and by our group, which has obtained the record of technology efficiency, reaching a conversion efficiency of 2.5% [Bla18].

1.5 Objectives

This thesis is focused on the study of the structural, morphological, electrical and optical properties of InN and AlInN layers deposited by radio frequency sputtering on Si (111), Si (100) and sapphire substrates with the aim of developing solar cells in combination with silicon. Particularly, the photoelectrical properties of devices based on (Al)InN on Si (111) and Si (100) are presented. The main targets of this thesis are explained below:

- To explore the theoretical limits of the proposed AlInN-on-Si structure working as a solar cell through the optimization of the main material and device parameters using the PC1D solver.
- To optimize the growth conditions of InN layers, namely the growth temperature from 20ºC to 450°C and the RF power applied to the In target P_{In} from 20 W to 40 W to obtain high-quality layers on silicon substrates. The optimized parameters (300ºC and P_{In} = 30 W) will serve as starting point for the optimization of the AlInN alloy.
- To optimize the growth conditions of the AlInN layers, namely the growth temperature from 20ºC to 550°C at P_{In} = 30 W, and the RF power applied to the Al target P_{Al} from 0 W to 225 W at 300ºC with the aim to obtain high quality AlInN layers covering the whole visible spectral range.
- To study the photovoltaic properties of AlInN devices on Si (111) and Si (100) as a function of the temperature (from RT to 550 ºC). The optimized temperature (550°C) will be used as starting point for the next study.
- To study the influence of the AlInN bandgap energy on the photovoltaic performance of AlInN on Si devices.
- To study the influence of the crystal orientation of the Si substrate on the material quality and device performance of all the (Al)InN on Si structures developed along this thesis.

1.6 Organization of the manuscript

This thesis is divided into 11 chapters. After the present introduction which corresponds to Chapter 1, Chapter 2 summarizes the main properties of III-nitrides materials, focusing on a wurtzite structure. After that, Chapter 3 describes the main concepts and theory of solar cell devices along with a updated state of art.

Chapter 4 details the principles of the growth technique (RF-sputtering) used along this thesis. Meanwhile, the characterization techniques used to study the properties of the layers and of the devices are described in Chapter 5. Chapter 6 relates the design and optimization of *n*-AlInN on *p*-silicon structures to operate as heterojunction solar cell by simulations.

Chapter 7 and 8 present the study of the III-nitride layers growth by RF-sputtering. Concretely, Chapter 7 is based on the study of the structural, morphological, electrical and optical properties of InN layers deposited on silicon (111), silicon (100) and sapphire as a function of the growth temperature and the indium power supply. Meanwhile, Chapter 8 describes the effect of the growth temperature and the aluminum power supply on the properties of AlInN layers deposited on the same substrates and under the same conditions than in previous chapter.

On the other hand, Chapter 9 and 10 describe the effect of the deposition conditions on the material properties of the nitride layers and on the photoelectrical properties of AlInN/Si (111 or 100) devices.

In that sense, in Chapter 9, analyze the effect of the growth temperature on the photovoltaic properties of the AlInN/Si heterojunctions and, once the optimum temperature is obtained, Chapter 10 relates the effect of the Al power supply as a function of the AlInN layer and AlInN/Si devices properties.

Finally, Chapter 11 summarizes the main conclusions achieved along this thesis and exposes various ideas to continue and complete the work here.

Chapter 2

Properties of III-nitrides

This chapter summarizes the main characteristics of III-nitride semiconductor materials. The first section shows the most common crystalline structures feasible for these materials (zinc-blend and hexagonal wurtzite phases) and their lattice parameters. After that, this study is focused on the wurtzite structure, as it is the most stable structure at room temperature. All the layers grown during this thesis own this structure.

In the second section of this chapter, the structural and optical properties of the III-nitrides are described and, finally the spontaneous and piezoelectric polarization generated along the *c*-axis are presented with the aim of explaining the properties of the layers that will be studied throughout the thesis.

2.1 Crystalline structure

The wurtzite phase of III-nitride semiconductors (AlN, GaN, InN and their alloys) is the most thermodynamically stable phase. However, zinc-blend and rocksalt structures can be achieved on cubic substrates (100 orientation) by epitaxial growth and under very high pressures, respectively.

In wurtzite structure, each group-III atom is coordinated with four nitrogen atoms, presenting a tetrahedral bonding between nearest neighbors. The main difference between zinc-blend and wurtzite phases is the stacking sequence: ABCABCA in the <111> direction for zinc-blend phase and ABABA for wurtzite phase along <0001> direction (figures 2.1 (a) and (b), respectively). This difference leads to the formation of inclusions of one structure in the other one in epitaxial layers, resulting in defects like stacking faults.

As said previously, this work is focused on wurtzite structure and the following chapters will only address the properties III-nitrides with this structure.

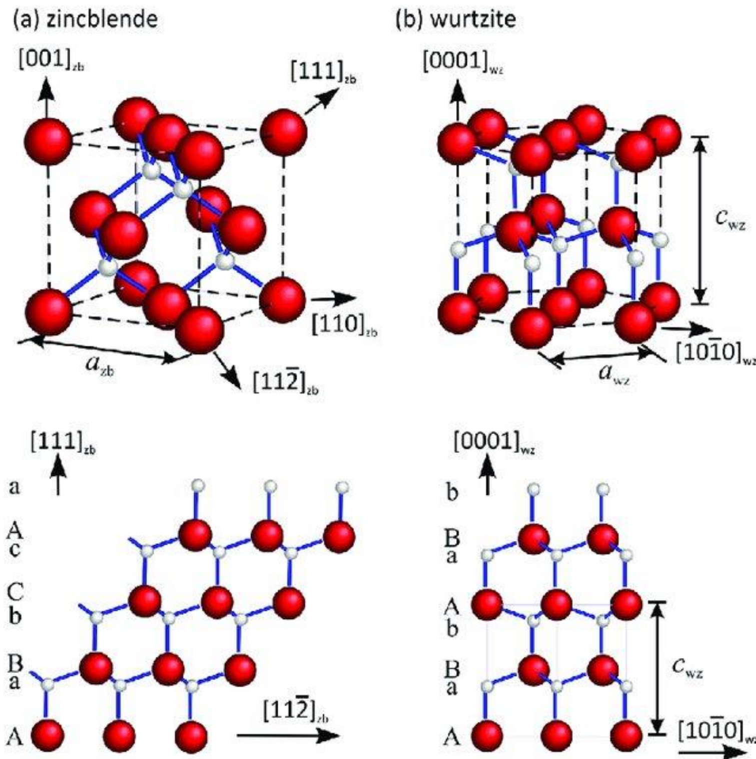

Figure 2.1. Crystalline structures and stacking periodicity of III-nitrides (a) zinc-blend and (b) wurtzite phases [Fre17].

The wurtzite structure consists of a hexagonal unit cell defined by the lattice constants *a* and *c*, the edge length of the basal hexagon and the height of the hexagonal prism, respectively (figure 2.1(b)). The third characteristic parameter is the anion-cation bond length along the [0001] axis, the so-called internal parameter, *u* (see figure 2.2 (a)).

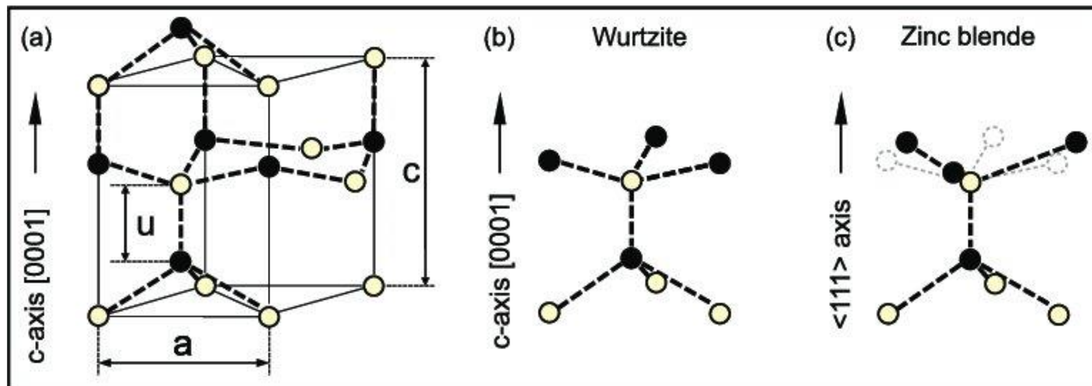

Figure 2.2 (a) Wurtzite unit cell with lattice parameters *a* and *c* together with the internal parameter *u*. (b and c) The differences in position of second nearest neighbors between wurtzite and zinc-blend structures [Sch14].

The structure has six atoms of each type and is formed by two hexagonal closed packaged interpenetrated sublattices, one constituted by metal atoms and another by nitrogen atoms. Both sublattices are shifted ideally by a distance 5/8 times the value of the c lattice constant along the [0001] direction. The deviation from the ideal ratios u/c = 0.375 and c/a = 1.633 is a measure of the non-ideality of the crystal.

Table 2.1 presents the lattice parameters (a, c and internal parameter u) and the thermal expansion coefficients of the III-nitride binary compounds. The a/c ratio is also shown in the table.

Parameters	**Ref.**	**AlN**	**GaN**	**InN**
a (Å)	[Rum01]	3.112	3.189	3.545
c (Å)	[Rum01]	4.982	5.185	5.703
c/a	[Rum01]	1.601	1.626	1.680
u (Å)	[Mat99]	1.892	1.949	2.156
u/c	[Mat99]	0.379	0.376	0.378
α (a) (10^6/K)	[Vur03]	4.2	5.6	3.8
α (c) (10^6/K)	[Vur03]	5.3	3.2	2.9

Table 2.1. Lattice parameters and thermal expansion coefficients of AlN, GaN and InN at room temperature. The values are taken from [Rum01] [Vur03] and [Mat99].

In the case of the ternary compounds, the lattice parameters can be obtained assuming a linear interpolation taking into account the mole fraction of the components using Vegard´s law [Veg21]:

$$a_{A(1-x)Bx} = (1-x)a_A + xa_B \tag{2.1}$$

The crystal planes of a hexagonal unit cell are identified by Miller-Bravais indices, denoted by the letters {h, k, i, l}. These indices are related to the projection of the given direction on the vectors of the basic cell $(\overrightarrow{a_1}, \overrightarrow{a_2}, \overrightarrow{a_3}, c)$ respectively. In that sense, $\overrightarrow{a_1}, \overrightarrow{a_2}, \overrightarrow{a_3}$ represent the basal axes and c represents the vertical axis of the hexahedron. Since the sum of the first three indices is zero $i = -h + k$ $(else\ \overrightarrow{a_3} = -\overrightarrow{a_1} + \overrightarrow{a_2})$; a (*hkl*) plane is equivalent to (*hkil*). In the case of the hexagonal system, the [*hkil*] direction is perpendicular to the (*hkil*) plane for some particular plane families.

As an example the planes perpendicular to (0001), $(1\bar{1}00)$ and $(11\bar{2}0)$ directions are the sop-called c-plane, m-plane and a-plane, respectively (see figure 2.3).

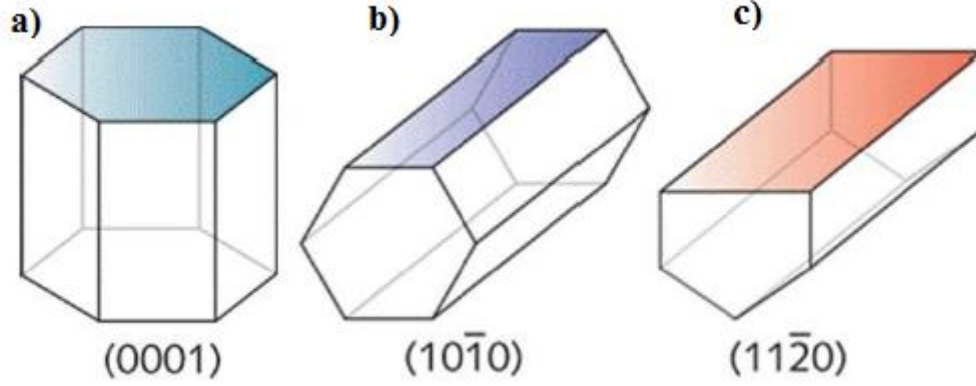

Figure 2.3. (a) *c*-plane (0001), *m*-plane $(1\bar{1}00)$ and *a*-plane $(11\bar{2}0)$ of an hexagonal unit cell [Jef10].

2.2 Elastic properties

The absence of an appropriate substrate for the deposition of III-nitrides, in terms of lattice parameters and thermal expansion coefficient, leads to an heteroepitaxial growth between the III-nitride layer and the substrate, generating tensile or compressive strain in the growth layers.

This effect is because the layers starts to grow with the same lattice parameter as the substrate but, this implies an accumulation of elastic energy, which increases with the layer thickness. When the accumulated elastic energy overcomes a given threshold, the relaxation of the layer starts with the formation of misfit defects. The corresponding thickness (critical thickness) depends on the substrate and the deposited material. Thereby, the heteroepitaxial deposition process can lead to the formation of independent hexagonal microcrystals called grains.

Furthermore, the growth of III-nitrides on substrates with different thermal expansion coefficient (table 2.1) can cause a residual stress in the layers during cooling down from the growth to room temperature [Amb98].

These stress effects affect the optical and electrical properties of the layers through the formation of clusters or dislocations.

The relation between the stress (σ_{ij}) and the strain (ε_{kl}) for a given material follows the Hooke´s Law:

$$(\sigma_{ij}) = \sum C_{ij} \, (\varepsilon_{kl}) \quad (2.2)$$

where C_{ij} is the elastic tensor of the material. In the case of hexagonal symmetry, five of the elastic components are independent and the elastic tensor becomes as follows:

$$\begin{pmatrix}\sigma_{xx}\\ \sigma_{yy}\\ \sigma_{zz}\\ \sigma_{yz}\\ \sigma_{zx}\\ \sigma_{xy}\end{pmatrix}=\begin{pmatrix}c_{11} & c_{12} & c_{13} & 0 & 0 & 0\\ c_{12} & c_{11} & c_{13} & 0 & 0 & 0\\ c_{13} & c_{12} & c_{33} & 0 & 0 & 0\\ 0 & 0 & 0 & c_{44} & 0 & 0\\ 0 & 0 & 0 & 0 & c_{44} & 0\\ 0 & 0 & 0 & 0 & 0 & \frac{c_{11}-c_{12}}{2}\end{pmatrix}\times\begin{pmatrix}\varepsilon_{xx}\\ \varepsilon_{yy}\\ \varepsilon_{zz}\\ \varepsilon_{yz}\\ \varepsilon_{zx}\\ \varepsilon_{xy}\end{pmatrix} \quad (2.3)$$

If the growth direction is the [0001] (z direction), the in-plane stress is uniform and the stress in the growth direction is zero ($\sigma_{xx}=\sigma_{yy}$ and $\sigma_{zz}=0$, respectively). Thus, the strain is zero when $i\neq j$ and the Hooke´s Law can be simplified to equation 2.4. Table 2.2 summarizes the elastic tensor coefficents of the III-nitrides compunds.

$$\begin{pmatrix}\sigma_{xx}\\ \sigma_{yy}\\ 0\end{pmatrix}=\begin{pmatrix}c_{11} & c_{12} & c_{13}\\ c_{12} & c_{11} & c_{13}\\ c_{13} & c_{12} & c_{33}\end{pmatrix}\times\begin{pmatrix}\varepsilon_{xx}\\ \varepsilon_{yy}\\ \varepsilon_{zz}\end{pmatrix} \quad (2.4)$$

	C_{11} (GPa)	C_{12} (GPa)	C_{13} (GPa)	C_{33} (GPa)	e_{31} (C/m^3)	e_{33} (C/m^3)
AlN	396	137	108	373	-0.5	1.79
GaN	390	145	106	398	-0.35	1.27
InN	223	115	92	224	-0.57	0.97

Table 2.2. Elastic tensor component [Vur03] and piezoelectric coefficients [Vur01] for AlN, GaN and InN.

As stated above, III-nitride compounds are grown on a substrate with different lattice parameter, and usually with the growth direction along the *c*-axis, generating thus strain along the [0001] direction (ε_{zz}) and in the perpendicular plane ($\varepsilon_{xx}, \varepsilon_{yy}$). This strain can be calculated using the following equation:

$$\varepsilon_{xx}=\varepsilon_{yy}=\frac{a-a_0}{a_0} \quad (2.5)$$

$$\varepsilon_{zz}=\frac{-2c_{13}}{c_{33}}\varepsilon_{xx}=\frac{c-c_0}{c_0} \quad (2.6)$$

where a and c are the lattice parameter of the grown layer and a_0 and c_0 are the lattice parameter of the relaxed crystal.

2.2.1 Structural defects

As explained in the previous section, the mismatch of the lattice parameter and the thermal expansion coefficients between III-nitrides and the substrates lead to residual strain in the layer and the emergence of structural defects due to the relaxation process. These defects are commonly classified according theirs dimensions as point (0D), line (1D), planar/surface (2D) and volume defects (3D).

2.2.1.1 Point defects

Point defects are common in semiconductors and affect their opto-electrical properties like carrier mobility or carrier lifetime, acting like recombination centers and reducing the efficiency of the devices. The most typical point defects are: the atom incorporation at non-substitutional lattice sites, called interstitials defects, the vacancies defects (absence of an atom at a lattice site) and the exchanged of anion-cation, called anti-sites defects (see figure 2.4) [Wal96, Wal04].

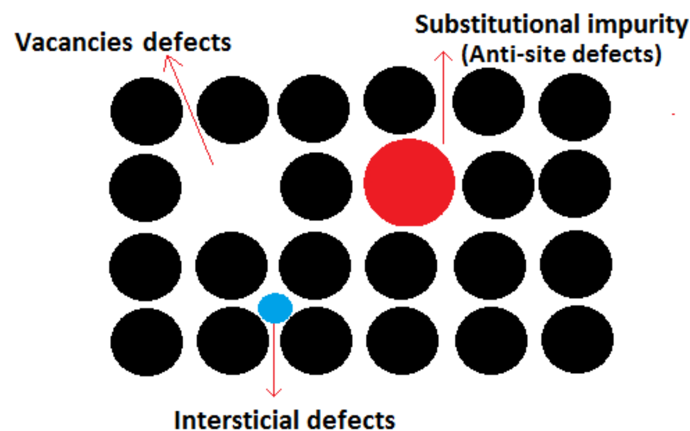

Figure 2.4. Schematic representation of the most common point defects in crystals

2.2.1.2 Line defects (dislocations)

Linear defects, or one dimensional defects, appear when the size in one dimension is higher or lower than the other two. The most commonly linear defects are the dislocations. Dislocations may appear and move when a stress is applied in a material and represent areas where the atoms are out of position in the crystal structure, that is, lines where the crystal pattern is broken.

Dislocations can be described by its dislocation line and the Burgers vector, which represents the magnitude and direction of the lattice distortion resulting from a dislocation in crystal lattice.

There are two types of dislocations depending on the angle (θ) between the dislocation line and its Burgers vector:

- Edge dislocations (θ = 90º), caused by a distortion of the planes of atoms due to the introduction of an extra half-plane of atoms (figure 2.5 a).
- Screw dislocations (θ = 0º), which happen when the halves of a cut of the crystal along a plane and a slip of one half across the other by a lattice vector fit back together without leaving a defect (figure 2.5 (b)). A simple way to explain it is by saying that a screw dislocation is a displacement of the crystal lattice by an amount of the burger vector in the direction parallel to burger vector.
- When (0º < θ < 90º) the dislocation is called mixed dislocation

Usually dislocations can attract point defects and act as a non-radiative recombination centers decreasing the efficiency of the devices [Sug98]. Besides, III-nitride devices stand apart because of their high density of dislocations, which propagate through the film along the growth direction. Dislocations propagate through the bulk of the heterostructure and reach the core part of the device.

As explained above, they form new energy levels inside the energy bandgap acting as non-radiative recombination centers and can act also as scattering centers. Then, electrons can be trapped in these energy levels by reaching a lower energy state and thus reducing the electrical performance of the device..

However, some studies as for example from Cao *et al.* [Cao02] or I. Mártil *et al.* [Mar97] shows that in III-V devices the non-radiative centers are saturated at similar levels than other technologies regardless the density defects of the layers, pointing that the non-radiative recombination centers are not as critical as expected assuming that the defects mainly affect the band structure.

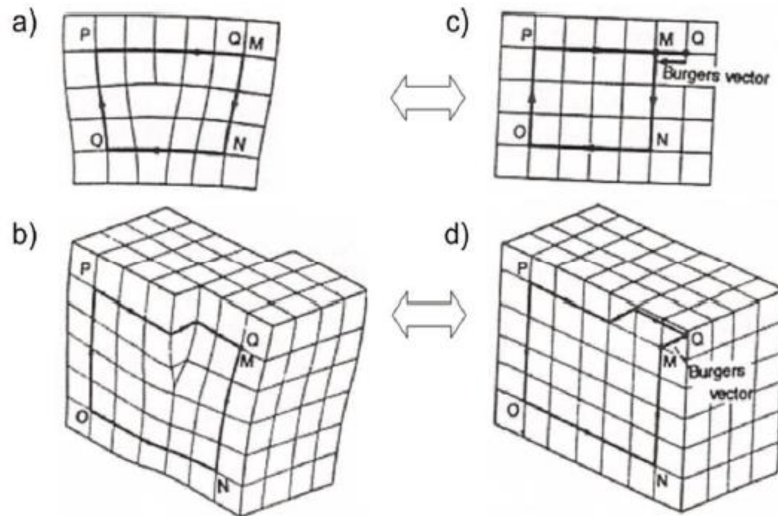

Figure 2.5. Determination of the Burgers vector for: (a), (c) an edge dislocation and (b), (d) a screw dislocation [Kit96].

2.2.1.3 Planar defects (grain boundaries)

The lattices mismatch between the layer and the substrate can cause a variation of the crystallographic direction of the material, which leads to a separation of two regions with different orientation or rotation, named grain boundary. Differences in grain orientation can lead to different crystal inclination (tilt) of the *c*-axis or a rotation of the basal plane around the *c*-axis (twist) (figure 2.6). These defects lead to an increase of the non-radiative recombination rate leading to a reduction of the carrier lifetime and the overall efficiency.

Additionally, planar, line and point defects could split a single crystal into nanocrystalls, increasing the electrical and optical losses of the devices, making thus very important to reduce the number of dislocations in the samples during growth.

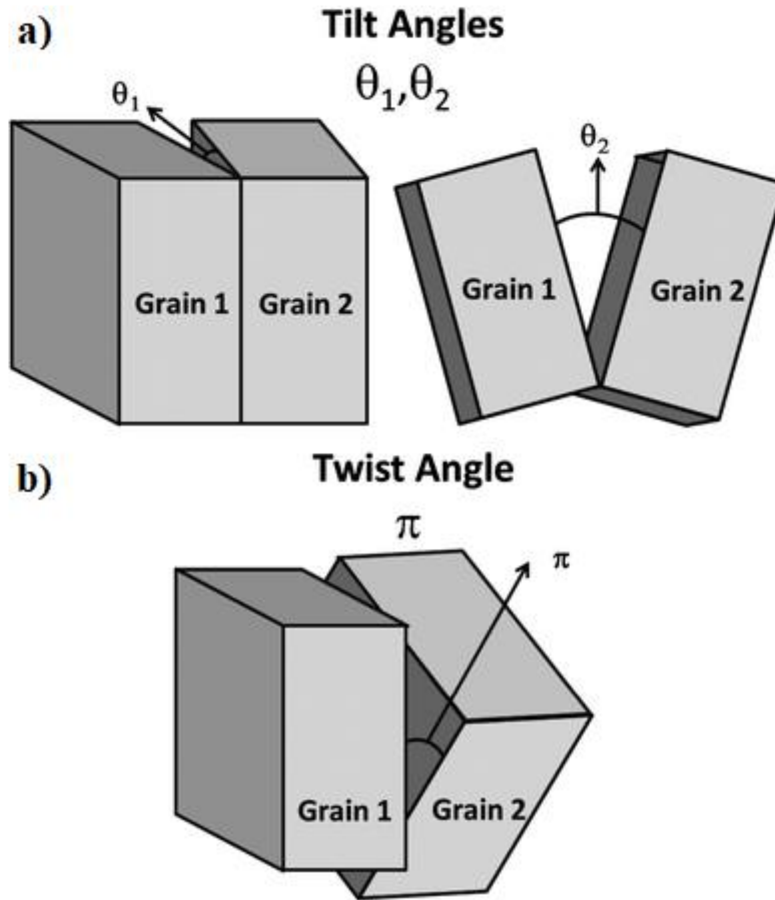

Figure 2.6. Schematic representation of the micro crystals of an epilayer when (a) tilt and (b) twist are presented [Gok13].

2.3 Optical properties

III-nitride semiconductors have direct bandgap, so, the maximum of the valence band and the minimum of the conduction band lie at the same point of the Brillouin zone. In the case of ternary alloys (AlGaN, InGaN and AlInN), a material with a wide range of bandgap energies ranging from the near infrared (≈0.69 eV) for InN, to the ultraviolet (≈6.25 eV) for AlN [Vur03] can be achieved varying the metal content (Al, Ga or In). This means that devices based on these materials can be developed for applications in a range between 200 nm and 1.79 μm.

The evolution of the bandgap energy with the temperature for semiconductors can normally be described by Varshni´s law [Var67]:

$$E_g(T) = E_g(0) - \frac{\gamma T^2}{\beta + T} \quad (2.7)$$

where $E_g(0)$ is the bandgap energy at T= 0K, the parameter γ is a constant and β is a parameter associated to the Debye temperature of the crystal [Var67]. Table 2.3 summarizes the Varshni parameters and the bandgap energy at 0 K and 300 K for InN, AlN and GaN deposited by molecular beam epitaxy (MBE).

	E_g (0) (eV)	**γ (meV/K)**	**β (K)**	**E_g (300K)**
AlN	6.25	1.799	1462	6.14
GaN	3.51	0.909	830	3.43
InN	0.69	0.311	580	0.64

Table 2.3. Experimental values of E_g (0), E_g at room temperature and Varshni parameters γ and β for the different III-nitride binary compounds. Data obtained from [Vur03].

The bandgap energy of the ternary alloys used along this thesis is calculated from the bandgap value of the binary constituents (InN and AlN) and the composition of the alloy, x, using a modified Vegard´s law [Veg21] that takes into account a deviation from the linearity through the non-linear parameter b known as bowing parameter [Lio04]:

$$E_{gAl_xIn_{(1-x)}N} = xE_{gAlN} + (1-x)E_{gInN} - bx(1-x) \tag{2.8}$$

The bowing parameter of the $Al_xIn_{1-x}N$ alloy varies as a function of the composition from 3 to 20 eV in samples grown by MOCVD [Sch13]. For MBE-grown-samples with similar bandgap as the layers used in this thesis the bowing parameter is of 4.96 eV [Ter06]. Besides, for samples grown by our group the estimated bowing parameter is of 5.2 eV (see figure 2.7) [Nuñ17].

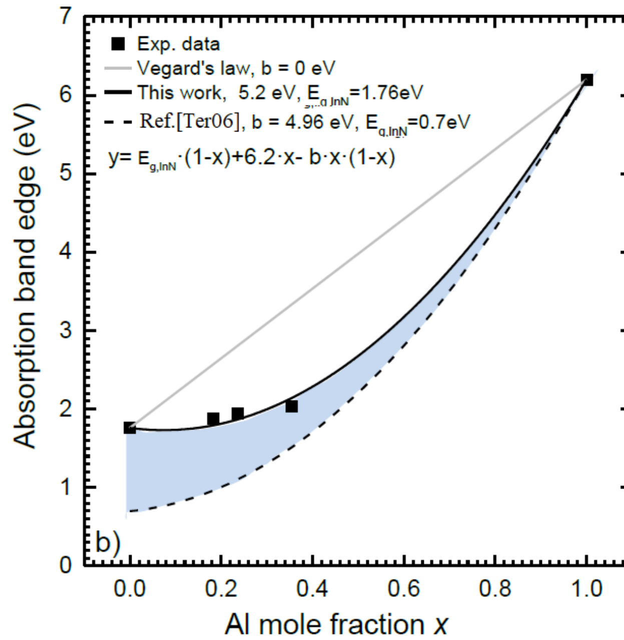

Figure 2.7. Relationship between the bandgap energy of $Al_xIn_{1-x}N$ and the Al content (from Wavelength dispersive X-ray (WDX)). The shadow area shows the difference from a bowing parameter expression using the band-gap of pure InN [Nuñ17].

Burnstein-Moss effect

The InN bandgap energy value has been studied in the last decades because it changes from 0.64 to 2 eV depending on the deposition technique. This variation is due to the high residual carrier concentration of the III-nitride films induced by impurities like oxygen and hydrogen during the deposition [Dar10]. Therefore, this variation produces an effect called Burnstein-Moss effect which induces a band filling and a blue shift on the bandgap energy of the high doped layers.

In the Burnstein-Moss effect the shift appears because the Fermi energy level lies in the conduction band for heavy *n*-type or in the valence band for heavy *p*-type doping. Therefore, the filled states block thermal or optical excitation. Consequently, the measured bandgap determined from the onset of interband absorption shifts to higher energy and thus suffer a blue shift, as decrypted in figure 2.8.

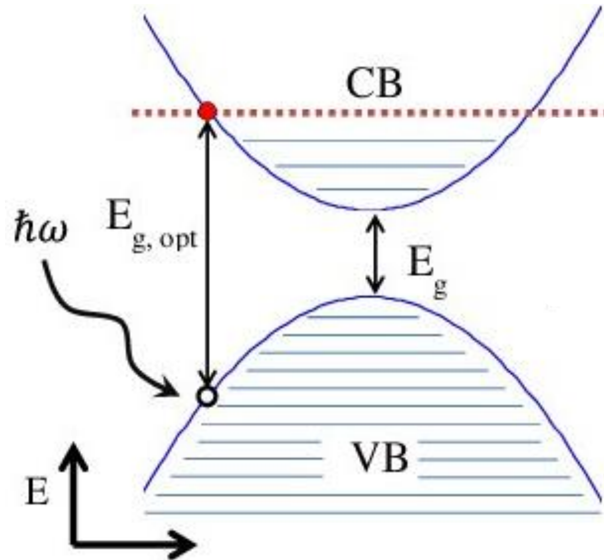

Figure 2.8. Bandgap filling due to the Burstein–Moss effect [Gib13].CB and VB stand for conduction and valence band respectively.

This effect provokes that more than 2000 groups had studied and presented different bandgap energy values for InN layers. Concretely the bandgap energy of InN layers grown by MBE varies from 0.64 to 0.9 eV [Sai02, Wu02], being quite larger for MOVPE depositions.

In the case of magnetron sputtering technique, the InN layers usually present high residual carrier concentration (≈ 10^{21} cm^{-3}) [Bhu03] caused by a non-intentional doping. These characteristics leads to a bandgap energy ranging from 1.4 to 2 eV [Sas10, But05, Nuñ17].

2.4 Spontaneous and piezoelectric polarization

The wurtzite structure of the III-nitride compounds, as can be seen in the figure 2.1 b, has an asymmetry in the inversion center. This asymmetry entails the existence of a polar axis and thus, a spontaneous polarization in the layer. In the wurtzite structure the polarity is determined by the vector associated to the metal-N bond along the [0001] axis.

Thereby there are two polarities as a function of the order of the atoms at the top position of the (0001) bilayer. If the bilayer is formed by Al, Ga or In cations on its basal surface, the polarity is called [0001], metal or Al, Ga, In-polarity. However, if the basal surface shows nitrogen anions, the polarity of the layer changes to [000$\bar{1}$] or N-polarity.

The properties of the layers change as a function of the polarity. For example, metal polarity layers lead to more flatter surfaces [Xu03] and more chemically stable than N-polarity surfaces [Mas05].

As the nitrogen atom is more electronegative than the metal ones, bonds can be considered as an electrostatic dipole. Besides, inasmuch as the structure shows a non-centrosymmetric nature along the [0001]-direction, the charge distribution in the tetrahedron is not compensated resulting thus in a macroscopic spontaneous polarization ($\vec{P}$sp).

The value of P_{sp} (see Table 2.4) increases with the deviation of the nitride material from the ideal wurtzite structure given by the *u/c* and *c/a* relationships shown in table 2.1. To obtain the P_{sp} of ternary compounds, Bernardini *et al.* [Ber99] have made a first approximation using Vegard´s law [Veg21] and also using density-functional techniques [Ber01].

	AlN	**GaN**	**InN**
P_{sp} (C/m^2)	-0.090	-0.034	-0.042

Table 2.4. Spontaneous polarization for wurtzite structure of AlN, GaN and InN with metal polarity. Data obtained from [Vur03].

On the other hand, the lattice and thermal mismatch between the III-nitride compound and the substrate causes a stress in the layer. This mechanical stress leads to a modification of the atomic position of the crystal causing a different spatial distribution of charges.

This effect produces a piezoelectric polarization ($\vec{P}_{pz}$). This polarization can be calculated from equation 2.5 using the piezoelectric coefficients of the material e_{ij} and the strain ε_i:

$$\vec{P}_{pz} = \begin{pmatrix} 0 & 0 & 0 & 0 & e_{15} & 0 \\ 0 & 0 & 0 & e_{15} & 0 & 0 \\ e_{31} & e_{31} & e_{33} & 0 & 0 & 0 \end{pmatrix} \begin{pmatrix} \varepsilon_1 \\ \varepsilon_2 \\ \varepsilon_3 \\ \varepsilon_4 \\ \varepsilon_5 \\ \varepsilon_6 \end{pmatrix} \quad (2.9)$$

The symmetry of the wurtzite crystal allows to consider only three piezoelectric constants: $e_{31}, e_{33}\ and\ e_{15}$.

III-nitrides are commonly grown on the (0001) plane. In this case, the nitride layer show a biaxial stress perpendicular to the [0001]-axis so, using equation 2.9, the polarization in each direction is described by:

$$\vec{P}_{pz}^{x} = \vec{P}_{pz}^{y} = 0 \quad (2.10)$$

$$\vec{P}_{pz}^{z} = 2\frac{a-a_0}{a_0}\left(e_{31} - e_{33}\left(\frac{c_{13}}{c_{33}}\right)\right) \quad (2.11)$$

For III-nitrides $\left(e_{31} - e_{33}\left(\frac{c_{13}}{c_{33}}\right)\right) > 0$ (see table 2.2). Thus the piezoelectric polarization along [0001]-axis is positive under compressive strain $(a < a_0)$ and negative under tensile strain $(a > a_0)$.

The sum of the spontaneous P_{sp} and piezoelectric polarization P_{pz} is called total polarization (equation 2.12) and induces a total internal electric field in the material described in equation 2.13.

$$P_{tot} = P_{sp} + P_{pz} \quad (2.12)$$

$$E_{tot} = \frac{P_{tot}}{\varepsilon_0 \varepsilon_r} \quad (2.13)$$

where ε_0 is the vacuum permittivity and ε_r is the dielectric constant of the material.

Chapter 3

Solar cells

This chapter describes mainly the basics of solar cells and it is divided into four parts. Firstly, there is an introduction to the photovoltaic effect and the History of solar cells. Then, a description of the properties and processes in semiconductors is presented, including the behavior of the *p-n* junction in the dark and under illumination. Finally, we present a summary of the nowadays-existing types of photovoltaic devices and the choice of using AlInN on Si heterojunctions to improve the silicon solar cells.

3.1 Introduction to solar cells

Solar cells are based on a *p-n* junction of a semiconductor that converts the sunlight into electricity through the photovoltaic effect - discovered by Edmond Becquerel in 1839 [Bec39] and the photoelectric effect, discovered by Heinrich Hertz in 1887. These effects relate the production of electric current or voltage in a semiconductor material exposed to radiation.

When a beam of photons with an energy above the material band-gap energy impinges on a semiconductor *p-n* junction, they can be absorbed, generating an electron-hole pair. In this case, the electron jumps to a higher energy state (in general, the conduction band) while the holes remain in the valence band creating electron-hole pairs (figure 3.1). The internal field produced by the junction separates the positive charges (holes) from the negative ones (electrons) and collected in the contacts of the device.

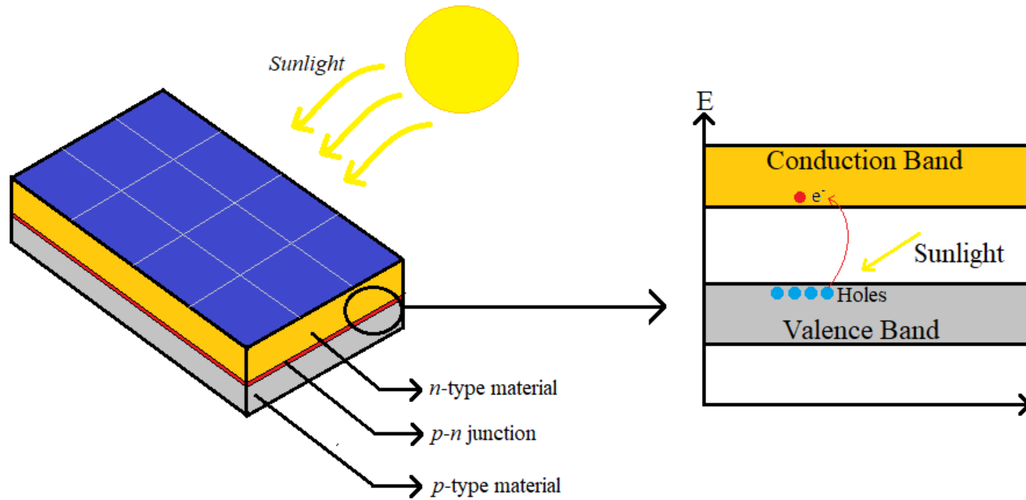

Figure 3.1. Scheme of the photovoltaic effect.

History of solar cells

From the discovery of the photovoltaic effect by Edmund Becquerel in 1839, scientifics began to study and develop the photovoltaic devices. In 1873, Willoughby Smith discovered the photoconductivity of selenium leading to the creation of the first solar cell by Charles Fritts with an efficiency of 1-2%.

Subsequently, in 1887 Heinrich Hertz observed for the first time the aforementioned photoelectric effect, from which Einstein obtained the Nobel Prize in 1921.

Due to the high price of selenium and the need for the development of quantum physics, solar cells started being only a scientific curiosity. However, in 1954 three scientists of Bell Labs (Daryl Chapin, Gerald Pearson and Calvin Fuller) discovered that silicon is more efficient than selenium, creating the first silicon solar cell with an efficiency around 6% [Cha54].

From the creation of this device, the economic support from the aerospace industry and the development of microelectronics made a remarkably development of the photovoltaic technology during the 20th and early 21th centuries. The existing types of solar cells will be described in section 3.4.

3.2 Basics of semiconductors

To understand the physics of solar cell it is necessary to explain some semiconductor characteristics, such as the energy bands, the carrier concentration and transport

properties, and generation and recombination processes. In addition, we will explain the operation principles of a *p-n* junction and its current-voltage characteristics in the dark and under illumination.

3.2.1 Energy bands

Solid-state materials are commonly grouped into three classes: insulators, semiconductors and conductors. This classification can be determined by the bandgap width and conductivity properties (figure 3.2). The bandgap of a solid material is the energy difference between the valence and the conduction bands and represents the minimum energy that is required to excite an electron from the maximum of the valence band to the minimum of the conduction band.

In that sense, the bandgap is a major factor determining the electrical conductivity of solid materials. As shown in figure 3.2, insulator materials have the widest bandgap, so that thermal energy is not enough to excite electrons from the valence to the conduction band. Because of that, the valence band is completely full while the conduction band is empty of electron.

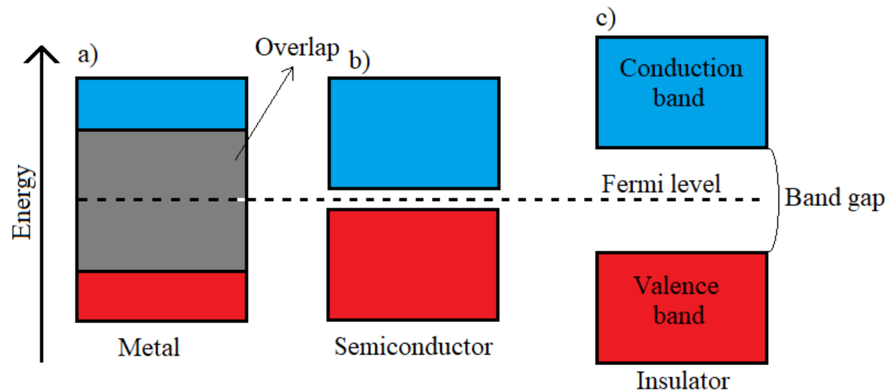

Figure 3.2. Scheme of band structure of a) metals, b) semiconductors and c) insulators.

In a conductor material, there is not a bandgap because the conduction band overlaps the valence band. In this case, when the energy of an electron increases, for example, by thermal excitation, it can move freely to higher energy levels in the conduction band.

In a semiconductor, the bandgap value is smaller than for insulator materials and higher than in conductor materials. As explained above, when photons with energy greater than the bandgap energy impinge into a semiconductor, they give their energy to the electrons of the valence band, which jump from the valence to the conduction band, generating a free hole in the valence band. In addition, if an electric field is applied to the

semiconductor, both electrons and holes gain a certain kinetic energy generating an electric drift current.

3.2.2 Solar spectrum, air mass and absorption by semiconductors

As explained above, solar cells convert the sunlight into electricity. Besides, the energy of the photons, can be calculated as a function of its wavelength using the Planck-Einstein relation:

$$E = hc/\lambda, \tag{3.1}$$

where h is the Planck constant ($h = 4.135\times10^{-15}$ eV·s), c is the speed of light ($c = 3\times10^{8}$ m/s), and λ is the wavelength.

In that sense, it is important to know the shape of the spectral power density of the Sun in the earth and on the earth surface, shown in figure 3.3.

The total power density of the solar radiation outside the atmosphere at the mean Earth-Sun distance on a plane perpendicular to the direction of the Sun is 1353 W/m^2 with a maximum value at a wavelength close to 500 nm (2.47 eV). However, the spectral power density decreases at the Earth surface (AM1.5 radiation) due to the light absorption along the atmosphere: in infrared region by water vapor (H_2O), carbon dioxide (CO_2), nitrous oxide (N_2O), etc., and in ultraviolet region by ozone and oxygen. Besides, the radiation increases with the mass of air crossed by it. In that sense, the air mass coefficient, which represent the ratio between the path length of the light, I, and the minimal distance, I_0, is used to obtain the solar spectrum intensity as a function of the angle of the sun to the zenith (α) as is shown in equation 3.2.

$$Air\ mass = (\cos\alpha) - 1 = {}^{I}/_{I_0} \tag{3.2}$$

In that sense, AM0 corresponds to the solar spectrum outside the atmosphere, and, for example, if the Sun is 60° to the zenith, the air mass is called AM2, and, if the sun is directly overhead, the Air Mass is 1. The standard angle for the zenith chosen to compare the solar cells efficiency is of 48.8°, which correspond to an air mass of 1.5 and is called AM1.5.

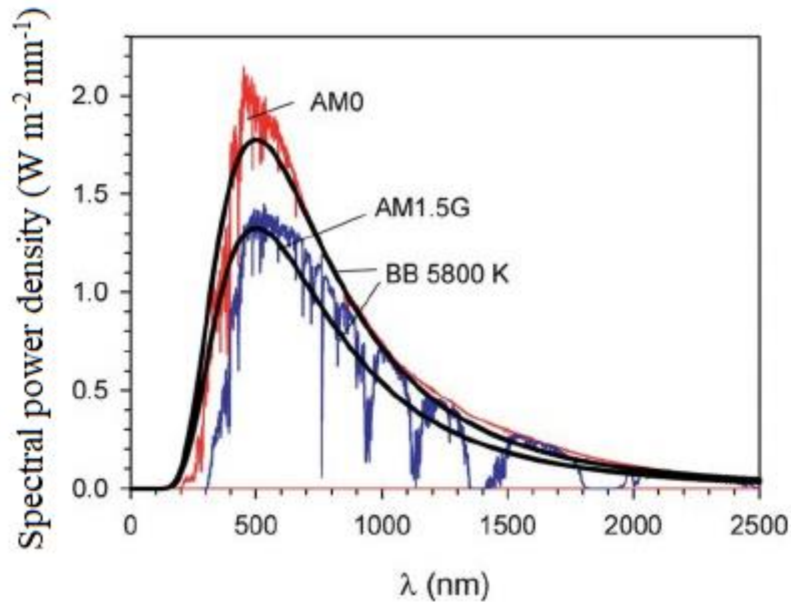

Figure 3.3. Spectral power density of the Sun as a function of the wavelength: just outside of the atmosphere (AM0 radiation) and on the Earth surface (AM1.5 radiation), the lines are reference spectra of a blackbody at T ¼ 5800K, normalized to a total power density of AM0 (~1366 W m^{-2}) and of AM1.5G (~1000 W m^{-2}) [Nay12].

Furthermore, the abbreviation of the air mass value can be described as AM1.5G, which entails the direct (arriving directly to the earth) and diffuse radiation (radiation scattered by the atmosphere). Besides, there are the description of the air mass called AM 1.5D, which only takes into account the direct radiation, but normally the AM1.5G is used to obtain the devices efficiency, and its value is around 970 W/m^2, but is usually normalized to 1000W/m^2.

So, as explained before, if the photons with an energy higher than the bandgap of the semiconductor, they can be absorbed by the semiconductor, but, if the energy is much higher than the bandgap, the excess of energy can be transformed mainly into heat through electron-phonon interactions (figure 3.4).

However, even if the photons have an appropriate energy to be absorbed, they can also be reflected or transmitted and, thus not generate an electron-hole pair. In order to decrease the reflection, different surface designs are applied to the solar cell, such as texturing and roughening, or introducing antireflection coatings [You14].

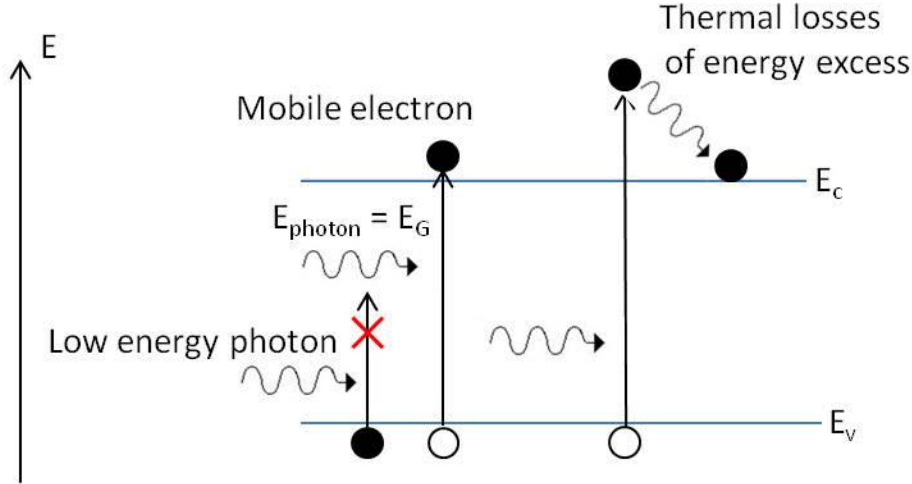

Figure 3.4. Absorption of incoming photons with creation of electrons in the conduction band [Muk15].

Furthermore, the photon transmission can be controlled through the thickness of the absorbed layer. So, the layer thickness can be determined, knowing the absorption coefficient α of the material, via the Beer-Lambert law:

$$I(x) = I(0)e^{-\alpha x}, \quad (3.3)$$

where $I(x)$ is light intensity transmitted through material, $I(0)$ is incident light intensity, α is absorption coefficient and x is thickness of absorption layer. So, in this study, the transmittance of the upper layer of the device will be modified by varying the composition of the samples and thus, the absorption coefficient of the layers.

3.2.3 Theory of semiconductors: properties and processes

Usually semiconductor materials are intrinsic (or undoped), which means that the number of holes in valence band and electrons in the conduction band are equal. However, charges can be modified by introducing a small number of impurity atoms. In this case, the semiconductor is doped and its behavior depends on the impurity concentration and the activation energy of the impurity, becoming extrinsic. In general, this doping leads to an increase of the semiconductor conductivity due to the increase of the carrier concentration. There are two types of dopants, *n*-type (electron donors) and *p*-type (electron acceptors) dopants. When the *n*-type dopants are incorporated into the atomic lattice of a semiconductor, the valence electrons of *n*-type dopants can be easily excited as free electrons to the conduction band. On the other hand, when a *p*-type dopant is incorporated into the atomic lattice of a semiconductor, it is able to host electrons from the conduction band, allowing the easy formation of free holes at the valence band.

3.2.3.1 Carrier concentration and transport

The carrier concentration density of a semiconductor can be calculated by the Fermi-Dirac (F-D) statistics using the fermi equation F(E), which shows the probability for an electron to occupy an electronic state with a certain energy E, as shown in equation 3.4:

$$F(E) = \frac{1}{1+e^{(E-E_F)/k_B T}} \tag{3.4}$$

where E_F is the Fermi level, defined as the energy level which has a 50% probability of getting occupied by an electron at a given temperature, k_b is the Boltzmann constant and T is the temperature.

However, an intrinsic semiconductor can be defined by having the same number of electrons and holes. So the probability of occupation of energy levels in conduction and valence bands are equals and, therefore, the Fermi level, called intrinsic Fermi level, is located in the middle of the gap.

The carrier density at room temperature, called intrinsic carrier density (n_i), which described as the number of electron in the conduction band or the number of holes in the valence band in an intrinsic semiconductor is obtained through equation 3.5:

$$n_i = \sqrt{N_C N_V} exp\left(-\frac{E_g}{2k_B T}\right) \tag{3.5}$$

where N_c and N_v are the effective density of states of the conduction and valence band respectively, E_g is the bandgap energy, k_b is the Boltzman constant and T is the temperature.

Besides, the relationship between the number density of electron (n) and holes (p) is described using the mass action law (equation 3.6), valid for intrinsic and doped semiconductors in thermal equilibrium:

$$n \cdot p = n_i^2 \tag{3.6}$$

So, in the case of an extrinsic or doped semiconductor, an increase of one type of carriers leads to a reduction of the other in order to remains constant the mass action law.

When a semiconductor is under neutral equilibrium, and the total density of positive and negative charges are equal, the charge densities are expressed as:

$$n + N_A = p + N_D \tag{3.7}$$

where N_D and N_A are the donor and acceptor concentrations. So, for example, when an *n*-type material where N_A= 0 and $n>>p$, the electron density can be obtained as $n \sim N_D$, meanwhile where *ND*= 0 and $p>>n$, the hole density can be obtained as $n \sim N_A$. Using equation 3.6, it is possible to obtain the minority carrier concentration as:

$$p \approx \frac{n_i^2}{N_D}; n \approx \frac{n_i^2}{N_A} \tag{3.8}$$

When an electric field is applied to the semiconductor, electrons and holes suffer a movement through the semiconductor. A random thermal velocity and a net drift velocity parallel to the direction of the applied field causes this movement. The combination generates a motion in the direction to the applied field (for holes) and to the opposite one (for electrons).

The relationship between the applied electric field and the drift velocity is expressed as follows (see figure 3.5):

$$\overrightarrow{v_n} = -\mu_n \overrightarrow{E}; \ \overrightarrow{v_p} = \mu_p \overline{E} \tag{3.9}$$

where $\overrightarrow{v_{n,p}}$ are the electrons and holes drift velocities, $\overrightarrow{E}$ is the electric field and $\mu_{n,p}$ are the mobility of electrons and holes, respectively.

From equation 3.9 the drift current can be defined as:

$$\vec{J}_{Drift} = q\mu_n n\overrightarrow{E}; \vec{J}_{Drift} = q\mu_n p\vec{E} \tag{3.10}$$

where q is the electron charge, and *n* and *p* are the electron and hole densities, respectively.

The change of the sign in equations 3.9 is because the holes move in the same direction as the electric field (figure 3.6). However, inasmuch as holes and electrons have opposite charges, the current sign is the same.

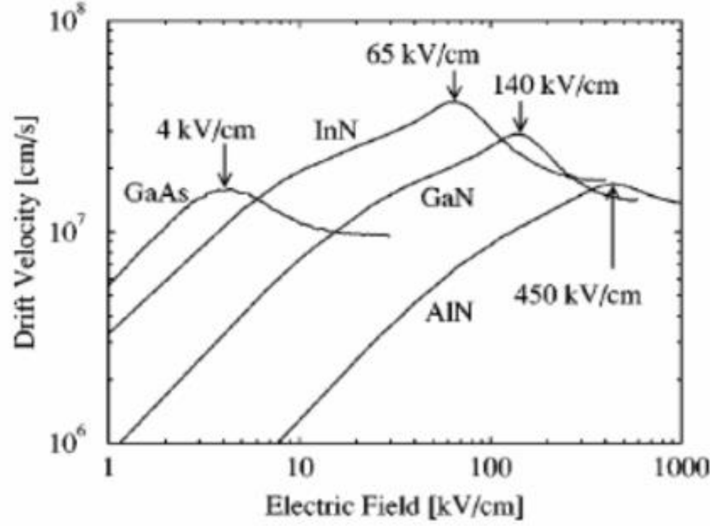

Figure 3.5. Drift velocity of nitrides semiconductors [Shu13].

As observed from figure 3.5, when the electric field is higher than 65, 140 and 450 kV/cm for InN, GaN and AlN materials, respectively, the drift velocity reaches a saturation velocity above 10^7cm/s. So, III-nitrides semiconductors can operate at really high electric fields, before the saturation of the drift velocity, which is described as the maximum velocity reached by the carriers in a semiconductor, in the presence of very high electric fields.

Furthermore, another important factor in semiconductors is the diffusion mechanism (figure 3.6). This mechanism emerges in non-uniformly doped semiconductor structures, like *p-n* junctions. In *p-n* junctions, the movement of electrons goes from the *n*-type side to the *p*-type side, meanwhile the holes moves in the opposite direction due to a pure diffusion mechanism. This carriers movement generate a current, called diffusion current, expressed as follows:

$$\vec{J}_{Dff} = qD_n\vec{\nabla}n\,; \vec{J}_{Dff} = -qD_p\vec{\nabla}p \qquad (3.11)$$

where $D_{n,p}$ are the electron and hole diffusion coefficients, and $\vec{\nabla}n, p$ are the electron and hole density gradients, respectively. As explained before, the sign of the hole diffusion current changes, because it moves in opposite direction as electron diffusion current (see figure 3.6).

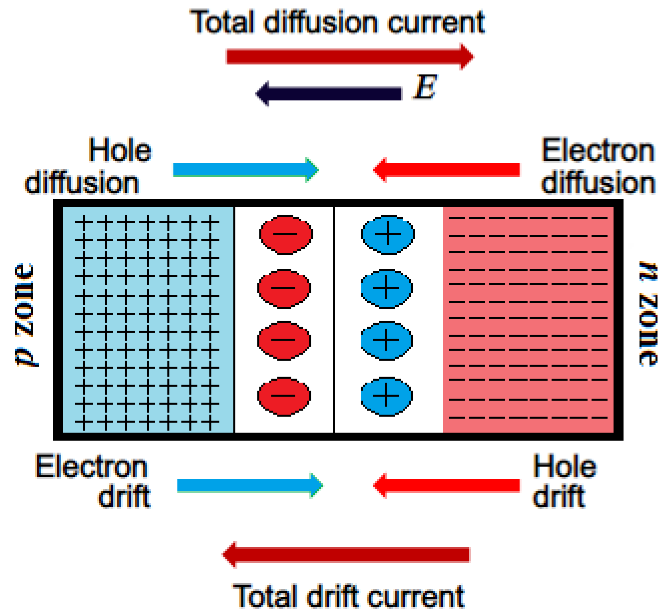

Figure 3.6. Scheme of the carrier movement (drift and diffusion) in a *p-n* junction in equilibrium.

Therefore, with the drift and diffusion currents is possible to describe the total current in a semiconductor as follows:

$$\vec{J}_{conduction} = \vec{J}_{Drift} + \vec{J}_{Dff} = q\mu_n n\vec{E} + qD_n\vec{\nabla}n + q\mu_p p\vec{E} - qD_p\vec{\nabla}p \qquad (3.12)$$

Those equations define the current density of a semiconductor in a low electric field regime. When the electric field is high enough, the saturation velocity should replace the factor $(\mu_{n,p}\vec{E})$.

3.2.3.2 Generation and recombination

When a photon hits on a semiconductor with an energy equal or higher than the bandgap energy ($E_{photon} \geq E_g$), the material absorbs this energy and an electron of the valence band is transferred to the conduction band generating an electron-hole pair.

There are three main types of recombination process in a semiconductor: band-to-band, Shockley-Read-Hall and Auger recombination, as depicted in figure 3.7.

- **Band to band recombination**. In this process, also called direct recombination, an electron of the conduction band recombines with a hole of the valence band releasing energy usually in the form of a photon (called radiative process) or a phonon or mechanical vibration (called non-radiative process). If the energy of the photons is much higher than the bandgap one, as is shown in figure 3.4, the exceed energy is usually lost in form of heat.

- **Shockley-Read-Hall recombination**. This recombination is due to lattice defects or impurities that are in the semiconductor and generate energy deep levels into the bandgap. The electron in transition between bands passes through theses energy states (localized state), usually called traps, and their energy is exchanged in the form of lattice vibration (non-radiative process), a phonon exchanging thermal energy with the material. This process is also called trap-assisted recombination.
- **Auger recombination**. The Auger recombination occurs with the collision of two carriers. When an electron of the conduction band recombines with a hole of the valence band, the energy released is transferred to another electron of the conduction band through a collision.

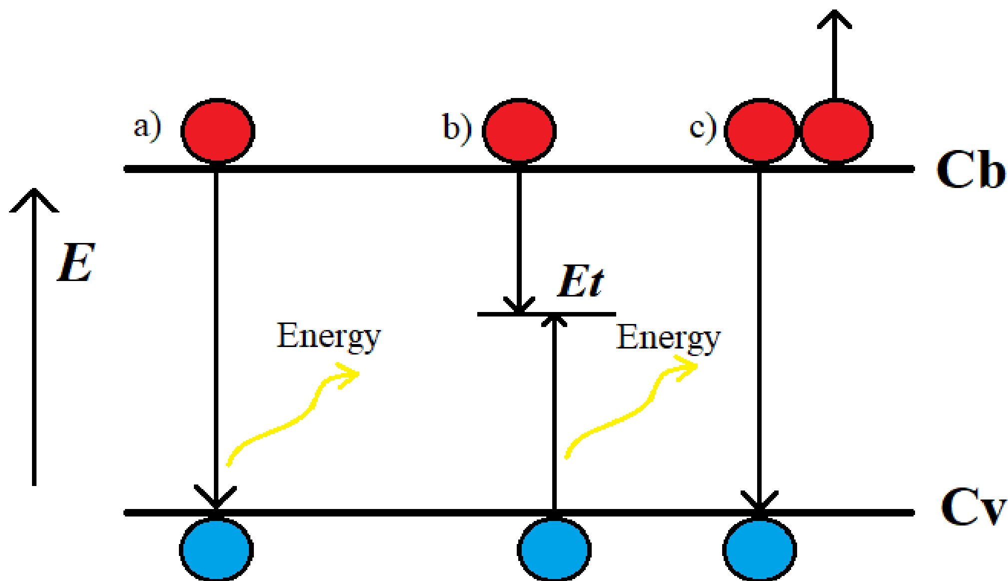

Figure 3.7. Scheme of carrier recombination process in a semiconductor: a) band to band, b) Shockley-Read-Hall and c) Auger recombination. Et stands for trap energy that occurs in the Shockley-Read-Hall process.

3.2.4 *P-N* junction

Under dark

P-N junctions are formed by joining *n*-type and *p*-type semiconductor materials, as shown in figure 3.8. As explained above, since there is a concentration difference of holes and electrons between the two types of semiconductors, holes diffuse from the *p*-type region to the *n*-type region and, similarly, electrons from the *n*-type region diffuse to the *p*-type region. When both semiconductor types joint, the Fermi energy level must be the same in

both *p and n* sides of the junction, as described in figure 3.8(b). As the carriers diffuse, the charged impurities (ionized acceptors in the p-type material and ionized donors in the n-type material) are uncovered, so no longer screened by the majority carriers. In this case, an electric field (or electrostatic potential difference) is produced, and is seen as a barrier for the carriers since limits the diffusion of electrons and holes. In thermal equilibrium, the diffusion and drift currents for each carrier type are in balance, so there is no net current flow. The transition region between the n-type and p-type semiconductors is called the space-charge region or depletion region, since it is effectively depleted of both holes and electrons. The electrostatic potential difference resulting from the junction formation is called the built-in voltage, V_{bi}. It arises from the electric field created by the exposure of the positive and the negative space charge in the depletion region and is proportional to the difference in work functions of both semiconductors:

$$V_{bi} = \frac{1}{q}\left(\Phi_n - \Phi_p\right) \qquad (3.13)$$

where q is the electron charge in coulombs and $\Phi_{n,p}$ is the work function of the n and p-type semiconductors, respectively.

Besides, if the semiconductor is doped the work functions can also be expressed as a function of the donor and acceptor concentration so that:

$$V_{bi} = \frac{kT}{q}\ ln\left(\frac{N_D N_A}{n_i^2}\right) \qquad (3.14)$$

where, N_D and N_A are the donor (n-type) and acceptor (p-type) concentration respectively, n_i is the intrinsic carrier concentration, k is the Boltzmann constant, q is the electron charge in coulombs and T is the temperature.

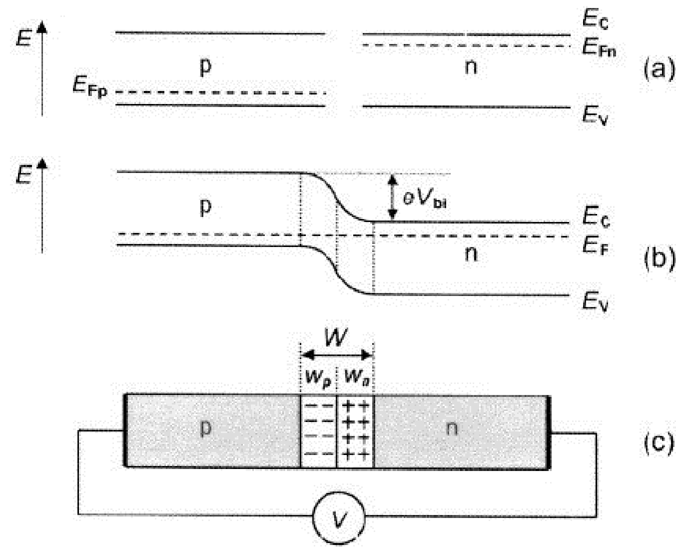

Figure 3.8. Scheme of a *p-n* junction: the energy band-diagram of a *p-n* semiconductor (a) before and (b) after the formation of the junction in thermal equilibrium. (c) The depletion region W of the *p-n* junction [Yac03].

As depicted in figure 3.8 (c), the total amount of charges on either side of the depletion region is equal and the net current flow through the junction is zero. The width of the depletion region can be obtained using the following equation:

$$W = W_n + W_p = \sqrt{\frac{2\varepsilon_r\varepsilon_0}{q}\left(\frac{1}{N_A}+\frac{1}{N_D}\right)(V_{bi})} \qquad (3.15)$$

Besides, despite under this conditions the Fermi energy level is constant, the width of the depletion region can be modified when applying an external voltage as:

$$W = \sqrt{\frac{2\varepsilon_r\varepsilon_0}{q}\left(\frac{1}{N_A}+\frac{1}{N_D}\right)(V_{bi}-V)} \qquad (3.16)$$

where N_D and N_A are the donor (*n*-type) and acceptor (*p*-type) concentration, respectively; ε_0 and ε_r are the dielectric permittivity of the vacuum and the semiconductor, respectively; and *V* is the applied voltage.

From equation 3.16 we can deduce that the width of the depletion zone depends on the carrier concentration and on the external bias. In that sense, high carrier concentrations induce smaller depletion widths and lower carrier concentrations result into wider depletion regions. Moreover, as depicted in figure 3.9, the depletion region or junction barrier becomes thinner for forward bias ($+V_{in}$), increasing thus the flow of current

through the material, whereas becomes wider for reverse bias (-V_{in}) increasing the resistance of the material to the flow of current.

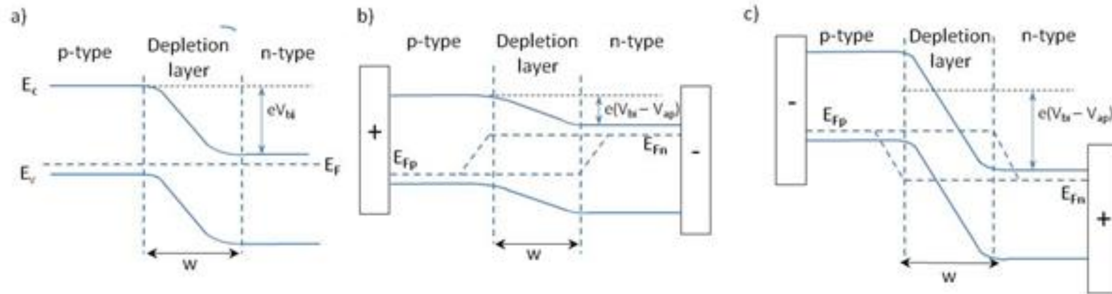

Figure 3.9. Evolution of the depletion region and the energy band diagram as a function of the applied voltage a) under equilibrium condition without external bias (V = 0), b) under forward external bias (V = +V_{in}), and c) under reverse external bias (V = -V_{in}). [Muk15].

When a moderate forward-bias voltage is applied to the junction the recombination current increases with the Boltzmann factor ($\exp\left(\frac{qV}{kT}\right)$) namely the Boltzmann approximation, so, the current of a *p-n* junction can be determined as the balance between the recombination current, which is related to the diffusion of minority carriers into the quasi-neutral region and the generation current, which is related to the drift of minority carriers in the corresponding doped regions (electrons in *p*-zone and holes in *n*-zone), as observed in equation 3.17 usually called Shockley equation.

$$J(V) = J_{recomb} - J_{gen} = J_0\left[\exp\left(\frac{qV}{kT}\right) - 1\right] \tag{3.17}$$

where, k is the Boltzmann constant, T is the temperature and q is the electron charge. Besides, (J_0) is also known as the diode reverse saturation current density can be obtained by the following equation (3.18):

$$J_0 = qA\left(\frac{D_e}{L_e}\frac{{n_i}^2}{N_A} + \frac{D_h}{L_h}\frac{{n_i}^2}{N_D}\right) \tag{3.18}$$

where *A* is the cross section of the PN diode, D_e is the electron diffusion coefficient, D_h is the hole diffusion coefficient, n_i is the number of electron-holes pairs and $L_{e,h}$ is the electron, hole diffusion length defined by equation 3.19:

$$L_{e,h} = \sqrt{D_{e,h}\tau_{e.h}} \tag{3.19}$$

where $\tau_{e.h}$ are the minority carrier lifetime.

The diffusion length can also be estimated using the Einstein relation and thus, extending the diffusion coefficient as a function of the carrier mobility:

$$L = \sqrt{\frac{\mu kT}{q}\tau} \tag{3.20}$$

Under illumination

When the *p-n* junction is illuminated with photons with energy above the band gap energy, light creates hole-electron pairs in the all three regions of the *p-n* junctions (depleted, *p*-doped and *n*-doped regions). Electrons and holes photogenerated in the depletion region are separated by the built-in electric field (drift transport) giving rise to a photocurrent. This implies that it is preferable to have a depletion region larger than the absorption length. This movement of the photo-generated carriers causes a new current, usually called photo-generation current J_{ph}, detailed in figure 3.10, which is added to the thermal generation current showed previously.

Mathematically, the behavior of a *p-n* junction can be explained using the diode equation:

$$J = J_0\left(e^{\frac{qV}{nkT}} - 1\right) - J_{ph} \tag{3.21}$$

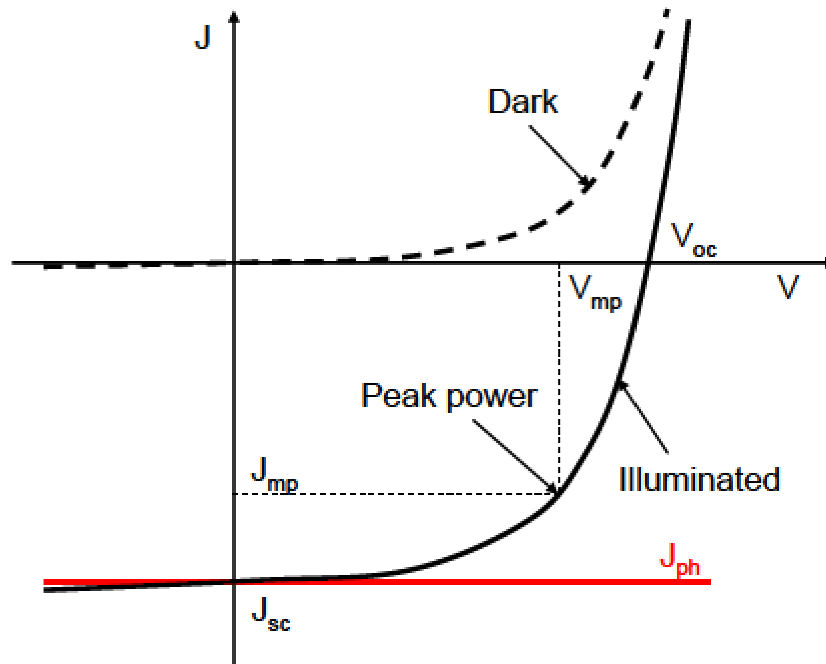

Figure 3.10. J-V curves of a *p-n* junction under dark and illumination conditions [Wür05].

The value of the photo-generated current under uniform generation rate (G) can be estimated, as a function of the hole and electron diffusion length, using the following equation:

$$J_{ph} = qG(L_e + L_h + W) \tag{3.22}$$

This equation can be used to design the thickness of the solar cell devices.

3.2.5 Analysis of current-voltage curves of solar cells

To analyze the characteristics of solar cells is necessary to carry out Current-Voltage (*J-V*) curves under dark and one sun AM 1.5G illumination conditions. From these measures is possible to obtain important parameters to describe the solar cell. Concretely, under dark conditions (Figure 3.11 a) is possible to estimate the diode factor (n) and the shunt (R_{sh}) and serial (R_s) resistances. On the other hand, through the *J-V* curve under one sun illumination conditions (Figure 3.11 b), is possible to get the values of the current that flows at zero voltage (0V), called the short-circuit current (J_{sc}), and the voltage at which the current becomes 0, called the open-circuit voltage (V_{oc}). Besides, the Fill Factor (FF), the maximum power intensity and thus, the device efficiency can be obtained through this measurement.

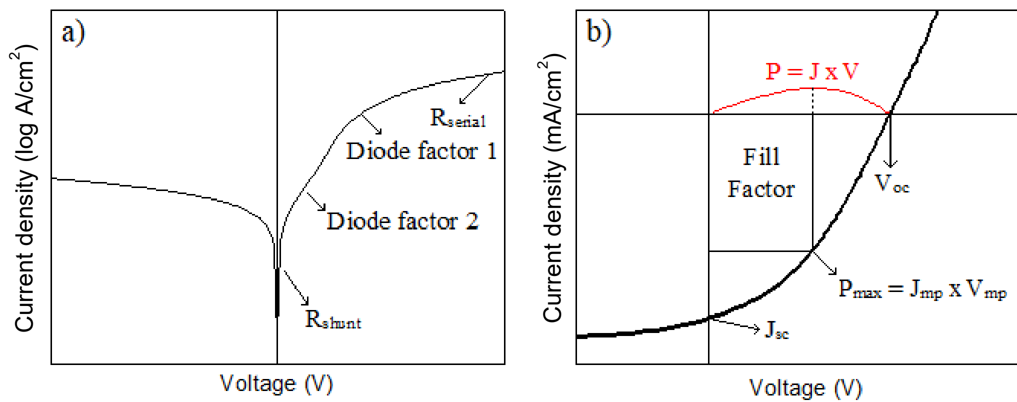

Figure 3.11. Typical Current density-Voltage curves and device parameters obtained under a) dark conditions and b) under one sun illumination.

Analysis of J-V curves under illumination

As explained above, through *J-V* curves of a solar cell measured under one sun illumination (AM 1.5G) there are 4 main parameters to take into account in order to understand the quality of the device:

- The open circuit voltage (V_{oc}) defined as the maximum voltage available from the device under open circuit conditions. Open circuit voltage can be estimated from the one diode model when the net current is equal to zero as follows:

$$V_{oc} = \frac{nkT}{q} \ln\left(\frac{J_{sc}}{J_0} + 1\right) \quad (3.23)$$

- The short circuit current (J_{sc}) defined as the output current delivered by the solar cell when the voltage across the device is zero (short-circuit conditions). Besides, as observed in figure 3.10, in most cases of solar cells, (meanwhile the serial resistance is below to 10 $\Omega\times cm^2$) the J_{sc} is equal to the photo-generated current (J_{Ph}) and the diode equation (equation 3.21) can be written using J_{sc}. For serial resistance values above this level, the J_{sc} is lower than J_{Ph} and the equation should be written with J_{Ph}.

Besides, the V_{oc} and J_{sc} parameters can be obtained graphically using the definitions explained at the beginning of this section.

- The maximum power (P_{max}) of the device is obtained at the point of the J-V curve where the maximum output power is located. Besides, the value of the voltage and the current at this maximum power point are defined as maximum power voltage (V_{mp}) and maximum power current (J_{mp}). This value is directly related with the device efficiency and is usually used to describe the economic efficiency of the device (Watt/$)

- The fill factor, commonly known by its abbreviation "*FF*", relates the V_{oc} and J_{sc} with the maximum power of the device. Concretely, the FF is defined as the ratio of the maximum power from the solar cell to the product of V_{oc} and J_{sc} as follows:

$$FF\ (\%) = \frac{V_{mp}J_{mp}}{V_{oc}J_{sc}} \times 100 \tag{3.24}$$

Graphically, the *FF* is a measure of the "squareness" of the solar cell and is also the area of the largest rectangle which will fit in the *J-V* curve.

- Device efficiency is defined as the ratio of the maximum energy output of the device to the maximum energy input from the sun. If we take into account the expressions seen above, the device efficiency can be described as a function of known and previously obtained parameters as following:

$$Efficiency\ (\%) = \frac{P_{max}}{P_{in}} \times 100 = \frac{V_{oc}J_{sc}FF}{P_{in}} \times 100 \tag{3.25}$$

where, P_{max} is the maximum power obtained by the solar cell, P_{In} is the incident power applied to the solar cell and V_{mp} and J_{mp} are the voltage and current density obtained at the maximum power point.

Analysis of Dark J-V curves

The equivalent circuit model of a solar cell (see Figure 3.12) involves a serial (R_s) and shunt (R_{sh}) resistances. Normally, the origin of R_s comes from the contacts and its resistance (between the metal and the semiconductor material). The serial resistance provokes a reduction of the fill factor (*FF*) and even (for high R_s values) can reduces the short circuit current.

On the other hand, the origin of the shunt resistance is due to fabrication processes, which affects to the quality of the material, such as impurities, dislocations or grain boundaries along the junction or a bad solar cell desing.

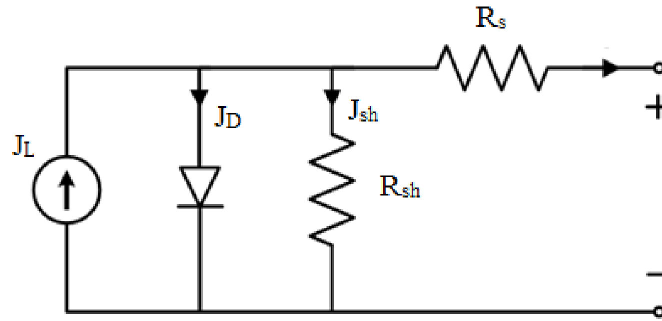

Figure 3.12. Electric scheme of a photovoltaic cell.

Therefore, if the effect of the shunt and the serial resistance are take into account in the equation 3.17 it is obtained the equation 3.23.

$$J = J_0\left(e^{\frac{q(V-JR_S)}{nkT}} - 1\right) + \frac{V-JR_S}{R_{shunt}} - J_{sc} \tag{3.26}$$

In some cases, the one diode model does not fit properly with the behavior of the solar cell and it is necessary to introduce another diode modifying the equation 3.26 into equation 3.27.

$$J = J_{01}\left(e^{\frac{q(V-JR_S)}{n_1kT}}\right) + J_{02}\left(e^{\frac{q(V-JR_S)}{n_2kT}}\right) + \frac{V-JR_S}{R_{shunt}} - J_{sc} \tag{3.27}$$

So, to obtain a solar cell with a good efficiency is necessary to optimize some parameters such as the serial and shunt resistance as much as possible, in addition to seeking the

maximization of the parameters previously seen, namely, the open circuit voltage (V_{oc}), the short circuit current (J_{sc}) and the fill factor (FF).

To obtain the values of serial (R_s) and shunt (R_{sh}) resistances, and of the diode factor (n), which determines how much the device resembles an ideal diode (n = 1), is necessary to fit the dark J-V curves from the device to the one or two diode models, to optimize the fit. However, in some cases, none of the models fit properly to the experimental obtained curve. In that sense, in order to find other methods to obtain these parameters, a comparison of the values obtained using those models and the values obtained fitting the parameters step by step has been made.

The method to fit the parameters step by step can be obtained following figure 3.11 a), where the serial resistance can be obtained by a linear fit of the values above 1V, the shunt resistance can be obtained as well by a linear fit of the parameters close to 0V and the diode factor can be obtained using an exponential fit of the values between 0 to 1V as can be shown in figure 3.13.

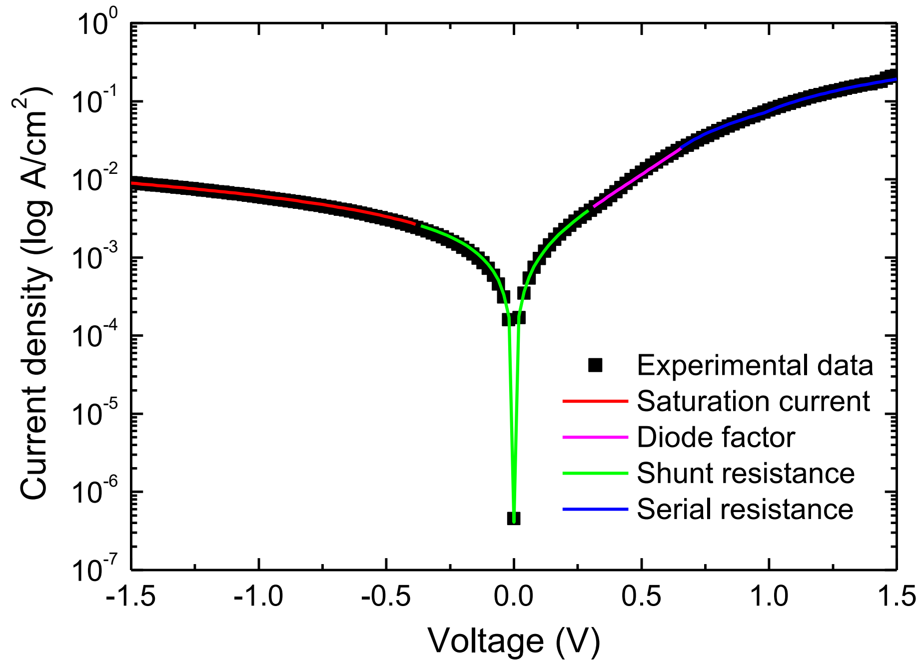

Figure 3.13. Example of dark J-V fit using the step by step process.

3.3 Type of solar cells

Nowadays there are many types of solar cells based on several material families and technologies. In general, solar cells are classified into three generations: crystalline silicon, thin films, and organic and novel technologies. In addition, we will also present

the state of the art of solar cells based on III-nitride materials, mainly InGaN and AlInN alloys.

3.3.1 1st generation: crystalline silicon solar cells

Silicon wafers are the responsible of the first generation of solar cells and, nowadays, they keep almost 80% of the global solar cells market. Generally, these devices own larger areas and are more efficient, in terms of dollar per Watt, than other technologies, as detailed below, being currently the most efficient solar cells for residential use. However, this type of devices have problems under high temperature conditions, decreasing their efficiency on hot days. First generation solar cells are divided into two main groups depending on their characteristics:

- **Monocrystalline silicon cells (c-Si)** [Dob12]

  This type of devices (see figure 3.14 (left)) are developed from the slides of large crystals of silicon grown under very controlled conditions called the Czochralski method [Fri16]**.** This technology reaches high efficiencies up to 24% [Gre19]. One of the main advantages of this technology is the long life production, around 25 years, which currently is the highest in the solar cells technology. However, growing large silicon crystals under these conditions raises their cost production and thus, its price per watt is quite higher than other technologies such as polycrystalline silicon technology.

- **Polycrystalline silicon cells (μ-Si)** [Dob13]

  These devices [see figure 3.14 (right)] are developed from ingots of molten silicon. The solidification of the silicon results in polycrystalline materials. This technology is much cheaper than the monocrystalline silicon one because the growth conditions are less restrictive. Moreover, polycrystalline solar panels tend to have slightly lower heat tolerance than monocrystalline solar panels and, thus, the degradation effect on this technology is quite lower than monocrystalline technology.

  However, their high density of defects in the polycrystalline layers result in less efficient devices achieving a maximal efficiency of ~22% [Gre19].

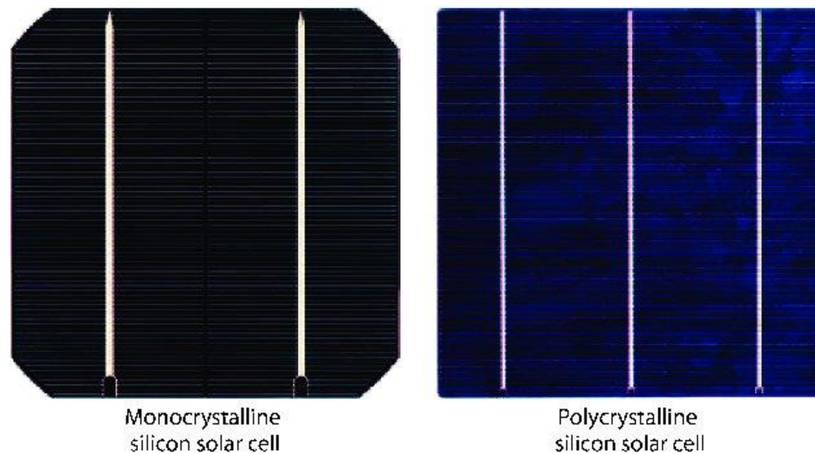

Figure 3.14. 1st generation solar cells based on (left) monocrystalline Si and (right) polycrystalline Si [Sag10].

- **Gallium Arsenide (GaAs)** [Luc19]

GaAs solar cells are obtained by direct combination of Ga and As via a vapour-phase reaction, usually by MOCVD, at low pressure and high temperature. This technology is one of the most commonly used for photovoltaic applications due to its direct bandgap around 1.4 eV and its high electron mobility.

Usually GaAs solar cells structure has a very thin window layer of AlGaAs as shown in figure 3.15 with the aim to generating the carriers close to the electric field at the junction.

However, this technology has some drawbacks, such as the high cost productions to obtain a single crystal substrate. Besides the combination of gallium, which is a rare material and arsenide, which is one of the most poisonous materials leads to an increase the manufacturing cost.

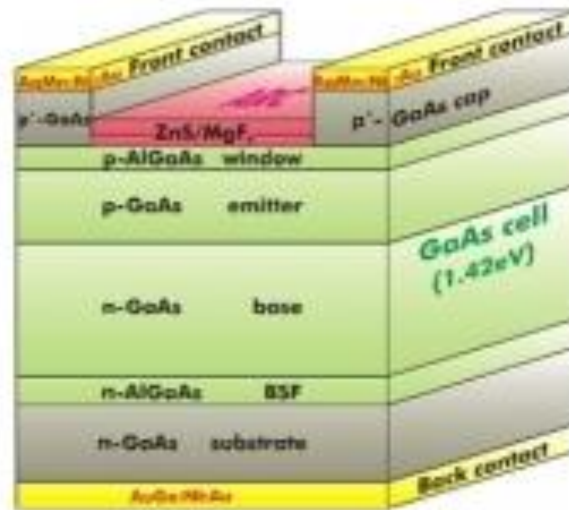

Figure 3.15. 1st generation solar cells based on AlGaAs/GaAs heterojunction [http://pvlab.ioffe.ru/about/solar_cells.html].

The conversion efficiency of GaAs solar cells varies from 18.4% to 28.8% depending on the GaAs layer properties [Gre19].

3.3.2 2nd generation: thin film solar cells

Second generation of solar cells (also called thin-film technology) are synthesized by epitaxial methods in order to create flexible devices with thin layers. The main target of this generation is to reduce the cost of manufacturing to generate a cheaper energy conversion than with the first generation. The thin-film technology is divided in three main types, which schemes are shown in figure 3.16:

- **Amorphous silicon solar cells (a-Si)** [Den03]

  This type of solar cell is usually based on a plasma-enhanced chemical vapor deposition (PECVD) of amorphous silicon onto a substrate such glass, metal or plastic. The aim of this technology is to reduce the manufacturing cost of the devices. Besides, the amorphous nature of silicon allows the deposition at very low temperatures (<75ºC). A variant of this technology, called hydrogenated amorphous silicon (a-Si:H) (figure 3.16 (a)) achieved very promising record efficiencies over 24% [Gre19], making it one of the most studied technologies nowadays.

- **Cadmiun telluride solar cells (CdTe)** [Wu04, Bai18]

This technology is based on *p-n* junctions of thin films of *n*-cadmium sulfide (CdS) and *p*-cadmium telluride (CdTe) (figure 3.16 (b)) or *p-i-n* junctions of *n*-CdS/i-CdTe/ *p*-zinc telluride (ZnTe). Currently this technology has already reached efficiency values close to 22% [Gre19], being one of the best-selling technologies behind silicon. However, the toxicity of the cadmiun and the low abundance of the tellurium make this technology quite expensive in comparison with other ones.

- **Copper indium gallium diselenide solar cells (CIGS)** [Ram17]

This technology is based on *p-n* junctions of *n*-cCdS/*p*-CIGS (figure 3.16 (c)) reaching efficiencies ~20% [Gre19]. However, CIGS solar cells have problems of reproducibility in comparison with the rest of technologies which has led to a decrease on its production.

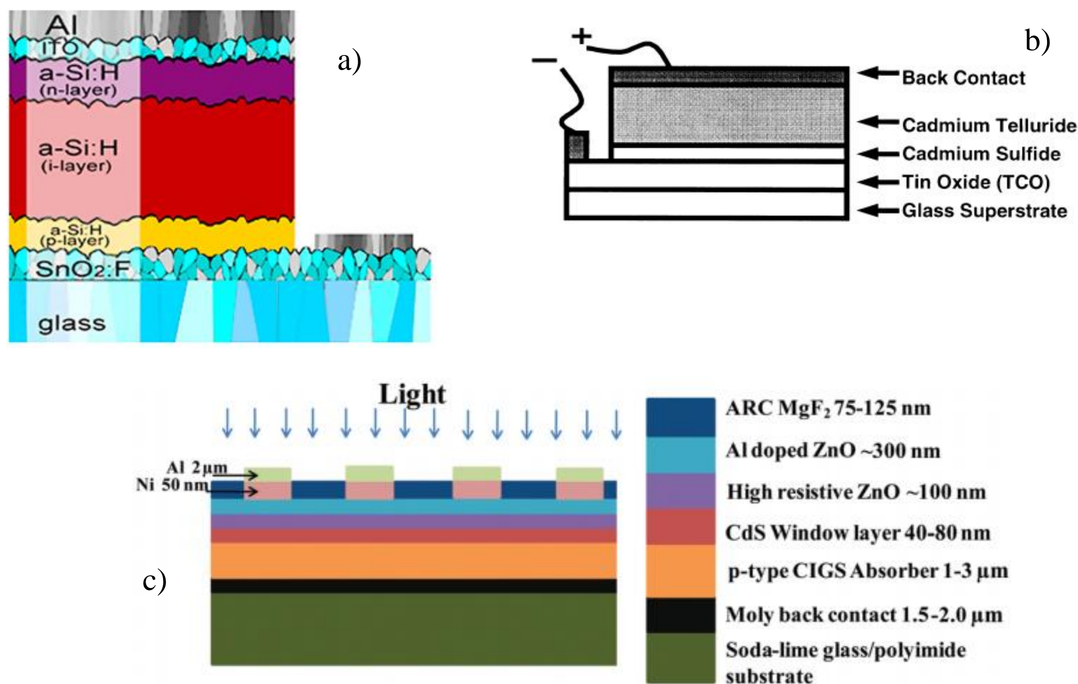

Figure 3.16. Schemes of solar cells based on a) amorphous silicon solar cells (a-Si) [Hua12] b) CdTe [Fer00] and c) CIGS [Ram17] technologies.

3.3.3 3rd generation: organic and novel technologies

The third generation of solar cells is based on the incorporation of new materials with the aim to obtain a real alternative to silicon devices with higher efficiency and lower cost

per watt of electricity generated. This generation is divided in four main types and the scheme of each technology is shown in figure 3.17.

- **Dye sensitized solar cells (DSSC)** [Naz11]

Dye sensitized solar cells are based on traditional roll-printing techniques using a photosensitive layer made of ultrathin, nano-sized semiconductor crystals over a thin layer of titanium dioxide. DSSC can be used in semitransparent and semi-flexible materials, allowing a range of uses that are not applicable to rigid photovoltaic technologies. Nowadays DSSC have reached efficiency values close to 12% [Sha18]. Nevertheless, the lifetime of DSSC solar cells is quite low in comparison with others technologies. In addition, the stability over time and the temperature range are two factors that also need to be improved for this technology to begin to be competitive.

- **Organic solar cells** [Ber08]

Organic solar cells are based on a thin layer of organic material with a thickness in the 100 nm range. This technology comprises small molecules and polymers (figure 3.17 (b)) solar cells.

The main difference between organic and inorganic solar cells is that the organic ones are based on the creation of excitons due to coulomb-interaction with a typical binding energy 0.3-0.5 eV, meanwhile in the inorganic ones there is a direct generation of free carriers. However their efficiency and lifetime is worse than conventional solar cells. Although this technology allows to develop flexible devices, they are more susceptible to moisture and rapidly degrade in ambient exposure.

- **Heterojunction with Intrinsic Thin layer solar cells (HIT)** [Ift13]

The HIT technology is based on the introduction of an intrinsic layer of a few nanometers in the *p-n* structure of a solar cell (see figure 3.17 (c)). The aim of this introduction is increase the device efficiency and reduce the cost of manufacture but, inasmuch as is usually used to complete Si solar cells, it still the disadvantages of the crystalline silicon solar cells.

- **Colloidal quantum dots solar cells** [Sog16]

Colloidal quantum dots technology is based on semiconductor nanostructures (figure 3.17 (d)), where at least one dimension is small enough to produce quantum

confinement effects. The aim of this technology is to use the remaining energy of the photons with an energy higher than the bandgap. In a typical solar cell, this energy is dissipated as heat, however, with this technology, this energy can be used thanks to a process known as multiple exciton generation [Sie17]. However, sometimes colloidal quantum dot solar cells can reduce the carrier collection [Ker17] mitigating thus the device efficiency. The efficiency record of this technology is ~10% [Dav16].

- **Perovskite solar cells** [Shi18]

As others techniques, perovskites solar cell (Figure 3.17 (e)) pretend to increase the efficiency and reduce the cost of the solar energy. This technology is based on the introduction of a thin film of a perovskite-structured compound as active layer, usually based on a hybrid organic-inorganic lead or tin halide-based material. These compounds are easy to produce and reduce the cost of the solar cells. Besides, the big advantage of perovskites is that they can react to different wavelengths of light and, thus, can convert a wider part of the solar spectrum into energy. The main disadvantage is the degradation with the exposure of heat and humidity.

Nowadays perovskites are the most promising technology in the photovoltaic field, reaching efficiency values above 20% in the laboratory [Sal18] and reaching a 25% for heterojunctions with c-Si [Bus18].

- **Tandem or multi-junction solar cells** [Ame09]

A single junction solar cell can only work properly in a certain solar spectrum range. That is because the energy of the photons does not contribute if it is lower than the bandgap and if the energy is much higher, the energy exceeding the bandgap is lost through thermalization.

In that sense, the aim of tandem solar cells (figure 3.17 (f)) is to absorb each wavelength of light with a material that has a bandgap energy equal or lower than the incident photon energy, absorbing more efficiently in the whole spectrum.

Nowadays, this technology is usually based on multi-junctions of III-V compounds based on phosphide or arsenide, such as GaAsP, AlGaAs, InGaP or AlInP deposited onto GaAs, InP, Si or even Ge substrates [Luc19] as is shown in figure 3.17 (f). In that sense, the manufacturing cost of large surface cells is quite expensive in comparison with other technologies being one of the mains challenges of this

technology. However, to solve this, the combination of small solar cells together with concentration technologies are carried out leading to higher energy production.

Nowadays this technology has achieved the record of efficiency of solar cells with efficiencies above 40% without concentration and close to 45% under concentration conditions based on three of four junctions [Tak14] as showed in figure 3.17.

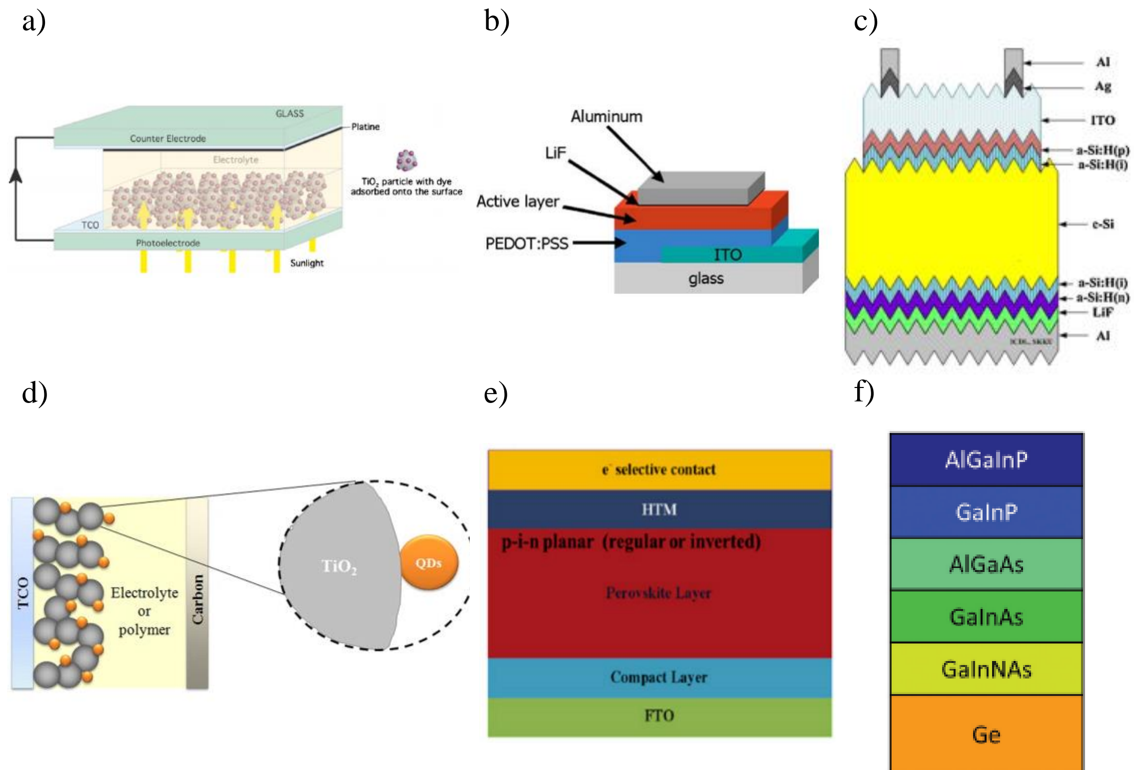

Figure 3.17. Schemes of solar cells based on a) dye sensitized [Naz11], b) polymers [Hop07], c) HIT solar cell [Kim12] , d) quantum dots [Emi11], e) perovskite materials [Shi18] and f) tandem solar cell [Bet14].

Figure 3.18 (obtained from the National Renewable Energy Laboratory (NREL)) displays the evolution of the different technologies along the years, highlighting the high efficiency values of the multi-junction technology and the great evolution of the perovskites, form ~14% to ~25% in the last 6 years.

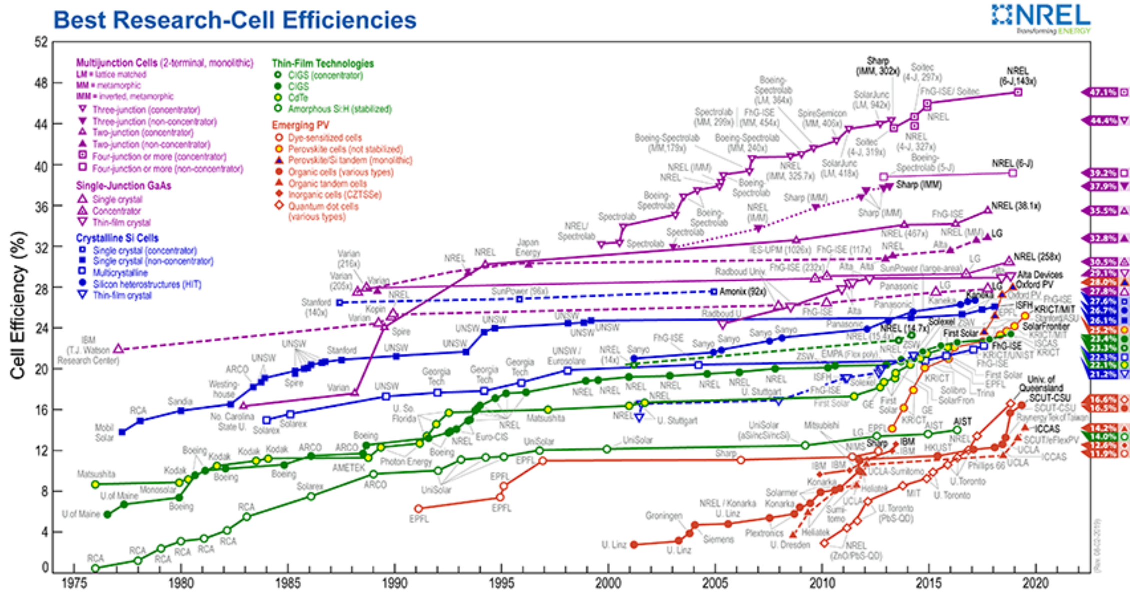

Figure 3.18. Evolution of the bets research-cell efficiencies year by year [https://www.nrel.gov/pv/cell-efficiency.html].

3.3.4 State of the art of III-nitride-based solar cells

Solar cell based on III-nitride materials are currently included in the third generation of solar cells, insomuch as III-nitrides are novel materials that claim to be an alternative to known technologies, seeking high efficiency and low cost per watt.

As explained in the first chapter of this thesis, one of the aims of this technology is to use the bandgap engineering to create a multijunction solar cell. In that sense, solar cells based on InGaN multijunction and quantum wells were developed along last decade grown by different deposition techniques.

However, one of the main problems of the MOCVD and MBE growth techniques is the growth temperature, which leads to obtain low In contents, thus limiting the bandgap energy of the compounds.

In that sense, one of the main targets of this technology is to develop compounds with high In content to cover a greater range of the solar spectrum as achieved by some studies [Çak14, Jan05] for layers deposited by MOCVD.

Despite this problem, there are some reports based on InGaN quantum wells layers deposited by MOCVD deposition technique for solar cells applications revealing conversion efficiency around 2.95% without concentration and reaches values close to

3% under a concentration of 30 suns as observed by Dahal *et al.* [Dah10] shown in figure 3.19.

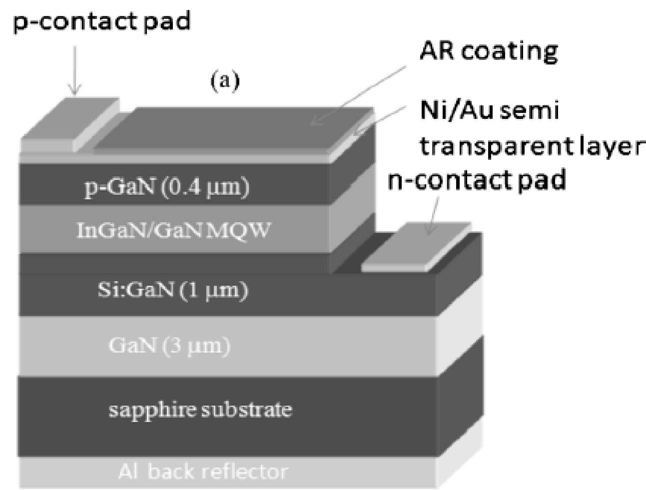

Figure 3.19. Scheme of GaN/InGaN quatum wells solar cells developed by Dahal *et al.* [Dah10].

On the other hand, InGaN layers grown by MBE have reached an efficiency record of 2% [Val14] without concentration and a 4% obtained under concentration of 300 sun by Mori *et al.* [Mor13]. The main drawbacks of this technology are based on the lack of an effective *p*-type doping of the layers and the dislocation density and the lattice mismatch between the layers.

Beside this, the III-nitrides materials have been proposed as *n*-type front layer in a homojunction with a *p*-type of an already known technology such as silicon or gallium arsenide substrates with the aim to use its wide direct bandgap to improve the efficiency of silicon solar cells. In that sense, the efficiency record of this technology has been obtained by an InGaN multijunction deposited on *n*-Si substrate with an efficiency value of 5.95% [Lio11]. Furthermore, some groups including the photonics engineering group (GRIFO) of the University of Alcala, have focused on the introduction of AlInN as a top layer of a heterojunction based on AlInN/Si obtaining a conversion efficiency values of 1.1% [Liu12] and of 1.5% [Nuñ18].

Chapter 4

Sputtering deposition technique

This chapter explains the sputtering deposition technique used for the growth of the III-nitride thin films and the heterojunctions exposed in this thesis.

The RF-Sputtering is a commonly used technique for thin film deposition (metals and semiconductors), etching and surface cleaning with several applications including solar cells and optoelectronic devices [Was92, Was04].

The main advantage of the sputtering deposition technique is that allows the growth of high quality films at low temperatures and even at room temperature, making it a low-cost technique widely used in the industry.

In order to introduce the principles of this deposition technique, the first section of the chapter contains a general introduction and the principles of the radio frequency (RF) sputtering technique followed by the different kind of plasma generation, cathodes and gases.

Then, I will describe the characteristics of the RF sputtering equipment of the Photonics Engineering Group of the Electronics Department of the University of Alcala.

Finally, the substrates used for the deposition of the III-nitride films are presented.

4.1 Principles of sputtering

The sputtering technique is based on the emission of atoms by the bombardment of a solid (named target) by energetic particles (named ions) formed by RF or direct current (DC) voltage. In this technique, the atoms of a gas (typically nitrogen and argon) are ionized by the application of a voltage between the target (cathode) and the substrate (anode) forming a plasma in the sputtering chamber. In the plasma, the ionized atoms are

accelerated into the surface of the target in order to sputter atoms from it. The collisions between the ions of the gas and the target atoms allow the deposition of these atoms under the right deposition conditions creating thus a thin film of material on the substrate. This deposition process takes place under high vacuum conditions (sputtering pressure ≈ 10^{-8} Torr) inside a high vacuum chamber in order to minimize the impurities in the deposited film. Figure 4.1 shows a scheme of the deposition chamber and the sputtering process with all species involved.

One of the most important parameters of the sputtering technique is the sputtering yield that represents the efficiency of the process. This parameter is defined as the ratio between the particles ejected from the target and the number of ions that collide with it.

Several parameters affect the sputtering yield. For example, if the energy of the ions is too low, it can produce a reflection of the ions damaging the surface. However, if the energy of the ions is too high, it can produce an ion implantation on the surface of the substrate. Besides, the mean free path of the particles, which describes the average distance traveled by a particle, is another important parameter and is inversely proportional to the pressure of the process. In that sense, if the mean free path is optimized the efficiency of the sputtering process increases.

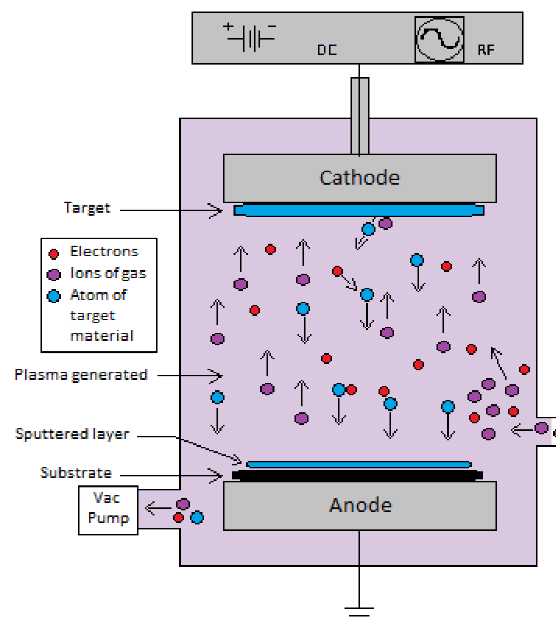

Figure 4.1. Scheme of a high-vacuum sputtering chamber and the sputtering process with all species involved.

4.1.1 Plasma generation

In the sputtering technique, the target is mounted on a cathode and the substrate is connected to an anode. The sputtering technique has two kinds of voltages applied to the cathode: static (DC) and alternating (RF).

DC voltage

To create plasma through DC voltage conductive electrodes to sustain the DC discharge are necessary. One of the electrodes is placed on the cathode (material to evaporate) and the other one is in contact with the substrate (anode) both under low-pressure gas conditions.

The DC voltage needs a conductive material in the cathode to avoid the accumulation of charges in the electrodes and arcs. However, it allows higher deposition rates than RF voltage.

In order to generate the plasma, the pressure has to be within a specific range in the sputtering chamber and a high DC voltage has to be applied in the electrodes so that the ionization of the gas is possible. In this way, the high intensity of the electric field near the cathode makes possible the ejection of atoms from cathode.

RF voltage

The deposition rate of RF voltage is lower than the DC one under the same growth conditions (approximately a half). However, this technique allows using non-conductive and isolating materials in the cathodes by applying an alternate voltage. The most commonly used frequency is typically in the radiofrequency range (13.56 MHz). In this sense, throughout the deposition process the target acts like an anode during the negative process and it changes the behavior during the positive process, acting like cathode, whereas in the substrate the reverse process happens. Thereby, during the negative process the ions sputter the target surface allowing the ejection of the atoms and thus the creation of the layer.

4.1.2 Type of cathodes

Nowadays there are three types of cathodes for the sputtering technique: planar diode, magnetron and unbalanced magnetron.

Planar diode

In the planar diode configuration (see figure 4.2 (a)) both electrodes are separated at a certain distance inside the vacuum chamber. When the plasma discharge happens there is an area with a huge electric field close to the cathode. When the ions cross this area they are accelerated and impact with the surface of the cathode.

This deposition method requires high pressures (≈ 3 Pa) due to the electron multiplication. However, the problems of using isolating targets and the low deposition rate limit this technique.

Balanced planar magnetron

In contrast, the balanced magnetron configuration uses a balanced magnetic field during the deposition to trap the electron closer to the cathode, increasing therefore the efficiency of the process and allowing working at low pressures. This effect is because the electrons follow helical paths around the magnetic field lines due to the Lorentz´s force generated between the electric and magnetic fields. In this sense, the probability of collision between the particles increases and so does the growth rate, which is defined as the ratio between the thickness of the layer and the deposition time.

In comparison with the planar diode method, the magnetron configuration presents many advantages like lower power discharge, higher ionization efficiency and lower working pressure (≈ 0.1 Pa), leading to higher deposition rates. Considering this, the RF voltage is usually used with the magnetron configuration in order to improve the deposition rate of the layers.

Unbalanced planar magnetron

The unbalanced magnetron (figure 4.2 c)), unlike the balanced one, is based on the increase of the magnetic field at the external magnets of a magnetron, resulting in the expansion of the plasma away from the surface of the target towards the substrate. The effect of the unbalanced magnetic field is to increase the number of additional ions and electrons in the substrate region by trapping fast moving secondary electrons that escape the target surface. This effect leads to an increasing of the ionic bombardment of the substrate which can be used to control the many properties of the layers.

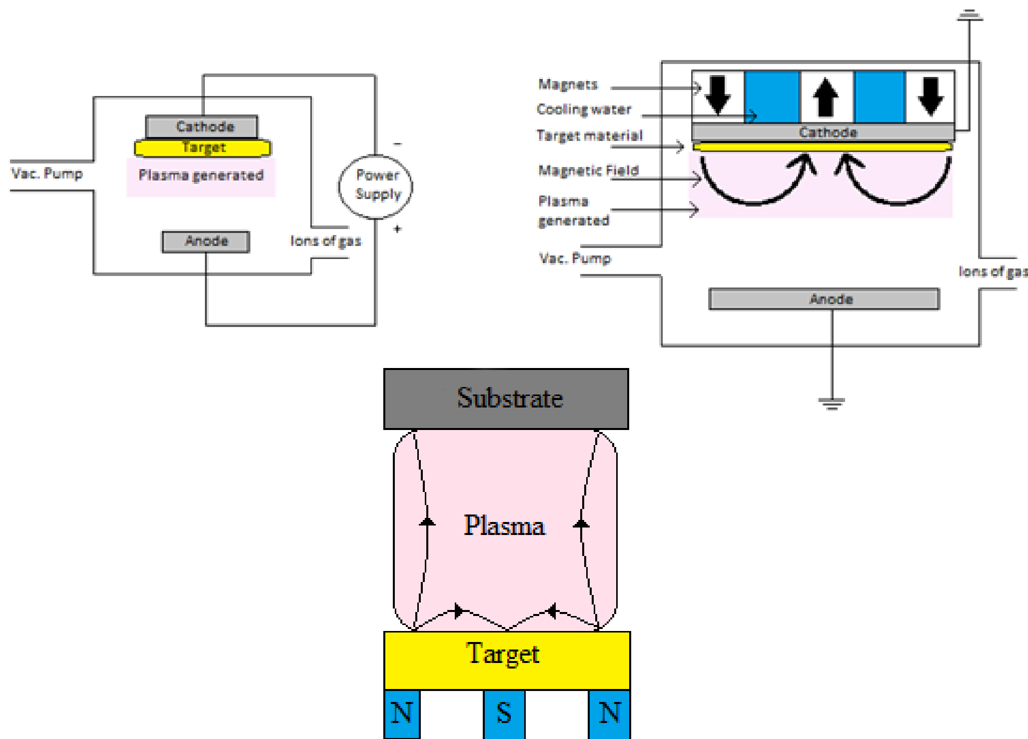

Figure 4.2. Scheme of planar a) diode b) balanced magnetron and c) unbalanced magnetron configurations.

4.1.3 Types of gas

To generate a plasma it is common to use a non-reactive gas, like the noble gas argon (Ar), or reactive gases like nitrogen, oxygen and methane.

Non-reactive gas

The non-reactive gas used for generating the plasma and for sputtering the target surface is a gas (usually a noble gas) which does not react with the atoms during the growth process. The most commonly gas used is argon due to its low cost and its high atomic mass, achieving high growth rates due to the enhancement of the transfer of the kinetic momentum to the target atoms.

Reactive gas

The reactive gas method usually uses nitrogen, oxygen and methane gases.

The aim of using a reactive gas is to create a compound with it, since it reacts with the atoms of the target during the sputtering process. The formation of the compound depends on the deposition conditions and will be formed mainly on the surface of the target and also can be formed between the target and the substrate and on the substrate.

One problem of reactive sputtering is that the atoms of the target can react with the plasma "poisoning" the target and forming a thin film of the compound on its surface. This effect will reduce the sputtering growth rate leading to the need of more reactive gas to increase it so forth in a feedback loop.

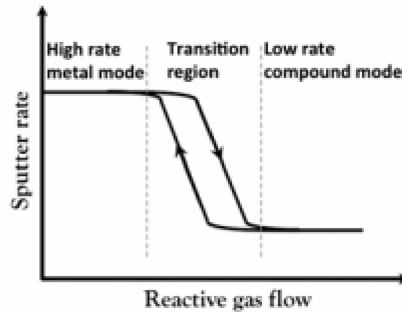

Figure 4.3. Hysteresis process in reactive sputtering [Lil12].

Figure 4.3 shows the feedback loop or hysteresis process in reactive sputtering. When the reactive gas flow is low the growth rate is not enough to obtain stoichiometric compounds, being quite similar to the metallic growth. This state is called as metallic mode. To avoid this metallic mode, it is necessary to increase the reactive gas flow reaching the reactive mode. This process happens in the transition region. The reactive mode is accompanied with a decrease of the growth rate reaching a low rate compound mode. This effect is caused by the aforementioned poisoning of the target, so the reactive gas has to be decreased to reduce it, returning thus to the metallic mode, increasing drastically the growth rate and reducing the poisoning of the target.

4.2 Magnetron RF sputtering system used in this thesis

All samples and contacts developed in this work were fabricated using the sputtering system ATC ORION-3-HV from AJA International (figure 4.4) placed in the laboratory of the Photonics Engineering Group of the Electronics Dept. from the University of Alcalá.

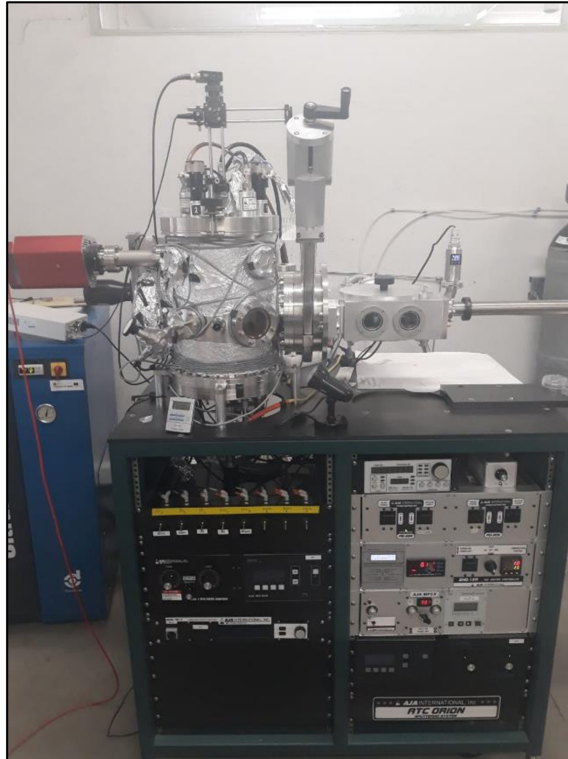

Figure 4.4. Magnetron reactive RF sputtering system used during this thesis at the University of Alcalá.

The main characteristics of this sputtering system are below:

- High-vacuum manual valve to control the pressure in the sputtering chamber.
- High-vacuum system formed by a turbomolecular (≥ 210 l/s) and a mechanical pump (≥ 12 m^3/h) with a minimum vacuum level ≈ 10^{-8} Torr.
- Three vacuum gauges:
    - An ionization gauge for achieving low-base pressures (~10^{-8} mBar).
    - A baratron gauge for pressures in the deposition range (~10^{-4} - 10^{0} mBar).
    - A convectron gauge for pressures close to atmosphere pressure.
- Introduction chamber equipped with a turbomolecular and a mechanical pump.
- Ar (5N) and N_2 (6N) gas sources.
- Leak valve for the sputtering chamber venting with nitrogen.
- Three 2-inch diameter confocal magnetron cathodes with shutters: one In target and two Al targets.
- Two RF power sources above 300 W for an Al (5N) and In (4N5) metal targets.
- DC power supply above 750 W for an Al (5N) target.
- Substrate holder (4-inch) with a rotatory system for optimized heating and so forth the growth homogeneity.

- Two quartz lamps placed under the substrate holder to heat the substrates up to 850ºC.
- A K-type thermocouple placed 2 mm below the holder and controlled by a PID with a resolution of ±1ºC for monitoring the substrate temperature.
- Close-cycled cooling system keeping cool the magnetron and the substrate heater.
- Residual gas analyzer (RGA) for *in situ* measurements of the gases of the chamber
- Reflectivity system for *in situ* measurements of the deposited layers.
- Thin film deposition monitor based on a quartz crystal to measure the thickness of the deposition of metal compounds.

During this thesis, the AlInN-based layers were grown using two planar magnetron cathodes with two RF voltage sources, one for the In and other for the Al, and nitrogen as reactive gas. On the other hand, the metallic Al layers used for the contacts of the devices were deposited under DC voltage and using argon as non-reactive gas. In all cases, the separation between the target and the substrate has been fixed at 10.5 cm and, unlike previous studies, no mount in the In target was used.

4.3 Substrates for III-nitrides deposition

The most commonly way to growth III-nitrides is the heteroepitaxyal mode due to the lack of an appropriate lattice-matched and thermally stable substrate for homoepitaxyal growth. In order to choose the best substrate it is necessary to take into account the lattice and thermal expansion mismatches between the deposited layer and the substrate. Besides, the prize of the substrate, the defect density and the crystalline quality are also parameters to take into account. In that sense, the mainly used substrates are sapphire (Al_2O_3), silicon (Si), GaN-on-sapphire templates and silicon carbide (SiC), but gallium arsenide (GaAs) and the zinc oxide (ZnO) are also used.

In this work, we analyze the material and device properties of the III-nitrides layers grown on three types of substrates: *p*-doped Si with crystallographic orientations (100) and (111) and sapphire.

4.3.1 Sapphire

Sapphire is a transparent substrate useful to analyze the optical properties by transmittance measurements and the electrical properties by Hall Effect measurements. It is relatively a low-cost substrate and can be commercialized in different sizes and orientations. Sapphire has a hexagonal structure with a lattice parameters $a = 12.99$ Å and $c = 4.76$ Å are higher than the III-nitrides ones.

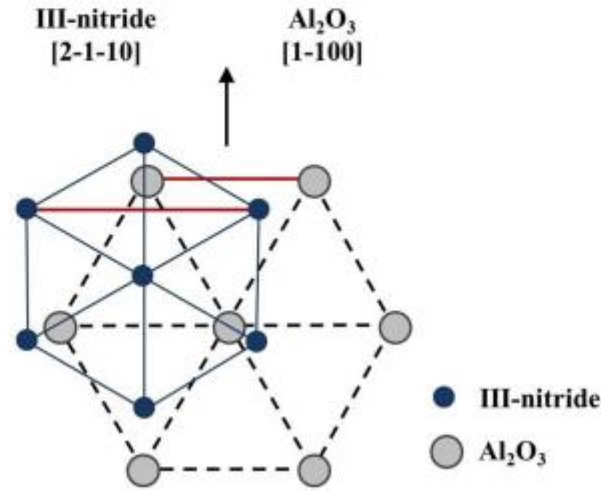

Figure 4.5. Scheme of the epitaxial relationship between the III-nitrides compounds and sapphire in the (0001) plane [Mon15].

When III-nitrides are grown on sapphire, the [2110] nitride direction and the [1100] are aligned since the nitride structure is rotated 30º with respect to sapphire as shown in figure 4.5. This rotation changes the lattice parameter, obtaining an effective lattice parameter given by:

$$a'_{III-nitride} = \sqrt{3}a_{III-nitride} \tag{4.2}$$

Through the results of the table 4.1, the different behavior of the III nitrides can be analyzed. In that sense, III-nitrides grow under tensile strain on Si (111) and Si (100) and under compressive strain on sapphire.

3-inch sapphire [0001] substrates (shown in figure 4.6 (a)) grown using the Czochlarski method [Fan12] and double side polished with a thickness of 525±25 μm have been also supplied by Semiconductor Wafers INC. Besides, the rms surface roughness obtained from AFM measurements (figure 4.6 (b)) is 0.33 nm.

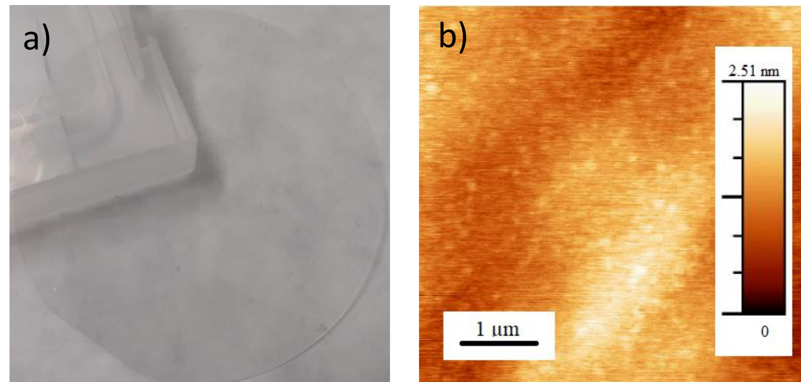

Figure 4.6. a) Photo of a sapphire substrate and b) the AFM image of the substrate used along this thesis.

4.3.2 Silicon (100) and (111)

Nowadays, silicon is one of the most commonly used material for electronic devices like solar cells or transistors [Opo16] due to the availability to obtain high dimension wafers at low prize with high crystalline quality. In the case of III-nitrides, silicon substrates offer their integration into the existent Si technology, the possibility of having *n*-type and *p*-type conductor substrates, easy cleavage and thermal stability.

Despite silicon crystallizes in a cubic crystal structure presents a hexagonal symmetry in the plane perpendicular to the [111] direction. This symmetry is related with the wurtzite symmetry along the [0001] direction, allowing the growth of III-nitrides compounds.

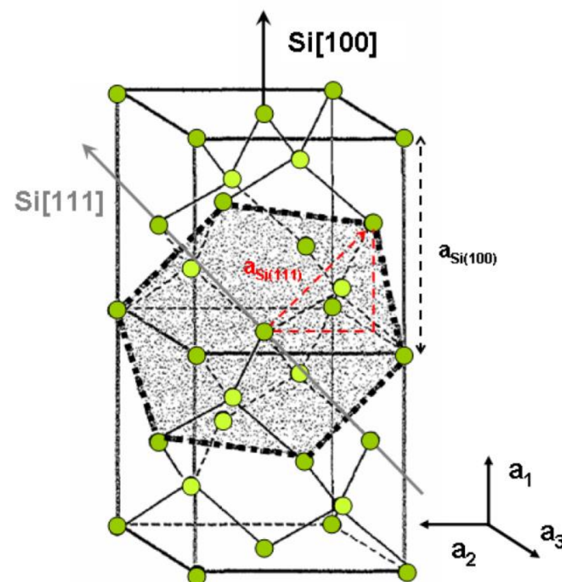

Figure 4.7. Relationship between hexagonal (111) and cubic (100) planes of silicon. The red-dashed triangle shows the relationship between Si cubic and hexagonal phases [Val11].

However, nowadays the silicon technology is based on its cubic orientation since it presents less electrical loses due to the reduce number of dangling bonds at the surface [Yu13]. In that sense, we will study the effect of growing III-nitrides on both Si (111) and Si (100) in order to improve the electrical properties of the devices.

Figure 4.7 shows the relation between the cubic and the hexagonal plane of Si. Through this relation, we obtain the lattice mismatch between the III-nitrides and the silicon substrate (red-dashed triangle), which is given by:

$$a_{Si\,(111)} = \frac{a_{Si\,(100)}}{\sqrt{2}} \quad (4.1)$$

Table 4.1 summarizes the lattice and thermal expansion coefficients of III-nitrides taking into account the epitaxial relationship obtained from equation 4.1 and the mismatch between Si (111), Si (100) and sapphire with the III-nitride compounds. It can be observed that the III-nitride compounds grow under tensile strain on Si substrates, being higher for the Si (100) one, and under compressive strain when growing on sapphire substrates. Moreover, the thermal expansion coefficient of InN is lower in comparison with the others compounds. This means that InN suffers a higher contraction than the substrate during cooling down after the growth leading to biaxial stress.

	a (Å)	a' (Å)	$\frac{\Delta a'_{epi}}{a_{sapp}}$ (%)	$\frac{\Delta a_{epi}}{a_{Si\,(111)}}$ (%)	$\frac{\Delta a_{epi}}{a_{Si\,(100)}}$ (%)	α_a (10^{-6} K^{-1})	$\frac{\Delta \alpha'_{epi}}{\alpha_{sapp}}$(%)	$\frac{\Delta \alpha_{epi}}{a_{Si\,(111)}}$ (%)	$\frac{\Delta \alpha_{epi}}{a_{Si\,(100)}}$ (%)
AlN	3.112	5.390	13.3	-19.0	-42.7	4.2	-44	17	43.8
GaN	3.189	5.524	16.1	-17.0	-41.3	5.59	-25.5	55.7	91.4
InN	3.545	6.14	29.0	-7.7	-34.7	3.83	-48.9	6.7	31.2
Sapphire	4.758	--	--	--	--	7.5	--	--	--
Si (111)	3.840	--	--	--	--	3.59	--	--	--
Si (100)	5.43	--	--	--	--	2.92	--	--	--

Table 4.1. Summary of lattice parameters and thermal expansion coefficients of III-nitrides [Vur03] and silicon (on both orientations) and sapphire substrates [Neu96]. Lattice and thermal mismatch between III-nitrides and the substrates are at 300 K and $\Delta\alpha_{epi}$ and Δa_{epi} are the difference between the lattices parameter and the thermal expansion coefficient of the layer and the substrate, respectively.

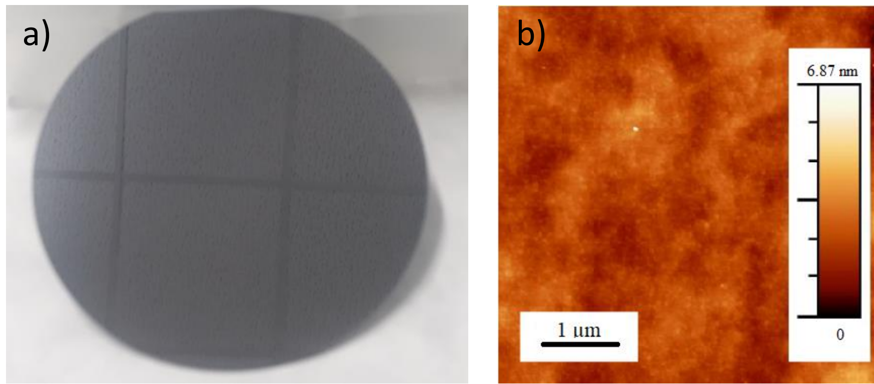

Figure 4.8. a) Photograph of *p*-silicon (111) substrate and b) the AFM image of the substrate used along this thesis.

Semiconductor Wafers INC supplied double side polished 4-inch diameter silicon (111) and 3-inch silicon (100) substrates (shown in figures 4.8 and 4.9 (a), respectively) grown using the Czochlarski method [Aub89]. Both substrates own a resistivity of 10–100 Ω·cm and 1–10 Ω·cm and a thickness of 525 µm and 300 µm, respectively. The RMS surface roughness obtained from AFM measurements shown in figure 4.5 and 4.6 (b) is 0.49 and 0.47 nm from Si (111) and Si (100) respectively.

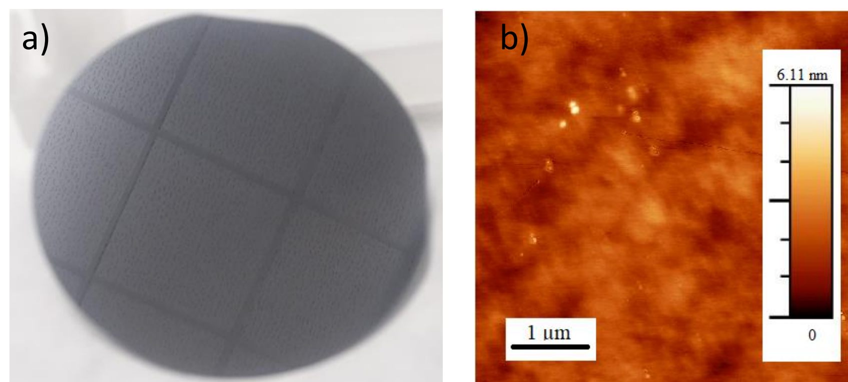

Figure 4.9. a) Photograph of *p*-silicon (100) substrate and b) the AFM image of the substrate used along this thesis.

Chapter 5

Characterization techniques

The aim of this chapter is to describe the experimental techniques used along this thesis to characterize the III-nitride layers and the devices. Concretely, I describe the structural, morphological, electrical and optical and characterization techniques for the developed material including high-resolution X-ray diffraction, atomic force microscopy, field emission scanning electron microscopy, Hall Effect, transmittance, reflectance and photoluminescence. Then a detailed study of the fabrication technology of the devices including the development and optimization of the contacts deposited by RF sputtering is presented. Finally, a description of the device characterization techniques, *i.e.* current-voltage curves in the dark and under 1 sun AM1.5G illumination) and responsivity measurements is carried out.

These measurements were carried out thanks to a collaboration with others research centers to which we would like to thank for their contribution to the development of this thesis.

5.1 Structural and morphological characterization

This section aims to summarize the methods used for the structural and morphological characterization of the layers. Through these methods, the crystalline structure and the structural and morphological quality of the layers and the interface can be studied.

5.1.1 High-resolution X-ray diffraction

High-resolution X-ray diffraction (HRXRD) measurements were used to determine the lattice parameter and the crystalline orientation of the layers among others to obtain thus their crystalline quality.

This technique is based on the interference of electromagnetic waves in the material. In that sense, an X-ray beam (λ ≈ 0.15 nm f ≈ 200 PHz) is focused on the sample, it being eventually diffracted by a given family of planes depending on the angle of incidence. The X-ray diffraction occurs when the radiation of a wavelength λ interfere with a periodic structure with parallel and equidistant atomic planes separated a distance close to λ (see figure 5.1). The condition of constructive interference is given by the Bragg´s law [Bra13], which determines the angle between the incident beam and the plane family for an incident wavelength λ as described by the following equation:

$$2d \sin \theta = n\lambda \tag{5.1}$$

where d is the distance between tow atomic planes, θ is the angle between the incident beam and the planes producing the diffraction, n is the diffraction order and λ is the incident wavelength.

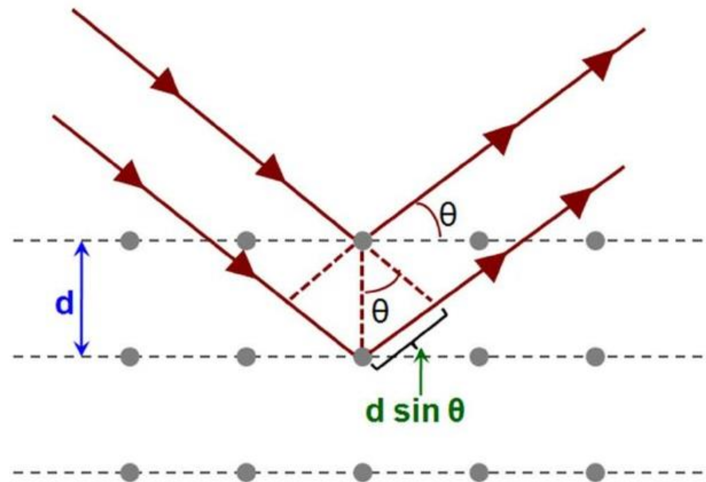

Figure 5.1. Bragg´s diffraction law [Bask10].

During this thesis two types of X-ray diffractograms under symmetrical configuration (the angle formed between the detector and the sample is equal to the one formed by the incident beam and the sample) were carried out: $2\theta/\omega$-scans and ω-scans. Also, a X-ray reflectometry measurements at low incidence angles were performed.

- $2\theta/\omega$ scan: In this scan the angle between the incident beam and the sample (θ) and the one between the incident beam and the detector (2θ) are scanned keeping the same relationship between them. That means that if the sample rotates an angle ω the detector rotates double of this magnitude. The position of the diffraction peak obtained gives information about the lattice distance between the crystal

planes parallel to the sample surface and allows to estimate the lattice parameter c of the material. This scan permits to detect also the existence of grains with different crystal orientations in the sample, which is related to the diffraction peak full with at half maximum (FWHM).

$2\theta/\omega$ scan measurements can be used to estimate the alloy composition assuming fully relaxed layers with the Vegard´s law [Vega21], which takes into account the lattice parameter c of the binary compounds AlN ($c_{AlN} = 4.982Å$) and InN ($c_{AlN} = 5.703Å$) [Vur03] (see equation 2.1).

The FWHM of the diffraction peak gives information about the average of the grain size of the crystal volume which originates the diffraction peak through the Scherrer equation [Pat39]:

$$G = \frac{0.9\lambda}{\Delta 2\theta} \cos\theta \qquad (5.2)$$

where λ is the X-ray wavelength, θ is the Bragg´s diffraction angle and $\Delta 2\theta$ is the FWHM of the diffraction peak.

- ω-scans (rocking curve): In this configuration the sample turns along the Bragg´s angle axis while the detector keeps his position fixed at a given diffraction peak. The FWHM of the rocking curve scan provides information about the degree of misorientation of the grains and then of the quality of the material. In that sense, a perfect crystal shows a very sharp peak, and the broadening increases due to different contributions like tilt and strain surrounding dislocations.
- X-ray reflectivity (XRR): In this measurement the angle between the source and the sample (θ) is lower than the first Bragg diffracted and the detector moves an angle 2θ. When the beam of X-rays reaches an interface, a portion of X-rays is reflected and create a reflectometry oscillation pattern. This method is used to estimate the roughness, surface density gradients, layer density and thickness of the samples using the Bragg´s equation 5.1.

HRXRD measurements were performed at the CAI X-ray Diffraction Service of the Complutense University using a PANalytical X´Pert Pro MRD system.

5.1.2 Atomic force microscopy

Atomic force microscopy (AFM) measurements provide information about the quality and the morphology of the sample through a topographic image. Through this image, the root-mean-square (rms) roughness can also be estimated.

AFM measurements are based on a short-range interaction between the surface of the sample and the probe tip assembled on a cantilever due to Van der Waals forces. The AFM system comprises a laser beam, a cantilever mounted on a piezoelectric actuator and a photodetector. The laser beam is reflected by the cantilever and collected by the photodetector (figure 5.2). The signal collected by the photodetector is used as input of the piezoelectric actuator to correct the position of the cantilever along the z-axis if it deviates.

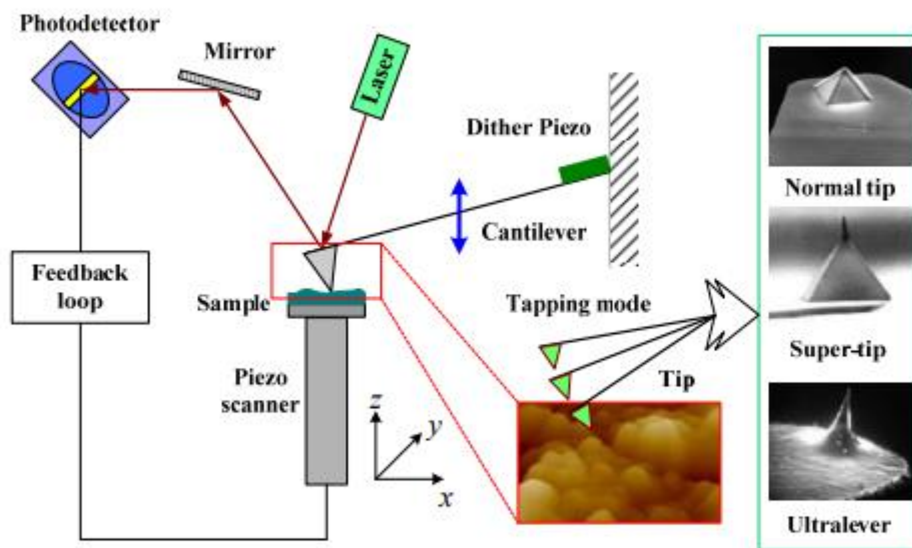

Figure 5.2. Scheme of a typical AFM setup in tapping mode [Zha09].

In this study, the AFM measurements are performed in the tapping mode. In this mode, the tip oscillates with a fixed frequency above its resonance frequency, while the amplitude of the oscillation is monitored. When the tip is close enough to the surface it is exposed to the Van der Waals interaction and then the oscillation amplitude is kept at the set point and the z-position is controlled by the feedback mechanism. To compose the topographic image, the variations of the z-position of the tip are plotted as a function of the position of the tip on the xy plane.

The AFM measurements of this work were carried out at the CEA-Grenoble laboratories using a Veeco Dimension 3100 microscope with a resonant frequency of 300-50 kHz and

probe tips Bruker OTESPA under the supervision of Dr. Eva Monroy. The data processing was performed with the WSxM software [Hor07].

5.1.3 Field emission scanning electron microscopy

Field emission scanning electron microscopy (FESEM) measurements scan point by point with a high-energy beam of electrons the surface of the sample. The backscattered electrons received from the sample leads to the formation of an image of the surface morphology of the layers.

FESEM measurements can generate high-resolution images of a surface with magnification up to 100.000 times revealing details in the range of nanometers. Through this kind of measurements we obtain information about the morphology and the type of growth (columnar or compact), the layer thickness and the surface topography using both cross section and surface images.

The FESEM images were performed at the CEA-Grenoble laboratories using a Zeiss 55 field-emission scanning electron microscope by Dr. Akhil Ajay under the supervision of Dr. Eva Monroy. This system includes a high resolution in-lens detector for secondary electrons positioned inside the microscope, which allows an efficient electron collection and the possibility to analyze non-conductive materials without a previous metallization process.

5.2. Optical characterization

The optical characterization of the samples analyzed in this thesis was carried out by optical transmittance (Tr), reflectance (R) and photoluminescence (PL) measurements. From these measurements it is possible to optimize the material growth taking into account the estimated bandgap energy of the layers and its relationship with impurities and crystal defects.

5.2.1 Transmittance

Transmittance measurements provide information about the thickness of the layer and several optical parameters like linear refractive index, linear absorption and the optical bandgap. When radiation propagates through an absorptive medium the evolution of its intensity can be described using the Beer-Lambert law:

$$I(\lambda, x) = I_0(\lambda) e^{-\alpha_{0(\lambda,x)} L} \quad (5.3)$$

where $I(\lambda, x)$ is the radiation intensity at the position x, $I_0(\lambda)$ is the radiation intensity of the incident beam, L is the layer thickness and $\alpha_{0(\lambda,x)}$ is the absorption coefficient of the sample.

The transmittance of the sample is defined as the ratio of the transmitted and incident intensity. So when the transmittance of the sample is known, it is easy to obtain the absorption coefficient of the material as:

$$T(\lambda) = {I(\lambda)}/{I_0(\lambda)} = e^{-\alpha_{0(\lambda)} L} \rightarrow \alpha(\lambda) L = -\ln[T(\lambda)] \quad (5.4)$$

It should be pointed out that the previous equation neglects the amount of reflected radiation at the interfaces of the sample. Along this thesis, the sigmoidal approximation of the absorption coefficient is used to estimate the effective bandgap energy of the III-nitride layers as in equation:

$$\alpha = \frac{\alpha_0}{1 + e^{\frac{E_0 - E}{\Delta E}}} \quad (5.5)$$

where α_0 is the linear absorption above the bandgap, ΔE is the absorption bad-edge broadening, E_0 is a fitting parameter that marks the inflection point of the sigmoidal function and E is the photon energy.

Transmittance measurements were carried out at the GRIFO facilities at the University of Alcala, which setup is illustrated in figure 5.3. The transmittance system owns a white broadband lamp which emission is collimated to obtain a homogeneous beam. The sample is located in the optical path of this beam, while a 20x magnification microscope objective is used to focus the transmitted beam into an optical fiber of 600 μm diameter which is connected directly to an Optical Spectrum Analyzer (OSA) with two detectors (Si and InGaAs) that cover the visible to the near infrared spectral range. During this work, all the transmittance measurements were done in the range of 350 to 1700 nm firstly without sample to obtain the spectrum of the lamp and then with the sample placed in perpendicular to the beam to obtain the ratio between them.

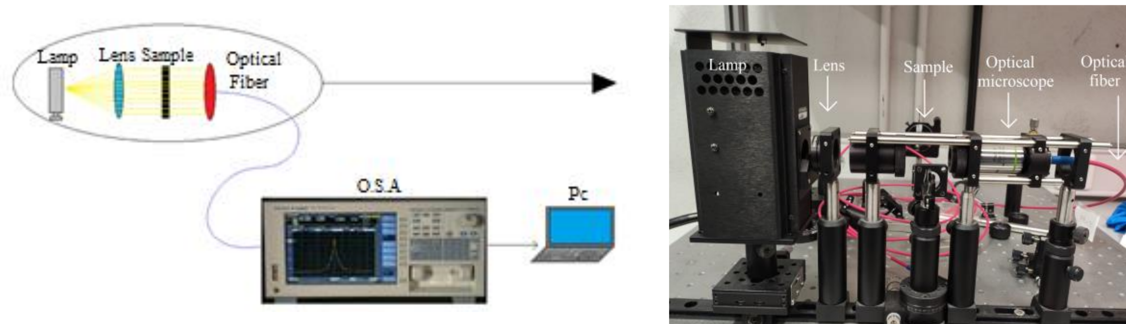

Figure 5.3. Scheme of the transmittance setup of GRIFO laboratories of the University of Alcalá.

5.2.2 Reflectance

The reflectance is defined as the ratio of the radiant flux received and reflected by a certain surface. It is an important parameter for the development of solar cells since it gives the amount of light that is reflected by the material and thus not entering to the device In this system, the beam is focused on the sample using mirrors to obtain a normal incidence on the sample surface. Dr. Susana Fernandez carried out the reflectance measurements presented in this thesis in the "Centro de Investigaciones Energéticas, Medioambientales y Tecnológicas" (CIEMAT) in Madrid using a Perking Elmer Lambda 1050 spectrophotometer working in the ultraviolet, visible and near infrared range and three detectors (PMT, InGaAs and PbS) to collect the data in all different wavelength ranges.

5.2.3 Photoluminiscence

Photoluminescence (PL) spectroscopy is a non-contact and non-destructive method widely used for the optical characterization of semiconductors. This technique consists of the study of the photon emission of a material which is excited by photons usually with and energy well above the bandgap energy of the semiconductor.

The excitation source is usually given by a laser beam which photons have an energy higher than the bandgap energy of the material. As depicted in figure 5.4 (a), this excitation leads to the generation of electron-hole pairs in the sample that relax emitting photons at an energy usually smaller than the bandgap energy of the material (radiative recombination). However, the PL process is also governed by a non-radiative recombination, which is usually caused by defects in the material, such as impurities or crystal disordes.

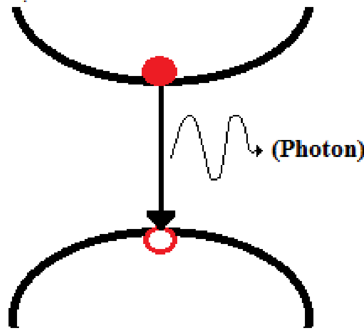

Figure 5.4. Schematic illustration of different types of radiative recombination.

PL measurements provide information about the optical quality of the layers. In that sense, materials with high crystal quality are characterized by an intense PL emission while emissions below the bandgap energy are usually associated with defects and impurities of the sample (see figure 5.4(b)). The observation of the PL emission peaks (intensity and broadening) can be related to the crystalline quality of the samples and its homogeneity. The means that layers with a high crystalline quality present an intense and sharp emission meanwhile a layer with lower quality presents usually a wider and less intense peak.

Besides the evolution of the PL emission peak energy and intensity as a function of the temperature (usually from 11 K to room temperature, 300 K) provides very useful information about the activation energy of the recombination process, the bandgap edge of the layers and also to detect impurities and defects.

Moreover, the thermal activation energy can be obtained using the following equation, which only takes into account one non-radiative recombination channel [Ler99]:

$$I(T) = \frac{I\,(T=0)}{1+a\cdot e^{-\frac{E_a}{k_B T}}} \tag{5.6}$$

where, E_a is the average energetic barrier required for carriers to escape from their localization and reach non-radiative recombination centers, a is a constant associated with the non-radiative-to-radiative recombination ratio and k_BT is the thermal energy.

PL measurements were carried out at GRIFO facilities using a continuous-wave diode laser at λ = 405 nm focused onto a 1-mm diameter spot with a power of 30 mW (see figure 5.5). The emission of the 193-mm-focal-length Andor spectrograph equipped with a UV-extended silicon-based charge-coupled-device camera operating at -60ºC by a 193-mm-focal-length Andor spectrograph equipped with a UV-extended silicon-based

charge-coupled-device camera operating at -60ºC. Besides, to remove the laser effect, a filter at 495 nm is used for filter the wavelengths below this value. To obtain the measurements at low temperature, samples are introduced in a cryogenic system, which reaches temperatures of 11 K.

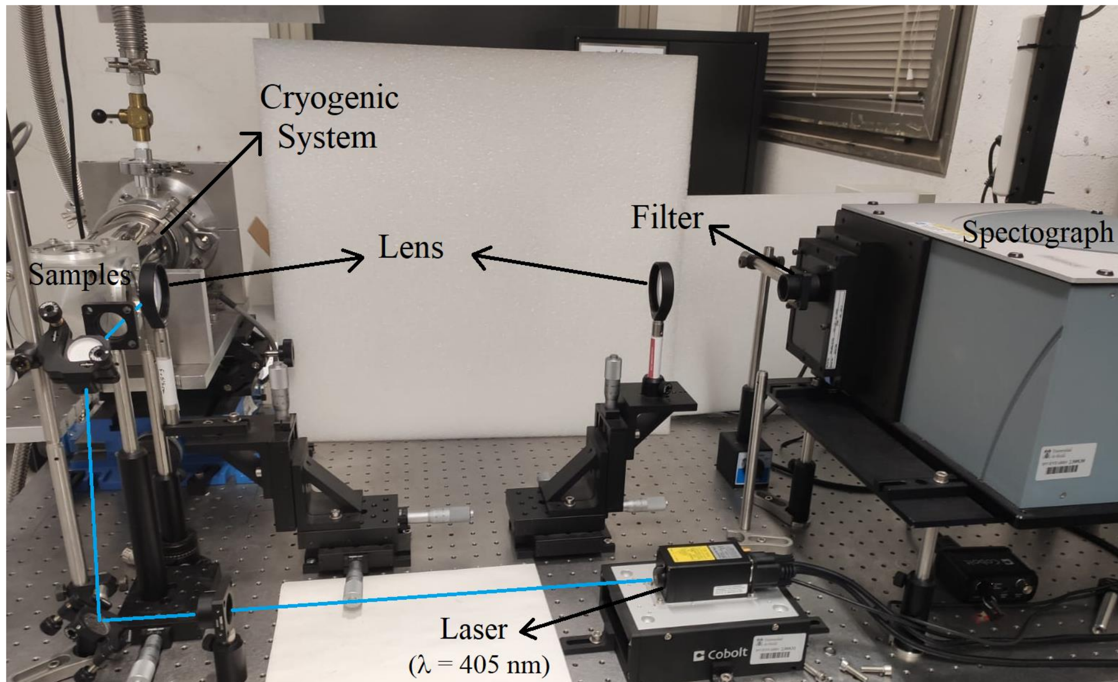

Figure 5.5. Scheme of the PL system of GRIFO laboratory of the University of Alcala.

5.3 Electrical characterization: Hall Effect

To analyze the electrical properties of the layers Hall Effect measurements were carried out using Van der Pauw configuration. This measurement gives information about the carrier concentration, the mobility and resistivity of the layer and the type of majority carriers responsible of the layer conductivity.

The Hall Effect technique is based on the generation of a voltage (Hall voltage) when a magnetic field is applied perpendicular to the direction of a current flowing through an electrical conductor (see figure 5.6). This measurement requires four ohmic contacts at the edges of a squared-shape layer deposited on a non-conductive substrate, as sapphire.

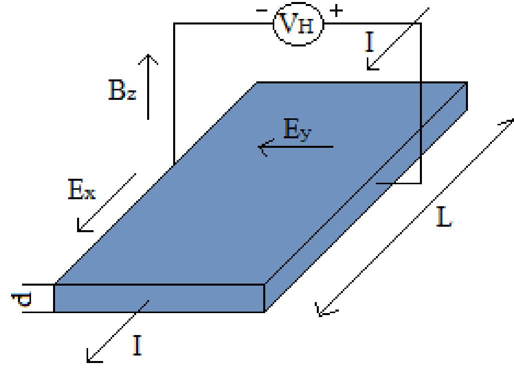

Figure 5.6. Scheme of Hall Effect measurements.

When an electric (E_x) and a magnetic (B_z) fields are applied along the x and z directions of a semiconductor respectively (figure 5.6), the charge carriers in the sample are affected by a Lorentz force. As a result of this force, a transverse voltage perpendicular to both current and magnetic fields, called Hall voltage, is developed in the semiconductor material and is given by:

$$V_H = \frac{I_x B_z}{nqt} \tag{5.7}$$

where q is the charge of the carriers, n is the carrier density, and t is the thickness of the sample.

The resistivity (ρ) of the material can be estimated by Hall Effect measurements without the magnetic field application by measuring the voltage between two contacts when a given current is flowing through the other two ones.

When this voltage is measured in the presence of a magnetic field perpendicular to the sample surface, the Hall scattering factor (R_H) is obtained. From this parameter the carrier concentration and the type of majority carriers (positive for p-type and negative for n-type samples) can be estimated using following equation:

$$n = \frac{1}{qR_H} \tag{5.8}$$

where i is the electron charge. In order to deduce the carriers mobility (μ) we need to know the thickness and the resistivity of the layers (ρ):

$$\mu = \frac{1}{q\rho n} \tag{5.9}$$

Hall Effect measurements were carried out in two different systems:

- In the CEA-Grenoble facilities under the supervision of Dr. Eva Monroy Hall Effect measurements were carried out in the Van der Pauw configuration at room temperature and as a function of the magnetic field varied between +1 T and -1 T. To carry out these measurements, ohmic indium contacts were deposited on the four corners of the AlInN on sapphire square samples.
- Hall Effect measurements carried out in the Complutense Univesity of Madrid system under the supervision of Dr. Javier Olea Ariza (figure 5.7) own similar characteristics to the one of the CEA-Grenoble. However, in this case the magnetic field was fixed to 0.88T and the contacts were made of Ti/Al bilayer.

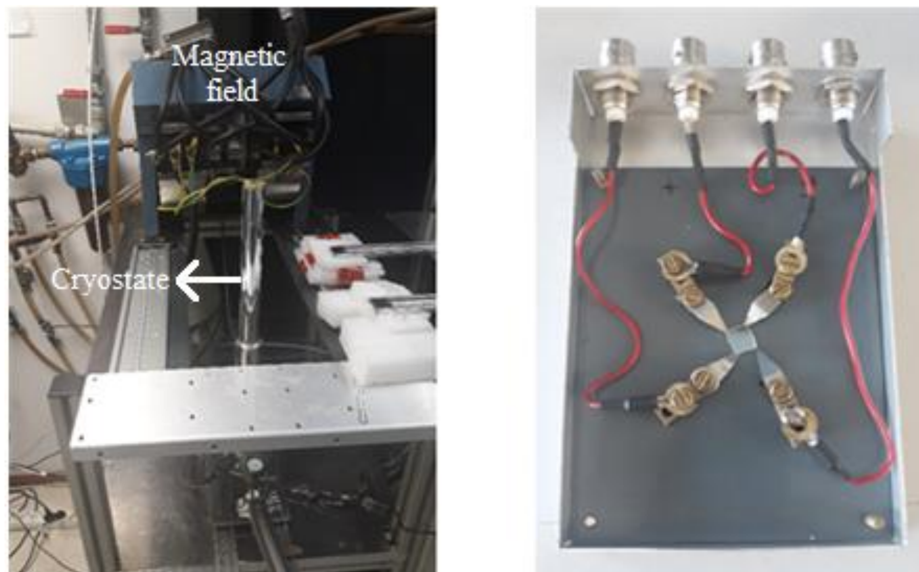

Figure 5.7. Hall Effect setup (left) and sample holder (right) of the Complutense University of Madrid.

5.4 Device fabrication

One of the main targets along this thesis is to fabricate devices based on AlInN on Si heterojunctions using only the RF sputtering technique. In that sense, the top and back contacts are both based on ~120 nm thick aluminum layers and were deposited by RF sputtering after the growth of the AlInN on Si junctions. This section reports the optimization of the top and back contacts to obtain an ohmic behavior depending on (i) the type of substrate for the back contact (*p*-type Si (111) and Si (100)) and (ii) the Al mole fraction of the *n*-type AlInN layer for the top contact. The growth process of both contacts is the same, but the manufacturing process is different. Therefore, the optimization of both contacts will be explained separately.

Both contacts were deposited at room temperature using 2” pure Al (5N), and Ar as reactive gas. Before the deposition, the surfaces were cleaned using a soft plasma etching with Ar (99.999%) with the aim to remove the impurities. The layers were deposited with an argon flow of 2 sccm under a pressure of 5 mTorr. The DC power applied to the Al target was fixed at 75 W. The growth time was calculated to obtain a thickness of the Al contacts of ~120 nm approximately.

5.4.1 Transmission line method

We used Transmission Line Method (TLM) measurements to analyze and optimize the value of the contact resistivity of both back and top contacts. For this purpose, two hard masks with different sizes were designed using AutoCAD software and fabricated. Figure 5.8 shows a photograph of the hard masks used for TLM measurements for the back (left) and top (right) contacts for *p*-type Si and *n*-type AlInN, respectively. The dimensions of the pads and the distance between them were chosen in order to obtain an adequate ratio between the thickness of the layer and the distance between pads as follows:

- The TLM of the back contact has a dimension of 6.7 × 2 cm. The size of the pads is 1× 0.5 cm and are separated from 1 mm to 6 mm every 1 mm.
- The TLM of the top contact has a dimension of 18 × 5 mm. The size of the pads is 2.5 × 1 mm and are separated from 0.5 mm to 3 mm every 0.5 mm.

These dimensions of the TLM make the components of the equation used for the calculation of the resistance of contacts shown below have an order of similar magnitude and cannot be hidden from each other.

The hard mask of the back contact was fabricated at the Ultrafast Laser Center (CLUR) of the Complutense University of Madrid in collaboration with Dr. Jesús González Izquierdo. Meanwhile the hard mask of the top contact was fabricated by Lasergran Madrid SL.

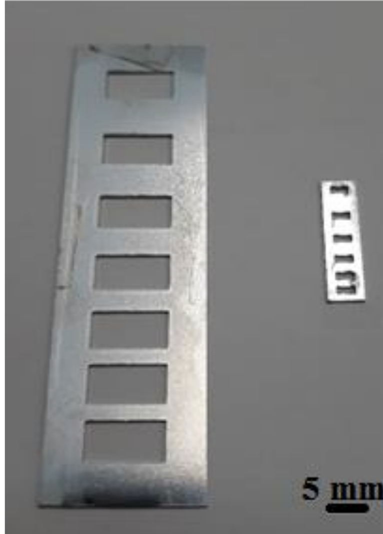

Figure 5.8. Photograph of the hard masks used for TLM measurements for the back (left) and top (right) contacts for *p*-type Si and *n*-type AlInN, respectively.

The TLM consists of measuring the current-voltage characteristics between two consecutive pads and plot the extracted resistance as a function of the distance between them. We assume that contacts are ohmic and not schottky so they have a linear current-voltage dependency. From this plot, we can deduce the contact and the semiconductor resistances as follows.

The measured total resistance R_T can be calculated using equation 5.10:

$$R_T = 2R_{metal} + 2R_c + R_{semi} \quad (5.10)$$

where R_{metal} is the resistance of the metal of the contact, R_{semi} is the semiconductor resistance and R_C is the resistance associated to the metal/semiconductor interface. Since R_{metal} is usually much lower than R_C Eq. 5.9 can be expressed as:

$$R_T = 2R_c + R_{semi} \quad (5.11)$$

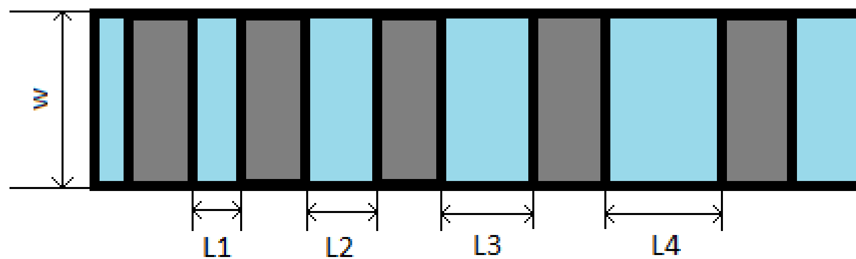

Figure 5.9. Scheme of a transmission length method (TLM).

Assuming the dimensions of the pads, we can express the semiconductor resistance as $R_{semi} = R_S \cdot L/W$, where L and W are the length and the width of the pad, respectively (see

figure 5.9). So if we plot the evolution of R_T as a function of the length between pads, we can obtain the contact and the semiconductor resistances as described in figure 5.10 following:

$$R_T = \frac{R_S}{W} L + 2R_c \tag{5.12}$$

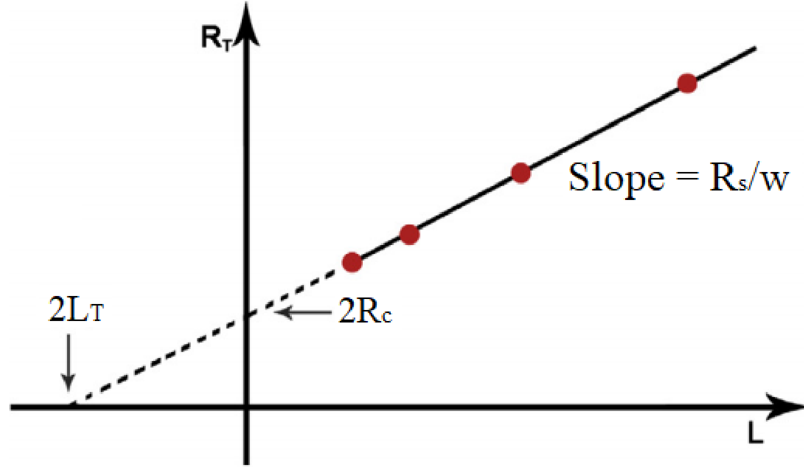

Figure 5.10. Evaluation of the contact and sheet resistances from TLM measurements [Ha13].

As decripted in figure 5.10 we can obtain the contact resistance as $2R_C$, which value corresponds to the resistance value at L = 0. However, in order to obtain the contact resistivity (ρ_c) in $\Omega \cdot cm^2$ we need to take into account the effective area of the contact, which is $L_T \cdot W$, being L_T the transfer length defined as the average distance that an electron travels in the semiconductor over the contact before it flows into the contact as follows:

$$L_T = \sqrt{\frac{\rho_c}{R_S}} \tag{5.13}$$

From equations 5.12 and 5.13 we obtain the contact resistance and resistivity as:

$$\rho_C = R_C L_T W \tag{5.14}$$

$$R_C = \frac{\rho_C}{L_T W} = \frac{R_S L_T}{W} \tag{5.15}$$

So the total resistance can be rewritten as a function of the transfer length L_T:

$$R_T = \frac{R_S}{W}(L + 2L_T) \tag{5.16}$$

Using equation 5.16 is possible to analyze the quality of the contact developed for our devices and compare them with other resistivity values from the literature.

5.4.2 Back *p*-type contact

The study of the back contact of the device is based on an aluminum TLM contact of 120 nm deposited by RF sputtering onto the *p*-type Si (111) and Si (100) substrates. Figure 5.11 shows a photograph of a standard TLM contact deposited on silicon. The resistivity of the substrates varies depending on the crystal orientation from 1 to 10 Ω·cm for *p*-Si (100) and from 10 to 100 Ω·cm for *p*-Si (111).

Figure 5.11. Photograph of an Al-based TLM contact deposited on silicon by RF sputtering.

The first set of samples shows a schottky contact with a rectifying current-voltage behavior, as displayed in figure 5.12 (a). However, several publications such as the one of Pai *et al*. indicate that a rapid thermal annealing (RTA) process markedly improves the ohmicity of the contacts on silicon substrates [Pai85, Wan11]. As an example, figure 5.12 (b) shows the results from Al on Si contacts annealed for 3 min at 450ºC under nitrogen atmosphere obtaining an ohmic behavior.

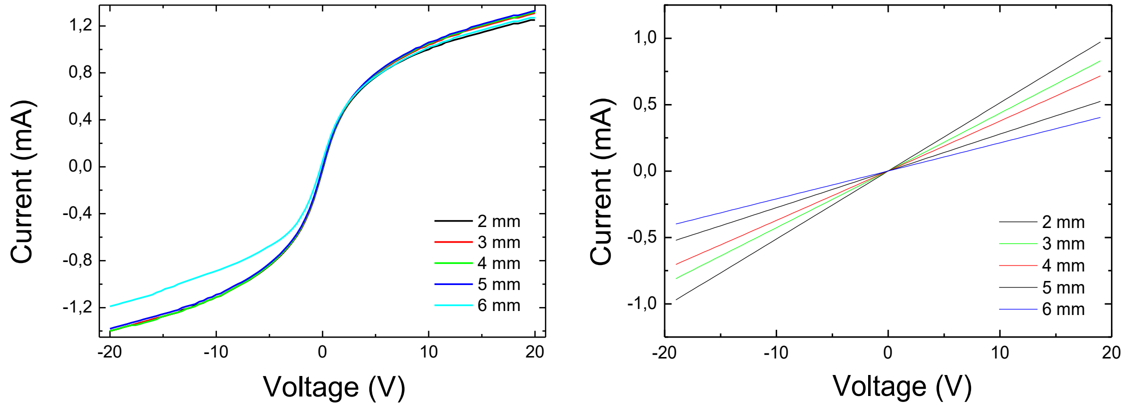

Figure 5.12. Current-voltage characteristics from TLM measurements. Each line corresponds to the measurement between two pads of the TLM with a different distance. Results of Al contacts deposited on *p*-type silicon (111) (a) without annealing and (b) after annealing the contacts for 3 min at 450ºC under nitrogen atmosphere (optimized receipt).

In order to get rid of the rectifying characteristics of our contacts, we carried out a series of experiments annealing our contacts in collaboration with the Research Support Center (CAI) of the Faculty of Physics of the Complutense University of Madrid. In particular, we studied the influence of the main RTA parameters: temperature (from 350ºC to 750ºC), time (from 1 to 10 minutes) and gas atmosphere (forming gas and nitrogen), on the electrical characteristics of our contacts in order to get an ohmic characteristic and minimize their resistivity.

Figure 5.13 (a) shows the evolution of the contact resistivity obtained using the above described TLM as a function of the temperature (350, 450, 550, 650 and 750ºC) under a fixed exposure time of 3 minutes and under a nitrogen atmosphere for Si (111) and Si (100) substrates. It can be seen that the contact resistivity increases from 6 to 11 $\Omega\cdot cm^2$ for Al on Si (111) and from 3.6 to 13.3 $\Omega\cdot cm^2$ for Al on Si (100) with the temperature. So, the optimal value for the annealing process for both substrates is 450ºC, where a minimum of ρ_c = 6 $\Omega\cdot cm^2$ and 3.6 $\Omega\cdot cm^2$ is obtained for Al on Si (111) and Si (100), respectively.

Then, we studied the dependence of the annealing exposure time on the contact resistivity for 450ºC and under nitrogen atmosphere. Figure 5.13 (b) shows how the contact resistivity increases up to almost 9 $\Omega\cdot cm^2$ for 10 minutes of annealing time, probably due to the degradation of the aluminum quality with the exposure time, so as with the increasing temperature. So, the minimum contact resistivity for both substrates was still obtained for 450ºC and 3 minutes of RTA process.

Finally, we studied the effect of the gas (pure nitrogen (5N) and forming gas based on 90% of nitrogen and 10% of hydrogen) on the contact resistivity. Forming gas has been selected because several studies [Cho14, Hör10] have shown a remarkable improvement of the contacts deposited on silicon, especially for Ag-containing contacts. However, as is shown in figure 5.13 (c), in our case the effect of the forming gas does not improve the Al on Si contact resistivity, being still the nitrogen atmosphere the selected to perform the annealing process.

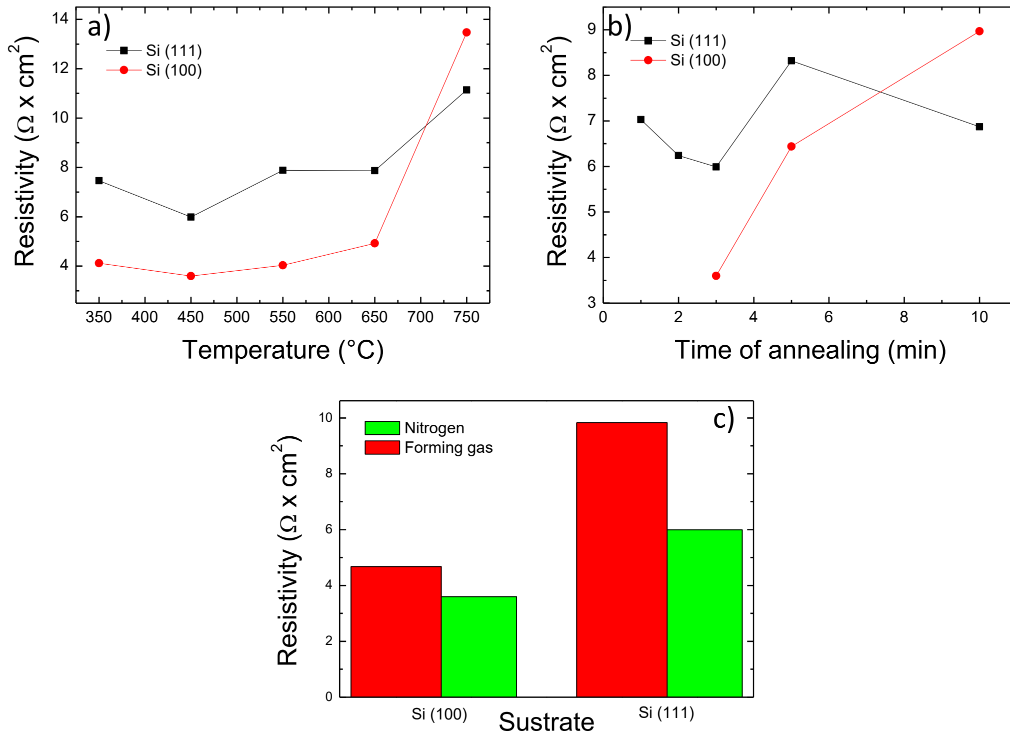

Figure 5.13. Evolution of the back-contact resistivity (120 nm of Al on *p*-type Si) as a function of a) the annealing temperature (for 3 min under nitrogen), b) the annealing time (at 450ºC under nitrogen) and c) the annealing atmosphere (at 450ºC for 3 min).

Besides, different studies to improve the contact resistivity of the layers have been carried out such as (i) the effect of varying the duration of the plasma etching prior the growth process or (ii) the etching process. However, we did not obtain any contact resistivity improvement with none of both processes.

In summary, the optimized annealing process for the Al on Si back contacts comprises 3 minutes of exposure at 450ºC under an atmosphere of pure nitrogen obtaining contact resistivity values of 6 and 3.6 Ω·cm^2 for Si (111) and Si (100), respectively.

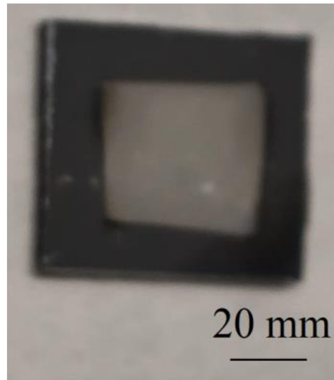

Figure 5.14. Image of the back contact (Al) deposited on silicon substrate.

The deposition conditions for the deposition by RF sputtering of the Al back contacts, depicted in figure 5.14, are the following: room temperature, 2" pure Al (5N), and Ar as reactive gas. The layers were deposited with an argon flow of 2 sccm under a pressure of 5 mTorr. The DC power applied to the Al target is fixed to 75 W. The growth process was calculated to obtain a thickness of the Al contacts of ~120 nm approximately.

5.4.3 Top *n*-type contact

The top contact to *n*-type AlInN consists of 120 nm of Al deposited by RF sputtering under the same deposition conditions than the bottom contact (figure 5.15). Accordingly to TLM measurements, these contacts were ohmic directly without any annealing process and regardless the aluminum concentration of the $Al_xIn_{1-x}N$ within the range of $x = 0 – 0.56$. This is probably due to the high *n*-type carrier concentration of the layers in the order of 10^{22} to 10^{19} cm^{-3}. Anyway, we studied the influence of the different parameters, such as the time of the annealing process, on the contact resistivity, obtaining almost no improvement (below 5%).

On the other hand, one of the parameters to take into account in top contacts is the aforementioned Al concentration or, in other words, the carrier concentration of the nitride layer.

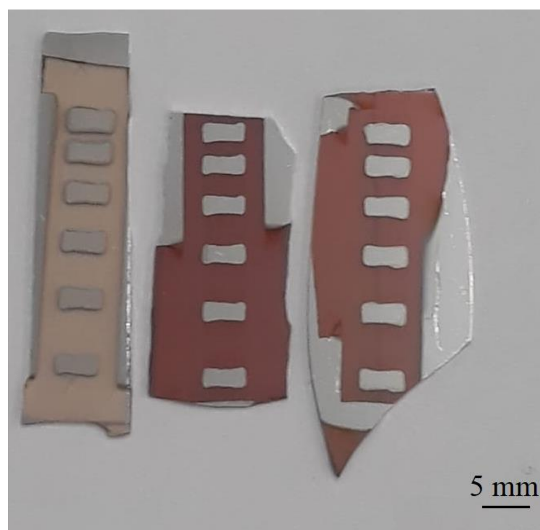

Figure 5.15. Photograph of an Al-based TLM contact deposited on AlInN layers by RF sputtering.

Table 5.1 shows the evolution of the top contact resistance, obtaining from TLM measurements, as a function of the Al mole fraction. We can observe how the resistivity remarkably increases with the Al content, affecting the efficiency of the device as will be explained in chapter 9.

Al mole fraction	Top contact resistance (Ω)
0	7.1×10^{-2}
0.20	5.1×10^{-1}
0.28	1.54×10^{3}
0.35	2.59×10^{4}
0.45	2.32×10^{6}

Table 5.1. Summary of the top contact resistance as a function of the Al mole fraction.

Once the top contact was optimized, we designed and fabricated a hard mask to implement it on the devices. The hard mask was fabricated at the Ultrafast Laser Center (CLUR) of the Complutense University of Madrid in collaboration with Dr. Jesús González Izquierdo. The top contact is based on 0.7-mm-wide fingers separated by 1.8 mm as shown in figure 5.16.

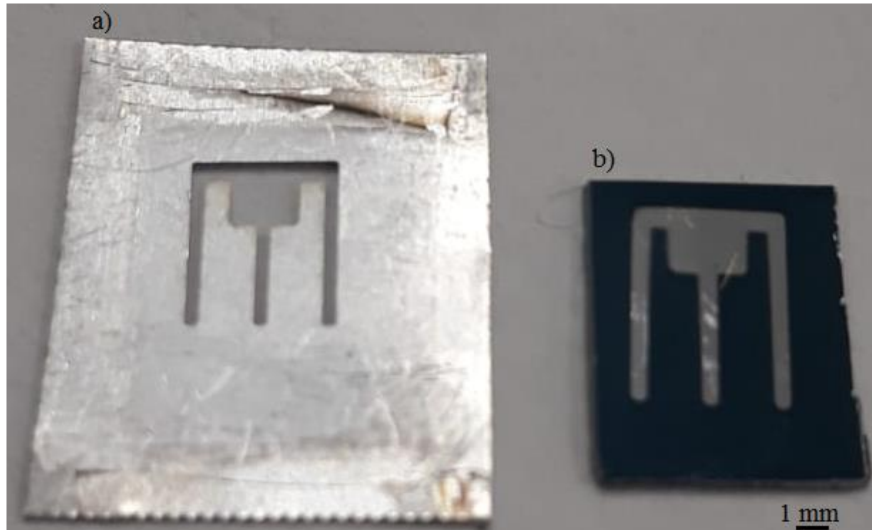

Figure 5.16. Image of a) a hard mask fabricated for the top contact to *n*-type AlInN and b) a real top contact of an AlInN on Si solar cell device deposited using the hard mask.

The deposition conditions of the Al-based top contact by RF sputtering are the same that for the back contact described previously.

5.5 Device characterization

This section summarizes the experimental techniques used to analyze the photoelectrical and photovoltaic properties of the AlInN on Si devices. Current-voltage measurements in the dark allow to estimate the shunt and serial resistances, the ideality factor and the dark current of the diode. On the other hand, the device conversion efficiency and the main parameters of the solar cell under operation such as V_{oc}, J_{sc} and FF are obtained by the current-voltage curves under solar illumination using a solar simulator with 1 sun of AM1.5G spectra.

In addition, to study the dependence of the photocurrent on the incident light wavelength, we analyzed the ratio between the electrons generated by the device vs the incident photons through responsivity measurements, allowing us to estimate the external quantum efficiency (EQE) of the device.

5.5.1 Current-voltage measurements

Current-voltage measurements in the dark are based on circulating an electrical current through a semiconductor that have two ohmic contacts on the top *n* and the back *p* sides. Thereby the current passes through the *n-p* junction and the electrical properties of the device can be analyzed, as described in chapter 3.

Figure 5.17. Photograph of the 4-point probe station located in the Complutense University of Madrid used for dark current-voltage measurements.

Dark current-voltage curves of the developed AlInN on Si devices were carried out in a 4-point probe station as displayed in figure 5.17 at the Applied Physics III Department of the Complutense University of Madrid in collaboration with Dr. Javier Olea Ariza. Measurements were recorded using a Keithley 4294A parameter analyzer.

Devices were also characterized operating as solar cells using a 4-point probe station to measure current-voltage curves under a lamp that provides an illumination close to the solar spectrum on earth. Particularly, devices were measured under 1 sun (1000 W/m^2) of AM1.5G illumination.

Current-voltage measurements under 1 sun of AM1.5G illumination were carried out in two different places:

- At the LETI laboratories of the CEA-Grenoble in France in collaboration with Dr. Louis Grenet. We used an A Spectra-Nova's CT series solar cell tester.

- At the Applied Physics Department of the Autónoma University of Madrid in collaboration with Dr. A. Braña. We used a solar simulator YSS-180AA from the company NPC INC.

All measurements were performed at room temperature.

5.5.2 Responsivity measurements

Responsivity measurements relates the electrons photo-generated by the device as a function of the incident photons. So, usually is calculated as the ratio between the current generated by the device vs the incident optical power using the following equation:

$$R = \frac{I_{inc}}{P_{out}} \tag{5.17}$$

To carry out these measurements we used a 250W halogen lamp coupled to a monochromator working in the 350–1200 nm range. The light extracted from the monochromator was focused on the device using optical lenses, as displayed in the image of figure 5.18. Then, we used a chopper and a lock-in amplifier to perform synchronous detection of the photogenerated voltage of the device vs the input wavelength.

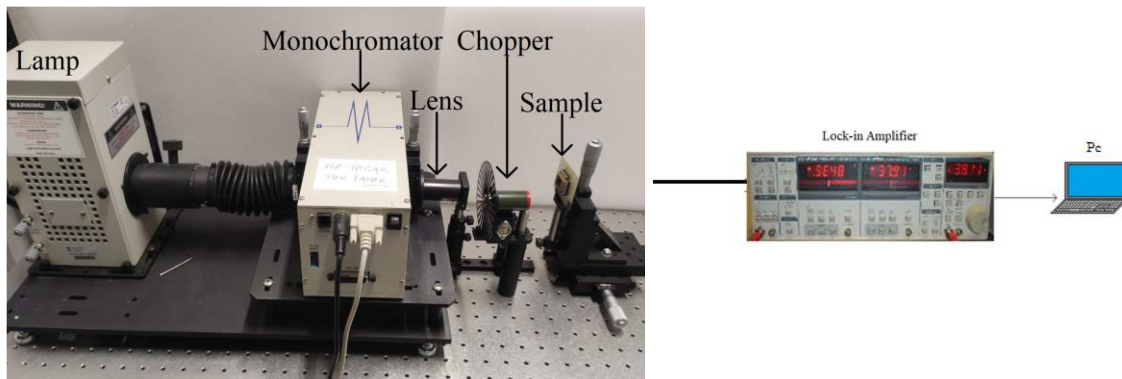

Figure 5.18. Scheme of the responsivity setup located at University of Alcalá.

In this way, the shape of the responsivity curve vs the wavelength was measured. However, the light after the monochromator is not completely monochromatic, so several wavelengths can be contributing simultaneously on the photogenerated current. So in order to get an accurate value of photocurrent at a precise wavelength we used an He-Ne laser diode (λ = 633 nm) with an output power of 0.6 mW to calibrate the photocurrent versus the optical power as $R = \frac{I_{633}}{P_{out}}$. Knowing this value, the responsivity curve was corrected to this point.

Through these measurements is possible to estimate the external quantum efficiency (EQE) of the devices, which is defined as the ratio of the number of carriers collected by the solar cell to the number of photons at a given incident energy, using equation 5.18:

$$EQE = R_{\lambda} \frac{hc}{q\lambda} \tag{5.18}$$

where R_{λ} is the responsivity at a certain wavelength (λ), h is the Planck's constant, c is the speed of the light and q is the electron charge.

Chapter 6

Design of AlInN on *p*-silicon heterojunction solar cells

As explained in previous chapters, there are some theoretical studies based on exploring the theoretical conversion efficiency of multijunctions solar cells [Mar96] showing theoretical values of conversion efficiency from 31% to 53% as a function of the number of junctions.

However, these results have been obtained taking into account only the value of the band gap energy and the number of junctions to be used in the device. In that sense, in order to obtain more realistic results, we have performed simulations of a structure based on the AlInN/Si heterojunction using experimental values previously obtained in the AlInN layers.

Therefore, this chapter summarizes the theoretical study the parameters of the AlInN/Si heterojunction in order to explore the potential of this structure for solar cells applications. Concretely, we study, through simulations, the influence of the AlInN bandgap energy, thickness and doping level. Besides, the interface defects, the silicon wafer quality, including its surface recombination, and the effect of an anti-reflective layer is also studied.

6.1 Pc1d software

Simulations were made with the Pc1d software [Bas03, Pc2d]. This software was selected because is one of the most used software for solar cell simulations and also because its simplicity made it easy to carry out the studies and quickly understand the results.

However, inasmuch as the Pc1d software does not have III-nitride materials, firstly we have introduced the materials parameters into the software. Then, in order to verify this implementation, we have compared the simulations of some InGaN-based junctions with results from the literature.

6.2 Checking the Pc1d software for III-nitrides: InGaN-based junctions

As stated before, the Pc1d software does not have III-nitride materials in the library, so, it is necessary to introduce them and their properties into the database. In that sense, a summary of the main optical and electrical properties of AlN, GaN and InN used for the simulations are listed in table 6.1 and table 6.3. Concretely, table 6.1 was used to compare the simulated structure with the Fabien *et al.* [Fab14] structures and table 6.3 was used to study the AlInN/Si heterojunction.

Material	GaN	InN
Bandgap energy (eV)	3.42	0.65
Electron affinity (eV)	4	5.6
Refractive index [Rum01]	2.3	2.9
Effective electron mass (m_0)	0.2	0.05
Effective hole mass (m_0)	1.25	0.6
Electron mobility (cm^2/Vs)	1000	1100
Hole mobility (cm^2/Vs)	170	340
Dielectric constant	8.9	10.5
Effective density of states in the conduction band Nc (cm^{-3})	3×10^{17}	3×10^{17}
Effective density of states in the valence band Nv (cm^{-3})	2×10^{17}	8×10^{18}
Intrinsic concentration at 300 K (cm^{-3})	1.9×10^{-10}	2.3×10^{13}

Table 6.1. Summary of the material parameters of GaN and InN included in the Pc1d software to develop the simulations of InGaN homo and heterojunctions [Fab14].

To obtain the parameters of the ternary compounds we followed the Vegard’s law [Veg21]. However, as explained in chapter 2, to obtain the bandgap energy it is necessary to modify the Vegard´s law introducing a parameter, called bowing parameter (b), which adequately adjusts the variation of the bandgap energy with the concentration of the ternary compound as follows:

$$a_{AB} = xa_A + (1-x)a_B - bx(1-x) \tag{6.1}$$

where x is the alloy mole fraction, a_A and a_B are the parameters of the binary compounds and b is the bowing parameter.

In this study simulations were carried out with two different compounds: InGaN and AlInN. So, there are two different bowings parameters. Concretely, for the $In_xGa_{1-x}N$ layers a bowing parameter of 1.43 was selected taking into account the value obtained from Wu *et al.* [Wu02] and Fabien *et al* [Fab14].

The intrinsic carrier concentration of the ternary compound was calculated using the Melissinos formula:

$$n_i^2 = N_c N_v e^{-\frac{E_g}{K_B T}} \quad (6.2)$$

where N_c and N_v are the effective density of states in the conduction and valence band respectively, K_B is the Boltzmann constant, T is the temperature and E_g is the bandgap energy of the alloy. For ternary compounds the Vegard´s law is applied to obtain the N_c and N_v values as a function of the mole fraction of its components.

Pc1d software also requires the absorption coefficient of the material as a function of the wavelength. In that sense, the absorption coefficient for InGaN layers was obtained using equation:

$$\alpha(E) = 10^5 * \sqrt{a(E - E_g) + b(E - E_g)^2} \quad (6.3)$$

where $\alpha_0 = 2 \times 10^5 cm^{-1}$ for GaN, the parameter E is the incoming photon energy and the parameters a and b are fitting parameters obtained from [Fab14].

The efficiency of the devices under 1 sun of AM 1.5G illumination was estimated from the simulated current-voltage curves obtained from the simulations using:

$$E_{ff} = \frac{V_{oc} J_{sc} FF}{P_{in}} \quad (6.4)$$

where the Fill Factor (FF) is the ratio of maximum obtainable power to the product of the open-circuit voltage (V_{oc}) and the short-circuit current (J_{sc}); the power intensity (P_{in}) is the input power, which corresponds to a one sun spectra of AM 1.5G (1000 W/m^2). The external quantum efficiency (EQE) was extracted as the ratio between the photogenerated collected carriers and the input optical density (incident photons) as a function of the wavelength.

In order to validate the material parameters of III-nitrides in the program we have compared our simulation results on InGaN-based homo and heterojuntions, with the ones obtained by Fabien *et al.* on the same structures [Fab14]. Results are listed in table 6.2.

Table 6.2 shows a comparison between the simulations obtained from Pc1d software and the Fabien *et al*. results. In particular, we have simulated two structures based on: 50 nm of *p*-doped $In_{25}Ga_{75}N$ ($p \sim 4\times10^{18}$ cm^{-3}) followed by 100 and 500 nm (S1 and S2 in table 6.2 respectively) of non-intentionally doped $In_{25}Ga_{75}N$ ($n \sim 1\times10^{17}$ cm^{-3}) and 1 μm of *n*-doped GaN layer ($n \sim 8\times10^{18}$ cm^{-3}).

Structure	**Reference**	**V_{oc} (V)**	**J_{sc} (mA/cm^2)**	**FF (%)**	**η (%)**
S1	**This work**	1.87	4.36	87.08	7.1
S1	**Fabien *et al.***	1.85	4.00	90.54	6.7
S2	**This wok**	1.89	5.85	87.14	9.6
S2	**Fabien *et al.***	1.85	5.80	86.41	9.5

Table 6.2. Comparison of the simulation results obtained for different InGaN-based junctions with Pc1d software and the ones obtained by Fabien *et al.* [Fab14].

From the comparison between our simulations and the ones obtained in [Fab14] we can deduce that our results on conversion efficiency are slightly over-estimated by a ~6%, which are in the error bars of the difference between both simulation programs.

6.3 AlInN on Si heterojunctions

Once it was verified capability of the Pc1d software to simulate heterostructures based on III-nitrides, the extension of the parameters to $Al_xIn_{1-x}N$ (x from 0 to 0.48) was carried out. The method of obtaining the parameters is identical to the one explained in the previous section except for the absorption coefficient, the bandgap energy and the carrier concentration, which were obtained by experimental measurements.

6.3.1 AlInN simulation parameters

As it said previously, the main parameters of the binary compounds for the AlInN simulations are listed in table 6.3. Using these values and Vegard´s law, some parameters of the ternary compounds such as the carrier effective mass, the dielectric constant or the bandgap energy were calculated.

Material	AlN		InN
Bandgap energy (eV)	6.2		1.7**
Electron affinity (eV)	1.9		5.6
Refractive index	2.15		2.9
Effective electron mass (m_0)	0.3		0.07
Effective hole mass (m_0)	3.5		1.63
Electron mobility (cm^2/Vs)	135		8.7**
Hole mobility (cm^2/Vs)	14		340*
Dielectric constant	8.5		15.3
Effective density of states in the conduction band Nc (cm^{-3})	200 K	3.4×10^{18}	4.9×10^{17}
	300 K	6.3×10^{18}	9.1×10^{17}
	400 K	9.6×10^{18}	1.4×10^{18}
Effective density of states in the valence band Nv (cm^{-3})	200 K	2.7×10^{20}	2.8×10^{19}
	300 K	4.8×10^{20}	5.3×10^{19}
	400 K	7.5×10^{20}	8×10^{19}
Intrinsic concentration at 300 K (cm^{-3})	9.4×10^{-34}		2.3×10^{13}

Table 6.3. Summary of the material parameters of AlN and InN included in the Pc1d software to develop the simulations of the AlInN/Si heterojunctions [Rum01]. Notes: *Obtained from Fabien et al. [Fab14]. **Obtained from experimental measurements.

Moreover, a minority carrier lifetime of ~1 ps was used for the AlInN in all simulations. This value was introduced taking into account the InN lifetime of 30 ps [Che05]. We consider a lower value for the alloy to take into account the high density of impurities and defects present in layers deposited by RF-sputtering (up to 10^8 cm^{-2}) [Laz13, Pri17].

The effect of surface recombination of the AlInN is also analyzed in this study. In that sense, the experimental values of nitride compounds deposited by MBE are around 10^3 cm/s [Kit08]. However, inasmuch as this study is based on ternary compounds deposited by sputtering with lower structural quality, the value assigned to the simulation is 10^8 cm/s.

The bandgap energy was obtained through transmission measurements of AlInN deposited on sapphire by RF-sputtering (Figure 1). Besides, the bandgap energy was also calculated using equation 6.2 and a bowing parameter of 5.1, as previously obtained by our group for $Al_xIn_{1-x}N$ layers deposited by RF-sputtering [Nuñ17]. The deviation between the results obtained from equation 6.2 and the experimental ones are below 2% for all samples, so both options are considered valid for the simulations. In this case, the experimental values of the bandgap were taken into account for the simulations.

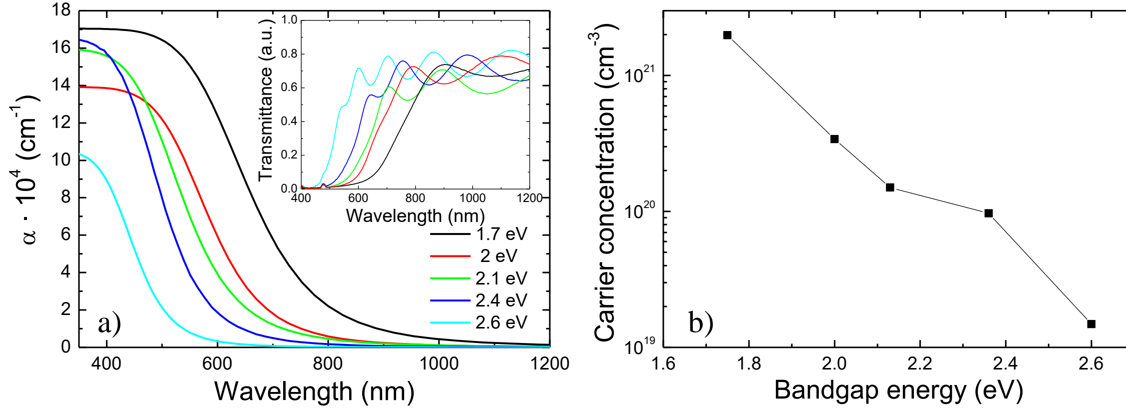

Figure 6.1. a) Absorption coefficient and transmittance (inset) spectra of the AlInN on sapphire samples as a function of the AlInN bandgap energy. (b) Carrier concentration vs the bandgap energy for the same samples. The Al mole fraction of each AlInN layer is also marked.

Furthermore, in order to obtain more realistic values from the simulations, some parameters of the AlInN ternary compounds were obtained from experimental data. In particular, the Pc1d software requires the absorption coefficient, carrier concentration and mobility of the layers. These parameters were obtained from transmission and Hall Effect measurements, of AlInN layers grown on sapphire by RF-sputtering for each Al content (Figure 6.1) respectively.

In the case of the carrier mobility, measurements extracted from Hall Effect show a decrease from 8.7 to 0.1 cm^2/Vs when the Al content increases from 0 to 48%. Moreover the mobility of the holes is supposed to be smaller due to its effective mass and as it happens in the binary compounds (table 6.3).

6.3.2 Optimization of AlInN on Si parameters

The main structure used for the simulations consists on an *n*-type $Al_xIn_{1-x}N$ layer ($x = 0 – 0.48$) on a *p*-Si substrate. As a start, we have chosen an AlInN thickness of 300 nm and a carrier concentration density that evolves in the range of $10^{19} – 10^{21}$ cm^{-3} decreasing with the Al mole fraction as is shown in figure 6.1(b). As explained before, a conservative AlInN recombination time of 1 ps and a high surface recombination rate of 10^8 cm/s were chosen due to the properties of the alloy deposited by RF-sputtering.

The 500-µm thick *p*-type doped Si substrate owns a resistivity of 10–100 Ω·cm, this value is provided by the manufacturer datasheets (Semiconductor Wafer INC company). On the other hand, a surface recombination rate of 10^8 cm/s and a recombination time of 200 µs, have been considered, in order to simulate a low-quality silicon wafer [Bae05, Wol17].

The effect of the recombination of the silicon surface is going to be studied throughout this work. For this purpose, the simulations start with a value of 10^8 cm/s, a quite higher value than the usually assigned to a low silicon quality 10^6 cm/s [Hsu08].

Beside this, the band structure of this heterojunction is the same that the previously described by this group in several paper such as Valdueza *et al.* [Val18].

On the other hand, it has been reported the creation of a highly-doped channel formed during the deposition of III-nitrides on silicon due to diffusion of metallic atoms inside the substrate during growth [Luo17, Nuñ18]. To account for this channel, an interface defects of 10^7 cm^{-3}/peak following an error function (ERC) at the first 7 nm of the silicon substrate has been introduced to obtain a more realistic model.

Starting from this structure we have analyzed the effect of the following parameters: AlInN bandgap energy, thickness and background doping; interface defects and Si surface recombination rate; and anti-reflective coating, on the photovoltaic properties of the heterojuntion. The effect of each one is separately studied while the rest parameters are kept fixed. The optimized structure will be compared with a Si-based *p-n* homojunction, where the *p*-silicon layer is the same than the *p*-silicon of the optimized AlInN/Si heterojunction, and the *n*-silicon layer has the same thickness and carrier concentration than the AlInN layer, in order to evaluate its performance improvement. The area of the devices is fixed to 1 cm^2 for all the simulations.

6.3.2.1 Effect of AlInN bandgap energy

The bandgap energy and the transparency of the AlInN material is of crucial importance in the design of the heterjunction in order to maximize the number of photons that will be absorbed by each layer and the number of generated photocarriers that will be collected as a function of the wavelength.

As said previously, the AlInN bandgap energy was obtained through transmission measurements of $Al_xIn_{1-x}N$ on sapphire samples deposited with Al mole fraction in the range $x = 0$ to 0.48. as obtained from X-ray diffraction measurements [Bla18].

Concretely, the optical bandgap energy (E_g) is obtained through a linear fit of the squared absorption coefficient as a function of the photon energy as shown in figure 6.1 a). From this method, a variation of the bandgap value from $E_g = 1.7$ eV (708 nm) for InN to $E_g =$ 2.6 eV (476 nm) for $Al_xIn_{1-x}N$ ($x \approx 0.48$) was obtained. As is explained before, the high

values of *Eg* are related to band filling and a blue shift of the bandgap energy of the alloy (Burnstein-Moss effect) caused by an unintentional doping caused by impurities like oxygen [Dar10].

Furthermore, the absorption of the samples is also estimated from these transmission spectra (depicted in the inset of figure 6.1(a)) considering the relation $\alpha(E) \propto -\ln(Tr)$, which neglects optical scattering and reflection losses.

On the other hand, the data of carrier concentration were obtained through Hall Effect measurements from AlInN on sapphire samples deposited by RF-sputtering [Nuñ17], obtaining a decrease of the *n*-type carrier concentration from 2×10^{21} to 2×10^{19} cm^{-3} accordingly to the bandgap energy, as illustrated in figure 6.1 (b).

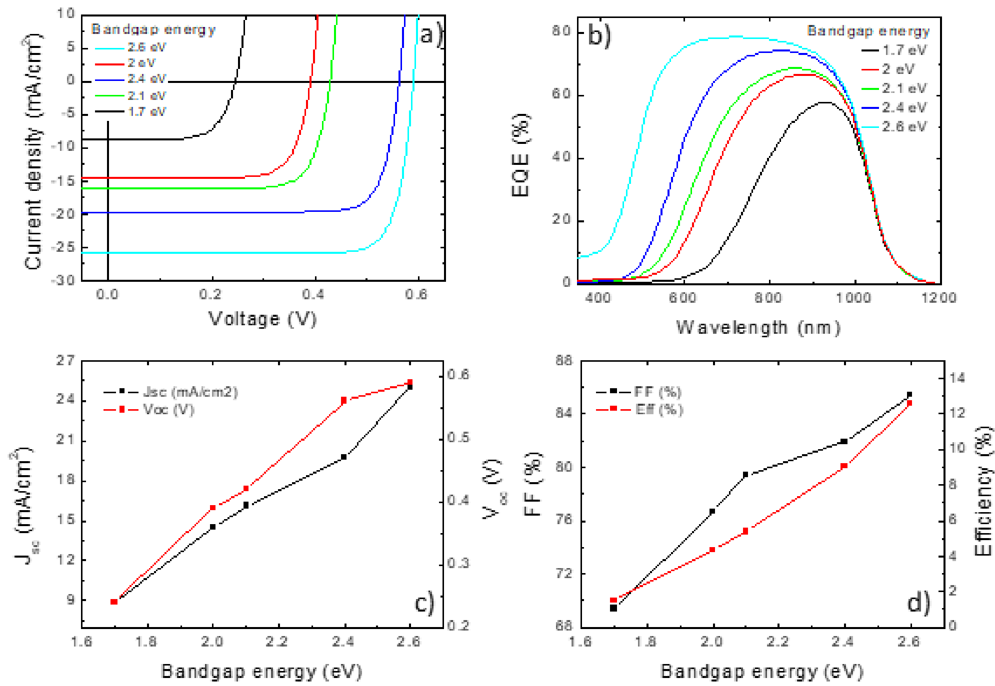

Figure 6.2. J-V (a) and EQE (b) curves of the AlInN on Si heterojunctions as a function of the AlInN bandgap energy. The evolution of the V_{oc} and J_{sc}, FF and efficiency vs the AlInN bandgap energy is plotted in (c) and (d), respectively.

The simulated current density vs voltage (J-V) curves under 1 sun of AM 1.5G illumination and the EQE spectra of the samples are presented in figure 6.2 (a) and (b),

respectively. The increase of the Al bandgap energy by 0.85 eV results in an increase of V_{oc} from 0.24 to 0.59 V, and of J_{sc} from 8.8 to 26 mA/cm^2 [figure 6.2(c)].

This enhancement of J_{sc} is accompanied by a blue shift of the EQE cutoff at short wavelengths according to the change of absorption band-edge energy of the AlInN layer with the Al content. At the same time, an enhancement of the maximum EQE of the devices from 58% for InN to 78% for $Al_{0.48}In_{0.52}N$ is also observed. This behavior leads to a *FF* and conversion efficiency improvement from 69 to 84% and from 1.8 to 12.6%, respectively (figure 6.2(d)). Taking into account these results, the Al mole fraction was kept fixed for the rest of the study to $x = 0.48$ ($E_g = 2.6$ eV), with a carrier concentration $n \sim 2\times10^{19}$ cm^{-3}. It should be pointed out that the maximum Al content in the layers is limited to $x = 0.48$ due to the insulator character showed by non-intentionally doped AlInN layers with $x>0.48$ deposited using RF-sputtering by our group.

6.3.2.2 Effect of AlInN thickness

The photovoltaic properties of the AlInN on Si heterojunctions were further analyzed by varying the AlInN thickness from 500 nm to 10 nm, while maintaining the rest of parameters fixed. Figures 6.3 (a) and (b) show the illuminated J-V curves under 1 sun of AM 1.5G illumination and the EQE spectra of the samples, respectively. The value of V_{oc} and the *FF* remain almost constant around 0.59 V and 83%, respectively, while J_{sc} rises from 24.5 to 30.4 mA/cm^2 when reducing the AlInN thickness from 500 to 10 nm, leading to an increase of the conversion efficiency from 11.9 to 14.9% (figure 3 (c) and (d)). This effect is correlated with an increase of the EQE at short wavelengths, which is attributed to the absorption by the AlInN layer close to its surface but far from the depletion region, disabling the electron-pair separation by the internal field and its further collection at the contacts. From now on, we will fix the AlInN thickness to 10 nm.

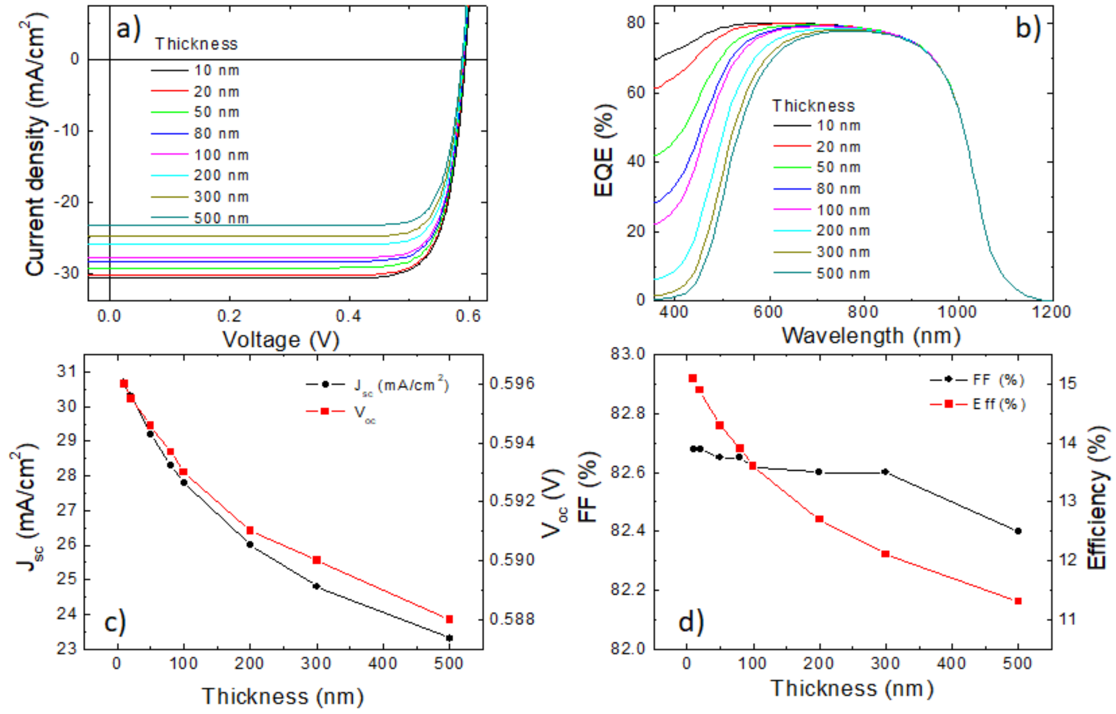

Figure 6.3. J-V (a) and EQE (b) curves of the AlInN on Si heterojunctions as a function of the AlInN thickness. The evolution of the V_{oc} and J_{sc}, FF and efficiency vs the AlInN thickness is plotted in (c) and (d), respectively.

6.3.2.3 Effect of AlInN *n*-type doping

In the following study, the carrier concentration was changed from $n = 1\times10^{17}$ to 1×10^{21} cm^{-3} considering a 10-nm thick AlInN on Si heterojunction with $E_g = 2.6$ eV. The simulated J-V curves (shown in figure 6.4) point to a constant J_{sc} for the whole analyzed range of carrier concentration, whereas the V_{oc} shows an increase from 0.34 to 0.6 V up to $n = 1\times10^{19}$ cm^{-3}, as expected from the increase of the built-in voltage of the heterojunction with the donor concentration. Besides, the decreasing of the V_{oc} as a function of the carrier concentration can be explained through equation 6.5:

$$V_{oc} = \frac{kT}{q} \ln\left[\frac{(N_A+\Delta n)\Delta n}{n_i^2}\right] \qquad (6.5)$$

where kT/q is the thermal voltage, N_A is the doping concentration, Δn is the excess carrier concentration and n_i is the intrinsic carrier concentration.

The simulation fails for carrier concentration above this number as the Pc1d software uses the M-B statistics, which does not describe properly the case of degenerate semiconductors.

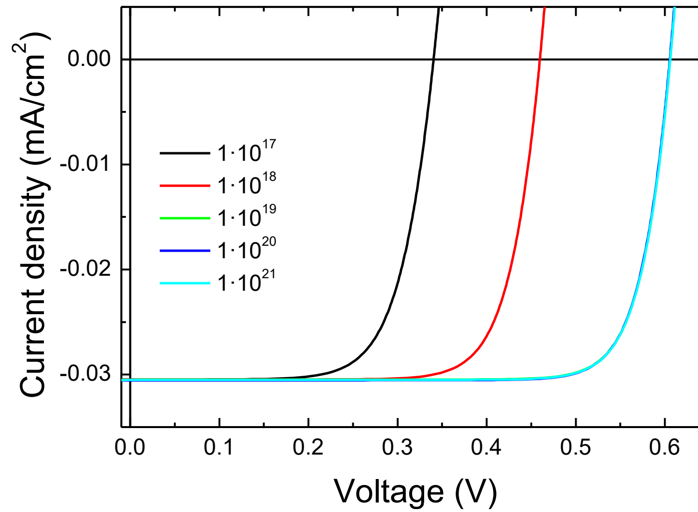

Figure 6.4. J-V (a) curves of the AlInN on Si heterojunctions as a function of the AlInN background doping.

The increase of the V_{oc}, leads to an increasing of the FF from 70 to 83% and thus, an increasing of the conversion efficiency of the heterojunction from 7.3% for a carrier concentration of $n = 1\times10^{17}$ cm^{-3} to 14.9% for a carrier concentration of $n = 1\times10^{19}$ cm^{-3}. The EQE spectra present similar values and shape independently of the AlInN doping level.

Although the maximum efficiency is obtained with a high doping level $n = 1\times10^{21}$ cm^{-3} (η = 15.1%), the fact that the program does not describe rightly degenerate semiconductors leads us to not consider this value. Therefore, and given that the efficiency variation is not significant, it has been decided to maintain a carrier concentration of 10^{19} that corresponds to a bandgap approximated to the maximum obtained in the previous study of 2.6 eV.

6.3.2.4 Effect of interface defects

A thin $p+$ doped layer at the first Si nanometers can emerge due to the Al diffusion during our AlInN deposition process. Some studies show an interface diffusion of GaN and AlN above 10^{17} cm^{-3} [Cha17, Sim12]. However, in order to cover a wider range we have varied the defects density at the AlInN on Si interface from 0 to 10^{19} cm^{-3}.

Figure 6.5 (a) and (b) show the illuminated J-V curves and the EQE spectra of the samples under study as a function of the interface defects. In this figure, it can be observed that the EQE drops in the 600 to 1000nm spectral range for a density of defects range above 10^{18} cm^{-3}, reducing the V_{oc} from 0.6 to 0.36V, the J_{sc} from 30.7 to 20.3 mA/cm^2 and conversion efficiency accordingly from 5.1 to 15.2% (figure 6.5 (c) and (d)).

In this study it is pointed out that the field generated by the *p+* zone at the interface hinders the electron drift towards the *n*-type semiconductor. This effect reduces the EQE and the efficiency of the heterojunction.

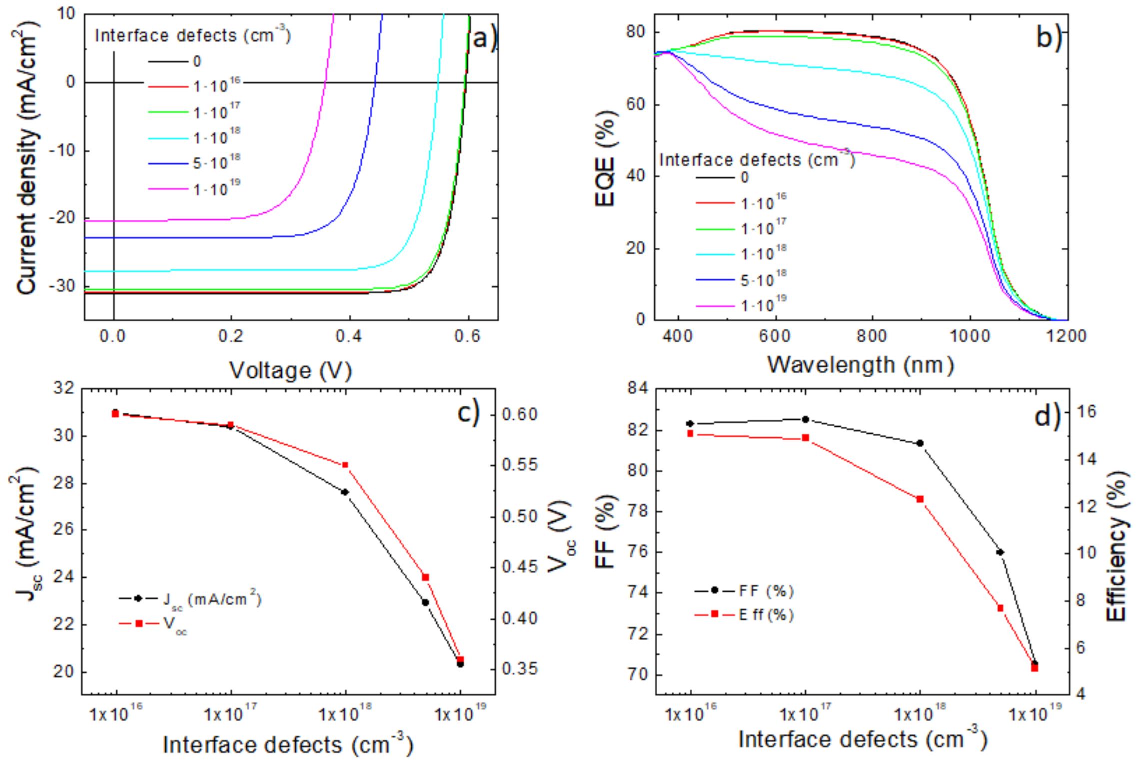

Figure 6.5. J-V (a) and EQE (b) curves of the AlInN on Si heterojunctions as a function of the interface defects. The evolution of the V_{oc} and J_{sc}, FF and efficiency vs the interface defects is plotted in (c) and (d), respectively.

From now on, with the aim to obtain an optimize structure, we select a structure without an interface defects.

6.3.2.5 Effect of surface recombination rate

One important issue in the development of Si-based devices is the passivation of the Si surface to reduce the effect of the Si dangling bonds. High-efficient devices present a reduced carrier recombination at the Si surface, thus increasing the carrier lifetime and the conversion efficiency [Neb12].

To study the effect of the Si surface passivation on AlInN on Si heterojunctions, we have modified the surface recombination rate of both sides of the silicon layer from S = 10^8 cm/s (low-quality Si) to S = 10 cm/s (high-quality Si) [Bae05]. Figure 6.6 (a) and (b) show the J-V and EQE curves obtained in this analysis.

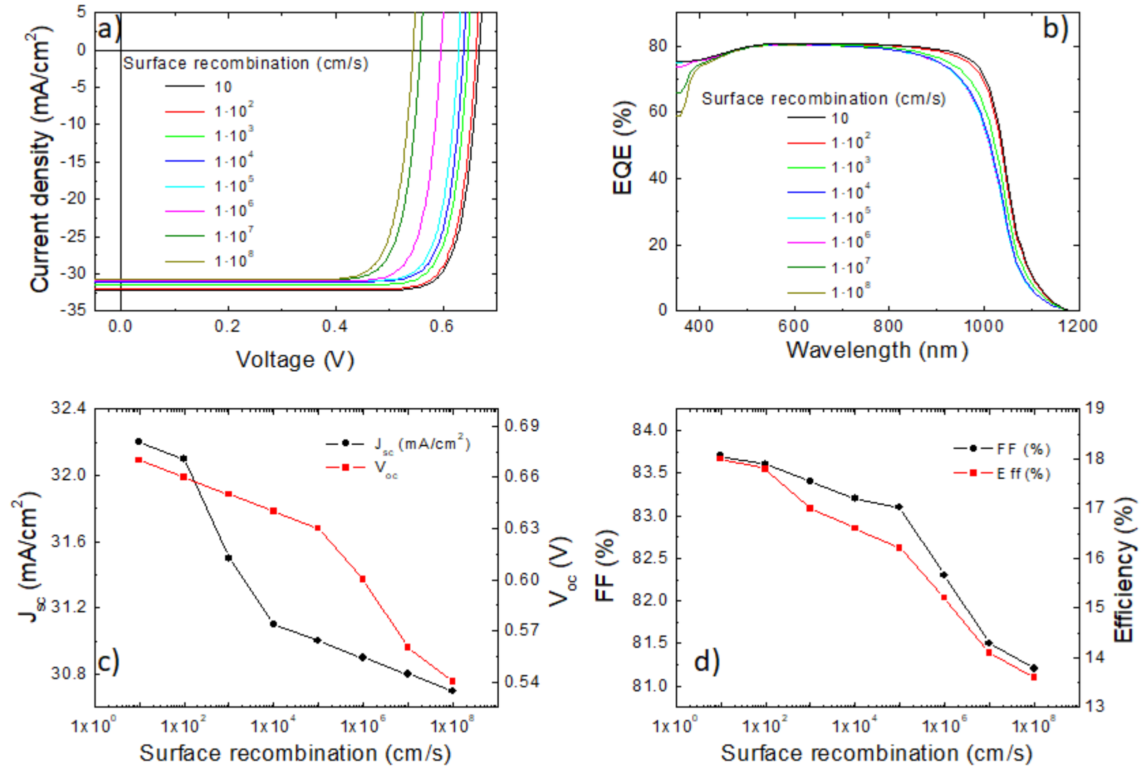

Figure 6.6. J-V (a) and EQE (b) curves of the AlInN on Si heterojunctions as a function of the surface recombination. The evolution of the V_{oc} and J_{sc}, FF and efficiency vs the surface recombination is plotted in (c) and (d), respectively.

In particular, an enhancement of the V_{oc} from 0.54 to 0.67V and of J_{sc} from 30.7 to 32.2mA/cm^2 is shown when decreasing the Si surface recombination. On the other hand, a reduced surface recombination results on a moderate improvement of the EQE at short wavelengths, and in the 900-1000 nm wavelength range, near the Si cut-off (figure 6.6 (c)). Those improvements lead to an increase of conversion efficiency from 13.6 to 18% when reducing S from 10^8 to 10 cm/s (see figure 6.6 (d)). This effect is due to the increase of the electron collection in both faces of silicon because of the reduction of the dangling bond density [Car93]. From now on, we will fix the Si surface recombination of the 10-nm thick $Al_{0.48}In_{0.52}N$ on Si heterojunctions to S = 10 cm/s.

6.3.2.6 Effect of silicon wafer quality

Considering the previous results, a maximum conversion efficiency of the devices of 18% under AM1.5G illumination has been obtained. However, as it was noted at the beginning of section 6.3.2, a Si with a low crystal quality was firstly selected. Here, we study the effect of increasing the quality of the Si substrate by adjusting the values of resistivity and bulk recombination time [Bae05]. Concretely, the Si resistivity was varied from 100 to 1 Ω·cm and the bulk recombination time from 200 to 2000 μs [Wol17]. Meanwhile, the Si surface recombination was maintained to S = 10 cm/s, assuming a properly passivated surface, taking into account the results presented in section 6.3.2.5.

Table 6.4 shows the electrical characteristic of the optimized AlInN on Si heterojunctions as a function of the Si wafer quality. We can observe an enhancement of V_{oc} from 0.67 to 0.71V and of J_{sc} from 32.2 to 32.7mA/cm^2 while maintaining the *FF* of the J-V curve, leading to a conversion efficiency to 19.7%.

6.3.2.7 Effect of anti-reflective layer

The conversion efficiency of the AlInN on Si heterojunctions can be further improved reducing the optical losses of the device caused by a high surface light reflectance. The introduction of an anti-reflective layers (ARL) at the surface reduces the light reflectance at a certain wavelength range, improving thus the transmission of the light to the AlInN on Si structure.

The transmission of light at a certain wavelength range is modulated by its refractive index and thickness. The ARL refractive index depends on the refractive index of the materials of each side, namely air (n_0 = 1) and semiconductor (n_1 = 2.54), obtained using Vergard´s law following $n_2 = \sqrt{n_0 n_1}$ [Rau11]. The ARL thickness is one quarter the wavelength of the incoming wave and depends on n_2 like $d = \frac{\lambda_0}{4n_2}$ [Rau11].

Taking into account that the maximum radiation of the solar spectrum corresponds to the wavelength region from 450 to 700 nm, the ARL is designed to improve the EQE around 600 nm, obtaining a refractive index of 1.59 and a thickness of 94 nm. However, the theoretical value obtained through this approach does not always give us the optimum value for the ARL, having to vary slightly both parameters to make sure to find the

maximum efficiency value of the device. In this case, the final values of the ARL is a refractive index of 1.6 and a thickness of 100 nm.

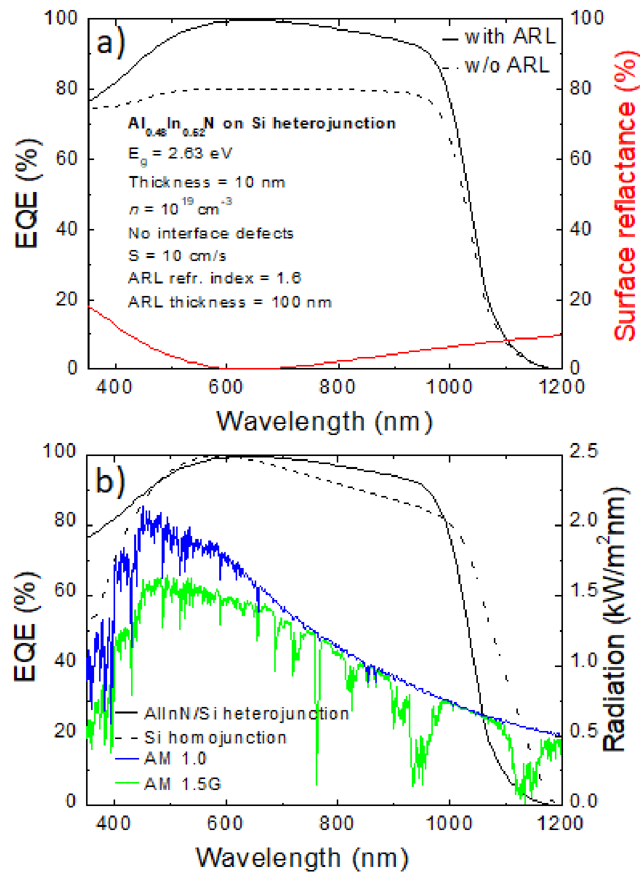

Figure 6.7. a) EQE spectra of the optimized AlInN on Si heterojunctions with and without ARL. Surface reflectance of the device with ARL. Inset: parameters of the optimized AlInN on Si structure. b) Comparison of the EQE between the optimized AlInN on Si heterojunction and the Silicon homojunction, both with high quality Si and ARL. The AM1.5G an AM1.0 sun radiation spectra are also plotted.

Figure 6.7(b) shows the evolution of the external quantum efficiency (EQE) vs the wavelength of the optimized AlInN on Si heterojunction with high quality Si with and without the designed ARL. The incorporation of the ARL reduces the surface reflectance of the device in the 600-nm wavelength range, increasing the peak EQE value from 81 to 99.6% (figure 6.7 (a)). This improvement comes with an increase of the J_{sc} from 32.7 to 38.9 mA/cm^2 and of the device efficiency reaching a value of 23.6% (see table 6.4).

This efficiency is close to the intrinsic limit of the silicon solar cells ~29% [And19] and to others technologies such perovskites ~ 27% [Kra15], leading to think that it could be a competitive technology for solar cells applications. Besides, the improvement of the EQE

in the range below 450 nm in comparison with Si homojunction devices leads to consider the potential of this heterojunction for space applications.

6.4 Comparison with a *p-n* silicon solar cell

Finally, in this section, the previously optimized AlInN on Si heterojunction, which optimized parameters are listed in the inset of figure 6.7(a), is compared with a Si homojunction solar cell to analyse the improvements achieved by the use of a nitride layer in photovoltaic devices. For this comparison, the Si homojunction is based on a *p-n* Si structure with the same high-quality *p*-Si than the one used for the optimized *n*-AlInN/*p*-Si structure, and a high-quality *n*-Si layer with the same thickness and carrier concentration then for the AlInN layer (10 nm and 1×10^{19} cm^{-3}, respectively).

Figure 6.7 (b) shows the comparison between the EQE of the optimized AlInN on Si heterojunction and the Si homojunction one, both with high quality Si and ARL. We observe that the EQE of the AlInN on Si heterojunctions presents a higher EQE in the wavelength region below 500 nm. This region is important because it covers the peak of the AM1.5G and AM1.0 solar spectra, as shown in the figure. This gain in EQE leads to a J_{sc} increase from 34.9 to 38.9mA/cm^2 while the V_{oc} remains almost constant.

Device	V_{oc} (V)	J_{sc} (mA/cm^2)	*FF* (%)	η (%)
AlInN/Si (low quality)	0.67	32.2	83.4	18.0
AlInN/Si (high quality)	0.71	32.7	84.4	19.7
AlInN/Si (high quality) with ARL	0.72	38.9	84.3	23.6
Si homojunction with ARL	0.74	34.9	84.1	21.7

Table 6.4. Comparison of the simulation results obtained for different InGaN-based junctions with Pc1d software and the ones obtained by Fabien *et al.* [Fab14].

These trends result in an increase in conversion efficiency from 21.7 to 23.6% (see table 6.4). Besides, this enhancement is especially effective for devices operating outside the atmosphere with AM1.0 illumination, pointing the AlInN/Si hetero-junction promising for space applications.

6.5 Conclusions

In this chapter a heterojunction solar cell with AlInN material and silicon has been designed and simulated using Pc1d software. The influence of AlInN bandgap, thickness and background doping, interface diffusion and silicon surface recombination on the

photovoltaic properties of the solar cell was studied and optimized to obtain the potential of a solar cell based on AlInN/Si heterojunction. The following main results were obtained:

- A successful adaptation of the simulation program Pc1d to group III-V materials was made, which were compared with previous results simulated by another software.
- The evolution photoelectrical properties of the devices as a function of the AlInN bandgap energy, from 1.7 to 2.6 eV, reveals the enhancement of the conversion efficiency with the bandgap energy, i.e. the increase of the Al mole fraction. This result leads to study AlInN layers with medium-to-high Al content.
- The study of the thickness of the III-nitride layer, from 10 to 500 nm, shows an improvement of the conversion efficiency of the devices with thinner layers, probably related to an increase of the transmittance, allowing the silicon layer to collect more electrons.
- The carrier concentration of the AlInN layers does not affect significantly to the device properties as long as it remains higher than 10^{19} cm^{-3}. Carrier concentration values below this levels causes a notable decrease of the conversion efficiency.
- The variation of the AlInN/Si interface defect density reveals the importance to reduce as much as possible this parameter. If the device has a defect density above 10^{18} cm^{-3} the conversion efficiency and the EQE decrease drastically. This effect can be induced by the Al diffusion during the deposition process and it causes a *p+* doped layer at the interface, which can repel carriers who want to cross the interface, causing significant electrical losses.
- The photoelectrical properties of the devices are not highly affected by the surface recombination. However, the conversion efficiency decreases from 18% to 13.6%, that means a 30%, when the surface recombination increases from 10 to 10^{8} cm/s, seeing a more noticeable effect for values above of 10^{5} cm/s. This effect is probably caused by the aforementioned dangling bonds and can be reduced by a passivation and the chemical cleaning process before the deposition.
- Besides, it has been observed that the choice of a better quality silicon substrate can significantly affect the efficiency of the device, improving the conversion efficiency from 18% to 19.7%.

- Finally, the optimization of the optical properties of the layer, through the introduction of an anti-reflective layer, causes an improvement in the efficiency of the device from 19.7% to 23.6%. This effect is produced by optimizing the reflections of the front layer of the device in a certain range of the solar spectrum, which leads to an increase in the electrons collected in that range and therefore to an increase in the excited carriers that will be collected.

Through this study, an optimized solar cell device based on AlInN/Si heterjunction reveals a conversion efficiency close to 20% without anti-reflective layer with a fill factor of 84.4%, a short circuit current of 32.8 mA/cm^2 and an open circuit voltage to be 0.72 V under one sun AM 1.5 G illumination. The incorporation of an anti-reflection coating increases the efficiency to 23.6% increasing the short circuit current to a 38.9 mA/cm^2 due to the improvement of the EQE in the spectral range below 480 nm. These results are better compared to the ones obtained of a silicon homojunction with similar design parameters and ARL which reach an efficiency value of 21.7%.

Chapter 7
InN layers deposited by RF sputtering

The development of InN material has been studied along the last decades due to its applications for opto-electronics devices or high power and high speed electronic devices and solar cells as stated in chapter 1.

In that sense, several reports of InN layers deposited by MOCVD [Ale06, Jai04, Yam94], MBE [Sai02, Lob16, Spe04] or sputtering [Kis90, Mot02, Shi06, Shi05, Sai01, Guo09, He10, Li17, Wan18] were carried out to analyze its properties as a function of different growth conditions, such as, the growth temperature, the indium power supply or the N_2/Ar ratio. One of the aims of these studies was to analyze the value of the bandgap energy, which evolves from 0.64 eV to ~2 eV depending on of the growth conditions and the level of impurities, as described in chapter 2.

Our research group has experience in the deposition of InN layers by RF sputtering on GaN-template, sapphire and Si (111), depending on several growth conditions [Val10] the effect of a low growth rate InN buffer layer [Val12] and also InN nanocolums [Mon16]. The aim of these studies was to improve the crystalline quality of the layers to be able to develop opto-electronic devices. The main difference between the studies developed by our group and the others is the plasma used along the deposition process. In that sense, most studies of III-nitrides layers deposited by sputtering usually use a plasma based on a mixture of argon and nitrogen in order to increase the growth rate of the layers. However, the layers developed by our group are deposited using a pure nitrogen plasma, which reduces the growth rate in comparison with other studies and improves its structural quality as observed by Valdueza *et al.* [Val10].

Furthermore, as stated in chapter 4, devices based on silicon technology are developed on Si (100) due to their lower amount of dangling bonds compared to Si (111). There are many studies on InN on Si (111) which crystal orientation adapts better to the hexagonal structure of III-nitrides. However, there are not so many on InN on Si (100) grown by

MOCVD [Kry07], MBE [Che12], and sputtering [Cai09, Shi05], and neither the comparison of the quality of the developed InN material deposited on both substrates.

So, in this chapter, we present the effect of the growth conditions (growth temperature and In RF power supply) on the structural, morphological, electrical and optical properties of InN layers deposited by RF sputtering simultaneously on Si (100), Si (111) and sapphire substrates. We will discuss the comparison of the obtained InN quality on the three substrates.

7.1 Effect of the growth temperature

The InN layers studied in this chapter were grown using the RF sputtering described in chapter 4 on 300-µm-thick Si (100), 500-µm-thick Si (111) and on 500-µm-thick sapphire substrates.

The sputtering system has 2” confocal magnetron cathodes of pure In (4N5) and pure nitrogen (6N) as reactive gas. Before the introduction in the deposition chamber, the substrates were chemically cleaned in organic solvents and, after that they were outgassed for 30 min at 550ºC and cooled down to the growth temperature. Besides, previously to the deposition, the targets and substrate were cleaned using a soft plasma etching with Ar (99.999%). InN layers were deposited with a nitrogen flow of 14 sccm at a pressure of 0.47 Pa. The RF power applied to the In target was fixed at P_{In} = 40 W, whereas the growth temperature was varied from 20°C to 450°C, listed in table 7.1 for samples A1 to A4, respectively. The nominal thickness of the layers is ~ 230 nm.

Sample	Ts (°C)
A1	20
A2	300
A3	400
A4	450

Table 7.1. Summary of the growth temperature of the InN samples deposited at P_{In} = 40 W.

7.1.1 Structural characterization

HRXRD measurements in 2θ/ω configuration show the diffraction peaks corresponding to the (0002) and (0004) reflections of InN and the related ones to each substrate, Si (100), Si (111) and sapphire, as displayed in figures 7.1 a), b) and c) respectively.

The 2θ/ω scan of samples deposited at 300°C shows non-other crystallographic orientations, pointing out that the InN layers are aligned along the growth direction well oriented with the *c*-axis.

These results are also observed by other authors in InN layers deposited on Si (111), sapphire and GaN templates under a pure nitrogen plasma [Val10, Mon16]. However, this is not the case for InN layers deposited under a plasma mixture of Ar and N_2 [Cai09, Anj18] which shows multiple diffraction peaks related to InN, In_2O_3 and InN_xO_y.

Besides, the effect of the N_2/Ar ratio was studied by Shinoda *et al.* [Shi05] for InN samples deposited on glass, showing the appearance of different diffraction peaks depending on the N_2/Ar ratio.

However, in our case, despite all of the samples are highly oriented at the *c*-axis regardless the growth temperature, layers grown at room temperature reveals other diffraction peaks at 2θ = 42° and 2θ = 56° related to the InN (102) and InN (103) diffraction peaks respectively. These behavior is probably caused by a decrease of the kinetic energy in the growth process.

As it is shown in figure 7.1, a higher order of the InN diffraction peak can be observed regardless the symmetry and type of substrate, confirming the ability of the sputtering technique to deposit crystalline InN layers with a wurtzite structure and similar quality in both silicon substrates despite the orientation of the substrate. This result is also observed by Valdueza *et al.* [Val10] for InN layers grown on Si (111) and on GaN template and by Bashir *et al.* [Bas18] in InN layers with a buffer layer of ZnO.

The structural characterization of the samples is summarized in table 7.2. For InN on sapphire layers, the FWHM of the rocking curve decreases from 6.3° to 2.3° when increasing the growth temperature from 20 to 450ºC. Meanwhile there is not clear trend on the evolution of the mosaicity with the temperature on InN samples deposited on both silicon substrates, reaching its lower value for samples deposited at 300°C in both cases. Besides, values obtained for InN layers deposited on both silicon substrates are similar, pointing to InN films with similar structural quality regardless the substrate orientation.

As observed in table 7.2, the FWHM of the rocking curve around the (0002) diffraction peak of the layers grown on sapphire substrate are lower than the silicon ones, this is probably due to an unintentional deposition of an amorphous SiO_xN_y layer between the

AlInN and the substrate when growing on Si substrates, as detailed in a previous study carried out by this group [Nuñ18].

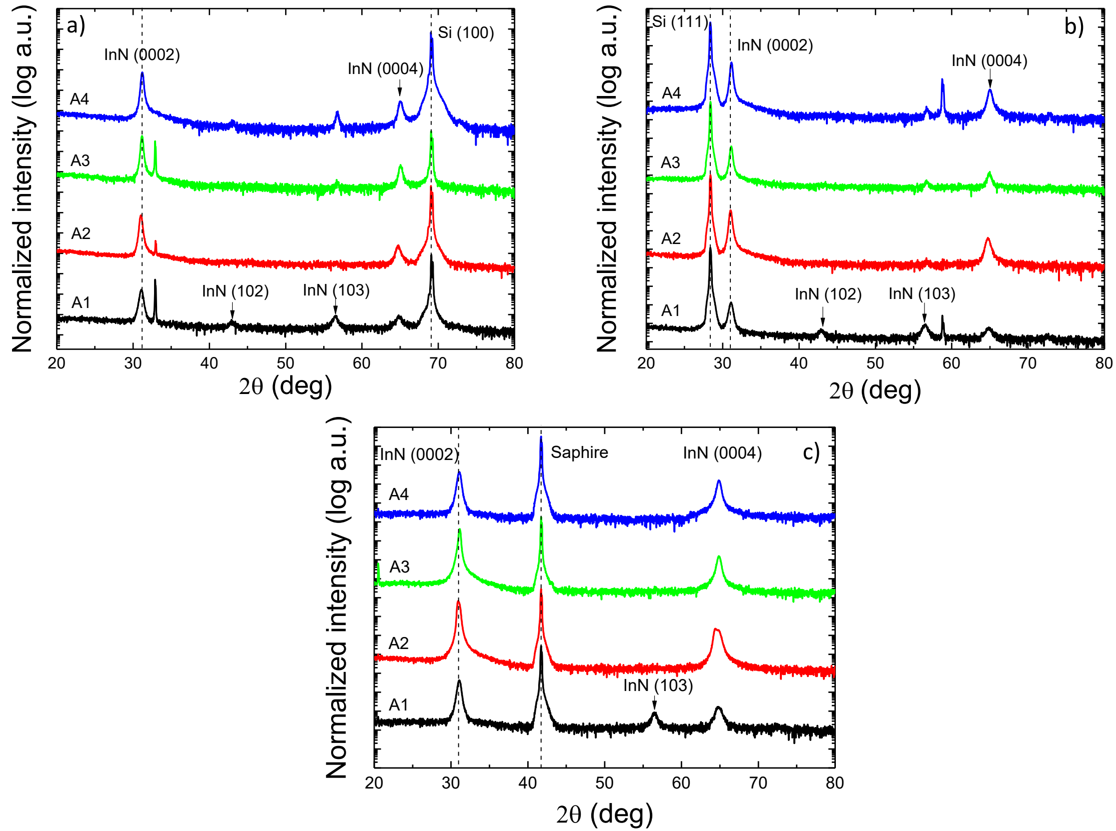

Figure 7.1. 2θ/ω scans of the InN layers deposited on a) Si (100), b) Si (111) and c) sapphire as a function of the growth temperature.

This layer is expected to be present when growing on Si (100) but not on sapphire substrates. This could be the origin of the observed reduction of the FWHM of the rocking curve around the (0002) diffraction peak, as the atomic arrangement of the substrate is lost for the layer growth in Si substrates. At the same time, the non-homogeneous distribution of the layer and eventually, the appearance of regions without the amorphous layer could lead to nucleation sites which promote the columnar growth of InN on silicon. Furtmayr *et al.* has detailed the unintentional nitridation on silicon (111) substrates which can produce nucleation sites and, thus changes the FWHM of the AlInN layer in comparison with sapphire substrate [Fur08], which can affect to the structural and morphological properties of the layer.

	FWHM rocking curve (°)		
Sample	**Si (100)**	**Si (111)**	**Sapphire**
A1	8.3	8.3	6.3
A2	6.5	6.3	3.0
A3	9.1	6.6	2.5
A4	7.8	8.7	2.3

Table 7.2. Evolution of the FWHM of the rocking curve of the InN layers grown on Si (100), Si (111) and sapphire extracted from HRXRD measurements.

The estimation of the strain of the layers along the *c*-axis (ε_{zz}), obtained using equation 2.6 reveals a tensile strain as shown in table 7.3, being lower for layers grown on sapphire than the ones grown on silicon substrates, probably affected by the aforementioned amorphous layer. Besides, as can be observed in table 7.3, the layers are more relaxed when the growth temperature increases, probably due to by an increase on the kinetic energy of the atoms.

	Strain ε_{zz} (%)		
Sample	**Si (100)**	**Si (111)**	**Sapphire**
A1	0.78	0.48	0.32
A2	0.43	0.41	0.26
A3	0.34	0.33	0.17
A4	0.24	0.26	0.14

Table 7.3. Evolution of the strain along the *c*-axis of the InN layers grown on Si (100), Si (111) and sapphire extracted from HRXRD measurements.

Table 7.4 shows an increase of the grain size, obtained using the Scherrer formula as described in chapter 5 (equation 5.2), with the growth temperature for layers grown on silicon substrates. This effect is probably due to an evolution on the morphology, from columnar layers to compact ones.

	Grain size (nm)		
Sample	**Si (100)**	**Si (111)**	**Sapphire**
A1	18	17	24
A2	23	25	21
A3	29	28	30
A4	27	31	20

Table 7.4. Evolution of the grain size of the InN layers grown on Si (100), Si (111) and sapphire estimated from HRXRD measurements.

However, this trend is not observed in layers deposited on sapphire, which suggests that this possible morphology evolution does not occur in these layers, obtaining columnar structures regardless of temperature.

7.1.2 Morphological characterization

Figure 7.2 shows the AFM images with 5×5 μm^2 size of all samples under study: InN layers deposited in Si (111) (first column), Si (100) (second column) and sapphire (third column), as a function of the growth temperature. It can be observed that the z-scale gradually increases with the growth temperature for all substrates. Z-scale values are similar for both silicon substrates, with the exception of the InN sample deposited on Si (100) at 400°C (A3). This result agrees with FWHM rocking curve data (table 7.2), which shows the highest value for the sample growth under these conditions.

The root mean square (rms) surface roughness of the samples was obtained from the average of the ones of AFM images taken on 1×1, 2×2 and 5×5 μm^2 surface areas. Table 7.5 shows the increasing trend of the rms surface roughness for InN on Si (111), Si (100) and sapphire substrates vs the growth temperature, as observed in previously studies [Val10, Guo09]. Particularly, the minimum rms surface roughness is obtained for InN samples deposited at room temperature, i.e. 2.6, 2.9 and 2.3 nm for InN on Si (100), Si (111) and sapphire, respectively.

This evolution of the rms surface roughness is associated to the increase of In desorption with the substrate temperature which is highly enhanced at temperatures above 425ºC as observed by Bi *et al.* [Bi05].

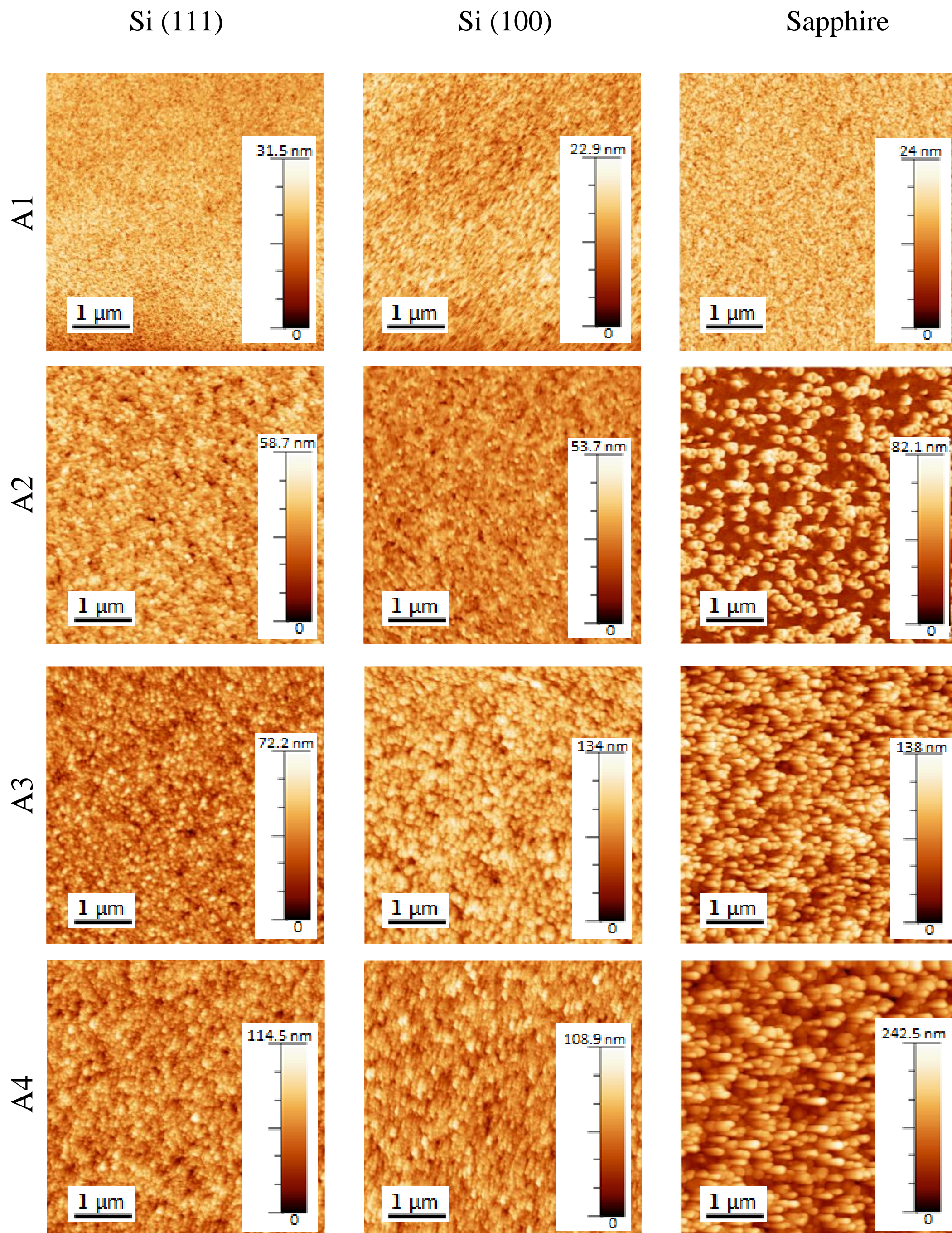

Figure 7.2. 5×5 µm^2 AFM images of InN layers deposited in Si (111) (first column), Si (100) (second column) and sapphire (third column), as a function of the growth temperature.

These results and the AFM images plotted in figure 7.2 reveal an evolution of the morphology of the samples changing from smooth layers, which indicates a more compact morphology, to rougher layers, which may indicate a more columnar morphology, as also observed by XRD measurements and in agreement with results previously obtained [Shi05, Guo09] in InN layers vs. the growth temperature on Si (100)

and Si (111). This change in the morphology of the InN from compact to columnar may lead to more grain boundaries affecting thus the electrical properties of the layers.

	Rms surface roughness (nm)		
Sample	**Si (100)**	**Si (111)**	**Sapphire**
A1	2.6	2.9	2.3
A2	5.6	7.6	16.3
A3	9.0	16.9*	24.4*
A4	14.6*	13.0*	37.1*

Table 7.5. Summary of the rms surface roughness values of the InN layers deposited on Si (100), Si (111) and sapphire as a function of the growth temperature. The values with an (*) can be affected by the morphology of the layers.

Besides, FESEM measurements of layers grown at 300° C displayed in figure 7.3 reveals a columnar morphology for Si substrates. However, the layer grown on sapphire (figure 7.3 c), shows a closely-packed columnar structure that seems to be compact in its first nanometers.

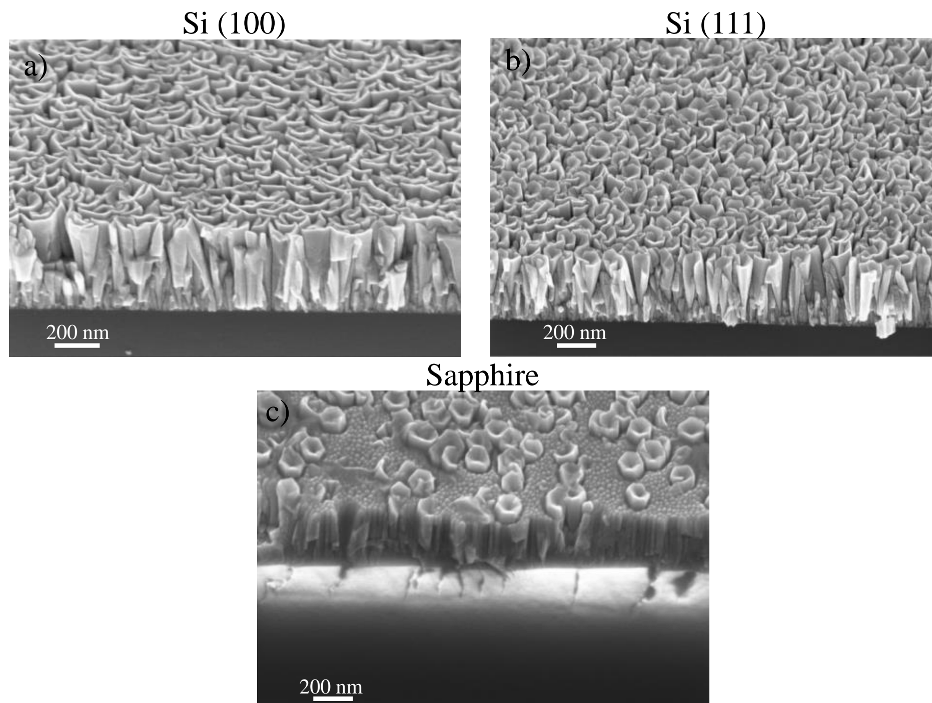

Figure 7.3. SEM images of layers grown at 300°C on a) Si (100), b) Si (111) and c) sapphire substrates.

7.1.3 Electrical characterization

Hall Effect measurements at room temperature were performed on InN layers grown on sapphire, the results of the characterization are summarized in table 7.6. The layer resistivity evolves from 3.9 to 0.7 mΩ·cm with the increase of the growth temperature,

while the carrier concentration remains almost constant in the 10^{21} cm^{-3} range. This effect is related to the increase of the adatom mobility with the growth temperature and, as observed by Nuñez *et al.* in AlInN on sapphire samples deposited by RF sputtering [Nuñ17]. The values of resistivity and mobility are close to the ones obtained by Motlan and Valdueza-Felip *et al.* on InN on glass and GaN template substrates, deposited by the same technique at 80°C and 450°C respectively [Mot02, Val11]. The high carrier concentration of the samples is related to the aforementioned (chapter 2) unintentional doping during the growth by several sources like hydrogen and oxygen impurities [Wu09, Dar10] or nitrogen vacancies as previously observed in studies performed by this group under similar conditions obtaining values of oxygen around 4% [Nuñ17].

Sample	Resistivity (mΩ·cm)	Carrier concentration (cm^{-3})	Mobility (cm^2/V·s)
A1	3.9	1.4×10^{21}	1.2
A2	0.8	1.5×10^{21}	5.0
A3	0.8	1.0×10^{21}	7.9
A4	0.7	1.0×10^{21}	9.5

Table 7.6. Summary of the electrical characteristics of the InN samples grown on sapphire: InN resistivity, carrier concentration and carrier mobility, obtained by Hall Effect measurements.

It should be mentioned that these measures have been taken taking into account the thickness of the layer. However, as observed in figure 7.4, samples grown on sapphire show a closely-packed columnar morphology that seems to be more compact in the first nanometers of the layer. So, it is possible that the conduction of the layer can mainly occur in this region.

These results lead to an increase of the carrier mobility with the temperature pointing to the possibility of obtaining devices with better electrical performance for higher temperatures.

7.1.4 Optical characterization

The optical properties of the layers were evaluated by transmission measurements of InN on sapphire samples at room temperature. Figure 7.4 shows the evolution of the squared absorption coefficient vs the energy obtained from the transmittance measurements for all samples, displayed in the inset of figure 7.4. The absorption coefficient as a function of the impinging wavelength $\alpha(\lambda)$ was estimated considering the Beer-Lambert law and neglecting the optical scattering and reflection losses in the sample's surface. Then, we

used the sigmoidal approximation described in equation 7.1 to fit the experimentally estimated absorption coefficient as explained in chapter 5.

$$\alpha = \frac{\alpha_0}{\left(1+e^{\frac{E-E_g}{\Delta E}}\right)} \tag{7.1}$$

where α_0 is the absorption coefficient, E_g is the bandgap energy and ΔE is the band edge broadening. This approximation takes into account the broadening of the bandgap edge induced by the Burstein-Moss effect.

The apparent optical bandgap energy (E_g) is estimated by the linear fit of the squared absorption coefficient, as displayed in figure 7.4 by the dotted lines, showing a slightly decrease from E_g = 1.77 eV to E_g = 1.72 eV with the growth temperature as detailed in table 7.7.

Besides, the blue-shift of the bandgap energy of these layers compared to the expected one in InN with low carrier concentration is probably induced by the unintentional high carrier concentration of the samples above 10^{21} cm^{-3}, which is affected by the Burnstein-Moss effect as explained in chapter 2.

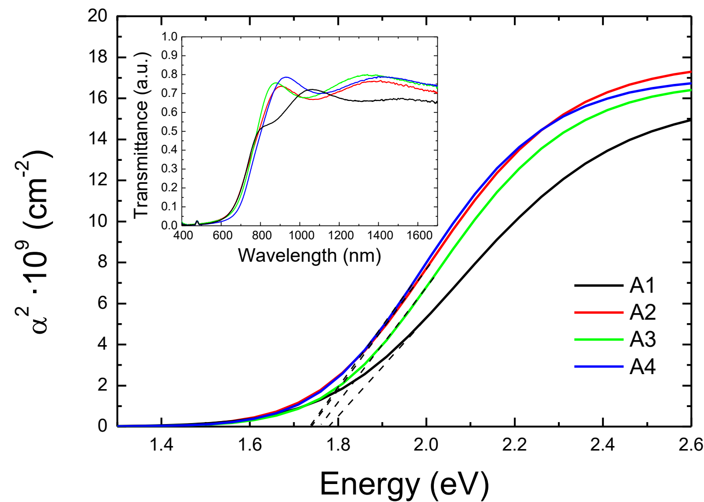

Figure 7.4. Squared absorption coefficient vs energy and transmittance vs wavelength (inset) of the InN on sapphire samples as a function of the growth temperature.

The absorption band edge broadening (ΔE) listed in table 7.7 decreases with the growth temperature, probably induced by the reduction in the layer impurities.

	E_g (eV)	ΔE (meV)
A1	1.77	196
A2	1.73	168
A3	1.75	163
A4	1.72	155

Table 7.7. Summary of the optical properties obtained at room temperature: apparent bandgap energy (E_g) and absorption band edge broadening (ΔE) of the InN on sapphire samples.

The structural and electrical properties of layers grown at 300°C reveals a lower FWHM (on layers grown on silicon substrates) with a higher carrier concentration, which can lead to the obtaining of better photoelectrical properties in the devices to be developed. In that sense, the layers analyzed in the following study were carried out at 300°C.

7.2 Effect of the In RF power

The samples presented in this study were deposited using the same procedure and substrates than the ones explained in section 7.1.

Here, we study the effect of the RF power applied to the In target, P_{In}, on the structural, morphological, electrical and optical properties of InN on Si (100), Si (111) and sapphire substrates deposited at 300°C. Particularly, the In RF power was varied from 20 to 40 W whereas the growth temperature was fixed to 300°C, following best results obtained in previous section. In this set of samples, the deposition time was decreased from 240 to 120 min along with P_{In} in order to obtain layers with similar thickness. The deposition conditions of samples R1-R3 are listed in table 7.8.

Sample	P_{In} (W)	Growth time (min)
R1	20	240
R2	30	180
R3	40	120

Table 7.8. Summary of the deposition conditions of the InN samples.

7.2.1 Structural characterization

The 2θ/ω scans of the InN samples shown in figure 7.5 reveal diffraction peaks corresponding to the InN (0002) and InN (0004) and to each substrate in a) Si (100), b) Si (111) and c) sapphire. These measurements confirm the wurtzite structure of all layers with the *c*-axis of the InN material aligned to the one of the substrate. Besides, it can be

seen two diffraction peaks at 35º and at 58º related to the silicon substrates, concretely the are related to (200) and (103) diffraction peaks respectively.

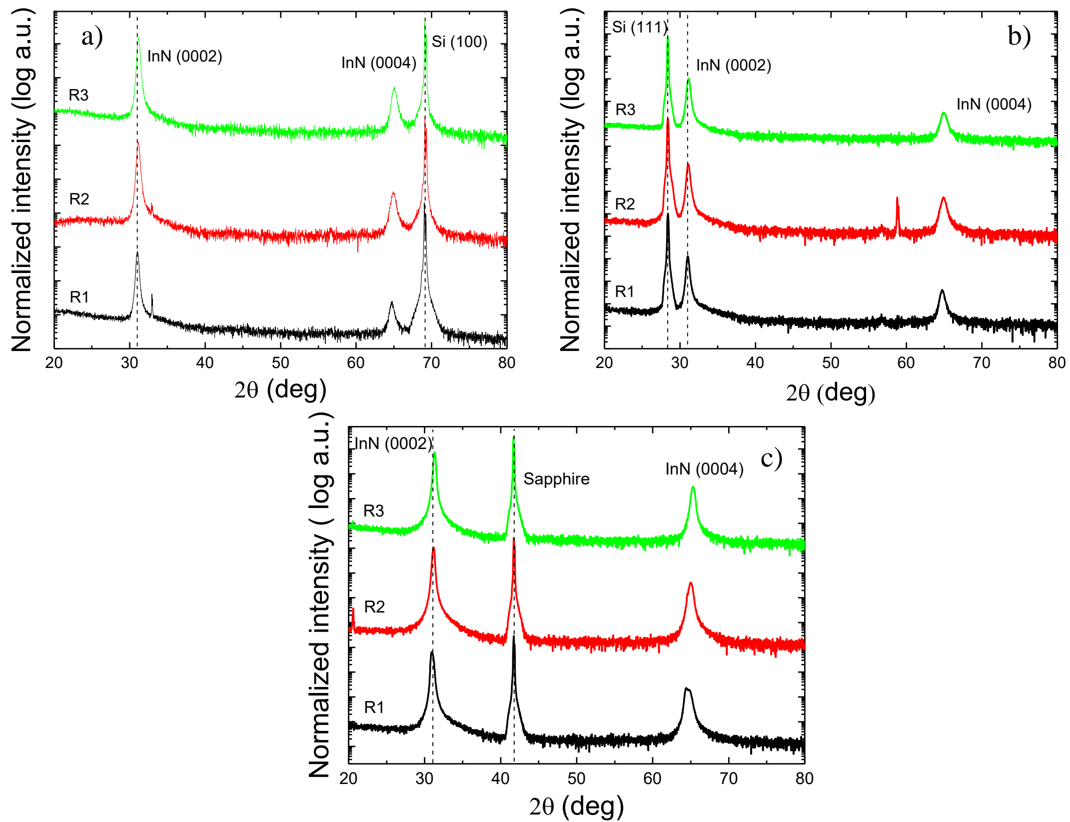

Figure 7.5. 2θ/ω scans of InN layers deposited on a) Si (100), b) Si (111) and c) sapphire as a function of the In power supply at 300ºC.

The evolution of the *c*-lattice parameter shown in figure 7.6 reveals an almost linear increase with the In power supply as already reported by Inoue *et al.* for Si (111) and sapphire substrates [Ino04].

However, despite this linear trend is quite similar for both silicon substrates it can be observed that the trend in samples grown on sapphire grows faster than those grown on silicon, which indicates that the strain of the layers increases with the aluminum power supply. This effect is probably due to applying excess power to the target, which can cause atoms to arrive with excessive energy.

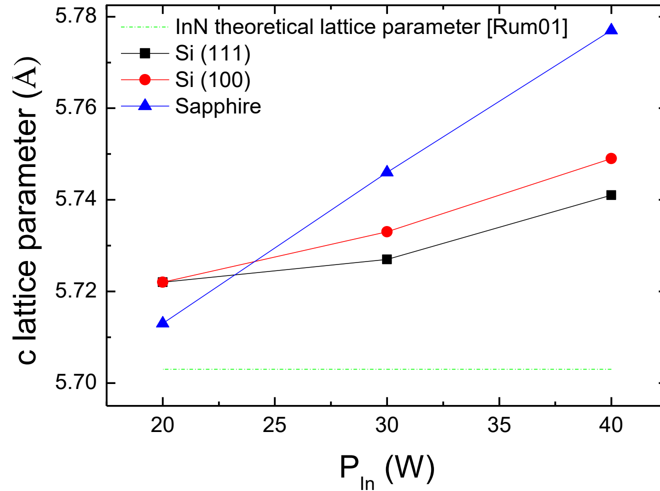

Figure 7.6. Evolution of the *c* lattice parameter as a function of the In power supply.

This evolution on the lattice parameter of the layers leads to an increase of the tensile strain along the *c*-axis (ε_{zz}) with the In power supply as detailed in table 7.9. As it is detailed in table 7.9, layers grown on sapphire show a remarkable increase of the tensile strain with the power supply which is probably attributed to a change in the layer morphology, meanwhile the layers grown on both silicon substrates show similar values, showing al milder increase of the tensile strain with the In power supply.

	Strain ε_{zz} (%)		
Sample	**Si (100)**	**Si (111)**	**Sapphire**
R1	0.33	0.33	0.17
R2	0.53	0.42	0.75
R3	0.81	0.67	1.30

Table 7.9. Evolution of the strain along the *c*-axis of the InN layers grown on Si (100), Si (111) and sapphire extracted from HRXRD measurements.

A summary of the FWHM of the rocking curve for InN layers deposited on Si (100), Si (111) and sapphire is summarized in table 7.10. We observe an increasing trend of the mosaicity regardless the substrate. This effect is probably due to a degradation on the surface produced by high-energy In atoms as also observed by Valdueza *et al.* [Val10] on samples grown on Si (111) and sapphire.

Besides, the FWHM of the InN layers is higher in InN on Si layers compared to their InN on sapphire counterparts, as shown in table 7.10. This effect is probably caused by the aforementioned unintentional nitridation of the substrate, which can create clusters at the interface, leading to high strain in layers grown on silicon substrates.

	FWHM rocking curve (°)		
Sample	**Si (100)**	**Si (111)**	**Sapphire**
R1	3.35	3.90	1.87
R2	4.64	4.67	1.87
R3	6.54	6.15	3.02

Table 7.10. Evolution of the FWHM of the rocking curve of the InN layers grown on Si (100), Si (111) and sapphire extracted from HRXRD measurements.

Table 7.11 shows a decrease of the grain size, obtained using the Scherrer formula with the In power supply for all the layers regardless the substrate selected. This effect is probably related to an evolution on the morphology, from compact or closely-columnar layers to columnar ones when the indium power supply increases.

	Grain size (nm)		
Sample	**Si (100)**	**Si (111)**	**Sapphire**
R1	26	26	29
R2	24	26	27
R3	23	25	21

Table 7.11. Evolution of the grain size of the InN layers grown on Si (100), Si (111) and sapphire estimated from HRXRD measurements.

Furthermore, as observed in previous section, InN layers growth on silicon substrates show similar values, leading to similar structural quality regardless the Si substrate orientation.

7.2.2 Morphological characterization

FESEM images of all samples shown in figure 7.7 reveal an strong evolution of the morphology of the layers from compact InN deposited at P_{In} = 20 W (figure 7.7 (a)), towards closely-packed nanocolumnar InN when increasing P_{In} to 40 W (figure 7.7 (c)).

Besides, InN samples deposited on both silicon substrates present a similar behavior independently of the Si crystal orientation. Moreover, this closely-packed nanocolumnar morphology shown in InN layers with P_{In} > 30 W is usually attributed to the nitride growth under N-rich conditions [Aza18].

However, InN samples grown on sapphire substrate (figure 7.7(c)) show a different behavior with the increase of P_{In} compared to their InN on Silicon counterparts, revealing a change in the layer morphology from compact layers to columnar ones.

This effect is probably due to the high-energy particles that bombard the In target with the RF power supply, leading to a degradation of the surface which slightly reduces the size of crystalline grain, as observed by Chaoumead *et al.* [Cha12].

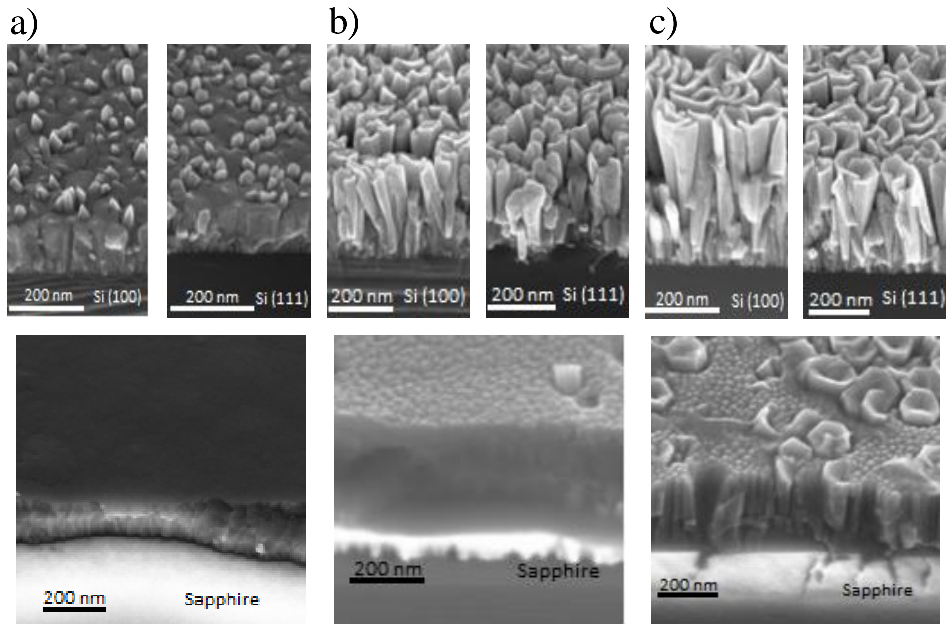

Figure 7.7. FESEM images of InN samples with a) P_{In} = 20 W, b) P_{In} = 30 W and c) P_{In} = 40 Won Si (100) (top left), Si (111) (top right) and sapphire (down) substrates at 300ºC.

The thickness of the layers and, therefore, the growth rate obtained by FESEM images are detailed in table 7.12, showing an increase of the growth rate, mainly due to the increase in power in the aluminum target.

Figure 7.8 shows the AFM images of 5x5 μm^2 size of all InN samples under study. From AFM measurements we estimated the rms surface roughness of the InN layers obtaining an increase with the InN power supply for layers deposited on sapphire.

Sample	Si (111)		Si (100)		Sapphire	
	Thickness (nm)	Growth rate (nm/h)	Thickness (nm)	Growth rate (nm/h)	Thickness (nm)	Growth rate (nm/h)
R1	110	25	160	40	175	45
R2	240	80	260	85	255	85
R3	310	155	400	200	265	130

Table 7.12. Summary of thickness and growth rate of layers grown on Si (111), Si (100) and sapphire.

This evolution of the rms is associated to a surface damage induced by the high energy of the incident In atoms as already reported by Guo *et al.* and Cheng *et al.* [Guo99, Che03]. However, no clear trend was obtained in InN layers grown on both silicon substrates due to the closely-packed nanocolumnar morphology of the layers, as presented in table 7.13.

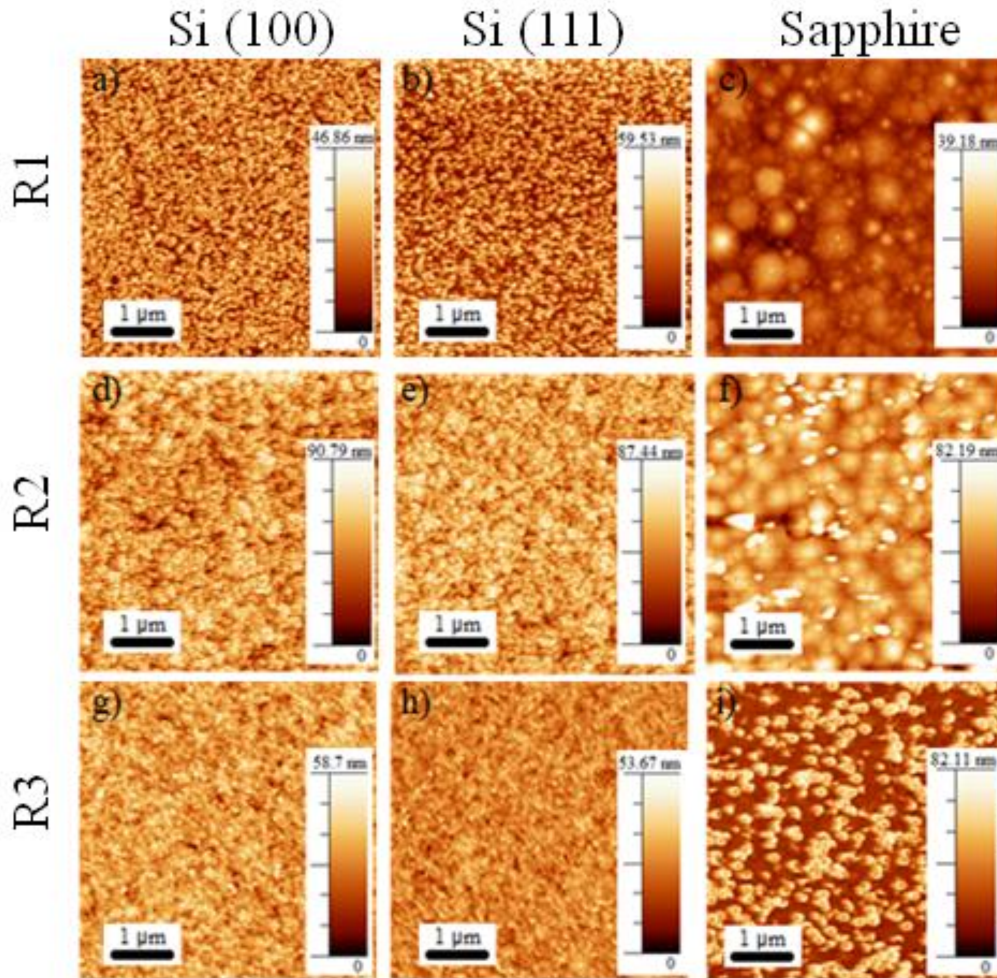

Figure 7.8. AFM images of InN samples with P_{In}= 20 W (R1) , P_{In}= 30 W (R2) and P_{In} = 40 W (R3) grown on Si (100) (a, d and g), on Si (111) (b, e and h) and on sapphire (c, f and i) at 300ºC.

These results reveal the importance of selecting an appropriate power supply to the targets in order to prevent the damage of the layer during growth and obtain the desired optimum morphology. So from now on and for next studies, we will choose an In power supply of P_{In} = 30 W in order to obtain a trade-off between the structural and surface quality of the layer and the higher growth rate compared to InN samples deposited at P_{In} = 20 Was detailed in table 7.10.

	Rms surface roughness (nm)		
Sample	**Si (100)**	**Si (111)**	**Sapphire**
R1	10.4	8.2	3.1
R2	12.8	11.6	11.2
R3	7.6	5.6	16.3

Table 7.13. Summary of the rms surface roughness values of InN layers as a function of P_{In} for the three substrates.

7.2.3 Electrical characterization

The electrical properties of InN layers deposited on sapphire were evaluated by Hall Effect measurements at room temperature, which results are summarized in table 7.14. The carrier concentration increases from 4.7×10^{20} cm^{-3} to 2.2×10^{21} cm^{-3} when increasing P_{In} from 20 to 40 W, probably due to the induced damage on the front surface during the deposition, which leads to an increase on the grain boundaries area and the possibility of an unintentional doping by oxygen.

Sample	Resistivity (mΩ·cm)	Carrier concentration (cm^{-3})	Mobility (cm^2/V·s)
R1	0.5	4.7×10^{20}	28.3
R2	0.4	1.7×10^{21}	9.5
R3	0.6	2.2×10^{21}	5.0

Table 7.14. Summary of the electrical characterization of the InN samples grown on sapphire: layer resistivity, carrier concentration and carriers mobility, obtained by Hall Effect measurements.

Meanwhile the resistivity does not show a clear trend with P_{In}, with values ~0.4-0.6 mΩ·cm, which, as in the previous study, are similar to the ones obtained by other authors on InN on sapphire and GaN templates [Mot02, Val11].

The electrical properties reveal a reduction of the carrier mobility with the In power supply. This effect is probably related to the previously mentioned layer degradation caused by the excessive power supply, which can causes an increase of grain boundaries in the sample.

Therefore, Hall Effect measurements reveals similar electrical properties of the InN layers regardless the power supply applied. However, the evolution of the carrier concentration and carriers mobility detailed in table 7.14 and the low resistivity obtained for the layer

grown at 30 W lead us to think that this power may be the most optimal for the development of the solar cell devices.

7.2.4 Optical characterization

The optical properties of the layers were evaluated by transmission measurements of AlInN on sapphire samples under the same growth conditions. The absorption coefficient of the layers is calculated using the transmittance spectra of the samples, shown in the inset of figure 7.9. As explained in the previous study, the apparent optical bandgap energy is obtained by a linear fit of the squared absorption coefficient, depicted in figure 7.9.

In that sense, figure 7.9 shows the evolution of the transmittance and of the squared absorption coefficient as a function of the In power supply, revealing a increasing of the bandgap energy from 1.73 to 1.87 eV when the In power supply decreases, as showed in table 7.15.

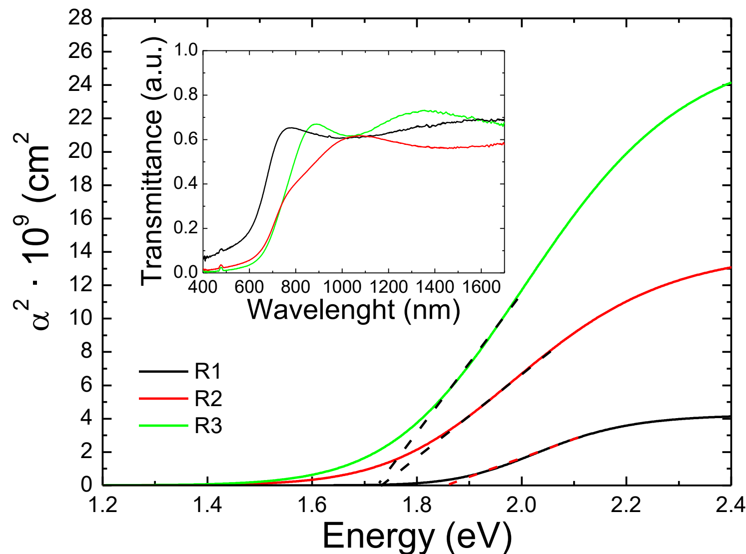

Figure 7.9. Transmittance as a function of the In power supply of the InN layers grown on sapphire.

This effect could be caused by a change in the crystalline quality of the layers as stated by Anjum *et al.* [Anj18] in InN layers grown on glass substrate by sputtering.

	E_g (eV)	ΔE (meV)
R1	1.87	100
R2	1.73	160
R3	1.74	168

Table 7.15. Summary of the optical properties obtained at room temperature: absorption edge (E_g) and absorption band edge broadening (ΔE) of the samples growth on sapphire.

The evolution of the optical bandgap energy as a function of the carrier concentration of the InN samples is shown in figure 7.10 (red triangles). Besides, the results obtained in this study are compared with InN samples grown by Walukiewicz *et al.* using MBE deposition technique [Wal04a] (open circles) and with InN layers grown using a MOVPE system depicted by Wu *et al.* [Wu03] (solid squares) with data from studies of Bhuiyan *et al.* [Bhu03a]. Besides, in order to compare InN layers grown by Sputtering deposition technique, the results were compared with the ones obtained by Sasaoka *et al.* [Sas10] (green circle) and with InN layers grown using the Sputtering system of this thesis by Valdueza *et al.* [Val11] (blue triangles) in order to observe the Burnstein-Moss effect.

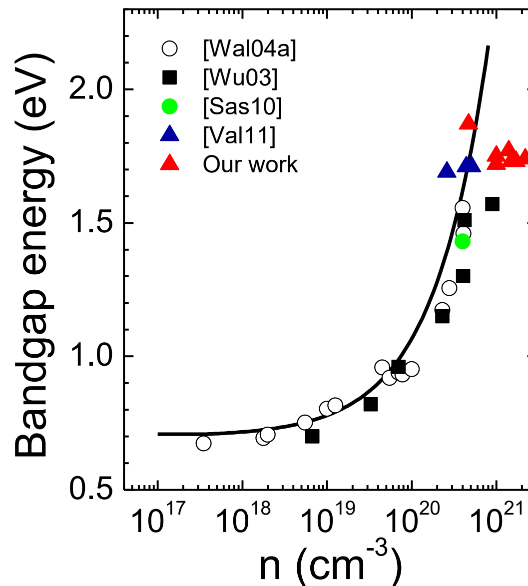

Figure 7.10. Evolution of the optical bandgap energy as a function of the carrier concentration. The line describes the optical bandgap energy values calculated taking into account the Burnstein-Moss effect and including the conduction band nonparabolicity [Wal04a].

The InN layers developed in this study present a bandgap energies from 1.7 to 1.9 eV with a carrier concentration above 10^{20} cm^{-3}. Taking into account the theoretical values of the bandgap energy (solid line) the carrier concentration of the layers is quite higher than expected, leading to a deviation from the theoretical values. This effect may be due

to the variation of the N/O ratio, which affects to the carrier concentration and also to the crystal quality, as also observed by Bhuiyan *et al*. [Bhu03a]. However, as related by Wu *et al.* [Wu03] this results, obtained from InN degenerated layers grown by sputtering, are in agreement with the theoretical values obtained taking into the Burnstein-Moss effect (black line). Besides, some results obtained from InN layers grown by MBE and MOVPE follows a similar deviation from the theoretical values, as observed in figure 7.11, probably affected by an unintentional dopping that does not directly affect the properties of the layers.

7.3 Conclusions

This chapter details the structural, morphological, electrical and optical properties of InN layers deposited on Si (100), Si (111) and sapphire, as a function of the growth temperature, from 20°C to 450°C obtaining the following conclusions:

- XRD measurements reveal InN wurtzite layers highly oriented with the *c*-axis without other crystallographic orientations for layers growth above 300°C. However, layers growth at room temperature shows other diffraction peaks such as InN (102) and (103) probably caused by the reduction of the kinetic energy.
- AFM measurements show an increase of the rms as a function of the growth temperature. Samples grown on silicon substrates present a similar values regardless the substrate orientation being both lower than for layers grown on sapphire.
- Hall Effect measurements reveal a high carrier concentration, above 10^{21} cm^{-3}, for the all the layers, probably induced by an unintentional doping by hydrogen or oxygen during the deposition.
- The optical properties of the layers show no clear differences for bandgap values as a function of the growth temperature (from 1.72 to 1.77). Besides, the high bandgap values in comparison with the theoretical ones (0.7 eV) are probably induced by the Burnstein-Moss effect.

Besides, the study of the In layers as a function of the power supply applied, from 20 W to 40 W, showing the following results:

- XRD measurements show InN layers with a wurtzite structure and highly oriented with the *c*-axis regardless the power supply applied with non-other crystallographic orientations.
- AFM measurements reveal a not clear trend of the RMS as a function of the In power supply. However, SEM images reveals the effect of applied high power supply to the In target, which leads to an evolution of the morphology from compact layers for 20W to a closely-columnar ones for layers grown under 30 and 40W. Besides, layers grown on sapphire are more compact than the ones grown on silicon, probably caused by the unintentional nitridation of the substrate before the InN deposition.
- Hall Effect measurements reveal a high carrier concentration, which increases from 4×10^{20} to 2×10^{21} cm^{-3}, for the all the layers, probably induced by an unintentional doping by hydrogen or oxygen during the deposition, leading to a Burstein-Moss effect in the bandgap energy.

Along this study, is has been demonstrated the feasibility to achieve InN layers deposited by RF sputtering on Si (100) with a similar quality than the obtained ones on Si (111), obtaining wurtzite layers and highly oriented along the *c*-axis regardless the substrate orientation.

Chapter 8

Growth of low-to-mid Al content $Al_xIn_{1-x}N$ on silicon by RF sputtering

This chapter is focused on the growth of low-to-mid Al content Al_xInN_{1-x} layers on silicon by RF sputtering for the development of AlInN on Si (100) devices.

Firstly we study the influence of the RF power applied to the Al target on the structural, morphological, electrical and optical properties of AlInN layers deposited at 300°C on Si (100) and (111) substrates in order to analyze the effect of the substrate orientation. Besides, the study of the AlInN layers grown on sapphire in order to analyze its electrical and optical properties. There are many studies of AlInN layers deposited on these substrates by MBE such as Cheng *et al.* [Che14] and also by RF sputtering, but they use plasma based on a mixture of Ar and N [Afz14, Afz15, Afz16, Yeh08, Don09, Guo03, Guo08]. Besides, despite there are studies of AlInN layers deposited on all the substrates, they do not include a comparison between samples deposited at the same run. In this study we perform an accurate analysis of the layers deposited in Si (100), Si (111) and sapphire substrates using pure nitrogen for the plasma generation.

Finally, we show the photoelectrical properties of devices based on the developed AlInN-on-Si structures with the aim to obtain the optimal deposition conditions for the devices.

8.1 Influence of the Al RF power

The $Al_xIn_{1-x}N$ layers studied in this chapter were grown using the RF sputtering described in Chapter 4 on the following substrates:

- 375-μm thick *p*-type doped Si (100) with a resistivity of 1−10 Ω·cm
- 500- μm thick *p*-type doped Si (111) with a resistivity of 1−10 Ω·cm

- 500- µm thick of (0001)-oriented sapphire substrates

Before the introduction in the deposition chamber, the substrates were chemically cleaned in organic solvents and after that, they were outgassed for 30 min at 400ºC and cooled down to the growth temperature. Besides, previously to the deposition, the targets and substrate were cleaned using plasma etching with Ar (99.999%). AlInN layers were deposited with a nitrogen flow of 14 sccm at a pressure of 0.47 Pa. The RF power applied to Al target, P_{Al}, was varied from 0 to 225 W, whereas the RF applied to In target, the temperature and the time of deposition were fixed to 30 W, 300ºC and 150 minutes, respectively. The value of P_{Al} used for each sample of the set is summarized in table 8.1.

Sample	P_{Al} (W)
S1	0
S2	100
S3	150
S4	175
S5	225

Table 8.1. Value of RF power applied to the Al target (P_{Al}) for each sample of the studied set.

8.1.1 Structural characterization

Figure 8.1 shows the HRXRD scan in 2θ/ω configuration of the $Al_xIn_{1-x}N$ layers grown on Si (100), Si (111) and sapphire (figures (a), (b) and (c), respectively). In all cases, the diffractograms show the diffraction peaks corresponding to the (0002) and (0004) reflections of $Al_xIn_{1-x}N$ and the ones related to the substrate. No other crystallographic orientations are detected, indicating that $Al_xIn_{1-x}N$ layers are well oriented with the *c*-axis aligned with the growth direction (perpendicular to the substrate). Moreover, within the studied range in P_{Al}, the AlInN material do not present any phase separation, as obtained in other studies of layers deposited under a pure nitrogen plasma carried out by our group [Nuñ17, Bla18]. However, as detailed by Chen *et al.* [Che14], AlInN layers with an Al mole fraction above 0.36 growth on silicon substrate by MBE present low crystal quality with other crystallographic orientations and even phase separations, this effect reduction of the crystal quality is related to the incorporation of aluminum as also related by Houchin *et al.* [Hou08] for AlInN layers grown by MOVPE. Besides, in some cases, the samples deposited under a plasma mixture of Ar and N shows phase separation probably caused by the increase of the kinetic energy [Afz14, Afz16, Don09].

The observation of higher order of diffraction peaks related to the $Al_xIn_{1-x}N$ layers growing on substrates with both hexagonal- and cubic-symmetry confirms the feasibly of the sputtering technique for the deposition of moderate quality crystalline $Al_xIn_{1-x}N$ layers with wurtzite structure despite the substrate orientation.

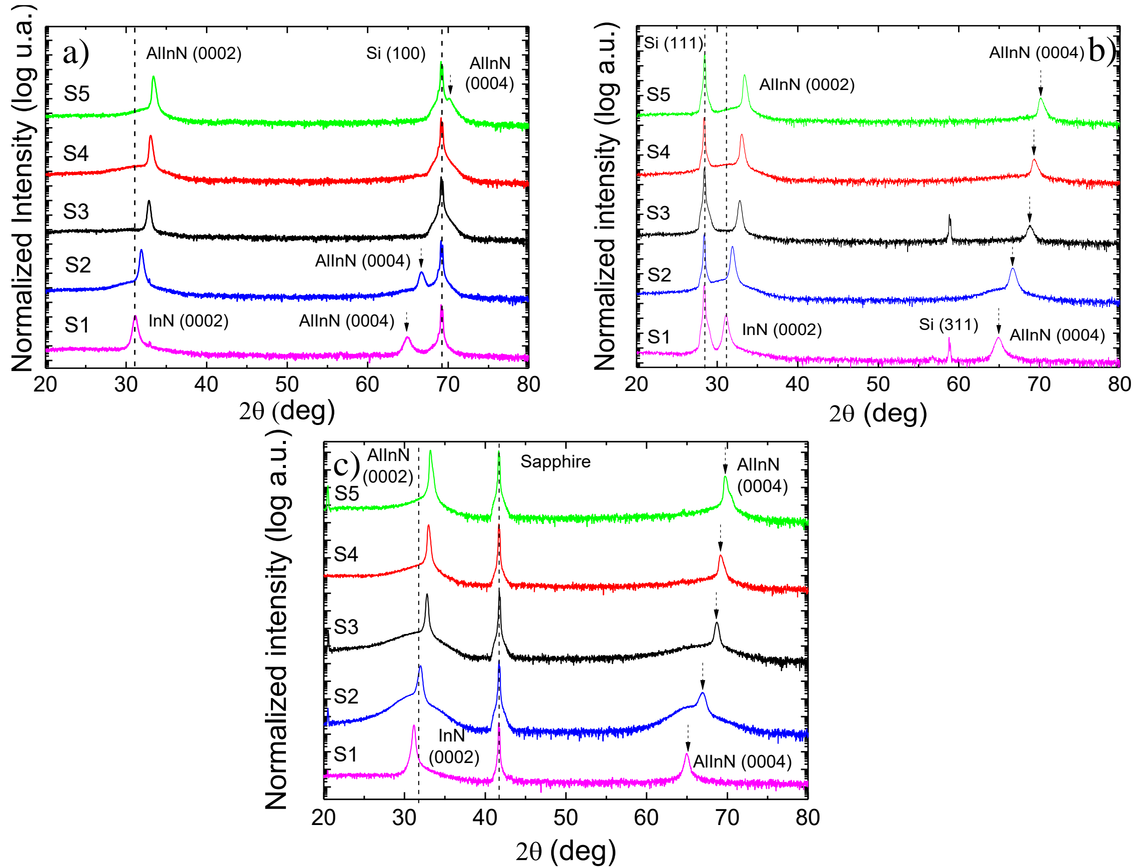

Figure. 8.1. 2θ/ω scans of the $Al_xIn_{1-x}N$ layers on a) Si (100), b) Si (111) and c) sapphire as a function of P_{Al} estimated from HRXRD measurements.

The (0002) reflection peak of the $Al_xIn_{1-x}N$ shifts towards the diffraction angle of relaxed AlN (2θ~36º) when increasing P_{Al}, pointing to a decrease of the *c*-lattice parameter from 5.73 Å for InN to 5.35 Å for $Al_xIn_{1-x}N$ deposited with P_{Al} = 225 W on both Si (100) and Si (111) substrates. Besides, it should be mentioned the existence of other diffraction peaks at in layers grown on Si (111) which corresponds with a Si (311) crystal orientation.

As explained in Chapter 5, the Al mole fraction of an alloy can be estimated from the measured *c*-lattice parameter and assuming fully relaxed layers and applying the Vegard's law to the estimated *c*-parameter of the layer. With this consideration, the Al mole fraction of the layers increases with P_{Al} from x = 0 to 0.49, 0.48 and 0.43 for $Al_xIn_{1-x}N$ layers on Si (100), Si (111) and sapphire, respectively, as displayed in figure 8.2. The error

introduced in the Al content estimation by the assumption of fully relaxed state of the layers has been stablished below 5%, taking into account results obtained by our group in samples deposited both in sapphire and Si (111) for samples with Al content in the range from 0 to 0.36 [Nuñ17]. The results from the structural characterization of the samples is summarized in tables 8.2, 8.3 and 8.4 for AlInN on Si (100), Si (111) and sapphire, respectively.

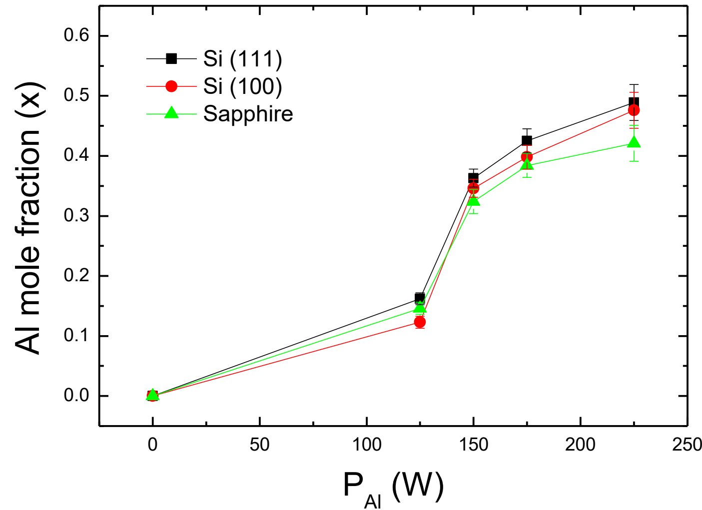

Figure 8.2. Evolution of the Al mole fraction as a function of the Al power supply during the growth of the samples deposited on Si (111), Si (100) and sapphire, assuming fully relaxed layers. The error bars were calculated taking into account the results obtained by Nuñez *et al.* [Nuñ17].

The FWHM of the ω-scan (rocking curve) of the (0002) AlInN diffraction peak gives information about the structural quality, *i. e.* the mosaicity, of the material. In this study, AlInN layers grown on Si substrates show similar values on substrates with both orientations, indicating that the structural quality is similar regardless the substrate orientation. However, the FWHM of the rocking curve of the (0002) diffraction peak of AlInN on both silicon substrates, remains almost constant showing values from 3 to 6 degrees without a clear trend, meanwhile, for layers grown on sapphire, it decreases with the Al content, probably attributed to an increase of the adatom mobility and thus, an enhancement of the crystal quality.

Besides, the layers deposited on sapphire show lower values than the ones deposited on silicon, the mosaicity in these samples is reduced showing a minimum value of 1.12º for $x = 0.43$. This value increases to 2.81° and 2.77° for AlInN layers grown on Si (100) and Si (111) respectively with the highest Al mole fraction in both substrates (see tables 8.2 to 8.4).

Furthermore, the samples grown on sapphire shows lower FWHM values of the rocking curve for each Al content. This effect is probably due to an unintentional deposition of an amorphous buffer layer onto both silicon substrates before the growth of the AlInN layer, as observed in previous studies carried out by this group [Nuñ18]. Besides, as related in chapter 7, Furtmayr *et al.* observed the unintentional nitridation on silicon (111) substrates which can produce nucleation sites and, thus changes the FWHM of the AlInN layer in comparison with sapphire substrate [Fur08].

Sample	Thickness (nm)	*c* (Å)	Estimated Al mole fraction *x*	FWHM rocking curve (º)
S1	393	5.733	0	4.64
S2	788	5.605	0.12	2.37
S3	648	5.452	0.35	6.19
S4	620	5.415	0.40	3.24
S5	906	5.358	0.48	2.77

Table 8.2. Summary of the structural analysis of $Al_xIn_{1-x}N$ on Si (100): layer thickness estimated from FESEM; *c*-axis parameter and Al mole fraction *x* extracted from HRXRD.

Sample	Thickness (nm)	*c* (Å)	Estimated Al mole fraction *x*	FWHM rocking curve (º)
S1	376	5.727	0	4.67
S2	783	5.587	0.16	2.98
S3	641	5.440	0.36	6.13
S4	631	5.396	0.42	3.05
S5	585	5.349	0.49	2.81

Table 8.3. Summary of the structural analysis of $Al_xIn_{1-x}N$ on Si (111): layer thickness estimated from FESEM; *c*-axis parameter and Al mole fraction *x* extracted from HRXRD.

Sample	Thickness (nm)	*c* (Å)	Estimated Al mole fraction *x*	FWHM rocking curve (º)
S1	247	5.734	0	1.87
S2	--	5.600	0.14	1.90
S3	322	5.469	0.32	1.37
S4	357	5.430	0.38	1.40
S5	564	5.391	0.43	1.12

Table 8.4. Summary of the structural analysis of $Al_xIn_{1-x}N$ on sapphire layer thickness estimated from FESEM; *c*-axis parameter and Al mole fraction *x* extracted from HRXRD. The thickness of sample S2 has not been calculated since the sample has no SEM measurements.

As observed in tables 8.2, 8.3 and 8.4, the *c* lattice parameter of the nitride layers decreases with P_{Al} as expected, taking into account that the lattice parameter of the AlN (~ 4.99 Å) is lower than the InN (~ 5.703 Å). The evolution of the lattice parameters in all substrates is shown in figure 8.3.

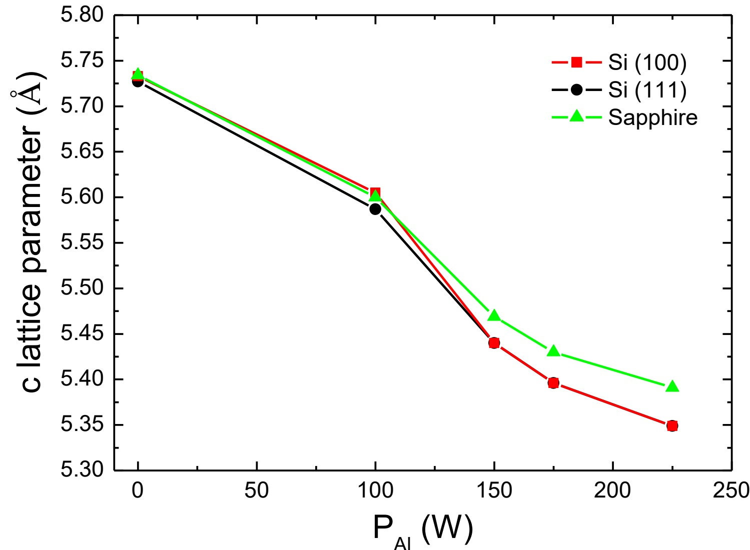

Figure 8.3. Evolution of the *c* lattice parameter as a function of the aluminum power supply.

8.1.2 Morphological characterization

The morphology of the layers evolves from closely-packed nanocolumns for InN towards compact ones when increasing the Al mole fraction up to x = 0.48-0.49, growing on Si, as displayed in FESEM images of figures 8.4(a), (b) and (c), respectively. We observe that this behavior is similar for AlInN layers deposited on both Si (100) and Si (111) substrates. The nanocolumnar morphology of the InN layer is usually attributed to the nitride growth under N-rich conditions [Aza18, Gra05]. Furthermore, the evolution to compact layers, could be supported by the increasing of the III/V ratio during growth, as observed in previous studies carried out by this group [Nuñ16]. This increase of the available metal ions to be incorporated to the layer is confirmed by the growth rate, obtained from FESEM images, which varies from 131 to 226 nm/h for silicon substrates.

However, the samples deposited on sapphire substrates show compact morphology over the whole studied range of P_{Al}. The different behavior between the layers grown on sapphire substrate and the ones grown on silicon can be due to the aforementioned initial nitridation of the silicon substrates, which can leads to a columnar morphology, as observed by Furtmayr *et al.* [Fur08] in GaN layers grown on Si (111).

Furthermore, from SEM images the thickness of the layers and thus, the growth rate, was estimated obtaining the results shown in figure 8.5, revealing a similar trend for both silicon substrates. The growth rate of the layers reveals a linear increase for low-to-mid-power applied (below 175W), meanwhile this trend increases for the sample growth under 225W of Al power supply, probably affected by a change in its morphology, which is more compact than the deposited at lower power supply.

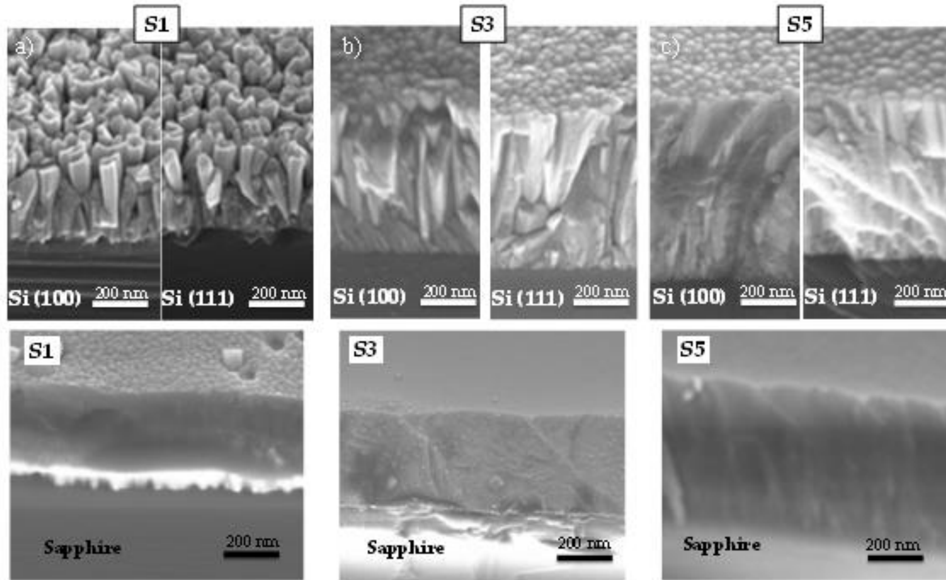

Figure 8.4. FESEM images of samples a) S1, b) S3 and c) S5 on Si (100) (top left), Si (111) (top right) and sapphire (down).

Figure 8.5 shows the 2×2 μm^2 AFM measurements of samples S1 (a), S3 (b) and S5 (c) on Si (100) (top), Si (111) (middle) and sapphire (bottom). We observe a clear reduction of the superficial features when increasing Al mole fractions, being similar for both substrates. The root mean square (rms) surface roughness of the layers was obtained from the average of AFM images taken on 1×1, 2×2 and 5×5 μm^2 surface areas.

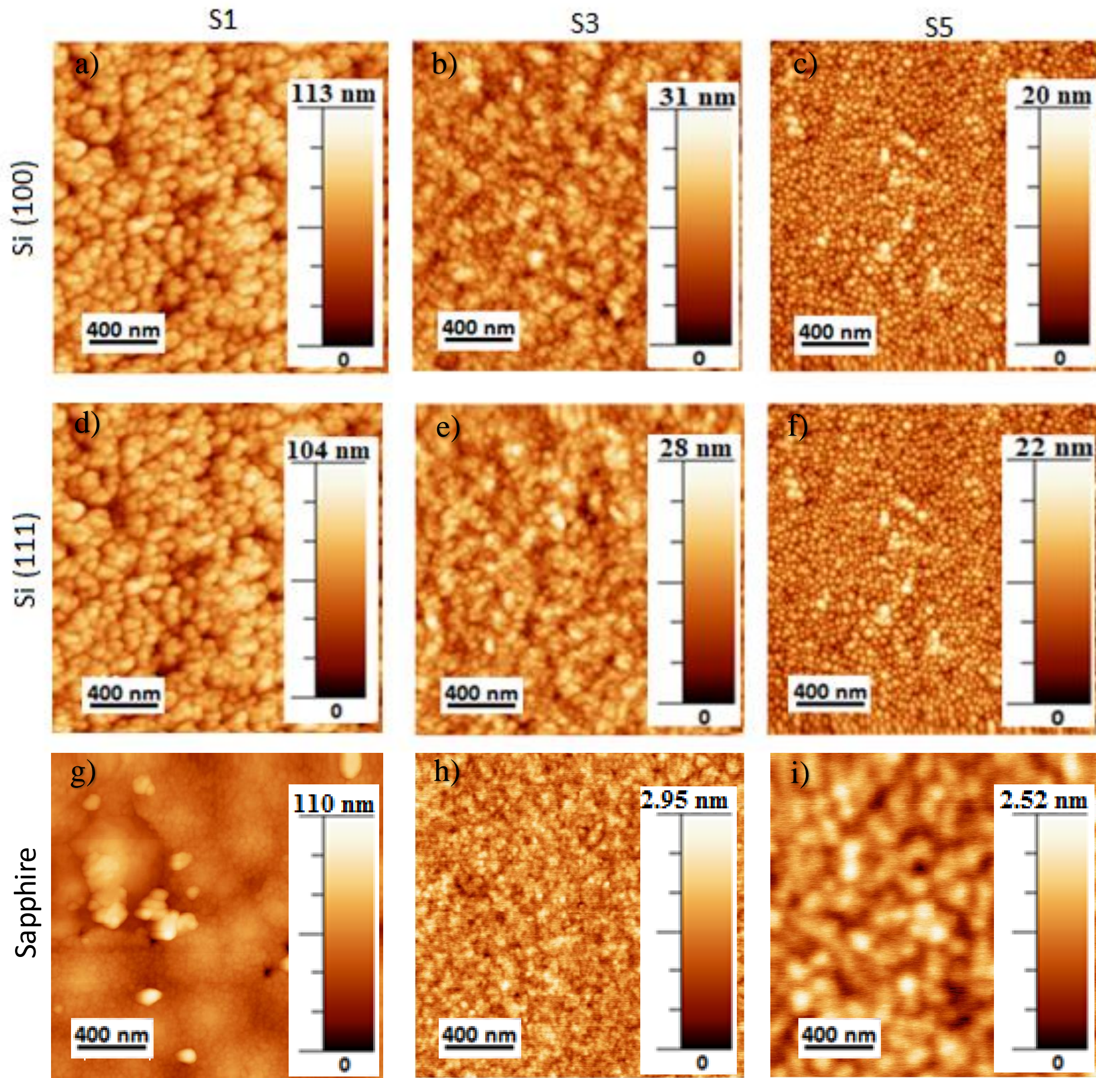

Figure 8.5. a) Variation of the rms surface roughness of $Al_xIn_{1-x}N$ layers as a function of the aluminum power supply; AFM images of InN, $Al_xIn_{1-x}N$, P_{Al} = 150W and $Al_xIn_{1-x}N$, P_{Al} = 225W grown on Si (100) (a, b and c), on Si (111) (d, e and f) and on sapphire (g, h and i).

A decrease of the rms is observed from 12.5 and 11.5 to 2.5 and 0.4 nm for silicon and sapphire substrates respectively with the increase of P_{Al} from 0 to 150 W (table 8.5) as observed in previously studies [Nuñ16] meanwhile it remains almost constant when the P_{Al} varies from 150 to 225 W. The observed reduction of the rms is associated to the observed change of morphology pointed out by the FESEM images shown in Figure 8.4.

	Rms surface roughness (nm)		
Sample	**Si (100)**	**Si (111)**	**Sapphire**
S1	11.6	12.8	11.2
S2	9.3	7.9	3.0
S3	3.5	3.6	0.4
S4	3.6	3.7	0.4
S5	2.4	2.6	0.37

Table 8.5. Evolution of the root mean square as a function of the Al power supply.

The evolution of the rms surface roughness and the FESEM images reveals similar trend in both silicon substrates demonstrating the possibility to produce moderate-quality low-to-mid Al content AlInN layers on Si by RF sputtering for substrates with different crystal orientations.

8.1.3 Electrical characterization

Hall Effect measurements at room temperature were performed in $Al_xIn_{1-x}N$ layers grown on sapphire, which summary is presented in table 8.6. The layer resistivity increases from 0.38 mΩ·cm for InN to 8 mΩ·cm for $Al_{0.32}In_{0.68}N$, while the carrier concentration decreases from 1.73×10^{21} for InN to 2.48×10^{20} cm^{-3} for $Al_{0.32}In_{0.68}N$, respectively. This effect is related to an increase of the bandgap energy with the incorporation of Al in the samples. The values of resistivity and mobility for the $Al_{0.32}In_{0.68}N$ layer (8 mΩ·cm and 3.1 $cm^2/V\cdot s$) are close to the ones obtained by Liu *et al.* of 1.2 mΩ·cm 11.4 $cm^2/V\cdot s$ for $Al_{0.28}In_{0.72}N$ layers. The high carrier concentration of the samples has been related to an unintentional doping during the growth by several sources like hydrogen and oxygen impurities or nitrogen vacancies as observed [Wu09, Dar10]. This unintentional doping has been also observed by Nuñez *et al.* [Nuñ17] obtaining a homogeneously O distribution of ~4% in similar AlInN layers grown on sapphire.

Sample	Al mole fraction (*x*)	Resistivity (mΩ·cm)	Carrier concentration (cm^{-3})	Mobility ($cm^2/V\cdot s$)
S1	0	0.38	1.73×10^{21}	9.5
S2	0.14	0.58	9.42×10^{20}	11.5
S3	0.32	8.00	2.48×10^{20}	3.2

Table 8.6. Summary of the electrical characterization of the $Al_xIn_{1-x}N$ samples grown on sapphire obtained by Hall Effect measurements.

Samples with Al mole fractions above 0.32 show a resistivity above 10 mΩ·cm, hindering the possibility of performing reliable Hall Effect measurement with the employed system. Figure 8.6 shows a comparison between the obtained results and the ones from Nuñez *et al.* [Nuñ17] for samples with similar Al content showing a similar trend for both studies.

Considering this trend, represented in figure 8.6 (dashed lines), the resistivity and carrier concentration were estimated for the samples with $x = 0.38$ an d 0.43, represented with circles in figure 8.6, obtaining carrier concentration values of 1.4×10^{20} and 6.7×10^{19} cm^{-3} and resistivity of 23.8 and 43.7 mΩ·cm, respectively.

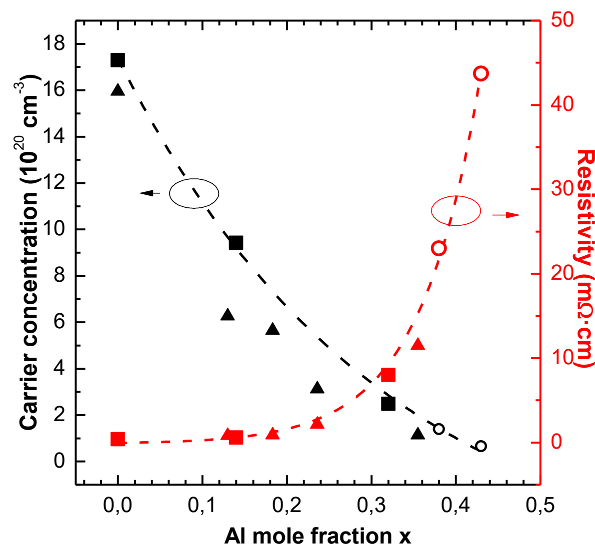

Figure 8.6. Evolution of the carrier concentration and resistivity as a function of the Al mole fraction (squares) and comparison with obtained by Nuñez *et al.* [Nuñ17] (triangles). Open circles show the expected value for samples with an Al mole fraction above 0.38.

8.1.4 Optical characterization

Transmittance measurements

The optical properties of the layers were evaluated by transmittance measurements performed on AlInN on sapphire samples depicted in the inset of figure 8.7 (a) and by photoluminescence of AlInN on Si (100), Si (111) and sapphire samples shown in figure 8.8. Figure 8.7 (a) shows the evolution of the squared absorption coefficient with the Al content. The absorption coefficient as a function of the wavelength α(λ) was estimated from transmission spectra considering the Beer-Lambert law and neglecting the optical scattering and reflection losses in sample surfaces, as explained in previous chapters.

The bandgap energy obtained from the α^2 vs E plot increases, as expected, with the Al mole fraction. Concretely, the bandgap energy varies from 1.73 eV for the InN sample (S1) to 2.56 eV for the $Al_{0.43}In_{0.57}N$ (S5) (see table 8.7).

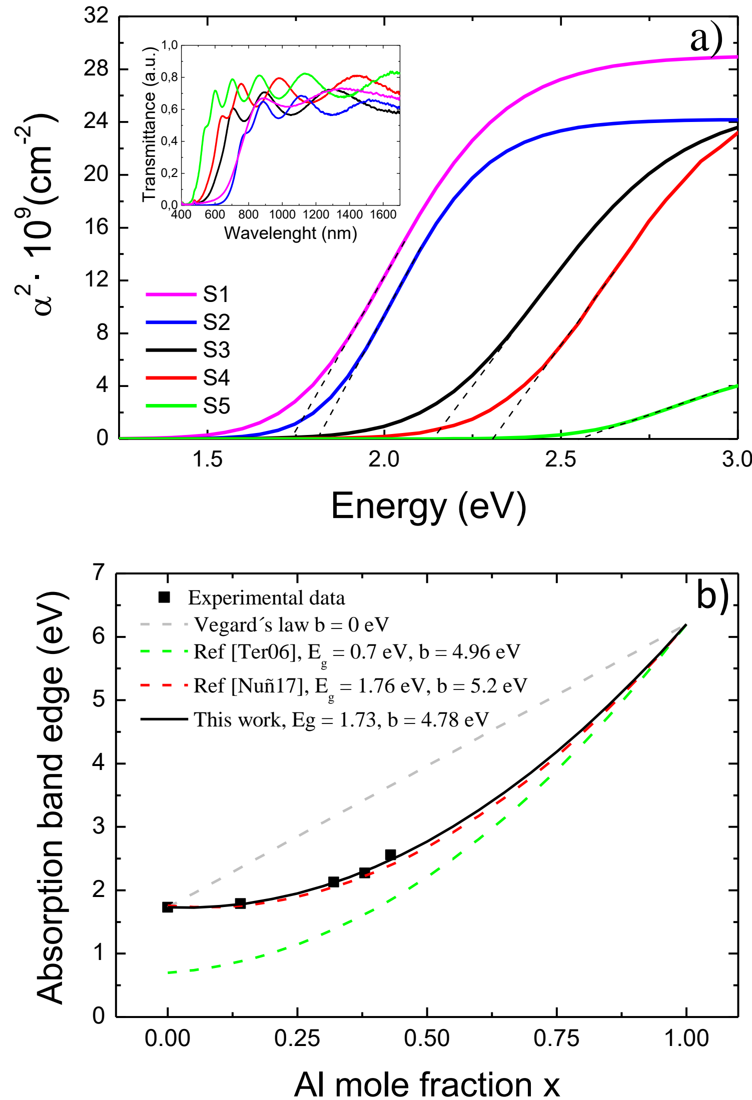

Figure 8.7. a) Squared absorption coefficient vs energy and transmittance of the $Al_xIn_{1-x}N$ layers grown on sapphire vs wavelength (inset) and b)The bandgap energy of $Al_xIn_{1-x}N$ as a function of the Al composition and the comparison with the bowing parameters obtained with this study (black line), other study using the sputtering technique by Nuñez *et al.* (red line) [Nuñ17] and a bowing parameter using the bandgap of a pure InN growth by MBE (green line) [Ter06].

Besides, the evolution of the bandgap energy as a function of the Al mole fraction is shown in figure 8.7 b), with a comparison between the results obtained in this study, the experimental data obtained by Nuñez et al. in layers deposited by RF sputtering under different conditions [Nuñ17] and samples grown by MBE showing low residual carrier concentration (in the range of 10^{18} cm^{-3}) [Ter06]. As it is observed, the samples deposited

by RF sputtering show higher bandgap energy for AlInN layers with low Al mole fraction in comparison with MBE layers, this difference can be explained by the Burnstein-Moss effect which it is expected to be reduced when increasing the Al content due to the reduction of the carrier concentration with the Al mole fraction.

	Eg (eV)	**ΔE(meV)**
S1	1.73	160
S2	1.79	117
S3	2.13	214
S4	2.27	207
S5	2.56	176

Table 8.7. Summary of optical properties obtained by transmittance measurements.

Photoluminescence measurements

Figure 8.8 displays the photoluminescence spectra obtained at low temperature of layers with an Al mole fraction below 0.36, showing a blue shift of the PL emission energy when increasing the Al content of the layer. No PL emission is detected for layers with a mole fraction above 0.36. It should be mentioned that, along the measurements a PL emission of an MBE sample, usually used to calibrate the system was measured and marked with dashed lines.

The FWHM of the photoluminescence measurements varies from 390 to 510 meV, which are similar values to the previously obtained by this group [Nuñ17]. Besides, the value of the PL emission peak and the absorption edge energy calculated previously from transmission measurements shifts from ~130 meV for S1 layer to ~330 meV for S3, these results are in agreement with Jiang *et al.* [Jia09] who assign the origin of this emission to recombination centers caused by impurities or defects in the layer. It should be pointed out that all samples show PL emission at room temperature.

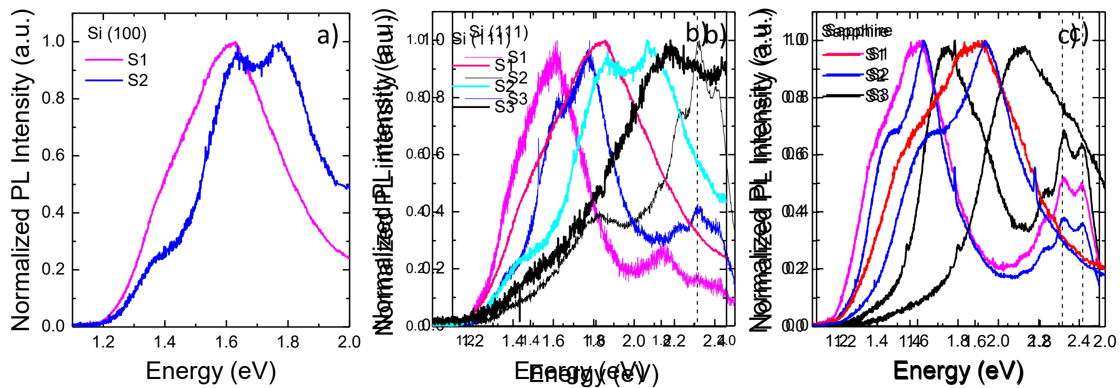

Figure 8.8. Normalized low-temperature (10 K) PL emission of the $Al_xIn_{1-x}N$ on a) Si (100) b) Si (111) and c) sapphire substrates. For $x > 0.36$ no PL emission was observed.

In order to investigate the origin of the luminescence, a study of the thermal evolution of the energy of the PL peak was carried out in layers grown on sapphire. In that sense, Figure 8.9 shows the evolution of the photoluminescence emission as a function of the temperature of the InN layer (S1)

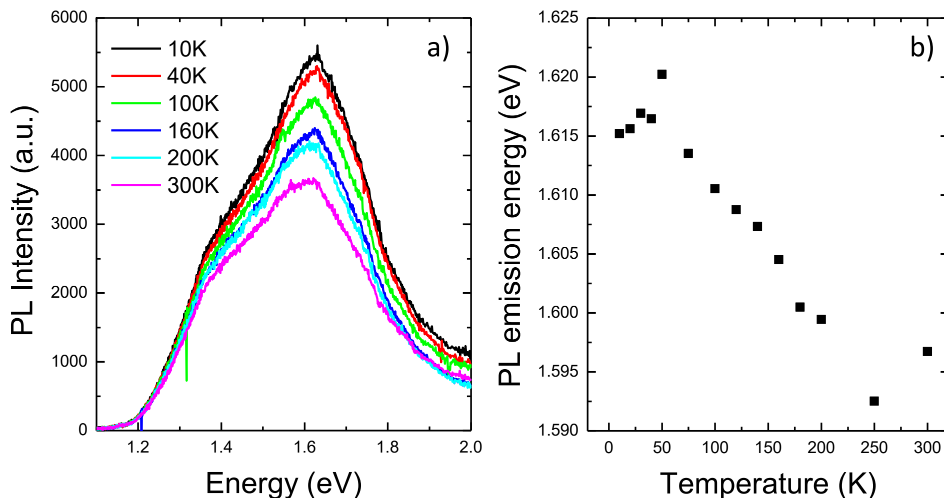

Figure 8.9. a) Photoluminescence spectra of InN layer grown on sapphire as a function of the temperature and b) its evolution of the PL emission energy vs the temperature.

As it is observed in figure 8.9 a), the PL intensity of the InN layer decreases a factor 1.5 when the temperature increases from 10 K to 300 K, caused by the activation of non-radiative recombination processes. Besides this, the evolution of the PL intensity of the layers grown on sapphire as a function of the temperature was carried out, in order to obtain the activation energy of the layers, obtaining the results showed in figure 8.10.

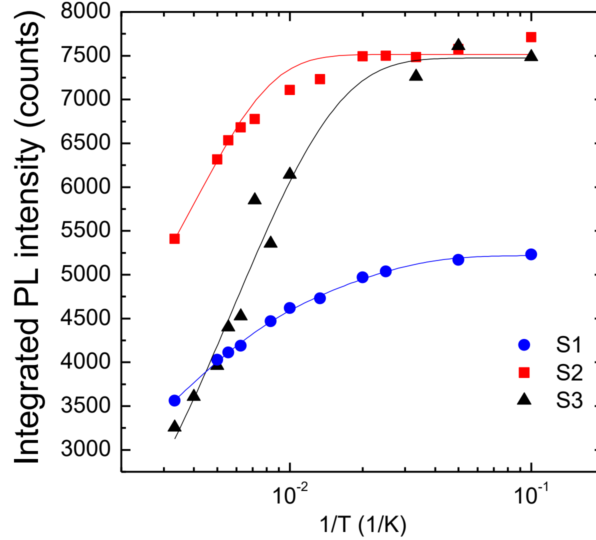

Figure 8.10. Evolution of the integrated PL intensity as a function of the temperature of samples (S1, S2 and S3) grown on sapphire.

As explained in chapter 5, the evolution of the integrated PL emission can be described considering non-radiative recombination channel. The solid lines of the figure 8.10 shows the fit of the experimental data to equation 5.6 $\left[I(T) = \frac{I\,(T=0)}{1+a\cdot e^{-\frac{E_a}{k_B T}}}\right]$. Through this equation the activation energy of the samples was obtained, with values of 50 ± 30 meV for S1, 36 ± 12 meV for S2 and 42 ± 18 meV for S3. The activation energy of the InN layer is similar to the obtained by Nuñez *et al.* [Nuñ17]. In that sense, the impurities which can affects the emission are mainly oxygen, hydrogen or nitrogen-related impurities [Wu09, Dar10].

8.2 Conclusions

The study of the properties of AlInN layers deposited on Si (100), Si (111) and sapphire, as a function of the Al mole fraction shows:

- The feasibility to growth polycrystalline wurtzite AlInN layers highly oriented with the growth direction in the *c*-axis on silicon, regardless the substrate orientation.
- The Al mole fraction of the alloy can be controlled with the aluminum power supply applied during the growth process regardless the substrate, reaching values from $x = 0$ to $x \sim 0.5$ when the PAl increases from 0 to 225 W.

- The layers morphology on Si (100) and Si (111) evolves from a closely-packed columnar to compact layers when the Al mole fraction increases. Besides, the layers show similar compactness and surface roughness. Meanwhile, the layers deposited on sapphire substrates present compact layers regardless the Al mole fraction and a lower rms than the samples grown on silicon.

- Hall Effect measurements reveals a high carrier concentration, above 10^{20} cm^{-3}, for the layers with an Al mole fraction below 0.36, probably induced by an unintentional doping by hydrogen or oxygen during the deposition.

- The optical properties of the layers show an evolution of the band gap energy from 1.75 to 2.56 eV as a function of the Al mole fraction, Besides, PL measurements reveals a blue shift of the PL emission when increasing the Al content and an activation energy of 50 ,36 and 42 meV for InN, $Al_{0.14}In_{0.86}N$ and $Al_{0.32}In_{0.68}N$ respectively.

Along this study, it has been demonstrated the feasibility to achieve AlInN layers deposited by RF sputtering on Si (100) with a similar quality than the obtained ones on Si (111), allowing to study the photovoltaic applications of the AlInN/Si heterostructure considering both substrate orientations.

Chapter 9

AlInN on Si heterojunctions: effect of deposition temperature

In this chapter we study the structural, morphological, electrical and optical properties of AlInN layers with mid-Al contents and the photoelectrical properties of the devices as a function of the growth temperature. In that sense, in order to analyze the effect of the deposition temperature, three different growth temperatures were selected: 550ºC, 300ºC and room temperature. One of the objectives of this study is to analyze the quality of the devices as a function of the growth temperature, in order to develop AlInN layers on plastic materials or even on hydrogenated amorphous silicon layers (a-Si:H) creating a HIT structure (see chapter 3), which requires low temperature deposition.

As in previous chapters, there are some studies of AlInN layers grown at different temperatures using other deposition techniques, such as MBE and MOCVD [Han10, Jam08, Udd12, Wan10] and also by the sputtering technique [Afz16, Jia08, Jia09, Nuñ17, Nuñ19] these studies are mostly done on Si (111) substrates, and there are not so many studies about the comparison of the deposition temperature on both silicon (111) and (100) substrates in order to see the effect of the growth temperature on different structures. Besides, inasmuch as the AlInN is a novel material in the solar cell community, there are only few studies of solar cells based on AlInN on Si heterojunctions, mainly developed by the group of Liu *et al.* [Liu12] and our group [Val18, Nuñ18].

9.1. Material deposition and characterization

The $Al_xIn_{1-x}N$ samples used were deposited, as in previous studies, on *p*-type doped 300-µm-thick Si (100) with a resistivity of 1−10 Ω·cm, and on *p*-type doped 500-µm-thick Si (111) with a resistivity of 10–100 Ω·cm with the reactive RF sputtering system described in chapter 4. The deposition procedure is the same as the one for the samples described in chapter 7 and 8. However, in this study, the RF power applied to the Al and In targets was fixed at 150 W and 30 W, respectively; while the growth temperature was varied between 20, 300 and 550ºC for samples L1, L2 and L3, respectively (see description in table 9.1). The deposition time, 75 min approximately, was calculated to obtain a thickness of the AlInN layers of ~90 nm.

Sample	Temperature (°C)
L1	20
L2	300
L3	550

Table 9.1. Summary of the deposition conditions of the AlInN samples vs the substrate temperature.

9.1.1 Structural characterization

HRXRD scans in 2θ/ω configuration of the $Al_xIn_{1-x}N$ layers grown on Si (100) and on Si (111) are shown in figure 9.1 (a) and (b) respectively. Both set of samples present the diffraction peaks corresponding to the (0002) and (0004) of the $Al_xIn_{1-x}N$ and the related ones with the substrate. No other diffraction peaks are observed, inasmuch as the peak at 58 degrees is related to the substrate (Si (311)), indicating that the $Al_xIn_{1-x}N$ layers are well oriented with the *c*-axis aligned with the growth direction (perpendicular to the substrate) and with non-phase separation. Besides, the AlInN diffraction peak does not change with the deposition temperature, revealing a similar alloy composition for all the samples regardless the substrate orientation.

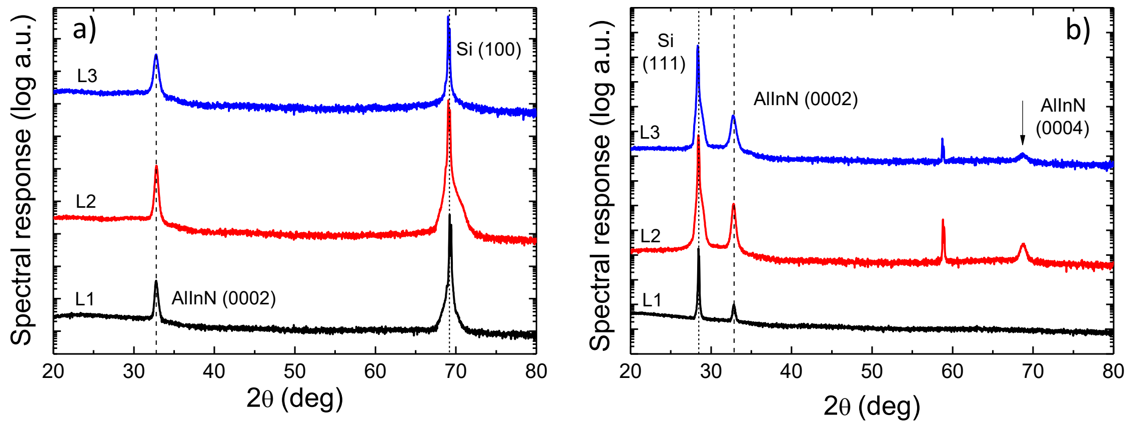

Figure 9.1. 2θ/ω scans of the $Al_xIn_{1-x}N$ layers on a) Si (100) and b) Si (111).

The Al mole fraction (x) of the AlInN layers was obtained using Vegard´s law and assuming fully relaxed layers. Data are sumarized in tables 9.2 and 9.3 for AlInN on Si (100) and Si (111), respectively. These values reveal an Al mole fractions from 0.31 to 0.36 (see tables 9.2 and 9.3), showing similar valyes for both silicon substrates regardless the orientation, as already observed in the studies carried out in previous chapters.

On the other hand, the FWHM of the rocking curve of AlInN layers deposited at room temperature show values ~6.5º. Concretely, the mosaicity of the layers is reduced when increasing the temperature up to 300°C (~4.5º) probably due to the higher adatom mobility. However, the mosaicity of the layers slightly degenerates again when reaching 550°C, maybe due to by an excess of the adatom mobility.

Sample	**Al mole fraction (x)**	**FWHM rocking curve (°)**
L1	0.36	6.27
L2	0.36	4.33
L3	0.37	6.10

Table 9.2. Summary of the structural analysis of $Al_xIn_{1-x}N$ on Si (100) layers.

Sample	**Al mole fraction (x)**	**FWHM rocking curve (°)**
L1	0.31	6.76
L2	0.35	4.54
L3	0.35	5.60

Table 9.3. Summary of the structural analysis of $Al_xIn_{1-x}N$ on Si (111) layers.

Finally, there are not clearly differences on the FWHM of the 2θ diffraction peak of the AlInN, which shows values between 0.28 to 0.33º, indicating similar grain sizes and thus probably a similar morphology of the layers regardless the growth temperature.

9.1.2 Morphological characterization

Atomic force microscopy measurements of the samples reveal an increase of the z-scale as a function of the substrate temperature in both silicon substrates, as displayed in figure 9.2. The rms surface roughness obtained from the average of AFM images taken on 1×1, 2×2 and 5×5 μm^2 surface areas, shows an increase from 0.91 nm and 1.2 nm for samples deposited at room temperature to 2.23 nm and 2.58 nm for layers deposited at 550°C, for Si (111) and Si (100), respectively (see figure 9.3).

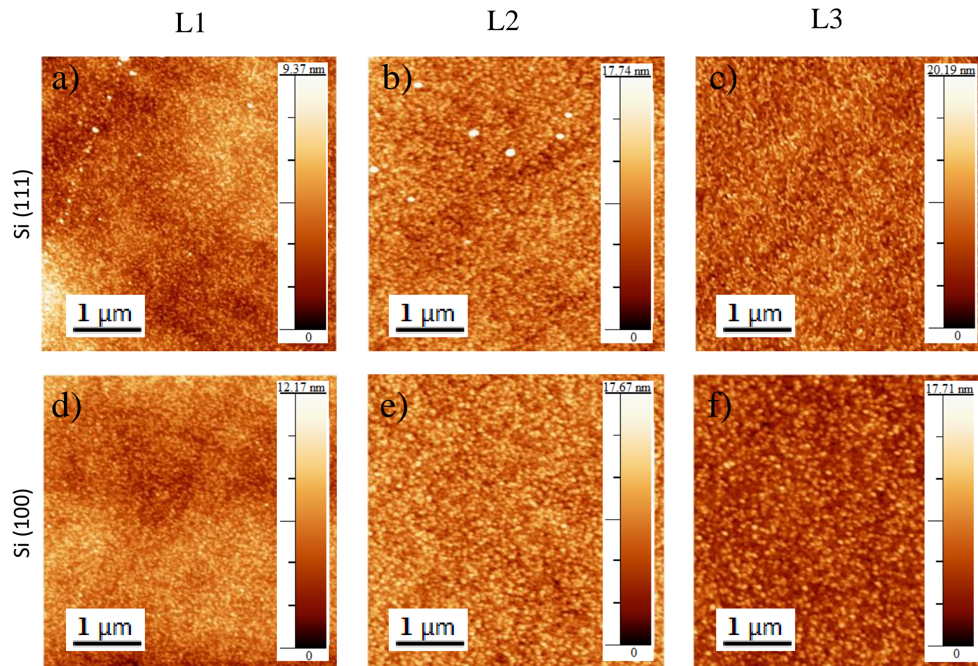

Figure 9.2. 5×5 μm^2 AFM images of of $Al_xIn_{1-x}N$ layers deposited on Si (111) and Si (100) at RT (a,d), 300°C (b,e) and 550°C (c,f).

This increase of the rms surface roughness, which has been also observed by Afzal *et al* [Afz16] and by previous studies developed by our group [Nuñ19], is probably associated to an increase of the kinetic energy with the growth temperature, which leads to an increase of the mobility of the sputtered atoms. Besides, as described by Nuñez *et al.* [Nuñ19] these results are accompanied with a similar closely-packed columnar morphology regardless the growth temperature.

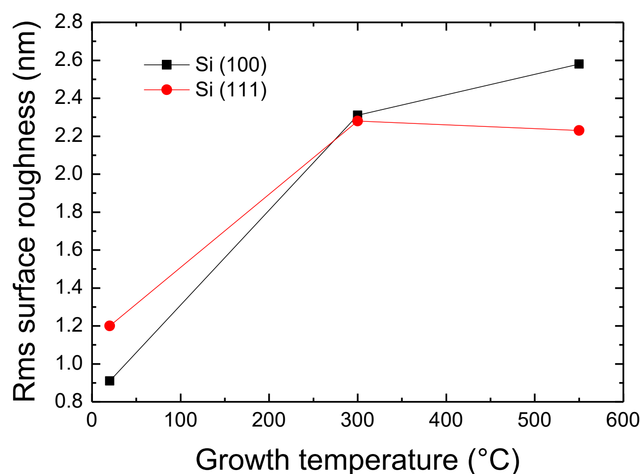

Figure 9.3. Evolution of the rms surface roughness of the AlInN on Si (111) and Si (100) layers as a function of the growth temperature.

9.1.3 Electrical characterization

The electrical properties of the layers were analyzed on AlInN deposited on sapphire substrates using Hall Effect measurements at room temperature. Results reveal an increase of the carrier concentration from 1.8×10^{17} to 1.0×10^{21} cm^{-3} and a decrease of the resistivity from 23.9 to 0.5 mΩ·cm when the growth temperature rises from 20 to 550ºC, as shown in table 9.4. The mobility of the layers varies similarly to the FWHM of the rocking curve, which may indicate that the structural improvement of the layers deposited at 300 ºC directly affects the mobility of the carriers, due to a reduction of defects in the crystalline structure. Besides, as observed in previous studies, the AlInN layers deposited at 300 ºC and above present a high carrier concentration, probably affected by the aforementioned unintentional doping caused by several sources like hydrogen and oxygen impurities [Wu09, Dar10] or nitrogen vacancies [Dar09].

Sample	Resistivity (mΩ·cm)	Carrier concentration (cm^{-3})	Mobility ($cm^2/V{\cdot}s$)
L1	23.9	1.8×10^{17}	1.5
L2	7.1	8.0×10^{19}	4.9
L3	0.5	1.0×10^{21}	1.3

Table 9.4. Summary of the electrical properties of $Al_xIn_{1-x}N$ on sapphire samples.

9.1.4 Optical characterization

As stated in previous chapters, the absorption coefficient α(λ) was obtained from transmittance measurements as a function of the wavelength considering the Beer-Lambert law and neglecting the optical scattering and reflection losses in sample surfaces. However, since the samples are relatively thin, the estimation of the bandgap energy by this method is not entirely adequate, inasmuch as the results are quite overestimated.

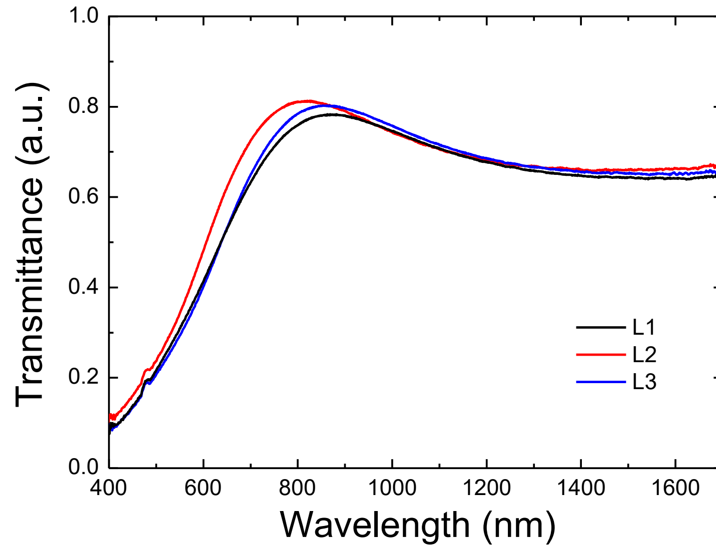

Figure 9.4. Transmittance of the $Al_xIn_{1-x}N$ layers grown on sapphire vs the deposition temperature.

In that sense, the results from theses layers were compared with the ones obtained for thicker layers (above 350 nm) deposited under the same conditions (see table 9.6). The band-gap energy obtained from transmittance measurements of thicker layers is almost constant, obtaining values around 2.1 eV. This effect is also observed in the transmittance measurements of samples L1-L3 displayed in figure 9.4, which shows no clear difference between the samples as detailed in table 9.5.

Sample	**E_g (eV) (this work) (~90 nm)**	**E_g (eV) (~550 nm)**	**ΔE (meV)**
L1	2.11	2.08	298
L2	2.15	2.13	356
L3	2.12	2.10	322

Table 9.5. Summary of the optical properties of $Al_xIn_{1-x}N$ on sapphire layers obtained from this work (~ 90 nm) and for thicker layers (~ 550 nm) vs the growth temperature.

These studies reveals the similar structural and optical properties of the AlInN layers grown on silicon (111) and (100) substrates regardless the deposition temperature, indicating the possibility to develop devices in the low temperatures regime with a low doping level. In that sense, doping AlInN layers grown at low temperatures can lead to obtain layers of similar characteristics and to be able to develop devices with a high concentration of carriers on plastic and organic substrates.

9.2 Effect of deposition temperature on AlInN on Si devices

As it was explained in previous section, the modification of the growth temperature entails a variation of the structural, morphological, electrical and optical properties of the AlInN layers. However, we do not know how these variations affect the electrical properties of the AlInN on silicon heterojunction.

In order to access to the junction, AlInN on Si structures were processed into solar cell devices were fully developed using the sputtering system, in which, the upper and lower contacts were deposited according to the procedure described in chapter 5 (section 5.5). The area of the devices is detailed in tables 9.6 and 9.7.

Devices were and characterized by current density-voltage (J-V) curves carried out in dark and under standard illumination at 25ºC. In that sense, dark measurements were recorded with a four-point probe station, whereas measurements under illumination were performed using a halogen lamp. With this lamp, the input energy which reaches the devices is approximately 0.002 W/cm^2.

9.2.1 Dark current-voltage curves

Current density-voltage measurements under dark are plotted in figure 9.5 (a) and (b) for AlInN on Si (100) and Si (111) as a function of the deposition temperature respectively. The analysis of these curves was carried out using the one-diode model, described in chapter 3.

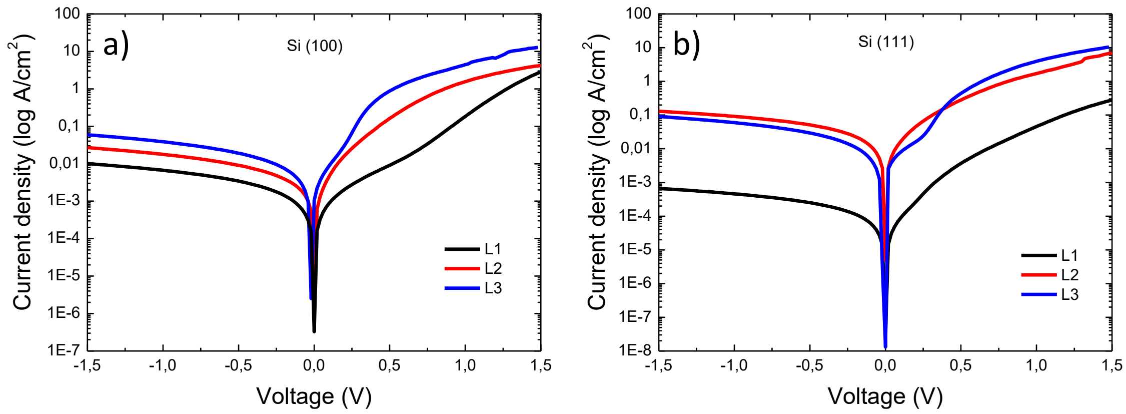

Figure 9.5. Dark current density vs voltage curves of AlInN devices deposited on a) Si (100) and b) Si (111) as a function of the deposition temperature.

The results of the analysis through this model are shown in tables 9.6 and 9.7 for devices based on AlInN on Si (100) and Si (111), respectively.

Both tables show similar values of the shunt resistance (R_{sh}), for AlInN devices silicon (100) and Si (111) respectively, in the order of ~ 490-650 kΩ × cm^2, without a clear trend, showing the highest values for layers grown at 300°C, probably due to an improvement of the quality of the AlInN. The serial resistance (R_s) decreases, from 36.4 to 5.6 Ω × cm^2 and from 11.8 to 3.7 Ω × cm^2 for Si (100) and Si (111) respectively, which means that the contact resistivity and the carrier mobility along the heterojunction improves with the deposition temperature. However this values are much higher than the obtained ones for a typical silicon solar cell (below 1.5 Ω × cm^2) [Bor16]. Finally, the dark saturation current (J_0) varies independently of the growth temperature, showing the lowest values for the layers grown at room temperature, probably affected by the resistivity of the layer and its low carrier concentration.

Sample	Area (cm^2)	R_s (Ω ·cm^2)	R_{sh} (kΩ · cm^2)	J_0 (µA/cm^2)	η	V_{oc} (V)	J_{sc} (mA/cm^2)	FF (%)
L1	0.66	36.4	562	7.8	6.2	0.19	0.22	12
L2	0.58	6.9	645	23	4.7	0.15	0.68	16
L3	0.7	5.3	487	64	3.6	0.23	0.56	35

Table 9.6. Summary of electrical properties of devices based on AlInN deposited on Si (100). * The area was calculated taking into account the shadow of the top contact (~ 0.13cm^2).

Sample	Area * (cm^2)	R_s ($\Omega \cdot cm^2$)	R_{sh} ($k\Omega \cdot cm^2$)	J_0 ($\mu A/cm^2$)	η	V_{oc} (V)	J_{sc} (mA/cm^2)	FF (%)
L1	0.59	11.8	511	0.64	5.9	0.28	0.35	22
L2	0.63	9.4	636	110	3.4	0.13	0.58	17
L3	0.6	3.7	561	82	4.6	0.29	0.60	37

Table 9.7. Summary of electrical properties of devices based on AlInN deposited on Si (111). The area was calculated taking into account the shadow of the top contact (~ $0.13cm^2$).

9.2.2 Current-voltage curves under illumination

Figure 9.6 shows the current density-voltage curves measured under illumination with a conventional halogen lamp with an optical power of P_{in} = 2 mW/cm^2, which would correspond to ~ 0.02 sun if the spectral response of the lamp would be the same as the one of a solar simulator AM1.5G.

From the analysis of these curves concerning the V_{oc}, J_{sc} and FF summarized in tables 9.6 and 9.7, we see an improvement of the FF up to 35% and 37% when increasing the deposition temperature to 550ºC on both substrates.

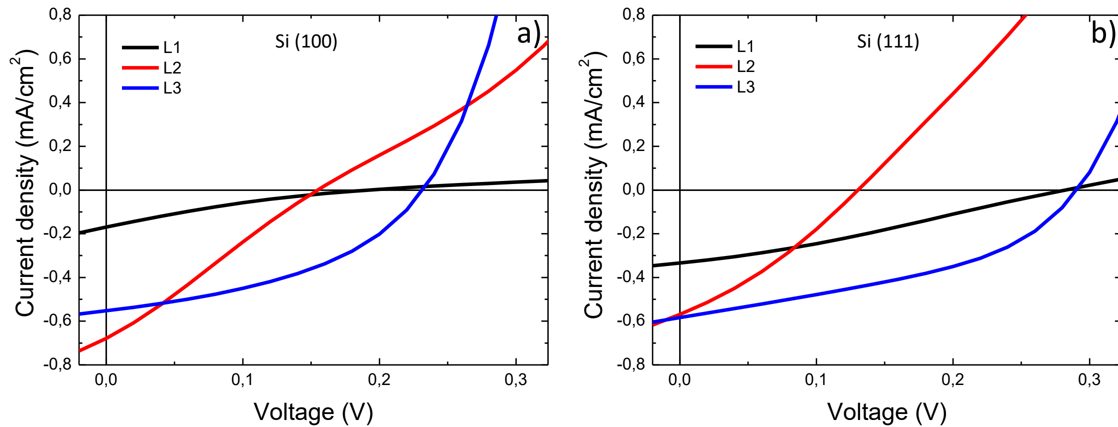

Figure 9.6. Current density-voltage curves of devices as a function of deposition temperature under halogen lamp illumination (P_{in} ~ 0.02 sun).a) Si (100) b) Si (111).

Concretely, the double kink that appears in devices grown at temperature below 550°C drastically reduces the FF to 12% for Si (100) and 22% for Si (111) substrates for layer deposited at room temperature. These kinks are probably induced by the existence of a thin buffer layer based on silicon oxide or silicon nitride at the interface, which can cause a double diode effect in the devices. This buffer layer was also observed by TEM in previous studies developed by this group [Nuñ18, Val18]. In this sense, we believe that

effect of the thin buffer layer created at the interface can be reduced by increasing the growth temperature up to 550°C, reducing thus the aforementioned double kink effect.

So, accordingly to the results obtained from this series of AlInN on Si structures, we conclude that the growth temperature improves the photoelectrical properties of the devices, leading us to select 550ºC for the development of next series of devices.

9.3 Conclusions

- The effect of growth temperature from 20 to 550°C does not strongly affect the structural properties of the AlInN layers, which show a good crystal quality with crystals highly oriented along the *c*-axis. Meanwhile the rms surface roughness slightly increases with the growth temperature, showing similar values for both silicon substrates.
- Hall Effect measurements reveal an increase of the carrier concentration and a crecrease of the layer resistivity with the deposition temperature probably due to an increase of the adatom mobility and a probably change in the layer morphology.
- Transmittance measurements reveals no differences on the apparent optical bandgap value regardless the deposition temperature, obtaining values around 2.1 eV.
- Despite there are not clear differences in the layer properties, the J-V curves of the devices reveal a clear reduction of the short circuit current and the open circuit voltage as a function of the growth temperature. This effect is due to a double kink in the J-V curve probably caused by a thin buffer layer based on silicon oxide or silicon nitride at the interface, which is probably reduced with the growth temperature. Beside this, all the devices shows a high series resistance in comparison with a typical silicon solar cell, probably induced by a high contact resistivity.

These results leads to develop and study devices at high temperatures (≥ 550°C) in order to explore the evolution of the double kink observed in the J-V curve.

Besides, despite the structural, morphological and optical properties of AlInN layers deposited at room temperature are quite similar than the layers grown at higher temperatures, devices developed at room temperature do not show good results, due

to the carrier concentration of the layers are much lower than the ones grown at higher temperatures, leading to obtain lower photoelectrical properties of the heterojunction. In that sense, doping AlInN layers grown at low temperatures can be develop devices with similar photoelectrical properties than devices developed at high temperature regime.

Chapter 10

AlInN on Si structures deposited at 550°C for solar cell devices

Results obtained in chapter 9 reveal an improvement of the devices efficiency with the growth temperature, so in this chapter we focus on the study of the material properties of AlInN layers and the related photelectrical ones of AlInN/Si devices deposited at 550° C.

In the first section of this chapter we study the structural, morphological, electrical and optical properties of AlInN layers deposited at 550°C as a function of the Al power supply from 0 to 225 W. As observed in chapter 8, the Al power supply changes the Al mole fraction of the alloy. This study was performed in order to analyze the effect of the Al mole fraction on the photovoltaic performance of the developed AlInN/Si devices and compare it with the theoretical results obtained in chapter 6.

There are some studies of AlInN layers grown at high temperatures by RF-sputtering such as [Liu13, Nuñ16, Nuñ17] and also by other deposition techniques like MBE and MOVPE [Guo10, Ter06, Ton10, Wan10]. Besides, as detailed in chapter 9, inasmuch as the AlInN is a novel material in the solar cell scientific community, there are only few studies of solar cells based on AlInN/Si heterojunctions, they being mainly developed by the group of Liu *et al*. [Liu12. Liu13] and also by this group [Val18, Nuñ18, Bla18], obtaining an efficiency between 0.8 to 2.5%, which is the currently record of this technology.

10.1 Influence of the Al RF power on the material properties of AlInN layers

As it was explained in previous chapters, the bandgap energy and the material properties of the AlInN layers can be tuned depending on the Al mole fraction, modifying the photoelectrical properties of the devices (see chapter 6 for further details). In this section, the morphology, the structural quality and the optical and electrical properties of the layers deposited on Si (111) and (100) has been studied in order to understand their influence on the photoeletrical properties of the developed devices.

The growth procedure of the layers studied is the same as the one explained in the previous section, using a *p*-doped 300 μm-thick Si (100) and a *p*-doped 500 μm-thick Si (111) substrate both with a resistivity of 1-10 Ω·cm. Substrates were chemically cleaned in organic solvents before being loaded in the chamber where they were outgassed for 30 min at 600ºC. Afterwards, substrates were cooled down to the growth temperature. Prior deposition, targets and substrate were cleaned using plasma etching with Ar (99.999%) in the growth chamber. Optimized AlInN layers were deposited with a nitrogen flow of 14 sccm at a pressure of 0.47 Pa. The RF power applied to Al target, P_{Al}, was varied from 0 to 225 W as detailed in table 10.1 (samples D1-D7), whereas the RF applied to In target and the temperature were fixed to 30 W and 550ºC, respectively. Besides, the growth time was adjusted to keep a layer thickness around 90 nm in all cases.

Sample	Al power supply (W)
D1	0
D2	100
D3	125
D4	150
D5	175
D6	200
D7	225

Table 10.1. Value of RF power applied to the Al target (P_{Al}) for each sample of the studied set.

Inasmuch as there are several samples in this study, the ones grown on Si (100) are called with the subscript (0) while the layers grown on Si (111) are called with the subscript (1).

10.1.1 Structural characterization

The structural quality of the AlInN films was evaluated with XRD measurements. All layers present wurtzite crystalline structure highly oriented along the *c*-axis as shown in the 2θ/ω scans of figure 10.1 a) and b). The AlInN samples present no phase separation showing a single peak coming from the diffraction of the AlInN (0002), which evoles from 31.1° to 33.3° with the increase of the Al power supply from 0 to 225 W. This increase of the AlInN (0002) diffraction peak as a function of the Al power correspond to a decrease of the *c* lattice parameter from the theoretical value of the InN (~5.729 Å) to values closer to the theoretical value of the AlN (~4.98 Å). Figures 10.1 a) and b) also display the diffraction peaks of Si (100) (~ 69.8°) and the Si (111) (~ 28.5°) respectively.

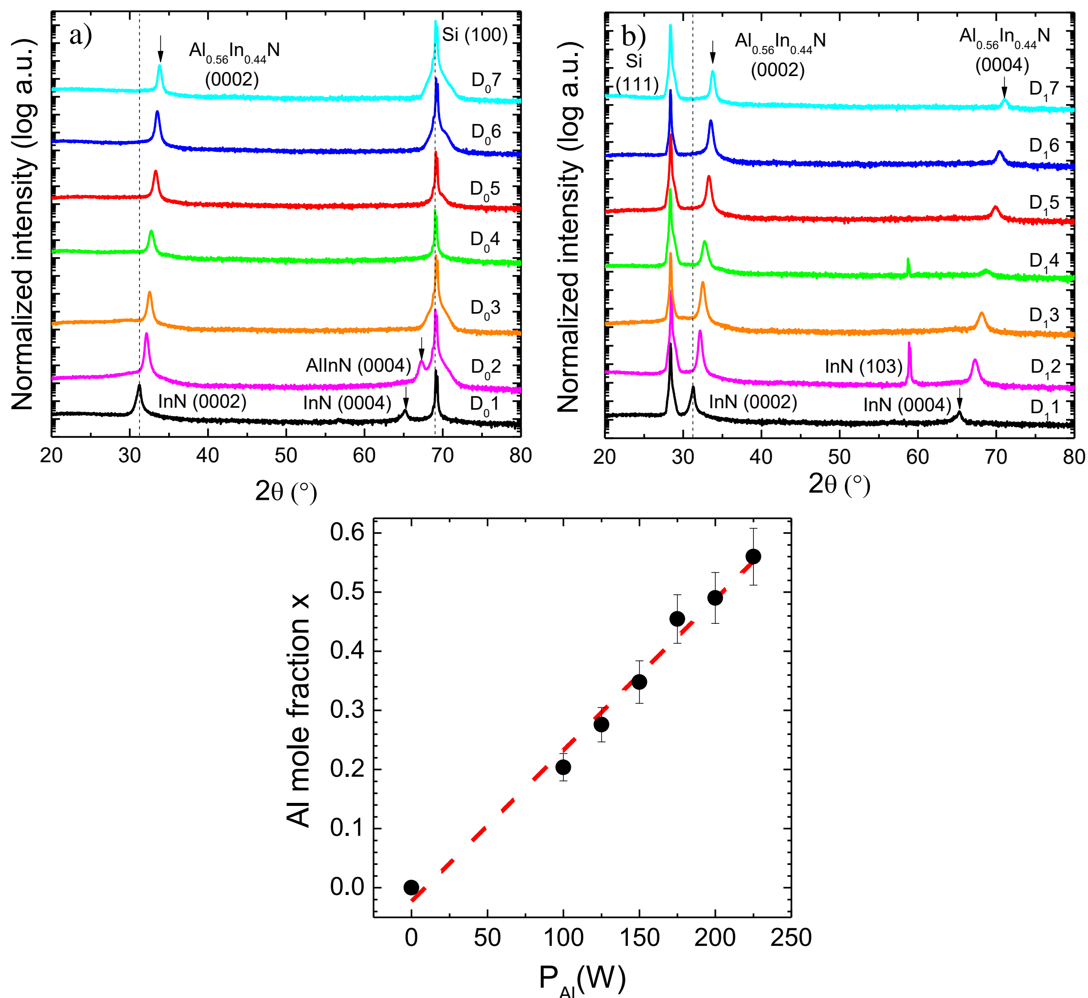

Figure. 10.1. 2θ/ω scans of the AlInN on a) Si (100) and b) Si (111) structures vs P_{Al}. c) Al mole fraction *x* of the $Al_xIn_{1-x}N$ layers estimated from the average of both XRD measurements for AlInN on Si (100) and Si (111) as a function of P_{Al}. The Al mole fraction estimation owns an error bar of ~1-4% depending on the Al mole fraction, as obtained previously by this group [Nuñ17].

If we assume that the $Al_xIn_{1-x}N$ layers are fully relaxed, we can deduce their Al mole fraction x which linearly increases with P_{Al} in the range of x~0-0.56, as displayed in figure 10.1 c) and tables 10.2 and 10.3. The error bars were estimated taking into account previous results obtained by this group on AlInN layers with similar Al mole fractions [Nuñ17].

Moreover, the crystallyne quality of the AlInN layers improves with the Al incorporation since the full width at half maximum (FWHM) of the rocking curve around the AlInN (0002) diffraction peak decreases when comparing the binary InN with the AlInN alloys even for low Al RF powers, as shown in figure 10.2 a) and b). These values are on the same order of magnitude than the ones obtained by Núñez-Cascajero *et al.* in similar AlInN on Si (111) samples [Nuñ16].

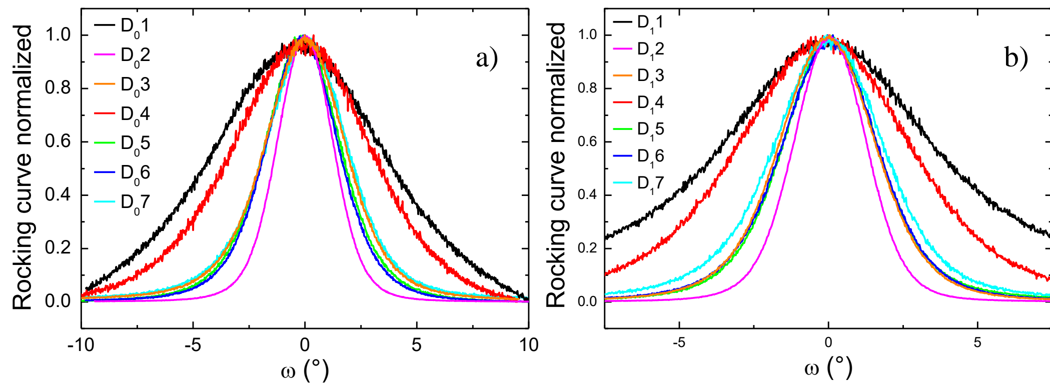

Figure 10.2. Evolution of the rocking curve of the $Al_xIn_{1-x}N$ layers deposited on a) Si (100) and b) Si (111) estimated from XRD measurements.

Furthermore, the real thickness of the AlInN layers was estimated from X-ray reflection (XRR) measurements pointing to an average of 88±8 nm and 91±7 nm for layers deposited on Si (100) and Si (111), respectively. The values of the thickness and deposition rate obtained for each sample are listed in tables 10.2 and 10.3.

	P_{Al} (W)	*x*	FWHM rocking curve (°)	Thickness (nm)	Deposition rate (nm/min)	Rms roughness (nm)
D_01	0	0	8.9	88	0.59	20
D_02	100	0.20	2.9	91	0.77	--
D_03	125	0.28	4.0	83	0.83	--
D_04	150	0.35	7.3	95	1.03	2.0
D_05	175	0.45	4.1	80	1.16	--
D_06	200	0.49	3.9	87	1.36	--
D_07	225	0.56	4.4	88	1.66	1.5

Table 10.2. Summary of the structural and morphological properties of the AlInN on Si (100) samples.

	P_{Al} (W)	*x*	FWHM rocking curve (°)	Thickness (nm)	Deposition rate (nm/min)	Rms roughness (nm)
D_11	0	0	7.6	94	0.63	32
D_12	100	0.20	2.8	98	0.81	--
D_13	125	0.29	3.7	88	0.88	--
D_14	150	0.36	6.7	98	1.05	2.7
D_15	175	0.47	3.9	84	1.23	--
D_16	200	0.52	3.8	92	1.45	--
D_17	225	0.58	4.4	95	1.8	1.6

Table 10.3. Summary of the structural and morphological properties of the AlInN on Si (111) samples.

10.1.2 Morphological characterization

The morphological characterization of the layers reveals that the aforementioned reduction of the AlInN mosaicity with the Al composition is accompanied with a change in the surface morphology of the samples. Their rms surface roughness evolves from 20 and 32 nm for InN on Si (100) and Si (111) respectively to 1.5 nm for $Al_{0.56}In_{0.44}N$ layers deposited on both silicon substrates, as shown in the 5×5 μm^2 AFM pictographs of figure 10.3. Besides, as observed in previous studies carried out by this group [Nuñ16, Nuñ17], this reduction in the surface roughness with the Al content may entail a change in the surface morphology of the samples from a closely compact structure for InN to a compact one for the $Al_xIn_{1-x}N$ material.

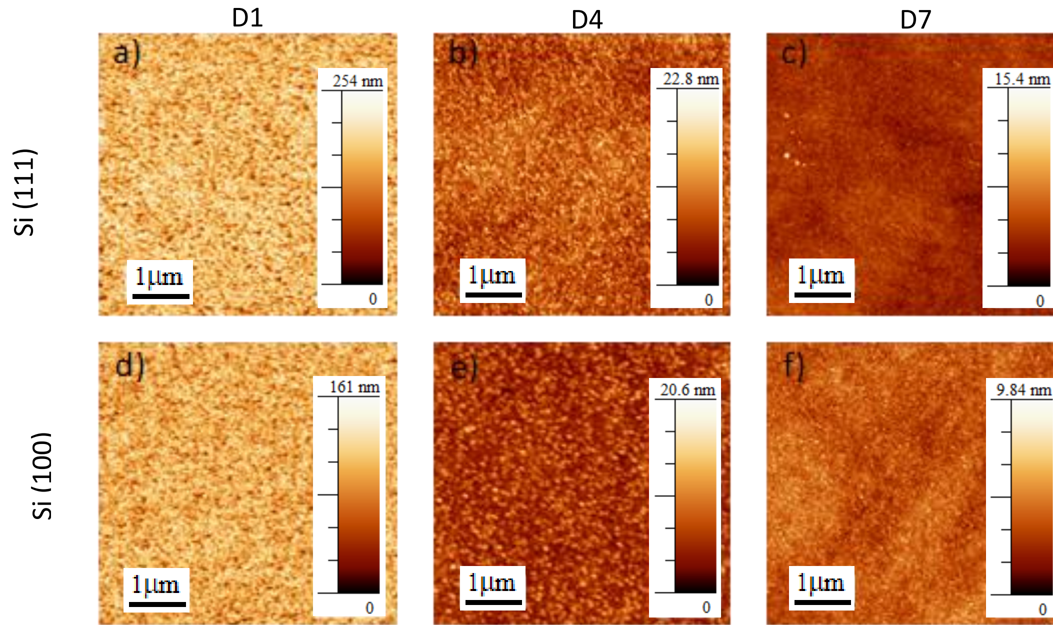

Figure 10.3. AFM (5×5 μm^2) pictographs of AlInN layers on Si (111) a), b) and c) and on Si (100) d), e) and f) as a function of the Al mole fraction.

Through these measurements we deduce that the properties of the layer does not change with the orientation of the silicon substrate. So *a priori* a variation on the device properties cannot be attributed to a variation on the layer morphology caused by the substrate orientation.

10.1.3 Electrical characterization

A proper control of *n*-type doping is of crucial importance to develop efficient devices. Hall Effect measurements were conducted for $Al_xIn_{1-x}N$ films simultaneously deposited on sapphire to explore the evolution of their electrical characteristics, such as carrier concentration, layer resistivity and carrier mobility as a function of the alloy mole fraction. As detailed in figure 10.4, the resistivity of the layers shows an increase from 0.2 mΩ·cm to 3.4 Ω·cm for the InN (D1) to the $Al_{0.45}In_{0.55}N$ samples (D5), respectively. Moreover, the residual *n*-type carrier concentration drops two orders of magnitude from 7.5×10^{21} cm^{-3} to 1.6×10^{19} cm^{-3}, and the carrier mobility drops from 4.2 cm^2/V·s to 0.1 cm^2/V·s within the same Al mole fraction range as shown in figure 10.4. This effect is caused by the increase of the bandgap energy with the incorporation of Al in the samples. Besides, as observed in previous chapters, the high carrier concentration obtained in the samples is probably due to the aforementioned unintentional doping during the growth.

For $x > 0.45$ electrical measurements were not reliable due to the high resistivity of the layers, above the resolution of the Hall Effect setup.

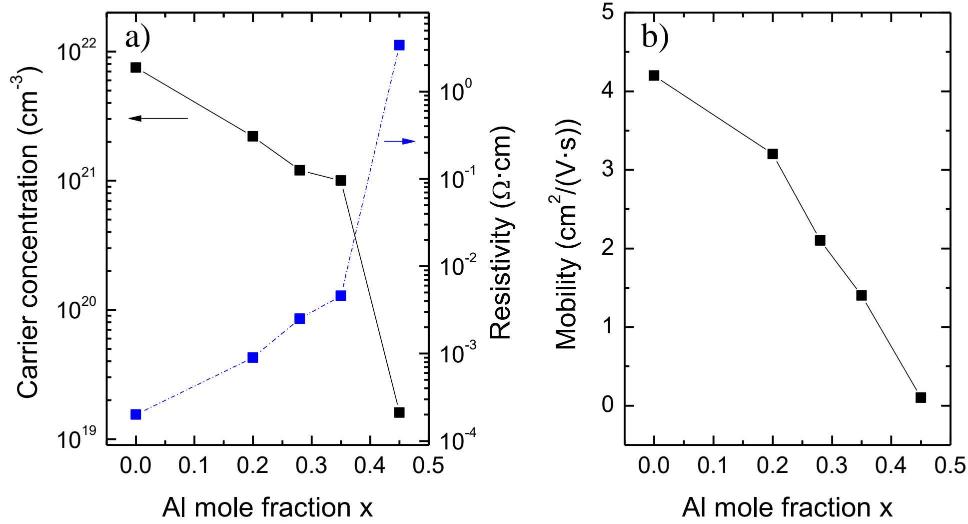

Figure 10.4. a) Evolution of the carrier concentration (solid line), the layer resistivity (dotted blue line) and b) the carrier mobility as a function of the Al mole fraction.

The high carrier concentration presented in the AlInN layers is related to an unintentional doping coming from hydrogen and oxygen impurities during the sputtering deposition and point defects such as nitrogen vacancies as observed in previous studies [Dar09, Dar10, Wu09].

10.1.4 Optical characterization

Trasnmittance measurements

Figure 10.5 shows the optical transmittance spectra measured in $Al_xIn_{1-x}N$ samples deposited simultaneously on sapphire under the same deposition conditions vs the Al mole fraction x. The optical absorption band-edge blue shifts as expected with the Al content. However, transmittance measurements of layers with thickness below 100 nm never reaches zero values at short wavelength. These results can affect to the calculation of the bandgap energy leading to an overestimation of it.

In that sense, in order to overcome this, the bandgap energy obtained from these data was compared with the one obtained from transmittance spectra measured in AlInN on sapphire samples were grown at 300ºC with thicknesses above 300 nm and an Al mole fraction similar to those of this study. These samples are the ones of chapter 8 and the comparison is depicted in table 10.4. From these data, the bandgap energy E_g increases

from 1.73 eV (804 nm) to 2.56 eV (484 nm) accordingly to the Al mole fraction rise from $x = 0$ to 0.56.

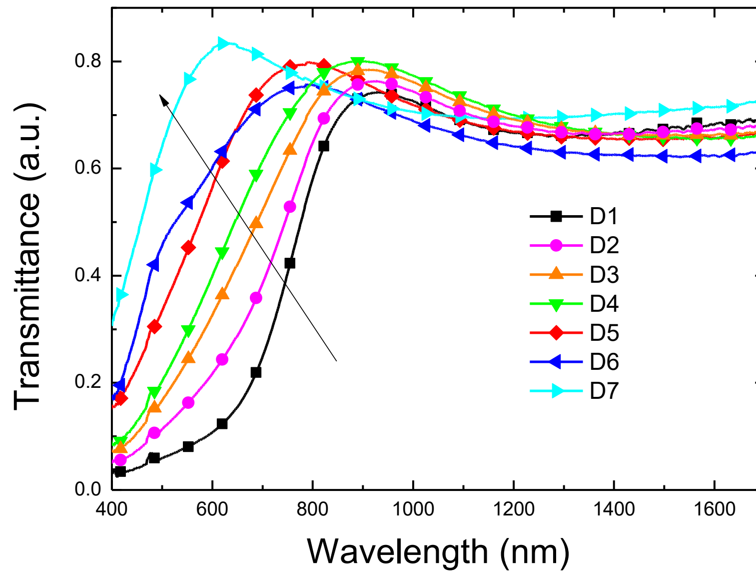

Figure 10.5. Optical transmission spectra of $Al_xIn_{1-x}N$ (~90 nm) on sapphire films vs the Al mole fraction *x*.

	P_{Al} (W)	Optical bandgap energy (eV)	Optical bandgap energy (eV) (at 300°C)
$D_0$1	0	1.74	1.73
$D_0$2	100	1.87	--
$D_0$3	125	2.03	1.79
$D_0$4	150	2.08	2.13
$D_0$5	175	2.24	--
$D_0$6	200	2.38	2.27
$D_0$7	225	2.57	2.56

Table 10.4. Summary of the optical properties of $Al_xIn_{1-x}N$ on sapphire layers obtained from this chapter and from thicker layers grown at 300°C (chapter 8).

Reflectance measurements

As could be seen in the study of the anti-reflective layer carried out in chapter 6, the reflectance of the device can reduce the ability to collect photons in a certain range of the solar spectrum, reducing thus the efficiency of the solar cell device. In that sense, a study of the reflectance has been carried out as a function of the Al mole fraction in order to analyze its evolution with the aluminum content of the layers.

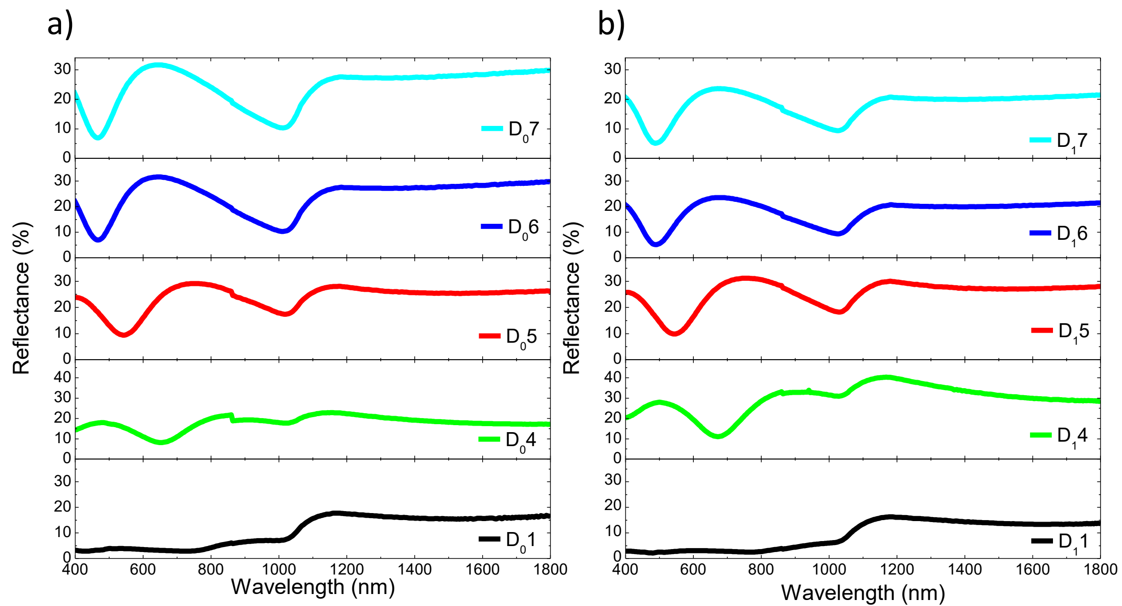

Figure 10.6. Reflectance measurements of AlInN layers deposited on a) Si (100) and b) Si (111).

The reflectance measurements of the samples displayed in figure 10.6 show the evolution from low reflectivity InN layers with values below 10% for wavelengths below 1000 nm. Meanwhile, when aluminum is incorporated to the alloy the reflectance increases up to 35%.

Besides, as can be observed in figure 10.6, there is a blue-shift of the reflectance peak at short wavelengths (~600 nm) as a function of the Al mole fraction, which may be due to a variation in the refraction index of the alloy.

Furthermore, reflectance measurements show an interference at long wavelength (1200 nm), probably attributed to interferences which occurs at the layer interface reflections as previously observed by Chen *et al*. [Che14].

These results could lead to a worsening in the photoelectric properties of the devices with the increase in the aluminum content. This effect can be reduced by means of an anti-reflective layer for devices based on AlInN as indicated in chapter 6, especially for layers with a high Al content.

Photoluminescence measurements

Photoluminescence measurements were carried out to analyze the material quality, the bandgap energy and the activation energy of the AlInN layers as a function of the Al mole fraction.

Low-temperature (T = 11 K) PL measurements were carried out in AlInN samples grown on Si (100). The results reveal a dominant PL emission coming from the $Al_xIn_{1-x}N$ layers with Al mole fractions below 0.35, as plotted in figure 10.7. No PL emission was observed coming from AlInN layers with $x > 0.35$. The high layer resistivity and the low carrier mobility of the $Al_xIn_{1-x}N$ samples with an Al mole fraction above 0.35 are probably the reasons why there is not PL emission coming from the material.

The PL emission energy blue shifts with the Al content from 1.59 eV (779 nm) for the InN (D_01) to 1.82 eV (681 nm) for the $Al_{0.35}In_{0.65}N$ layer (D_04), showing a similar broadening of the emission with a FWHM of ~300 meV in all cases. In order to investigate the origin of the luminescence, the thermal evolution of the PL peak energy was studied between 11 K and room temperature for InN (D_01) and $Al_{0.28}In_{0.72}N$ samples (D_03).

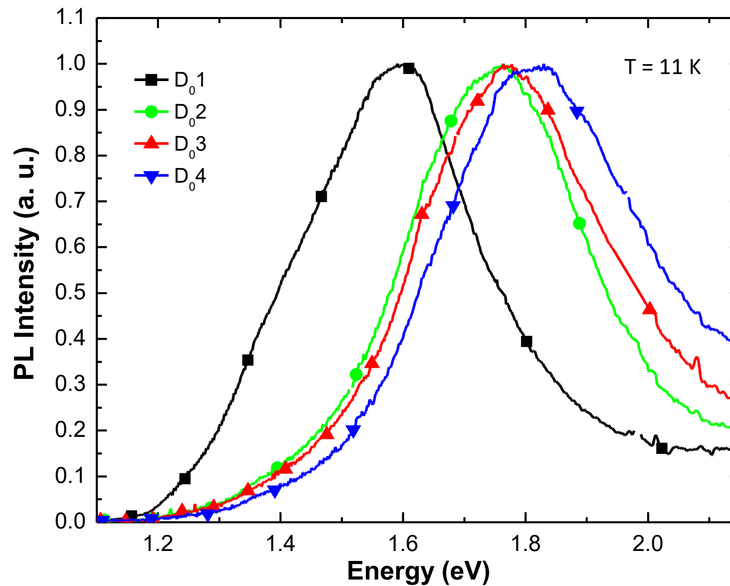

Figure 10.7. Normalized low-temperature PL emission of the $Al_xIn_{1-x}N$ on Si (100) samples vs the Al mole fraction. For $x > 0.35$ no PL emission was observed.

Besides, figures 10.8 a) and 10.9 a) show the evolution of the PL emission for the InN and the $Al_{0.28}In_{0.72}N$ on Si (100) samples, respectively. The latter was chosen since it showed the highest optical quality in terms of emission intensity and FWHM.

Concerning the InN sample (see figure 10.8 (b)), an almost constant emission energy is measured independently of the temperature for the analyzed range, with a weak S-shape evolution and a red-shift or the emission as low as ~5 meV between 11 K and room temperature.

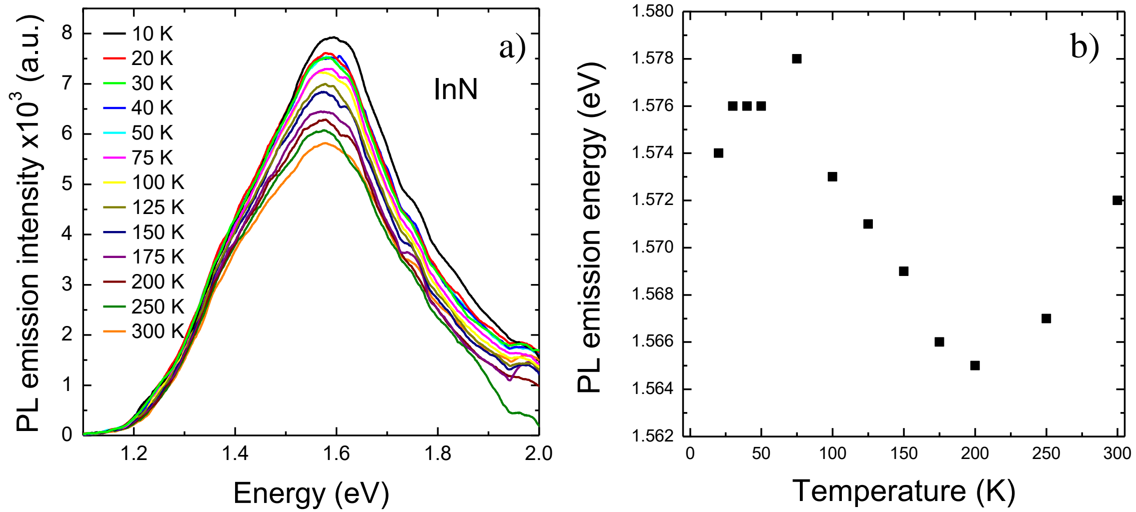

Figure 10.8. a) Evolution of PL emission spectra as a function of the temperature for InN on Si (100) sample ($D_0$1) and b) Evolution of the PL emission energy vs the temperature of the same sample.

On the contrary, the PL emission of the $Al_{0.28}In_{0.72}N$ sample (see figure 10.9 (b)) shows a clear red-shift of the emission energy of ~35 meV between 11 K and room temperature. At the same time, the FWHM of the emission peak at room temperature 390 meV and 420 meV for the InN ($D_0$1) and $Al_{0.28}In_{0.72}N$ samples ($D_0$3), respectively. This points out an emission origin related with an energy-band of impurities, in agreement with the high carrier concentration measured in the samples. This behavior has been previously observed in both InN and AlInN samples deposited by RF sputtering on sapphire [Nuñ17], being attributed to the existence of an important concentration of impurities like oxygen and probably nitrogen vacancies in the layers.

It is remarkable the reduced effect of the alloy disorder in the FWHM of the observed PL when increasing the Al content in the layers. This effect is attributed to the high growth temperature used in this study (550ºC) that promotes the adatom diffusion, as reflected in the aforementioned reduction of the rms surface roughness measured by AFM.

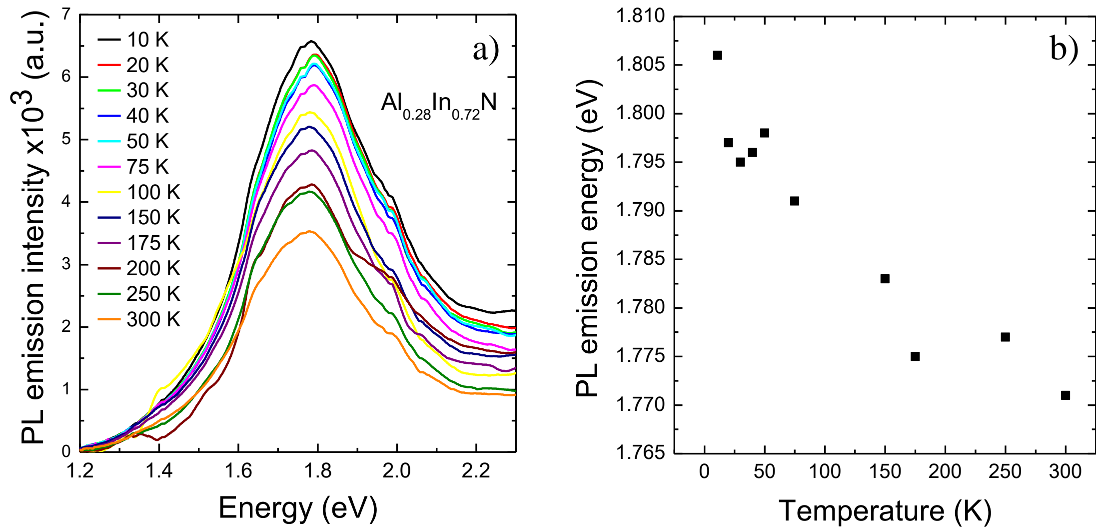

Figure 10.9. a) Evolution of PL emission spectra as a function of the temperature for InN on Si (100) sample $D_0$3 and b) evolution of the PL emission energy vs the temperature of the same sample.

Figure 10.10 shows the thermal quenching of the normalized integrated PL intensity for the InN and $Al_{0.28}In_{0.72}N$ samples. The activation energy of the main process involved in this emission quenching, E_A, was estimated using equation 5.6, $I(T) = I_0 / \left(1 + ae^{\frac{-E_A}{k_B T}}\right)$, where I_0 is the integrated intensity at T = 0 K, k_BT is the thermal energy, and *a* is a fitting constant that is related to the nonradiative-to-radiative recombination ratio of the process. Activation energies of E_A = 20±2.0 meV and E_A = 24± 4.4 meV were estimated for the InN and $Al_{0.28}In_{0.72}N$ samples, respectively. The value obtained for InN is lower than the one of E_A = 51 meV estimated in InN on sapphire samples deposited at lower substrate temperature (300ºC) [Nuñ17b].

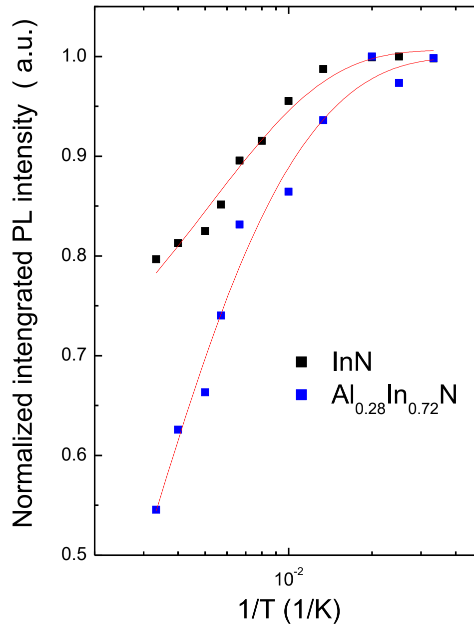

Figure 10.10. Evolution of the normalized integrated PL intensity as a function of the temperature for the InN ($D_0$1) and the $Al_{0.28}In_{0.72}N$ on Si (100) samples ($D_0$3).

This difference can be attributed to a change in the formation of impurity complexes with the temperature. However, the obtained value for the $Al_{0.28}In_{0.72}N$ is in agreement with the one estimated in AlInN on Si (111) samples with similar Al mole fraction [Nuñ16]. The extracted fitting parameters are $a = 0.6$ and $a = 1.9$ for InN and $Al_{0.28}In_{0.72}N$ samples, respectively.

10.2 Effect of the Al RF power on the photoelectrical properties of AlInN on Si devices

In order to study the photovoltaic performance of the structures, the developed AlInN on Si structures were processed into ~0.9 cm^2 devices, with an *n*-type top and a *p*-type bottom contacts formed by 120 nm-thick Al deposited by RF sputtering under the conditions explained in section 5.5.

In that sense, and taking into account the evolution of the electrical properties obtained by Hall Effect measurements, a study of the top contact resistivity was carried out, using a transmission line method similar to the one explained in chapter 5, in order to analyze the effect of the AlInN resistivity on the resistance of the top contact.

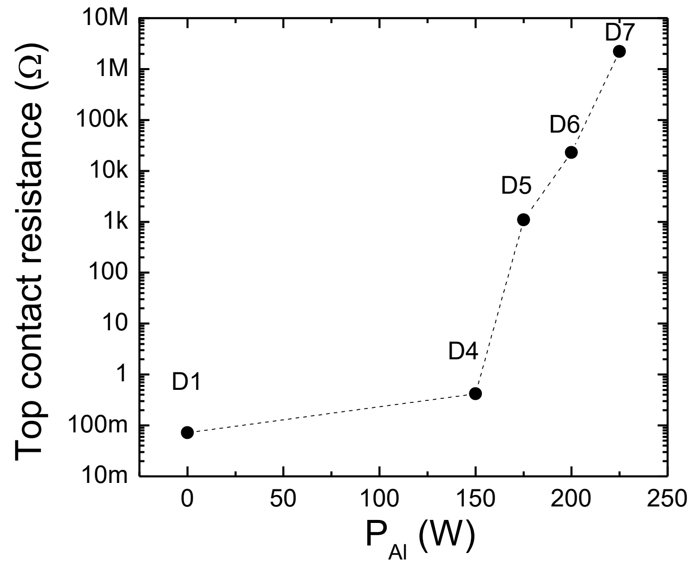

Figure 10.11. Evolution of the top contact resistivity as a function of the Al power supply (P_{Al}).

Figure 10.11 reveals a huge increase of the top *n*-type contact resistivity with the Al power supply (i.e. Al content) which will affect the photovoltaic performance of the devices. This is probably caused by the reduction of the carrier concentration of the layers when increasing the Al content, as previously explained.

Devices were characterized by current density-voltage (J-V) curves carried out in dark and under standard illumination at 25ºC. Dark measurements were recorded using a four-point probe station, whereas measurements under illumination were performed with a solar simulator with an AM1.5G spectrum under one sun (100 mW/cm^2) irradiation. The spectral response of the devices was measured at zero bias in the 400-1100 nm spectral range using a 250 W halogen lamp coupled to a monochromator. These results were calibrated using the response of the cell to a laser diode emitting at 633 nm with a known output power of 0.6 mW to obtain the device responsivity.

10.2.1 Dark current-voltage curves

J-V curves of the processed devices were measured under dark conditions (figure 10.12) at the Complutense University of Madrid to estimate the series and shunt resistances (R_s, R_{sh}), the saturation current (J_0) and the ideality factor (η).

Curves were analyzed using the one diode model depicted in chapter 5, which results are summarized in tables 10.5 and 10.6 for AlInN on Si (100) and on Si (111) devices respectively. We observe an increase of R_{sh} that can be related to the evolution of the

layer morphology, as observed in chapter 8 for samples deposited at 300°C, from closely packed columnar (InN layers) to a compact (AlInN) structures.

Besides, the serial resistance R_s increases as expected for AlInN layers compared to InN-based devices, probably due to its insulating behavior, which leads to a high top *n*-contact resistivity. On the other hand, the obtained ideality factor and the reverse saturation current density does not show a clear trend as a function of the Al content, obtaining values of ideal factor from 2.1 to 4.3, while the reverse saturation current varies from 3×10^{-4} to ~ 0.04 mA being probably affected by the layers quality.

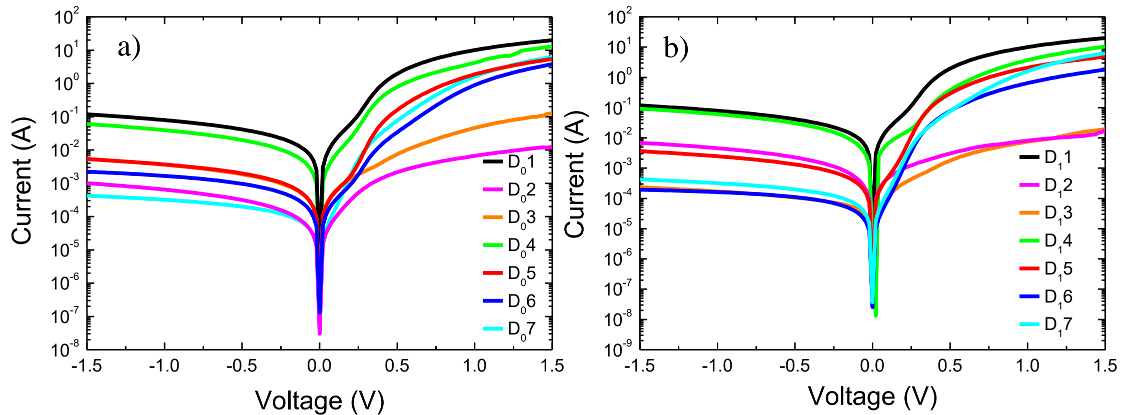

Figure 10.12. Dark J-V measurements of a) AlInN/Si (100) and b) AlInN/Si (111) devices.

As summarized in tables 10.5 and 10.6, the evolution of the devices properties obtained under dark conditions show similar trends for both silicon substrates. However, as observed in both graphs, sample D_13 (grown at 125 W) shows a clear variation on the serial resistance, revealing a high serial resistance values. This effect is probably affected by an increase on the *n*-type conctact or by an increase on the structural defects, which can leads to a reduction of the R_{sh} caused by the low Al power supply used in this sample. On the other hand, samples D_02 and D_12, grown at 100 W has also high values of R_s, which can be caused by the low crystal quality of the layers, however, the good values of the R_{sh} are in disagreement with this theory. Therefore, this effect is probably due to by a problem in the top *n*-type contact or even in the interface between the contact and the AlInN, which can induce a high contact resistivity.

10.2.2 Current-voltage curves under one sun AM 1.5G illumination

Measurements under 1 sun AM1.5G illumination (figure 10.13) were carried out in Autónoma University of Madrid facilities to evaluate their photovoltaic characteristics in

terms of open circuit voltage (V_{oc}), short-circuit current density (J_{sc}), Fill Factor (FF) and power conversion efficiency. It should be noted that the J_{sc}, and thus the device efficiency is calculated taking into account the net area of the devices presented in table 10.5 and 10.6 without the shadow of the top contact fingers of ~0.13 cm^2.

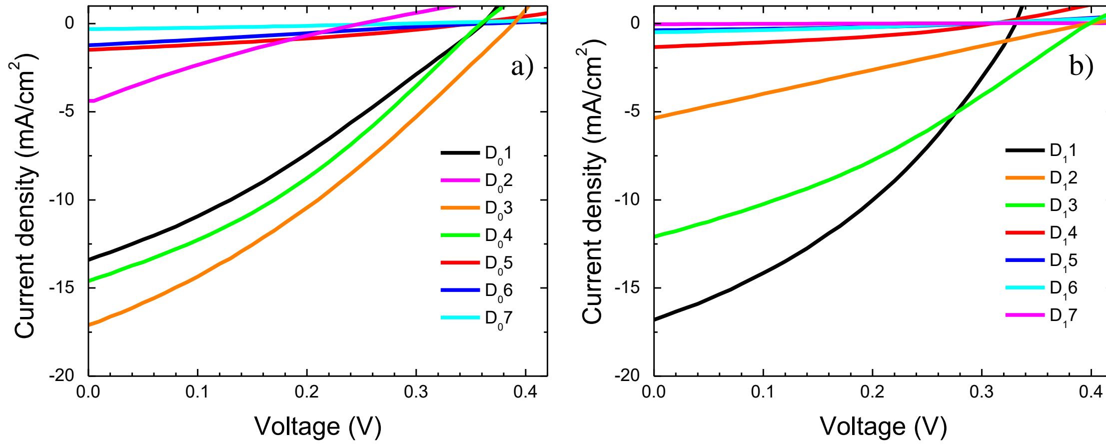

Figure 10.13. Current density-voltage curves of devices deposited on a) Si (100) and b) Si (111) as a function of Al power supply under ones sun AM 1.5G illumination.

The analysis of current density-voltage characteristics measured under 1 sun AM1.5G illumination of devices on Si (100) (table 10.5) reveals that the sample $D_0 3$ ($x = 0.28$) has the best open-circuit voltage (0.39 V) and short-circuit current density values (17.1 mA/cm^2), whereas the fill factor remains ~30% for all devices. This values leads to a maximum conversion efficiency of 2.2% for this sample. However, the aforementioned high value of R_s obtained for the sample grown under the same conditions on Si (111) ($D_1 3$) leads to a reduction of the short circuit current (5.36 mA/cm^2) leading to a decrease of a factor of 4 of the device efficiency (0.53%).

Besides, it should be mentioned that the evolution of the J_{sc} decreases drastically for Al mole fractions above $x = 0.35$ for both substrates, obtaining values below 2.5 mA/cm^2 and thus low values of device efficiency. Despite theoretically the contact resistivity does not strongly affect to the J_{sc}, the high values presented in figure 10.11 probably cause this trend, hiding the predicted improved effect of the photovoltaic properties of the devices with the increase of the Al mole fraction and the AlInN bandgap energy.

	x	Area (cm^2)	R_s ($\Omega \times cm^2$)	R_{sh} ($M\Omega \times cm^2$)	J_0 (μA) (@ -1V)	η	V_{oc} (V)	J_{sc} (mA/cm^2)	FF (%)	Eff. (%)	EQE (%) (at 860 nm)
$D_0$1	0	0.67	3.4	0.49	36	3.5	0.36	13.4	30.7	1.49	66.7
$D_0$2	0.20	0.60	58.9	0.99	0.38	3.6	0.25	7.3	21.6	0.40	29.9
$D_0$3	0.28	0.62	4.2	0.48	3.8	3.6	0.39	17.1	31.4	2.12	73.8
$D_0$4	0.35	0.70	4.4	0.95	22	4.3	0.36	14.6	33.8	1.77	58.3
$D_0$5	0.45	0.60	9.0	13.38	4.4	2.3	0.35	2.5	32.8	0.28	20.1
$D_0$6	0.49	0.48	10.6	23.81	1.7	2.1	0.36	2.5	25.2	0.23	21.4
$D_0$7	0.56	0.64	30.8	60.60	0.21	2.4	0.29	0.47	31.0	0.05	1.1

Table 10.5. Summary of the electrical and photovoltaic characteristics of the AlInN on Si (100) devices. The area was calculated taking into account the shadow of the top contact (~ $0.13cm^2$).

However, as observed in tables 10.5 and 10.6, the aforementioned high serial resistance of devices growth under an Al power supply of 100 W ($D_0$2 and $D_1$2) leads to low open circuit voltage and short circuit current values. This effect can be attributed to some alloy disorder on the nitride/Si interface that can be found at low Al power supply that strongly degrades the electrical behavior of the junction.

Although there are not notable differences in the structural, optical and morphological properties of the AlInN layers on both substrates (as is shown in chapters 7, 8 and in this chapter), the electrical properties of the devices change with the substrate orientation.

Tables 10.5 and 10.6 reveal lower serial resistance in devices developed on Si (100), leading to better efficiency values. This effect may be due to the reduction of electrical losses in the upper layers of silicon (dangling bonds) [Lan90] that occurs when using this orientation.

However, the values obtained from the InN layers, which shows similar values for both substrates are in disagreement with this theory. Therefore, the decrease of the device efficiency could be due to an Al diffusion on the substrate, which can be higher on Si (111) as is previously observed by Dolbak *et al.* for Ge depositions on both substrates [Dol06].

	x	Area (cm^2)	R_s ($\Omega \times$ cm^2)	R_{sh} (M$\Omega \times$ cm^2)	J_0 (μA) (@ -1V)	η	V_{oc} (V)	J_{sc} (mA/ cm^2)	FF (%)	Eff. (%)	EQE (%) (at 860 nm)
$D_1$1	0	0.66	3.3	0.42	38	2.5	0.33	16.8	36.1	2.02	72.8
$D_1$2	0.20	0.60	59.5	0.92	4.1	2.8	0.17	0.05	23.6	5×10^{-3}	12.4
$D_1$3	0.29	0.66	49.5	0.44	0.18	3.7	0.40	5.36	24.9	0.53	--
$D_1$4	0.36	0.68	5.2	0.46	26	3.2	0.40	12.1	32.9	1.58	64.3
$D_1$5	0.47	0.57	10.5	12.42	2.3	3.1	0.31	2.5	25.2	0.23	22.7
$D_1$6	0.52	0.58	25.5	48.50	0.15	2.7	0.29	0.64	35.5	0.07	--
$D_1$7	0.58	0.57	60.2	24.27	0.31	2.9	0.29	0.84	31.4	0.08	--

Table 10.6. Summary of the electrical and photovoltaic characteristics of the AlInN on Si (111) devices. The area was calculated taking into account the shadow of the top contact (~ 0.13cm^2).

The results obtained from this study show a reduction of the devices efficiency with the increase of the Al content, due to the high top contact resistance above $x = 0.35$, being in disagreement with the theoretical results obtained in Chapter 6. So, in order to overcome this issue, new strategies are needed such as dopping of the AlInN layers with mid-Al content with silicon to increase the carrier concentration and thus reduce the top contact resistance.

10.2.3 Spectral response of the devices

To investigate the influence of the impinging wavelength on the photocurrent of the devices, responsivity measurements were carried out in the 375-1100 nm wavelength range. The spectral evolution of the EQE curves of the devices are displayed in figure 10.14 a) and b) for AlInN on Si (100) and Si (111) devices respectively and summarizes in table 10.5 and 10.6. Besides, responsivity values for all $Al_xIn_{1-x}N$ on Si (100) devices at 860 nm are 454 mA/W ($x = 0$), 195 mA/W ($x = 0.20$), 491 mA/W ($x = 0.28$), 402 mA/W ($x = 0.35$), 130 mA/W ($x = 0.45$), 136 mA/W ($x = 0.49$), and 2 mA/W ($x = 0.56$). The best device based on an $Al_{0.28}In_{0.72}N$ on Si (100) structures presents a maximum EQE of ~ 80.2 % at 750 and with values above 70 % in the 670-870 nm spectral range.

Devices developed on Si (111) reveals similar values of EQE for AlInN layers with an Al mole fraction of $x = 0$, $x = 0.36$ and $x = 0.47$, being quite lower for the sample with $x = 0.20$. The other devices cannot be measured due to the low signal received from the samples, probably due to bonding problems.

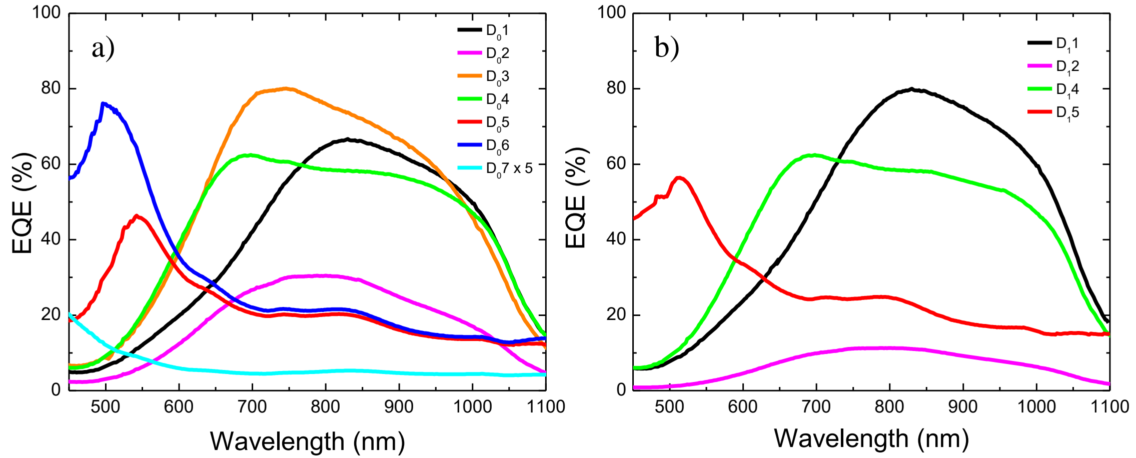

Figure 10.14. Influence of the Al mole fraction x on the responsivity of the $Al_xIn_{1-x}N$ on (a) Si (100) and (b) Si (111) devices vs the wavelength.

For Al mole fractions below 0.35, the EQE presents a broad spectral response covering the visible to near infrared range with a peak in the visible above the (Al)InN bandgap energy followed by a photoresponse in the near infrared with a cutoff ~1100 nm related to the Si band edge.

However, accordingly with conversion efficiency results, for Al mole fractions above 0.35 the responsivity drops probably due to the decrease of the carrier concentration that lead to the increase of the top contact resistance of six orders of magnitude (see figure 10.10) strongly lessening the overall photovoltaic performance of the devices.

10.3 Conclusions

Throughout this chapter the structural, morphological, electrical and optical properties of $Al_xIn_{1-x}N$ layers deposited by sputtering at 550°C on Si (111), Si (100) and sapphire substrates as a function of the Al content have been studied. Besides, a study of the photo-electrical properties of devices based on the samples deposited on both silicon substrates has been carried out in order to analyze the effect of the Al mole fraction on the device efficiency obtaining the following conclusions:

- All the samples present wurtzite structure highly oriented in the *c*-axis and non-phase separation. Besides, the evolution of the Al mole fraction with the Al power applied to Al target can be considered linear from both silicon substrates, obtaining values from 0 to 0.58.
- The root mean square surface roughness decreases from 20 and 32 nm for InN layers deposited on Si (100) and (111) respectively to 1.5 nm for $Al_{0.56}In_{0.44}N$ layers on both silicon substrates.
- Hall Effect measurements reveal a decrease of the carrier concentration, from 7.5×10^{21} cm^{-3} for InN to 1.6×10^{19} cm^{-3} for the $Al_{0.46}In_{0.54}N$ sample while the layer resistivity increases from 0.2 mΩ×cm for InN to 3.87 Ω×cm for $Al_{0.46}In_{0.54}N$.
- Optical characterization reveal a blue shift of the bandgap energy with the Al mole fraction, from 1.74 eV to 2.57 eV for the Al content range under study. Furthermore, the reflectance of the layers reveals an increase of at least a factor 2 with the increase of Al mole fraction in the wavelength range from 400 to 1000 nm.
- Photoluminescence measurements reveal a strong emission at low and at room-temperature for Al mole fractions up to $x = 0.35$ showing a blue shift from 1.59 eV (779 nm) for InN to 1.82 eV (681 nm) for $Al_{0.35}In_{0.65}N$ samples at 11 K.
- J-V curves in the under dark reveal an increase of the shunt resistance R_{sh} and of the serial resistance R_s with the Al mole fraction, probably due to the morphological and electrical properties of the layers respectively.
- On the other hand, J-V curves under 1 sun illumination reveal a clear reduction on the device efficiency for Al mole fractions above 0.36 probably due to the high back and top contact resistances.
- The spectral responsivity of the devices covers the visible to near-infrared spectral range for layers with an Al mole fraction below 0.35 and also displays a peak associated to Si and a band edge at shorter wavelengths that follows the AlInN absorption shift with the Al content. For samples with Al mole fractions above 0.35 the responsivity drops drastically, probably affected to the aforementioned high top contact resistivity.
- Best devices are obtained for InN layers on Si (111) and on $Al_{28}In_{72}N$ on Si (100) pointing to a conversion efficiency of 2.02 and 2.12%, respectively.

Chapter 11
Conclusions and perspectives

Along this thesis, the study of the structural, morphological, electrical and optical properties of InN and $Al_xIn_{1-x}N$ layers deposited by RF sputtering on silicon (111) and (100) and sapphire substrates has been reported. Besides, the photoelectrical properties of solar cells devices based on $Al_xIn_{1-x}N$ on both silicon substrates has been analyzed. In addition, a theoretical study about thr optimization of the properties of the $Al_xIn_{1-x}N$/Si heterostructure has been carried out in order to explore the potential of the AlInN on Si heterojunctions for solar cell devices.

One of the main conclusions obtained through this study is the feasibility to obtain $Al_xIn_{1-x}N$ material well oriented along the *c*-axis regardless the substrate orientation, and independently of the growth temperature and the In/Al RF power supply. This implies the possibility to develop AlInN/Si devices on the (100) orientation without significant changes in the quality of the layers and the photoelectrical performance of the devices compared to their counterparts.

Besides, the main conclusions obtained from each study are detailed as follows:

11.1 Simulations of AlInN on Si solar cells

Theoretical simulations of AlInN/Si heterojunctions obtained by Pc1d software, reveal a clear dependence of the device efficiency on the AlInN bandgap energy and thickness, obtaining optimized values of 2.56 eV and 10 nm, respectively. Besides, through the simulations it can be observed the importance of the interface defects, the carrier concentration of the nitride layer and the substrate passivation, obtaining an improvement of the device conversion efficiency from 15 to 18% with the optimization of those parameters. In addition, the effect of the quality of the silicon wafers was also studied, improving the conversion efficiency from 18 to 19.7% from the optimization of the resistivity and the bulk recombination of silicon.

Finally, the incorporation of an anti-reflective coating was also studied, reducing the reflections at the front surface of the device, improving the quantum efficiency of the device in a certain selected wavelength range and improving the conversion efficiency of the solar cell from the aforementioned 19.7% to 23.6 % showing the high potential of these heterojunctions. Besides, the external quantum efficiency of AlInN on Si heterojunctions reveals higher values than silicon homojunctions in the range below 450 nm, pointing to their potential for space applications.

11.2 Study of InN layers deposited by RF sputtering

InN layers (≥100 nm thick) grown by RF sputtering were studied in two main sets: the properties of the first set of samples was studied as a function of the deposition temperature, from room temperature to 450° C, keeping constant the indium power supply at 40 W. Meanwhile, the second set of samples was studied as a function of the indium power supply, from 20 W to 40 W, with a fixed growth temperature of 300°C. The others growth parameters were fixed in both series.

Both set of samples show InN wurtzite layers highly oriented along the *c*-axis perpendicular to the substrate surface without other crystallographic orientations with the exception of InN layers grown at room temperature. Besides, the samples grown on silicon substrates present similar results regardless the substrate orientation, indicating similar crystalline and structural quality of the nitride layer for both substrates.

The evolution of the FWHM of the rocking curve of the (0002) AlInN diffraction peack reveals lower values for layers grown at 300°C on silicon substrates, meanwhile the values of layers grown on sapphire decreases with the growth temperature. On the other hand, the mosaicity of the InN layers increases with the In power supply regardless the substrate used.

SEM images show an evolution of the morphological properties, pointing to an enhancement of the columnar morphology with the increase of In power supply regardless the substrate under study.

Hall Effect measurements of InN samples grown on sapphire reveal a decrease of the carrier mobility from 28.3 to 5 $cm^2/V{\cdot}s$ with the In power supply, probably affected by the evolution of the morphology. Besides this, InN layers show a carrier concentration above 10^{20} cm^{-3} regardless the growth temperature or the power supply applied to the

indium target. The high carrier concentration of the layer leads to a Burnstein-Moss effect in the bandgap energy, which values range from 1.72 to 1.87 eV.

11.3 Study of AlInN layers deposited by RF sputtering at 300°C

The properties of AlInN layers were studied as a function of the aluminum power supply, from 0 W to 225 W, with a fixed growth temperature at 300°C. Identically to the previous study, the others growth parameters were fixed in both series. This study reveals the feasibility of controlling the aluminum mole fraction of the layers from 0 to 0.56 by modifying the Al power supply during the deposition process.

As in the previous study, all samples present a wurtzite structure highly oriented along the *c*-axis. The evolution of the layer mosaicity, obtained from the FWHM of the rocking curve of the (0002) AlInN diffraction peak, decreases with the Al mole fraction with the exception of the layer grown at 150 W, probably due to a change in the layer morphology at this Al power supply. Besides, the lower values are obtained for layers grown on sapphire substrates, compared to the silicon ones. This effect is probably due to an unintentional deposition of an amorphous thin layer onto both silicon substrates before the growth of the AlInN layer.

The morphology of the layers evolves from closely-packed nanocolumns for InN on Si layers to compact ones when increasing the Al mole fraction. This effect is probably induced by the increase of the III/V ratio that leads to obtain smoother layers with the increase of the aluminum content. This trend is also observed in the evolution of the rms roughness, which decreases with the Al power supply reaching values below 3.6 for layers grown on both silicon substrates and 0.5 nm for layers grown on sapphire for Al contents above 0.32.

The electrical properties of the AlInN layers reveals a decrease of the carrier concentration from 1.73×10^{21} cm^{-3} to 2.48×10^{20} cm^{-3} and an increase of the layer resistivity when the Al content increases from 0 to 0.32, probably related to the increase of the bandgap energy. These high carrier concentration values leads to a Burnstein-Moss effect in the bandgap energy, which varies from 1.75 to 2.56 eV within this Al content range, which implies the possibility to develop solar cells devices covering that wavelength range of the solar spectrum.

Samples with an Al mole fraction below 0.36 show PL emission at room temperature, revealing a red-shift of the PL emission peak in comparison with the absorption edge energy calculated.

11.4 AlInN on Si heterojunctions: effect of the growth temperature

Firstly, the properties of thin AlInN layers (~ 90 nm) grown on silicon (100) and (111) substrates were studied as a function of the growth temperature from room temperature to 550° C keeping constant the indium and aluminum power supply at 30 and 150 W, respectively. Afterwards, the photoelectrical properties of devices developed from these AlInN on silicon samples were analyzed in order to study the effect of the growth temperature on the solar cell devices.

This study reveals wurtzite structure layers highly oriented along the *c*-axis with a low rms surface roughness below 2.6 nm for all layers.

The electrical properties, of the layers grown on sapphire reveals a rise of the carrier concentration from 10^{17} to 10^{21} cm^{-3} and a decrease of the layer resistivity with the growth temperature. Furthermore, the optical bandgap remains almost constant with values from 2.08 to 2.13 eV.

The photoelectrical characterization of the AlInN/Si devices as a function of the growth temperature shows a decrease of the serial resistance and an increase of the shunt resistance with the growth temperature in the dark, and a clear reduction of the fill factor of the J-V curve under illumination for layers deposited at a temperature below 550° C. These layers show a double kink ("S" shape) probably due to the existence of a thin layer based on silicon oxide or silicon nitride at the interface, reducing thus the conversion efficiency.

These results leads to study the material and photoelectrical properties of the layers and devices developed at 550° C.

11.5 AlInN on Si structures grown at 550°C: effect of the Al content

AlInN layers were grown at 550°C on Si (111), Si (100) and sapphire, varying the Al power supply to initially study the effect of the Al mole fraction on the structural, morphological, electrical and optical properties of the layers and then on the photoelectrical properties of the devices. All the layers, identically to the others studies, present a wurtzite structure highly oriented along the (0002) orientation. Besides, the Al mole fraction can be ranged from 0 to ~ 0.58 by modifying the Al power supply, showing similar values for layers deposited on both silicon orientations. The optical bandgap energy obtained for this set of samples ranges from 1.6 to 2.56 eV for InN to $Al_{0.58}In_{0.42}N$, respectively.

The rms of the layers decreases from 32 to 2 nm showing smoother layers when the Al content increases, in agreement to the study of AlInN layers deposited at 300°C. Besides, the electrical properties show a decrease of the carrier concentration and an increase of the layer resistivity. These trends leads to an increase of the top contact resistance, which reaches values above 1 KΩ for Al mole fraction up to 0.35.

In that sense, layers with an Al mole fraction below 0.35 reveals a device efficiency above 1.5 %, with the exception of layers growth at Al power supply of 100 W. However the sample grown on Si (111) under an Al power supply of 125 W shows a low value of serial resistance and device efficiency, probably affected by the quality of the top contact.

On the other hand, the insulating behavior and the increase of the top contact resistance with the Al mole fraction cause a decrease of the photoelectrical properties of the devices, leading to a device efficiency below 0.23%.

The photoelectric properties of the devices have shown the importance of obtaining a good quality of the $Al_xIn_{1-x}N$ layer and a low resistance for the top and back contacts.

External quantum efficiency measurements show values above 50% in the 650-1000 nm wavelength range for layers with Al content below 0.36. Besides, accordingly with the device efficiency values, the increase of the top contact resistance leads to a strongly decrease of the EQE for layers with Al content up to 0.36.

The maximum conversion efficiency values were obtained for In/Si (111) with an efficiency of 2.02% and for $Al_{0.28}In_{0.72}N$/Si (100) with an efficiency of 2.12%.

11.6 Perspectives

As explained along this thesis, solar cells devices based on AlInN compounds are really novel and there are very few studies of them. This implies that several optimization studies of the material and of the device must be carried out.

Taking into account the results obtained along this thesis, several approaches can be carried out to improve the photovoltaic performance of the AlInN-based solar cells:

- First of all, the low fill factor obtained in all the samples, regardless the substrate and the growth conditions reveals the need to improve the top and back contact, inasmuch as the resistance values of both contacts are larger than those used currently in commercial solar cells. In that sense, there are several options to be explored:
  - The first one is based on the improvement of the annealing process of the back contact, being able to change the annealing method using an annealing via laser (laser firing method) in which the annealing points are selected taking into account the life-time of the carriers.
  - Other possibility is to develop both contacts with other materials such as titanium and aluminum (Ti/Al) or titanium, aluminum, nickel and gold (Ti/Al/Ni/Au), which are the most used in current technologies.
  - Besides, the high top contact resistivity for layers with Al mole fractions above 0.36 caused by the decrease of the carrier concentration leads to find a way to *n*-dope the III-nitride layer. In that sense, it is possible to use a silicon target in the RF sputtering system to dope $Al_xIn_{1-x}N$ layers with high Al content.
- On the other hand, the simulation results obtained through this thesis and the reflectance measurements of the $Al_xIn_{1-x}N$ layers reveals the importance of developing anti-reflective layers in order to improve the optical properties of the material and thus the efficiency of the device. There are several materials, such as indium tin oxide (ITO) or ZnO doped with Al (AZO) that can be used as anti-reflective layers to analyze their effect on the devices. In addition, the index of refraction of these materials and their thickness should be optimized.

- Furthermore, the study of the photoelectrical properties as a function of the growth temperature shows an improvement on the device properties when the temperature increases. In that sense, we propose a study of the layer and device properties at higher temperatures than 550°C, taking into account that the limit of growth temperature of the RF sputtering system of the University of Alcala facilities is close to 650°C. However, the outgassing process and the growth process can be analyzed at higher temperature than 550°C in order to achieve better crystal quality and improve the AlInN/Si interface.
- Finally, as observed in chapter 6, the passivation of the silicon substrate leads to an increase of the device efficiency. In that sense, the use of a thin silicon nitride (SiN) layer to passivate the front surface of the silicon substrate could be studied in order to improve device efficiency. In order to optimize the SiN layer, the time and the flow of nitrogen should be studied. Furthermore, the chemical cleaning process of electronic devices based on Si is usually based on several steps and includes the use of acids such as sulfuric and hydrofluoric. Therefore, in order to improve the device efficiency it would be necessary to optimize this process and include the cleaning of the substrate with hydrofluoric acid.

Although these are the main ways of developing the devices, there are many others studies to be developed such as the study of gradual AlInN junctions and AlInN multijunctions with different Al contents (bandgap energy) and the growth of multicrystalline silicon substrates by RF sputtering to reduce the oxide layer at the interface.

References

[Ama16] A. Amal, F. Po-Han, K.Y. Lai, W. Hsin-Pin, L. Lain-Jong and H. Jr-Hau, Efficiency Enhancement of InGaN-Based Solar Cells via Stacking Layers of Light-Harvesting Nanospheres. Scientific Reports, 6, 28671, (2016).

[Abh04] J. Abhishek, R. Srinivasan and M.R. Joan, Evolution of surface morphology and film stress during MOCVD growth of InN on sapphire substrates, Journal of Crystal Growth, Vol 269, Iss 1,128-133, (2004).

[Afz14]N. Afzal, M. Devarajan and K. Ibrahim, Growth of polycrystalline indium aluminum nitride thin films on silicon (111) substrates, Materials Science in Semiconductor Processing, 27, 975–984, (2014).

[Afz15] N. Afzal, M. Devarajan, K. Ibrahim, Growth of AlInN films via elemental layers annealing at different temperatures, Modern Physics Letters B 29 (28), 1550169, (2015).

[Afz16]N. Afzal, M. Devarajan and K. Ibrahim, A comparative study on the growth of InAlN films on different substrates, Materials Science in Semiconductor Processing, 51, 8–14, (2016).

[Aka97] I. Akasaki and H. Amano, Crystal Growth and Conductivity Control of Group III Nitride Semiconductors and Their Application to Short Wavelength Light Emitters, Japanese Journal of Applied Physics, 36 (9A): 5393, (1997).

[Ale06] M. Alevli, G. Durkaya, A. Weerasekara, A. G. U. Perera, and N. Dietza, Characterization of InN layers grown by high-pressure chemical vapor deposition, Applied Physics Letters, 89, 112119, (2006).

[Amb98] O. Ambacher, Growth and applications of group III-nitrides, Journal of Applied Physics D: Applied Physics Bd. 31, Num 20, 2653-2710, (1998).

[Ame09] T. Ameri, G. Dennler, C. Lungenschmied and C. J. Brabec, Organic tandem solar cells: A review, Energy and Enviromental Science, 2, 347–363, (2009).

[Ami11] M. Amirhoseiny, Z. Hassan, S.S. Ng, M.A. Ahmad, Characterizations of InN thin films grown on Si (110) substrate by reactive sputtering, Journal of Nanomaterials Bd, 579427, 1-7, (2011).

[And19] R. L. C. Andreani, A. Bozzola, P. Kowalczewski, M. Liscidini and L. Redorici, Silicon solar cells: toward the efficiency limits, Advances in Physics: X, 4:1, 1548305, (2019).

[Anj18] F. Anjum, R. Ahmad, N. Afzal and G. Murtaza, Characterization of InN films prepared using magnetron sputtering at variable power, Materials Letters, 219, 23-28, (2018).

[Aub89] J.J. Aubert and J.J. Bacmann, Czochralski growth of silicon bicrystals, Revue de Physique Appliquée, Vol 22, Num 7, (1987).

[Aza18] M. Azadmand, L. Barabani, S. Bietti, D. Chrastina, E. Bonera, M. Acciarri, A. Fedorov, S. Tsukamoto, R.Nötzel and S. Sanguinetti, Droplet Controlled Growth Dynamics in Molecular Beam Epitaxy of Nitride Semiconductors, Scientific Reports, vol 8, Article number: 11278, (2018).

[Bab13] M. Babar, A. A. Rizvi, E. A. Al-Ammar and N. H. Malik, Analytical Model of Multi-junction Solar Cell, Arabian Journal for Science and Engineering,39, 547–555, (2014).

[Bae05] D. Baek, S. Rouvimov, B. Kim, T.C. Jo and D. Schroder. Surface recombination velocity of silicon wafers by photoluminescence, Applied Physics Letters, 86,11, (2005).

[Bai18] T. Baines, T. P. Shalvey and J. D. Major, A Comprehensive Guide to Solar Energy Systems, Academic Press, 215-232, (2018).

[Bas03] P.A. Basore and D.A. Clugston, Pc1d Version 5.9, Sydney, Australia: Univ. New South Wales, (2003).

[Bas10] S. Baskaran, Structure and regulation of yeast glycogen synthase, Ph. D. thesis in the Department of Biochemistry and Molecular Biology Indiana University, (2010).

[Bas18] U. Bashir, Z. Hassan, N.M. Ahmed and N. Afzal, Structural, electrical and optical properties of sputtered-grown InN films on ZnO buffered silicon, bulk GaN, quartz and sapphire substrates, Journal of Electronic Materials, 47 (8), (2018).

[Ber99] F. Bernardini and V. Fiorentini, Spontaneous versus piezoelectric polarization in III-V nitrides: Conceptual aspects and practical consequences, Physica Status Solidi (b) Bd. 216, Num 391, 391-398, (1999).

[Ber01] F. Bernardini and V. Fiorentini, Nonlinear macroscopic polarization in III-V nitride alloys, Physical Review B Bd. 65, 129903, (2001).

[Ber08] J. C. Bernède, Organic photovoltaic cells: History, principle and techniques, Journal of Chilean Chemical Society, 53, Nº 3, (2008).

[Ber13] C. Berger, A. Dadgar, J Blasing, and K. Alois, In-situ growth monitoring of AlInN/GaN distributed Bragg reflectors for the UV-spectral range, Journal of Crystal Growth Bd. 370, 87-91, (2013).

[Ber15] C. Berger, A. Dadgar, J Blasing, A. Lesnik, P. Veit, G. Schmidt, T. Hempel and J. Christen, Growth of AlInN/GaN distributed bragg reflectors with improved interface quality, Journal of Crystal Growth Bd. 414, 105-109, (2015).

[Bhu03] A.G. Bhuiyan, A. Hashimoto and A. Yamamoto. Indium nitride (InN): A review on growth, characterization and properties. Journal of Applied Physics Bd. 94, Nr.5, 2779-2808, (2003).

[Bhu03a] A.G. Bhuiyan, K. Sugita, K. Kasashima, A. Hashimoto, A. Yamamoto and V.Y. Davydov, Single-crystalline InN films with an absorption edge between 0.7 and 2 eV grown using different techniques and evidence of the actual band gap energy, Applied Physics Letter, 84, 452, (2004).

[Bhu12] A.G. Bhuiyan, K. Sugita, A. Hashimoto, and A. Yamamoto, InGaN Solar Cells: Present State of the Art and Important Challenges, IEEE Journal of Photovoltaics, Vol. 2, Num. 3, (2012).

[Bi05] Z.X. Bi, R. Zhang, Z. L. Xie, X. Q. Xiu, Y. D. Ye, B. Liu, S. L. Gu, Y. Shi, Y.D. Zheng, the Temperature Dependence of In Desorption during InN Growth and Annealing, Materials Science Forum, Vol 475-479, 3717-3720, (2005).

[Bla18] R. Blasco, A. Núñez-Cascajero, M. Jiménez-Rodríguez, D. Montero, L. Grenet, J. Olea, F. B. Naranjo, and S. Valdueza-Fe lip, Influence of the AlInN Thickness on the Photovoltaic Characteristics of AlInN on Si Solar Cells Deposited by RF Sputtering, Physica Status Solidi A, 1800494, (2018).

[Bla18] R. Blasco, A. Núñez-Cascajero, A. Ajay, E. Monroy, S. Valdueza-Felip, F.B. Naranjo, Low-to-mid Al content AlInN layers deposited on Si(100) and Si(111) by RF sputtering, presented at the Compound Semiconductor Week (CSW), Boston, United States, (2018).

[Bla19] R. Blasco, D. Montero, A.Braña, J. Olea , F. B. Naranjo and S Valdueza-Felip, AlInN on silicon heterojunctions deposited by RF sputtering for solar cell applications. Influence of Al mole fraction, presented at the Reunión española de optoelectrónica (Optoel), Zaragoza, Spain, (2019).

[Bor16] B. Bora, O.S. Sastry, R. Singh, M. Bangar, S. Rai, Renu, Y.K. Singh, B.K. Das, F. Azlan, P. Anand, R. Kuber and V. Krishnan, Series Resistance measurements of Solar PV Modules using Mesh in Real outdoor condition, Energy Procedia, 90, 503-508, (2016).

[Boy10] M.T. Boyd, Evaluation and validation of equivalent circuit photovoltaic solar cell performance models, Ph.D. thesis at the University of Wisconsin-Madison, (2010).

[Bra13] W. Bragg, The structure of some crystals as indicated by their diffraction of X-rays, Proceedings of the Royal Society A, 89(610), 248, (1913).

[But05] K.S.A. Butcher and T.L. Tansley. InN, latest development and a review of the bandgap controversy. Superlattices and Microstructures Bd. 38, Nr. 1, 1-37, (2005).

[But06] K.S.A. Butcher, H. Hirshy, R. M. Perks, M. Wintrebert-Fouquet and P. P-T. Chen, Stoichiometry effects and the Moss–Burstein effect for InN, Physica Status Solidi A, 203, 66-74, (2006).

[Cai09] X.M. Cai, F. Ye, Y.Q. Hao, D.P. Zhang, Z.H. Zhang and P. Fan, The properties of direct current sputtering deposited InN thin films under different gas flow rates, Journal of Alloys and Compounds, 484, 677–681, (2009).

[Cao02] X. A. Cao, K. Topol, F. Shahedipour-Sandvik, J. Teetsov, P.M. Sandvik, S. F. LeBoeuf, A. Ebong, J. Kretchmer, E. B. Stokes, S. Arthur, A. E. Kaloyeros and D. Walker, Influence of defects on electrical and optical characteristics of GaN/InGaN based light-emitting diodes, Proceedings of SPIE - The International Society for Optical Engineering, 4776, (2002).

[Car93] E. Cartier, J.H. Stathis and D.A. Buchanan, Passivation and depassivation of silicon dangling bonds at the Si/SiO2 interface by atomic hydrogen, Applied Physics Letters, 63 (11), (1993).

[Cha54] D. M. Chapin, C. S. Fuller, *and* G. L. Pearson, A New Silicon *p-n* Junction Photocell for Converting Solar Radiation into Electrical Power, Journal of Applied Physics 25, 676, (1954).

[Cha12] A. Chaoumead, Y. M. Sung, and D.J. Kwak, The Effects of RF Sputtering Power and Gas Pressure on Structural and Electrical Properties of ITO Thin Film, Advances in Condensed Matter Physics, vol. 2012, Article ID 651587, 7 pages, (2012).

[Cha17] H. Chandrasekar, K. N. Bhat, M. Rangarajan, S. Raghavan and N. Bhat, Thickness Dependent Parasitic Channel Formation at AlN/Si Interfaces, 7, 15749, (2017).

[Che03] H. Cheng, Y. Sun and P. Hing, The influence of deposition conditions on structure and morphology of aluminum nitride films deposited by radio frequency reactive sputtering, Thin Solid Films, 434 (1-2), 112, (2003).

[Che05] F. Chen, A.N. Cartwright, H. Lu and W.J. Schaff, Temperature dependence of carrier lifetimes in InN, Physica Status Solidi A, 202, 768-772, (2005).

[Che12] W.C. Chen and S.Y. Kuo, Study of High Quality Indium Nitride Films Grown on Si (100) Substrate by RF-MOMBE with GZO and AlN Buffer Layers, Journal of Nanomaterials Special issue on Functional Nanomaterials for Optoelectric Conversion and Energy Storage Volume 2012, Num 1, (2012).

[Che14] W.C. Chen, Y.H. Wu, C.Y. Peng, C.N. Hsiao and L. Chang, Effect of In/Al ratios on structural and optical properties of InAlN films grown on Si(100) by RF-MOMBE, Nanoscale Research Letters, Bd. 9,Nr. 1, 1-7,(2014).

[Che14] W.C. Chen, Y.H. Wu, J. Tian, T.C. Yen, P.Y. Lin, J.Y. Chen, C.N. Hsiao and L. Chang, Effect of Growth Temperature on Structural Quality of InxAl1-xN Alloys on Si (111) Substrate by RF-MOMBE, ISRN Nanomaterials Bd. (2014).

[Cho14] S.B Cho, H.S. Kim and J.Y. Huh, Mechanism underlying the beneficial effect of forming gas annealing on screen-printed Ag contacts of crystalline Si solar cells, Acta Materialia, Vol 70, Pag 1-7, (2014).

[Col13] R. Collazo and N. Dietz, The Group III-Nitride Material Class: from Preparation to Perspectives in Photoelectrocatalysis, Preprint of book chapter 8: Photoelectrochemical Water Splitting: Issues and Perspectives, ed. H-J. Lewerenz and L.M. Peter (2013).

[Çör11] S. Çörekc¸ M. K. Öztürk, A. Bengi, M. Çakmak, S. ÖzÇelik and E. Özbay, Characterization of an AlN buffer layer and a thick-GaN layer grown on sapphire substrate by MOCVD, Journal of Materials Science, 46, 1606–1612, (2011).

[Dah10] R. Dahal, J. Li, K. Aryal, J. Y. Lin, and H. X. Jiang, InGaN/GaN multiple quantum well concentrator solar cells, Applied Physics Letters, 97, 7, (2010).

[Dar09] V. Darakchieva, N.P. Barradas, M.-Y. Xie, K. Lorenz, E. Alves, M. Schubert, P.O.Å. Persson, F. Giuliani, F. Munnik, C.L Hsiao, L.C. Chen, L.W. Tu, W.J. Schaff, Role of impurities and dislocations for the unitentionial n-type conductivity in InN, Physica B: Condensed Matter, 404, 4476-4481, (2009).

[Dar10] V. Darakchieva, K. Lorenz, N.P. Barradas, E. Alves, B. Monemar, M. Schubert, N. Franco, C.L Hsiao, L.C. Chen, W.J. Schaff, L.W. Tu, T. Yamaguchi, Y. Nanishi. Hydrogen in InN: A ubiquitous phenomenon in molecular beam epitaxy grown material. Applied Physics Letters, 96, 081907, (2010).

[Den03] X.Deng and E. A. Schiff, Amorphous Silicon–based Solar Cells, Handbook of Photovoltaic Science and Engineering, ISBN: 0-471-49196-9, (2003).

[Dob12] L.A. Dobrzański, A. Drygała, M. Giedróc and M. Macek, Monocrystalline silicon solar cells applied in photovoltaic system, Journal of Achievements in Materials and Manufacturing Engineering, Vol 53, Iss1,(2012).

[Dob13] L.A. Dobrzański, M. Szczęsna, M. Szindler and A. Drygała, Electrical properties mono- and polycrystalline silicon solar cells, Journal of Achievements in Materials and Manufacturing Engineering, Vol 59,Iss 2,(2013).

[Don09] C. J. Dong, M. Xu, Q. Y. Chen, F. S. Liu, H. P. Zhou, Y. Wei, and H. X. Ji, Growth of well-oriented $Al_xIn_{1-x}N$ films by sputtering at low temperature, Journal of Alloys and Compounds, 479, 812-815, (2009).

[Emi11] S. Emin, S. P. Singh, L. Han, N. Satoh and A. Islam, Colloidal quantum dot solar cells, Solar Energy, 85, 1264–1282, (2011).

[Esp15] N. Espinosa, S. Schwarz, V. Cimalla and O. Ambacher, Detection of different target-DNA concentrations with highly sensitive AlGaN/GaN high electron mobility transistors, Sensors and Actuators B: Chemical Bd. 210, 633-639, (2015).

[Fab14] C.A.M. Fabien, and W.A. Doolittle, Guidelines and limitations for the design of high efficiency InGaN single junction solar cells, Solar Energy Materials and Solar cells, Vol. 130, pp.354-363, (2014).

[Fan12] H. Fang, J. Tian, Q. Zhang, Y. Pan and S. Wang, Study of melt convection and interface shape during sapphire crystal growth by Czochralski method, International Journal of Heat and Mass Transfer, Vol 55, Iss 25–26, 8003-8009, (2012).

[Fer00] C.S. Ferekides, D. Marinskiy, V. Viswanathan, B. Tetali, V. Palekis, P. Selvaraj and D.L. Morel, High efficiency CSS CdTe solar cells, Thin Solid Films, 361-362, 520-526, (2000).

[Fer17]R. A. Ferreyra, C. Zhu, A. Teke and H. Morkoç, Group III Nitrides, S. Kasap, P. Capper (Eds.), Springer Handbook of Electronic and Photonic Materials, DOI 10.1007/978-3-319-48933-9_31 (2017).

[Fre17] M. Frentrup, L.Y Lee, S.L.Sahonta, M.Kappers, F. Massabuau, P. Gupta, R. Oliver, C. Humphreys and D. Wallis, X-ray diffraction analysis of cubic zincblende III-nitrides, Journal of Physics D: Applied Physics, 50, 433002, (2017).

[Fri05] J. Friedrich and G. Müller, Methods for Bulk Growth of Inorganic Crystals: Crystal Growth, Encyclopedia of Condensed Matter Physics, Pages 262-274, (2005).

[Fur08] F. Futmayr, M. Vielemeyer, M. Stutzmann, J. Arbiol, S. Estradé, F. Peirò, J.R. Morante and M. Eickhoff, Nucleation and growth of GaN nanorods on Si (111) surfaces by plasma-assisted molecular beam epitaxy – The influence of Si- and Mg-doping, Journal of Applied Physics 104, 034309, (2008).

[Gib13] Z. M. Gibbs, A. LaLonde and G. J. Snyder, Optical band gap and the Burstein–Moss effect in iodine doped PbTe using diffuse reflectance infrared Fourier transform spectroscopy, New Journal of Physics 15(7):075020, (2013).

[Gil17] M. Gillinger, M. Schneider, A. Bittner, P. Nicolayand U. Schmid, Impact of annealing temperature on the mechanical and electrical properties of sputtered aluminum nitride thin films, Journal of Applied Physics 117, 065303, (2015).

[Gok13] S. Gokhale, K. Hima Nagamanasa, R. Ganapathy and A.K. Sood, Grain growth and grain boundary dynamics in colloidal polycrystals, Soft Matter, 29, (2013).

[Gra05] J. Grandal, M. Sanchez-Garcia, F. Calle and E. Calleja, Morphology and optical properties of InN layers grown by molecular beam epitaxy on Silicon substrates, Physica Status Solidi (c), 2, 2289 – 2292, (2005).

[Gre19] M. A. Green, E. D. Dunlop, D. H. Levi, J.Hohl-Ebinger, M. Yoshita and A.W.Y. Ho-Baillie, Solar cell efficiency tables (version 54), Progress in Photovoltaics: Research and Applications, 27, 7, 565-575, (2019).

[Guo 99] Q.X. Guo, N. Shingai, Y. Mitsuishi, M. Nishio and H. Ogawa, Effects of nitrogen/argon ratio on composition and structure of InN films prepared by r.f. magnetron sputtering, Thin Solid Films Bd. 343-344, S. 524-527, (1999).

[Guo03] Q.X. Guo, T. Tanaka, M. Nishio and H. Ogawa, Optical Bandgap Energy of Wurtzite In-Rich AlInN Alloys, Japanese Journal of Applied Physics, Volume 42, Part 2, Number 2B, (2203).

[Guo06] Q.X. Guo, T. Tanaka, M. Nishio and H. Ogawa, Deposition of InN thin films by radi frequency magnetron sputtering, Journal of Crystal Growth Bd, S. 466-470, 189-190, (1998).

[Guo08] Q.X. Guo, T. Tanaka, M. Nishio and H. Ogawa, Structural and optical properties of AlInN films grown on sapphire substrates, Japanese Journal of Applied Physics Bd. 47, Num 1S, S. 612, (2008).

[Guo09] Q. Guo, M. Ogata, Y. Ding, T. Tanaka and M. Nishio, Heteroepitaxial growth of InN layers on (111) silicon substrates, Journal of Crystal Growth, Vol 311, Iss 10, 2783-2786, (2009).

[Guo10] S. Guo, X. Gao, D. Gorka, J. W. Chung, H. Wang, T. Palacios, A. Crespo ,J. K. Gillespie, K. Chabak, M. Trejo, V. Miller, M. Bellot, G. Via, M. Kossler, H. Smith and D. Tomich, AlInN HEMT grown on SiC by metalorganic vapor phase epitaxy for millimeter-wave applications, Physica Status Solidi a, 207, 6, 1348-1352, (2010).

[Ha13] J. Ha, S. Park, D. Kim, J. Ryu, C. Lee, B. H. Hong and Y. Hong, High-performance polymer light emitting diodes with interface-engineered graphene anodes, Organic Electronics, 14, 2324–2330, (2013).

[Han10] Q. Han, C. Duan, G. Du, W. Shi, and L. Ji, Magnetron sputter epitaxy and characterization of wurtzite AlInN on Si (111) substrates, Journal of Electronic Materials, 39, 489, (2010).

[Har16] V. Harotoonian and J. Woodall, Growth and characterization of single crystalline InN growth on GaN by RF Sputtering for robust schottky contacts, Journal of Electronic Materials Bd 45, Num 12, 6305-6309, (2016).

[He10] H. He, Y. Cao, R. Fu, H. Wang, J. Huang, C. Huang, M. Wang and Z. Deng, Band gap energy and bowing parameter of In-rich InAlN films grown by magnetron sputtering, Applied Surface Science Bd. 256, Num 6, S. 1812-1816, (2010).

[Hsu08] L. Hsu and W. Walukiewicz, Modeling of InGaN/Si tandem solar cells, Journal of Applied Physics, 104, 024507, (2008).

[Hop17] H. Hoppe and N. S. Sariciftci, Polymer Solar Cells, Chapter *in* Advances in Polymer Science, (2007).

[Hor07] I. Horcas, R. Fernández, J.M. Gómez-Rodríguez, J. Colchero, J. Gómez-Herrero and M.A Baro, WSXM: A software for scanning probe microscopy and a tool for nanotechnology. Review of Scientific Instruments Bd, 78, Nr 1, 13705, (2007).

[Hör10] M. Hörteis, T. Gutberlet, A. Reller and S. W. Glunz, High Temperature Contact Formation on n-Type Silicon: Basic Reactions and Contact Model for Seed-layer Contacts. Advanced Functional Materials, 20, 476−484, (2010).

[Hou08] Y. Houchin, A. Hashimoto, A. Yamamoto, Atmospheric-pressure MOVPE growth of In-rich InAlN, Physica Status Solidi (c), 5:1571–1574, (2008).

[Hua12] J.Y. Huang, C.Y. Lin, C.-H. Shen, J.-M. Shieh and B.T. Dai, Low cost high-efficiency amorphous silicon solar cells with improved light-soaking stability, Solar Energy Materials & Solar Cells, 98, 277–282, (2012).

[Hum07] C. Hums, J. Bläsing, A. Dadgar, A. Diez, T. Hempel, J. Christen, A. Krost, K. Lorenz, and E. Alves, Metal-organic vapor phase epitaxy and properties of AlInN in the whole compositional range, Applied Physics Letters, 90, 022105, January 2007.

[Ift13] S. M. Iftiquar, Y. Lee, V. A. Dao, S. Kim and J. Yi, High efficiency heterojunction with intrinsic thin layer solar cell: A short review, Materials and process for energy: communicating current research and technological developments (A. Méndez-Vilas, Ed.), (2013).

[Ino04] S. Inoue, T. Namazu, T. Suda and K. Koterazawa, InN films deposited by rf reactive sputtering in pure nitrogen gas, Vacuum, 74, 443–448, (2004).

[Jai00] S.C. Jain, M. Willander, J. Narayan, and R. Van Overstraeten, III-nitrides: Growth, characterization, and properties, Journal of Applied Physics, 87, 965, (2000).

[Jai04] A. Jain, S. Raghavan and J.M. Redwing, Evolution of surface morphology and film stress during MOCVD growth of InN on sapphire substrates, Journal of Crystal Growth, Vol 269, Iss 1, 128-133, (2004).

[Jam08] M. Jamil, H. Zhao, J.B. Higgins and N. Tansu, Influence of growth temperature and V/III ratio on the optical characteristics of narrow band gap (0.77 eV) InN grown on GaN/sapphire using pulsed MOVPE, Journal of Crystal Growth, 310, 4947-4953, (2008).

[Jan08] O. K. Jani, "Development of wide-band gap InGaN solar cells for highefficiency photovoltaics," Ph.D. thesis at Georgia Instute of Technology. Atlanta, (2008).

[Jef10] Jeff Hetch: Photonic frontiers: Shortwave laser diodes: The quest for practical green laser diodes. URL http://www.laserfocusworld.com/articles/2010/12/photonic-frontiers-shortwave-laser-diodes-the-quest-for-practica-gree-laser-diode.html

[Jeo15] M.W. Jeong, S.W. Jeon, S.H. Lee and Y. Kim, Effective heat dissipation and geometric optimization in an LED module with aluminum nitride (AlN) insulation plate, Applied Thermal Engineering Bd. 76, 212-219, (2015).

[Jia08] L. F. Jiang, W.Z. Shen, H. Ogawa and Q.X Guo, Temperature dependence of optical properties in AlInN thin films, Proceedings of SPIE - The International Society for Optical Engineering 6984, (2008).

[Jia09] L. F. Jiang, W.Z. Shen and Q.X Guo, Temperature dependence of the optical properties of AlInN, Journal of Applied Physics 106(1):013515 - 013515-8, (2009).

[Kar97] S. Karmann, H.P.D. Schenk, U. Kaiser, A. Fissel and W. Richter, Growth of columnar aluminum nitride layers on Si (111) by molecular beam epitaxy, Materials Science and Engineering B, Bd. 50, 228-232, (1997).

[Kel03] S. Keller and S. P. DenBaars, Metalorganic chemical vapor deposition of group III nitrides—a discussion of critical issues, Journal of Crystal Growth, Vol 248,479-486, (2003).

[Kis90] T. J. Kistenmacher, W. A. Bryden, J. S. Morgan, and T. O. Poehler, Characterization of rf-sputtered InN films and AlN/InN bilayers on (0001) sapphire by the x-ray precession method, Journal of Applied Physics 68, 1541 (1990).

[Kit96] C. Kittel, Introduction to Solid State Physics, 7th edition, John Wiley & Sons, Inc, pp 592–593, (1996).

[Kit08] H. Kitagawa, T. Suto, M. Fujita, Y. Tanaka, T. Asano, S. Noda, Green Photoluminescence from GaInN Photonic Crystals, Applied Physics Express 1, 032004, (2008).

[Kne07] M. Kneissla, Z. Yang, M.Teepe, C. Knollenberg, O. Schmidt, P.Kiesel, and N.M. Johnson, Ultraviolet semiconductor laser diodes on bulk AlN, Journal of Applied Physics 101, 123103, (2007).

[Kra15] L. Kranz, A. Abate, T. Feurer, F. Fu, E. Avancini, J. Löckinger, P. Reinhard, S. M. Zakeeruddin, M. Grätzel, S. Buecheler, and A. N. Tiwari, High-Efficiency Polycrystalline Thin Film Tandem Solar Cells, Journal of Physical Chemistry Letters 6, 14, 2676-2681, June 2015.

[Kro10] A. Krost, C. Berger, J. Blasing, A. Franke, T. Hempel, A. Dadgar and J. Christen, Strain evaluation in AlInN/GaN bragg mirrors by in situ curvature measurements and ex situ x-ray grazing incidence and transmission scattering, Applied Physics Letters Bd. 97, Num 18, 3-6, (2010).

[Kry07] O. KrylIouk, H. J. Park, Y. S. Won, T.Anderson, A. Davydov, I. Levin, J. H. Kim and J. A. Freitas Jr, Controlled synthesis of single-crystalline InN nanorods, IOP Publishing Ltd, Nanotechnology, Vol 18, Num 13, (2007).

[Kua12] X.P. Kuang, H.Y Zhang, G.G. Wang, L. Cui, C. Zhu, L. Jin, R. Sun and J.C. Han, AlN films prepared on 6H-SiC substrates under various sputtering pressures by RF reactive magnetron sputtering, Applied Surface Science, Bd. 263, S. 62-68, (2012).

[Kum17] A. Kumar, R.P Yadav, V. Janyani and M. Prasad, Structural study of aluminum nitride thin film grown by radio frequency sputtering technique, International Conference on Computer, Communications and Electronics (Comptelix), (2017).

[Lal17] N.N Lal, Y. Dkhissi, W. Li, Q. Hou, Y-B. Cheng adn U. Bach, Perovskite tándem solar cell, Advanced Energy Materials, 1602761, (2107).

[Lan90] M. Lannoo, The role of dangling bonds in the properties of surfaces and interfaces of semiconductors, Revue de Physique Appliquee, 25 (9), 887-894, (1990).

[Laz13] S. Lazarev, X-ray investigation of defects in III-Nitrides andtheir alloys, Ph.D thesis at Fakultätfür Physik des Karlsruher Instituts für Technologie (KIT), (2013).

[Ler99] M. Leroux, N. Grandjean, B, Beaumont, G. Nataf, F. Semond, J. Massies and P. Gibart, Temperature quenching of photoluminescence intensities in undoped and doped GaN, Journal of Applied Physics Bd, 86, Nr 7, 3721-3728, (1999).

[Li17] H.Z. Li, R. Li, J.H. Liu, J.H. Han and M. Huang, Morphology and Optical Properties of RF Sputtering Deposited Indium Nitride Layers Under Different N 2 /Ar Ratio. Journal of Nanoscience and Nanotechnology. 17, 524-529, (2017).

[Lio04] B.T. Liou, S.H. Yen and Y.K. Kuo, Vegard´s law deviation un band gaps and bowing parameters of the wurtzite III-nitride ternary alloys, Semiconductors Laser and Applications li Bd. 5628, 296-305, (2004).

[Lio11] B. W. Liou, Design and fabrication of $In_xGa_{1-x}N$/GaN solar cells with a multiple-quantum-well structure on SiCN/Si (111) substrates, Thin Solid Films, vol. 520, no 3, 1084–1090,(2011).

[Lil12] L. Liljeholm, Reactive sputter deposition of functional thin films, Digital comprehensive summaries of Uppsala dissertations form the faculty of science and technology, 965, 2012.

[Liu12] H. F. Liu, C. C. Tan, G. K. Dalapati, and D. Z. Chi. Magnetron-sputter deposition of high-indium-content n-AlInN thin film on p-Si (001) substrate for photovoltaic applications, Journal of Applied Physics, 112, 063114, (2012).

[Liu13] H. F. Liu, S. B. Dolmanan, S. Tripathy, G. K. Dalapati, C. C. Tan and D. Z. Chi, Effects of AlN thickness on structural and transport properties of In-rich n-AlInN/AlN/p Si(0 0 1) heterojunctions grown by magnetron sputtering, Journal of Physics D: Applied Physics, 46, 095106, (2013).

[Liu17] Z. Liu, D. Li, S. Wei, W. Wang, F. Tian, K. Bao, D. Duan, H. Yu, B. Liu and T. Cui, Bonding properties of aluminum nitride at high pressure, Inorganic Chemistry, 56, 13, 7494-7500, (2017).

[Lob16] D. N. Lobanov, A. V. Novikov, B. A. Andreev, P. A. Bushuykin, P. A. Yunin, E. V. Skorohodov and L. V. Krasilnikova, Features of InN growth by nitrogen-plasma-assisted MBE at different ratios of fluxes of group-III and -V elements, Semiconductors Februar, Vol 50, Iss 2, 261–265, (2016).

[Lu13] N. Lu and I. Ferguson, III-nitrides for energy productions: photovoltaic and thermoelectric applications, Semiconductor Science and Technology, 28, 7, 074023, (2013).

[Luc19] J.A. Luceño-Sanchez, A.M. Diez-Pascial and R. Peña Capilla, Materials for Photovoltaics: State of Art and Recent Develpoments, International Journal of Molecular Sciences, 20, 976, (2019).

[Luo17] T.T. Luong, F. Lumbatoruan, Y.Y. Chen, Y.T. Ho, Y.C. Weng, Y.C. Lin, S. Chang and E.Y. Chang, RF loss mechanisms in GaN-based high-electron-mobility-transistor on silicon: Role of an inversion channel at the AlN/Si interface, Physica Status Solidi A, 214, Num 7, 1600944, (2017).

[Mar97] I. Mártil, E. Redondo, and A. Ojeda, Influence of defects on the electrical and optical characteristics of blue light-emitting diodes based on III–V nitrides, Journal of Applied Physics, 81(5), 2442 – 2444, (1997).

[Mas05] M. Mastro, O. Kryliouk, T. Anderson, A. Davydov and A. Shapiro, Influence of polarity on GaN thermal stability, Journal of Crystal Growth, 274, 38, 646, (2005).

[Mat99] T. Mattila and A. Zunger, Predicted bond length variation in wurtzite and zinc-blende InGaN and AlGaN alloys, Journal of Applied Physics,85, 160, (1999).

[Mal03] V. Malakhov, Potential PV materials-based InN thin films: Fabrications, structural and optical properties, Solar Energy Materials and Solar Cells Bd. 76, Num 4, 637-646, (2003).

[Mar96] A. Martí and G.L. Araújo, Limiting efficiencies for photovoltaic energy conversión in multigap systems, Solar Energy Materias and Solar Cells, 43, 203-222, (1996).

[Mon16] L. Monteagudo-Lerma, S. Valdueza-Felip, A. Núñez-Cascajero, A. Ruiz, M. González-Herráez, E. Monroy and, F.B. Naranjo, Morphology and arrangement of InN nanocolumns deposited by radio-frequency sputtering: Effect of the buffer layer, Journal of Crystal Growth, Vol 434, 13-18, (2016).

[Mot02] Motlan, E.M. Goldy and T.L. Tansley, Optical and electrical properties of InN grown by radio-frequency reactive sputtering, Journal of Crystal Growth, Vol 241, Iss 1–2, 165-170, (2002).

[McL13] D. V. P. McLaughlin and J. M. Pearce, Progress in Indium Gallium Nitride Materials for Solar Photovoltaic Energy Conversion Metallurgical and Materials Transactions A44(4) pp. 1947-1954 (2013).

[Muk15] A. Mukhtarova, Puitsquantiques de composésnitruresInGaN/GaN pour le photovoltaïque, Ph.D thesis in Laboratoire Nano-Physique et Semi-Conducteurs, CNRS/CEA/UJF-Grenoble, (2015).

[Muz15] G. Muziol, M. Siekacz, H. Turski, P. Wolny, S. Grzanka, E. Grzanka, A. Feduniewicz-Zmuda and J. Borysiuk, High power nitride laser diode grown by plasma assited molecular beam epitaxy, Journal of Crystal Growth Bd. 425, 398-400, (2015).

[Nao07] H. Naoi, K. Fujiwara, S. Takado, M. Kurouchi, D. Muto, T. Araki, H. Na and Y. Nanishi, Growth of in-rich in x Al 1-x N films on (0001) sapphire by RF-MBE and their properties, Journal of Electronic Materials Bd. 36, Nr. 10, 1313-1319, (2007).

[Nay12] P.K. Nayak, G. Garcia-Belmonte, A. Kahn, J. Bisquert and D. Cahen, Photovoltaic efficiency limits and material disorder, Energy & Environmental Science, 5 (3), 6022-6039, (2012).

[Naz11] Md. K. Nazeeruddin, E. Baranoff and M. Grätzel, Dye-sensitized solar cells: A brief overview, Solar Energy, 85, 1172–1178, (2011).

[Neb12] E. Neburchilova, A. Osipov, L. Rubin, T. Wardle, W. Zhu, Surface Passivation of Silicon by Electrochemically Formed Oxide Layers, Energy Procedia, Vol 27, 372-378, (2012).

[Neu96] A. D. Neumayer and G.J. Ekerdt, Growth of group III nitrides, A review of precursors and techniques, Chemistry of Materials Bd 8, Nr 1, 9-25, (1996).

[Nuñ16] A. Nuñez-Cascajero, L. Monteagudo-Lerma, S. Valdueza-Felip, C. Navio, E. Monroy, M. Gonzalez-Herraez, and F.B. Naranjo, Study of high In-content AlInN deposition on p-Si (111) by RF-sputtering, Japanese Journal of Applied Physics, 55, 05FB07, (2016).

[Nuñ17] A. Nuñez-Cascajero, S. Valdueza-Felip, L. Monteagudo-Lerma, E. Monroy, E. Taylor-Shaw, R.W. Martin M. Gonzalez-Herraez, and F.B. Naranjo, In-rich $Al_xIn_{1-x}N$ grown by RF-sputtering on sapphire: from closely-packed columnar to high-surface quality compact layers, Journal of Physics D: Applied Physics, 50, (2017).

[Nuñ17b] A. Núñez-Cascajero. PhD Thesis Development of Nitrides based on InN for sensor applications, University of Alcalá, (2017).

[Nuñ18] A Núñez-Cascajero, R. Blasco, S Valdueza-Felip, D. Montero, J. Olea and F. B. Naranjo, Quality improvement of AlInN/p-Si heterojunctions with AlN buffer layer deposited by RF-sputtering, Journal of Alloys and Compounds, Vol 769, (2018).

[Nuñ19] A Núñez-Cascajero, R. Blasco, S Valdueza-Felip, D. Montero, J. Olea and F. B. Naranjo High quality $Al_{0.37}In_{0.63}N$ layers grown at low temperature (<300°C) by radio-frequency sputtering, Material Science in Semiconductor Processing, 100, 8-14, (2019).

[Opo16] C. Opoku, R. Sporea, V. Stolojan, S.R. Silva and M. Shkunov, Source-Gated Transistors Based on Solution Processed Silicon Nanowires for Low Power Applications, Advanced Electronic Materials, 3, 1600256, (2016).

[Pai85] C. S. Pai, E. Cabreros, and S. S. Lau, Rapid thermal annealing of Al-Si contacts, Applied Physics Letters, 46, 652, (1985).

[Pam17] P. Pampili and P. J. Parbrook, Doping of III-nitride materials, Materials Science in Semiconductor Processing, Vol 62, 180-191, (2017).

[Par05] I.K. Park, M.K. Kwon, S.H. Baek, Y.W. Ok, T.Y.Seong, and S.J. Park, Enhancement of phase separation in the InGaN layer for self-assembled In-rich quantum dots, Applied Physics Letters**87**, 061906,(2005).

[Pat39] A. L. Patterson, The Scherrer Formula for X-Ray Particle Size Determination, Physical Review, **56**, 978, (1939).

[Pc2d] www.pc2d.info

[Pra09] J. Prazmowska, R. Korbutowicz, M. Wosko, R. Paszkiewicz, J. Kovac, R. Srnanekand M. Tłaczała, Influence of AlN Buffer Layer Deposition Temperature on Properties of GaN HVPE Layers, Proceedings of the III National Conference on Nanotechnology NANO (2009).

[Pri17] M. Pristovsek, A. Bao, and R. A. Oliver, Effect of wavelength and defect density on the efficiency of InGaN based light emitting diodes, DOI: 10.17863/CAM.12709, (2017).

[Ram17] J. Ramanujam and U. P. Singh, Copper indium gallium selenide based solar cells – a review, Energy and Enviromental Science, 10, 1306, (2017).

[Ras16] M. A. K. Rash, Structure, morphology, optical and electrochemical properties of indium- and aluminum-based nitride thin films deposited by plasma-assisted reactive evaporation, Ph. D thesis at faculty of science University of Malaya Kuala Lumpur, (2016).

[Rau11] H. K. Raut, V. Anand, A. Sreekumaran and S. Ramakrishna, Anti-reflective coatings: A critical, in-depth review, Energy and Enviromental Science, 4, 3779, January 2011.

[Rig20] G.C. Righini and F. Enrichi, Solar Cells and Light Management, Materials, Strategies and Sustainability, Chapter 1, (2020).

[Rou17] S. R. Routray and T. R. Lenka, InGaN-based solar cells: a wide solar spectrum harvesting technology for twenty first century, CSI Transactions on ICT, Vol 6, 1, 83–96, (2017).

[Rum01] S. Rumyantsev, M. Shur and M. Levinshtein Properties of advanced semiconductor materials, .New York, NY, USA, Wiley-interscience, pp.1-66,(2001). [Online].Available:https://www.researchgate.net/publication/289099215_Properties_of_advanced_semiconductor_materials_GaN_AIN_InN_BN_SiC_SiGe.

[Sal18] M. Saliba, J.P. Correa-Baena, C. M. Wolff, M. Stolterfoht, N. Phung, S. Albrecht, D. Neher, and A. Abate, How to make over 20% efficient perovskite solar cells in regular (n-i-p) and inverted (p-i-n) architectures, Chemistry of Materials, 30, 13, (2018).

[Sag10] T. Saga, Advances in crystalline silicon solar cell technology for industrial mass production, NPG Asia Materials, 2, 96-102, (2010).

[Sai01] N. Saito and Y. Igasaki, Electrical and optical properties of InN films prepared by reactive sputtering, Applied Surface Science, Vol 169–170, 349-352, (2001).

[Sai02] Y. Saito, T. Yamaguchi, H. Kanazawa, K. Kano, T. Araki, Y. Nanishi, N. Teraguchi, A. Suzuki, Growth of high-quality InN using low-temperature intermediate layers by RF-MBE, Journal of Crystal Growth, Vol 237–239, Part 2, (2002).

[Sai15] I. Saidi, H. Mejri, M. Baira and H. Maaref, Electronic and transport properties of AlInN/AlN/GaN high electron mobility transistors, Superlattices and Microstructures Bd. 84, 113-125, (2015).

[Sas10] T. Sasaoka, M. Mori, T. Miyazaki and S. Adachi, Room-temperature infrared photoluminescence from sputter-deposited InN films, Journal of Applied Physics, 108 (6), (2010).

[Sch11] R. Schreiner, D. Fahle, B. Schineller, D. Brien, H. Kalisch, M.Heuken1, A. Vescan and G. Strauch, Growth of GaN, AlGaN and AlN Layers for LED Manufacturing: Investigations on Growth Conditions using a Hotwall MOCVD System, CS MANTECH Conference, Palm Springs, California, USA, (2011).

[Sch13] S. Schulz, M.A. Caro, L.T. Tan, P.J. Parbrook, R.W. Martin and E.P O`Reilly, Composition-dependent band gap and Band-edge bowing in AlInN: A combined theoretical and experimental study, Applied Physics Express Bd. 6, Num 12, 121001, (2013).

[Sch14] A. Schliwa, G.M.O Hönig and D. Bimberg, Electronic Properties of III-V Quantum Dots, Lecture Notes in Computational Science and Engineering 94:57-85, (2014),

[Sha18] K. Sharma, V. Sharma, and S. S. Sharma, Dye-Sensitized Solar Cells: Fundamentals and Current Status, Nanoscale Research Letters, 13: 381, (2018).

[Shi04] H. Shinoda and N. Mutsukura, Temperature dependence of InN film deposition by an RF plasma-assisted reactive ion beam sputtering deposition technique, Thin Solid Films, Vol 476, Iss 2, 276-279, (2004).

[Shi05] H. Shinoda and N. Mutsukura, Structural and optical properties of InN films prepared by radio frequency magnetron sputtering, Thin Solid Films, Vol 503, Iss 1–2, 8-12, (2005).

[Shi18] Z. Shi and A. H. Jayatissa, Perovskites-Based Solar Cells: A Review of Recent Progress, Materials and Processing Methods, Materials, 11, 729, (2018).

[Shu13] M. Shur, Physics of GaN-based Power Field Effect Transistors, ECS Transactions, 50,129-138, (2013).

[Sie17] N. Siemons, A. Serafini, Multiple Exciton Generation in Nanostructuresfor Advanced Photovoltaic Cells, Journal of Nanotechnology Volume 2018.

[Sim12] E. Simoen, D. Visalli, M. Van Hove1, M. Leys, P. Favia, H. Bender, G. Borghs, A.P.D. Nguyen and A. Stesmans, Electrically active defects at AlN/Si interface studied by DLTS and ESR, Physica Status Solidi A, vol. 209, 10, 1851–1856, (2012).

[Spe04] P. Specht, R. Armitage, J. Ho, E. Gunawan, Q. Yang, X. Xu, C. Kisielowski, E.R. Weber, The influence of structural properties on conductivity and luminescence of MBE grown InN, Journal of Crystal Growth, Vol 269, Issue 1, Pages 111-118, (2004).

[Sta00] C. Stampfl, C. G. Van de Walle, D. Vogel, P. Krüger, and J. Pollmann, Native defects and impurities in InN: First-principles studies using the local-density approximation and self-interaction and relaxation-corrected pseudopotentials, Physical Review B 61, R7846(R), (2000).

[Tan86] T.L. Tansley and C.P. Foley. Optical bandgap of indium nitride. Journal of Applied Physics. Bd 59, Nr. 9, 3241-3244, (1986).

[Tap10] K. Tapily, O. Moutanabbir, D. Gu, H. Baumgart, A. A. Elmustafa, Thermal Behavior of the Mechanical Properties of GaN throughout Hydrogen-Induced Thin Layer Transfer, ECS Transactions, 33 (4) 241-248, (2010).

[Ter06] W. Terashima, S.B. Chem, Y. Ishitani and A. Yoshikawa, Growth and characterization of AlInN ternary alloys in whole composition range and fabrication of InN/AlInN multiple quatum wells by RF molecular beam epitaxy, Japanese Journal of Applied Physics bd. 45, Num 21, L539-L542, (2006).

[Ton10] H. Tong, J. Zhang, G. Liu, J. A. Herbsommer, G. S. Huang, and N. Tansu, Thermoelectric properties of lattice-matched AlInN alloy grown by metal organic chemical vapor deposition, Applied Physic Letters, 97, 112105 (2010)

[Udd12] MD.R. Uddin, M. Pandikuntam V. Mansurov, S. Sohal, D. Myasischev, G.M. Guryanov, V. Kuryatkov, M. Holtz and S. Nikishin, Effect of growth temperature on indium incorporation in InAlN alloys grown by GSMBE on Si (111), Journal of Electronic Materials, Vol 41, Num 5, (2012).

[Val10] S. Valdueza-Felip, F.B. Naranjo, M. González-Herráez, L. Lahourcade, E. Monroy and S. Fernández, Influence of deposition conditions on nanocrystalline InN layers synthesized on Si (1 1 1) and GaN templates by RF sputtering, Journal of Crystal Growth, Vol 312, Iss 19, 2689-2694, (2010).

[Val11] S. Valdueza-Felip, Nitride-based semiconductor nanostructures for applications in optical communications at 1.5 μm, Ph.D thesis at Universidad de Alcala, (2011).

[Val12] S. Valdueza-Felip, J. Ibañez, E. Monroy, M. González-Herráez, L. Artús and F.B. Naranjo, Improvement of InN layers deposited on Si (111) by RF sputtering using a low-growth-rate InN buffer layer, Thin Solid Films Bd, 520, Num 7, 2805-2809, (2012).

[Val18] S. Valdueza-Felip, A. Núñez-Cascajero, R. Blasco, D. Montero, L. Grenet, M. de la Mata, S. Fernández, L. Rodríguez-De Marcos, S. I. Molina, J. Olea, F. B. Naranjo, Influence of the AlN interlayer thickness on the photovoltaic properties of In-rich AlInN on Si heterojunctions deposited by RF-sputtering, AIP Advances 8(11):115315, (2018).

[Var67] Y.P. Varshni, Temperature dependence of the energy gap in semiconductors, Physica Bd. 34, Num 1, 147-154, (1967).

[Veg21] L. Vegard, Die Konstitution der Mischkristalle und die Raumfüllung der Atome, In: - ZeitschriftfürPhysikBd, 5, Nr.1, S, 17-26, (1921).

[Vur01]I. Vurgaftman, J.R. Meyer and L. Ram-Mohan, Band parameters for III-V compound semiconductors and their alloys, Journal of Applied Physics Bd. 89, Num 11, 5815-5875, (2001).

[Vur03] I. Vurgaftman and J.R. Meyer, Band parameters for nitrogen-containing semiconductors, Journal of Applied Physics Bd, 94, Nr 6, 3675-3696, (2003).

[Wal96] C.G. Van de Walle and J. Neugebauer, Defects, Impurities and Doping Levels in Wide-Band-Gap Semiconductors, Brazilian Journal of Physics, 26, 163, (1996).

[Wal04] C.G. Van de Walle and J. Neugebauer, First-principles calculations for defects and impurities: Applications to III-nitrides, Journal of Applied Physics, 95, 3852, (2004).

[Wal04a] W. Walukiewicz, S.X. Li, J. Wu, K.M. Yu, J.W, Ager, E.E. Haller, H. Lu and W.J. Schaff, Optical properties and electronic structure of InN and In-rich group III-nitride alloys. Journal of Crystal Growth, 269 (1), 119, (2004). Proceedings of the first ONR International Indium Nitride Workshop.

[Wan08] H. Wang, Y. Zhao, X. Li, J. Li, Z. Zhang, S. Wan, W. Gu and F. Yang, Growth of well-oriented InN nanodots by magnetron sputtering with varying sputtering temperature, Journal of Vacuum Science & Technology B. 36, 041204, (2018).

[Wan09] Z. Wang, S. Tsukimoto, M. Saito, K. Ito, M. Murakami, and Y. Ikuhara, Ohmic contacts on silicon carbide: The first monolayer and its electronic effect, Physical Review B 80, 245303, (2009).

[Wan10] Z.Y. Wang, B.M. Shi, Y. Cai, W. Yue, H. Nikita and M. Xie, Molecular-beam epitaxy of AlInN: An effect of source flux and temperature on indium atom incorporation in alloys, Journal of Applied Physics, 108 (3), (2010).

[Wan11] Z. Wan, S. Huang, M. A. Green and G. Conibeer, Rapid thermal annealing and crystallization mechanisms study of silicon nanocrystal in silicon carbide matrix, Nanoscale Research Letters, Vol 6, Num. 129, (2011).

[Was92] K. Wasa and S. Hayakawa, Handbook of sputter deposition technology: principles, technology, and applications (Noyes Publications, 1992).

[Was04] K. Wasa, M. Haber and H. Adachi, Thin film materials technology, Sputtering of Compound Materials (William Andrew Inc, 2004).

[Wei15] C. Weisbuch, M. Piccardo, L. Martinelli, J. Iveland, J. Peretti and J. Speck, The efficiency challenge of nitride light-emittin diodes for lighting, Physica Status Solidi (a) Bd. 212, Num 5, 899-913, (2015).

[Wol17] F. Wolny, M. Müllera , A. Krause and H. Neuhaus, Study of the bulk lifetime and material saturation current density of different p-type monocrystalline silicon materials, Energy Procedia 124, 235–239, (2017).

[Wu02] J. Wu, W. Walukiewicz, K.M. Yu, J.W. Ager, E.E. Haller, L. Hai, W.J. Schaff, Small band gap bowing in $In_{1-x}Ga_xN$ alloys, Applied Physics Letters, 80, 4741–4743, (2002).

[Wu02] J. Wu, W. Walukiewicz, K.M. Yu, J.W. Ager, E.E. Haller, H. Lu, W.J. Schaff, Y. Saito, and Y. Nanishi, Unusual properties of the fundamental band gap of InN, Applied Physics Letters 80, 3967, (2002).

[Wu03] J. Wu and W. Walukiewicz, Band gaps of InN and group III nitride alloys, Superlattices and Microstructures, 34, (2003).

[Wu04] X. Wu, High-efficiency polycrystalline CdTe thin-film solar cells, Solar Energy, 77, 803–814, (2004).

[Wu09] J. Wu, When group-III nitrides go infrared: New properties and perspectives, Journal of Applied Physics Bd. 106, 1, 11101, (2009).

[Wu14] Y.H. Wu, Y.Y. Wong, W.C. Chen, D.S. Tsai, C.Y. Peng, J.S. Tian, L. Chang and E. Yi-Chang, Indium-rich InAlN films on GaN/sapphire by molecular beam epitaxy, Materials Research Express Bd. 1, S.15904, (2014).

[Wu15] H. Wu, R. Zheng, Y. Guo and Z. Yan, Fabrication and characterization of non-polar M-plane AlN crystals and LEDs, Materials Research Innovations, Vol 19 Suppl 5 S5-1153, (2015).

[Wür05] P. Würfel, Physiscs of solar cells: From principles to new conceptrs, Wiley-WCH: Weinheim, (2005).

[Xu03] K. Xu and A. Yoshikawa, Effects of film polarities on InN growth by molecular-beam epitaxy, Applied Physics Letters, 83, 251, (2003).

[Yac03] B. G. Yacobi, Semiconductor Materials: An Introduction to Basic Principles, Kluwer Academic Publishers, New York (2003).

[Yam94] A. Yamamoto, M. Tsujino, M. Ohkubo and A. Hashimoto, Metalorganic chemical vapor deposition growth of InN for InN/Si tandem solar cell, Solar Energy Materials and Solar Cells, Vol 35, 53-60, (1994).

[Yam09] T. Yamaguchi, D. Muto, T. Araki and Y. Nanishi, Growth and characterization of N-polar and In-polar InN films by RF.MBE, Journal of Crystal Growth Bd. 311, Nr.10, S.2780-2782, (2009).

[Yeh08] T.S. Yeh, J.M. Wu and W.H. Lan, Electrical properties and optical bandgaps of AlInN films by reactive sputtering, Journal of Crystal Growth, Vol 310, Iss 24, 5308-5311, (2008).

[Yim73] W. M. Yim, E. J. Stofko, P. J. Zanzucchi, J. I. Pankove, M. Ettenberg, and S. L. Gilbert Epitaxially grown AlN and its optical band gap, Journal of Applied Physics, 44, 292, (1973).

[Yu13] B. Yu and Q. Linmao, Effect of crystal plane orientation on the friction-induced nanofabrication on monocrystalline silicon, Nanoscale research letters, vol. 8, 1, 137. 25, (2013).

[Yu19] J. Yu, Z. Hao, J. Wang, J. Deng, W. Yu, L. Wang, Y. Luo, Y. Han, C. Sun, B. Xiong and H. Li, Study on AlN buffer layer for GaN on graphene/copper sheet grown by MBE at low growth temperature, Journal of Alloys and Compounds, Vol 783, 633-642, (2019).

[Zha09] W.M. Zhang, G. Meng, J.B. Zhou and J.Y. Chen, Nonlinear Dynamics and Chaos of Microcantilever-Based TM-AFMs with Squeeze Film Damping Effects, Sensors, 9, 3854-3874, (2009).

[Zou16] C. Zou, Q. Zhao, G. Zhang and B. Xiong, Energy revolution: From a fossil energy era to a new energy era, Natural Gas Industry B, Vol 3, Iss 1, 1-11, (2016).

List of publications

The following publications have provided the material for this doctoral dissertation.

International Journals

1. **Influence of the AlN interlayer thickness on the photovoltaic properties of in-rich AlInN on Si heterojunctions deposited by RF sputtering**, S. Valdueza-Felip, A Núñez-Cascajero, R. Blasco, D. Montero, L. Grenet, M. de la Mata, S. Fernández, L. Rodríguez-De Marcos, S.I. Molina, J. Olea and F.B. Naranjo, AIP Advances 8 (11), 115315, (2018).
2. **Quality improvement of AlInN/p-Si heterojunctions with AlN buffer layer deposited by RF-sputtering**, A. Núñez-Cascajero, S.Valdueza-Felip, R. Blasco, M. de La Mata, S.I. Molina, M. González-Herráez, E. Monroy and F.B. Naranjo, Journal of Alloys and Compounds 769, 824-830, (2018).
3. **Intersubband absorption in GaN nanowire heterostructures at mid-infrared wavelengths**, A. Ajay, R. Blasco, J. Polaczyński, M. Spies, M.I. Den Hertog and E Monroy, Nanotechnology 29 (38), 385201, (2018).
4. **Influence of the AlInN Thickness on the Photovoltaic Characteristics of AlInN on Si Solar Cells Deposited by RF Sputtering**, R. Blasco, A. Núñez-Cascajero, M. Jiménez-Rodríguez, D. Montero, L. Grenet, J. Olea, F. B. Naranjo and S.Valdueza-Felip, Physica Status Solidi (a) 216 (1), 1800494, (2018).
5. **High quality $Al_{0.37}In_{0.63}N$ layers grown at low temperature (< 300 C) by radio-frequency sputtering**, A. Núñez-Cascajero, R. Blasco, S. Valdueza-Felip, D. Montero, J. Olea and F.B. Naranjo, Materials Science in Semiconductor Processing 100, 8-14, (2019).
6. **Electrical and optical properties of heavily Ge-doped AlGaN**, R. Blasco, A. Ajay, E. Robin, C. Bougerol, K. Lorenz, L.C. Alves, I. Mouton, L. Amichi, A. Grenier and E. Monroy, Journal of Physics D: Applied Physics, (2019).

7. **Low-to-Mid Al Content (x= 0-0.56) $Al_xIn_{1-x}N$ Layers Deposited on Si (100) by Radio-Frequency Sputtering**, R. Blasco, S. Valdueza-Felip, D. Montero, M. Sun, J. Olea and F.B. Naranjo, Physica Status Solidi B, 1900575, (2020).

Submitted

1. **Design of n-AlInN on p-silicon heterojunction solar cells**, R. Blasco, F.B. Naranjo and S. Valdueza-Felip. Submitted to Materials Letters (2020).

2. **AlInN on Si solar cells with an Al content ranging from 0 to 56% deposited by RF sputtering**, R. Blasco, A. Braña, F. B. Naranjo and S. Valdueza-Felip, Submitted to Materials (2020).

National book chapters

1. **Design and optimization of thin film AlInN on Silicon junctions deposited by sputtering for solar cells**, R. Blasco, A. Nuñez-Cascajero, D. Montero, J. Olea, M. González-Herráez, F.B. Naranjo, S. Valdueza-Felip, Libro de Actas de la 10ª Reunión Española de Optoelectrónica, ISBN: 978-84-16989-81-2, (2017).
2. **Effect of AlN interfacila laye ron the photovoltaic properties of AlInN on Si (111) heterojunctions deposited by sputtering**, S. Valdueza-Felip, A. Nuñez-Cascajero, R. Blasco, D. Montero, L. Rodríguez, J.A. Méndez, J. Olea, M. González-Herráez, E. Monroy and F.B. Naranjo, Libro de Actas de la 10ª Reunión Española de Optoelectrónica, ISBN: 978-84-16989-81-2, (2017).
3. **Influencia del contenido de aluminio (0-60%) en hetereouniones de AlInN depositado sobre Si por RF sputtering Influence of the Al content (0-60%) on AlInN on Si heterojunctions deposited by RF sputtering**, R. Blasco, D. Montero , A. Braña, J. Olea , F.B. Naranjo , and S. Valdueza-Felip. Libro de Actas de la 11ª Reunión Española de Optoelectrónica.

Contributions to conferences

- 22 contributions to international (16) and national (6) conferences